Maximizing Solid-state NMR Sensitivity for Materials Science Characterization

by

Michelle Ha

A thesis submitted in partial fulfillment of the requirements for the degree of

Doctor of Philosophy

Department of Chemistry
University of Alberta

# Abstract

A major challenge that plagues nuclear magnetic resonance (NMR) spectroscopists is the inherently low sensitivity of this workhorse characterization technique. This low sensitivity results in long acquisition times and/or costly isotopic-labelling to obtain good resolution and signal-to-noise (S/N) ratios. Therefore, in this thesis, different approaches used to maximize NMR sensitivity are explored. While increasing the magnetic field strength or experimental time can aid in this dilemma, this is not always feasible. Thus, spectroscopic techniques can be used to alleviate these problems. Firstly, variable temperature NMR spectroscopy is explored to manipulate the different phases of organic/inorganic perovskite materials such that ordering about the $^{119}$Sn centre can be achieved. As more ordered samples provide better S/N with fewer number of experimental scans in comparison to amorphous (disordered) material, we can maximize NMR sensitivity, as well as remove anisotropic interactions which would result in spectral distortions. Another technique to improve sensitivity is to manipulate the magnetization of a highly abundant nucleus and transfer this magnetization to the insensitive nucleus of interest, namely cross-polarization (CP). This technique can be used to experimentally probe structural layers of a material, as well as minimize the time needed between each experiment. This is beneficial when studying $^{29}$Si nuclei in silicon nanoparticles as $^{29}$Si has very long relaxation delays. While CP can help with boosting NMR sensitivity, a sister technique, namely dynamic nuclear polarization (DNP) NMR spectroscopy, has become more popular in the recent decade due to its sensitivity enhancements over conventional methods. Thus, DNP NMR is utilized in the later part of this research to demonstrate the evolution of magnetic resonance techniques. One of the most challenging aspects for NMR-active nuclei are their natural abundances (for example: oxygen-17 has a natural abundance of < 0.037% even

though oxygen makes up 21% of the air in the Earth's atmosphere). Additionally, it can be quite challenging to obtain maximum labelling with minimal costs. In this thesis, a fast and cost-effective labelling protocol is introduced for labelling oxygen atoms in amino acids with optimal incorporation of $^{17}O$, reducing cost from ~ \$110 USD/100 mg of amino acid to ~ \$25 USD/100mg. An emerging NMR instrumentation called cross-polarization magic-angle spinning (CPMAS) cryoprobe technology is also introduced to boost sensitivity gains. Overall, this research explores the traditional and emerging NMR technology for pushing the limits of sensitivity gains for studying next-generation materials.

# Preface

This thesis is an original work by Michelle Ha.

Chapter 3 of this thesis has been reprinted with permission from Ha, M.; Karmakar, A.; Bernard, G.M.; Basilio, E.; Krishnamurthy, A.; Askar, A.M.; Shankar, K.; Kroeker, S. and Michaelis, V.K. Phase Evolution in Methylammonium Tin Halide Perovskites with Variable Temperature Solid-State $^{119}$Sn NMR Spectroscopy. *The Journal of Physical Chemistry C*. **2020**, *124*, 15015-15027. Copyright 2020 American Chemical Society. All samples were prepared by Abdelrahman M. Askar & Enoc Basilio. Data acquisition and analysis of $^{119}$Sn NMR performed at $B_0$ = 7.05 & 11.75 T and quantum chemical (DFT) calculations were completed by me, Michelle Ha. High-temperature $^{119}$Sn NMR spectrum acquired at $B_0$ = 9.39 T were collected by Arun Krishnamurthy at the University of Manitoba in Winnipeg, MB, Canada and analyzed by me. All $^1$H, $^{13}$C, and $^{207}$Pb NMR experiments acquired at $B_0$ = 7.05 T were collected and analyzed by Abhoy Karmakar. Vladimir K. Michaelis, Abhoy Karmakar, and I prepared the manuscript for publication.

Chapter 4 of this thesis has been reprinted with permission from Thiessen, A.N.; Ha, M.; Hooper, R.W.; Yu, H.; Oliynyk; Veinot, J.G.C and Michaelis, V.K. Silicon Nanoparticles: Are They Crystalline from the Core to the Surface?. *Chemistry of Materials.* **2019**, *31*, 678-688. Copyright 2019 American Chemical Society. Sample preparation and analysis of FTIR, XPS, TEM, and powder XRD data were completed by Alyxandra N. Thiessen and Riley W. Hooper. All $^{29}$Si NMR data acquisition and analysis were completed by me, Michelle Ha, and Riley W. Hooper. Alyxandra N. Thiessen and I contributed equally to this work and prepared the manuscript for publication.

Chapter 5 of this thesis has been reprinted with permission from Ha, M.; Thiessen, A.N.; Sergeyev, I.V.; Veinot J.G.C. and Michaelis, V.K. Endogenous dynamic nuclear polarization NMR of hydride-terminated silicon nanoparticles. *Solid State Nuclear Magnetic Resonance.* **2019**, *100*, 77-84. Copyright 2019 Elsevier Inc. All samples were prepared by Alyxandra N. Thiessen. Dynamic nuclear polarization sample preparation was completed by me, Michelle Ha, with DNP NMR experiments collected at the Bruker BioSpin Corporation in Billerica, Massachusetts, USA and

analyzed by Ivan V. Sergeyev and myself. The manuscript and figures were prepared by myself for publication.

Chapter 6 of this thesis has been reprinted with permission from Ha, M.; Nader, S.; Pawsey, S.; Struppe, J.; Monette, M.; Mansy, S.S.; Boekhoven, J. and Michaelis, V.K. Racing Toward Fast and Effective $^{17}$O Isotopic Labeling and NMR Spectroscopy of N-formyl-MLF-OH and Associated Building Blocks. *Journal of Physical Chemistry B.* **2021**, *125*, 11916-11926. Copyright 2021 American Chemical Society. All samples were prepared by me, Michelle Ha, with the labelled N-formyl-MLF-OH and N-acetyl-MLF-OH tripeptides prepared by Serge Nader. Kinetic studies using high-performance liquid chromatography (HPLC) was done by myself. Oxygen-17 NMR spectra acquired at $B_o$ = 14.1 T were performed and analyzed by me, Michelle Ha. DNP NMR spectra were acquired by Shane Pawsey at Bruker BioSpin Corporation in Billerica, Massachusetts, USA. Cross-polarization magic-angle spinning (CPMAS) cryoprobe experiments were performed by Martine Monette and Jochem Struppe at Bruker BioSpin Corporation in Fällanden, Switzerland. Oxygen-17 NMR spectra analysis, figure preparation, and manuscript preparation was performed by me, Michelle Ha.

*To my family*

# Acknowledgments

There are countless number of individuals who have supported me throughout my graduate degree, and I am forever grateful for everyone I have encountered during this journey. First, I would like to acknowledge my PhD supervisor, Professor Vladimir K. Michaelis for his endless support and encouragement. As an undergraduate student volunteering in his lab to one of his first graduate students, it was a tremendous adventure and I have learned so much technically, as well as how to be a better mentor. His academic drive and mentorship helped push me to be the researcher and educator I am today. Next, I would like to thank Dr. Guy M. Bernard for starting my journey as an NMR spectroscopist by introducing me to what NMR spectroscopy was and how exciting research can be. His friendship and willingness to share has been a constant pillar of support throughout this journey and I am indebted to him for all the training and "dumb questions" I ask multiple times a day. I would like to acknowledge Professor Roderick E. Wasylishen for trusting me as a first-year biology student to come into his lab and learn about NMR spectroscopy. His endless wisdom and vast knowledge of the field has been inspiring and I thank him for his support throughout my studies.

I would like to thank all the past and present members of the Michaelis group. Our impromptu chats in the NMR room and research discussions have been inspiring and we have all grown so much as researchers and individuals throughout these years. Thank you to Dr. Alexandra Faucher for our late-night chats, secret codes, and shenanigans, which kept me sane during the low periods of the graduate school rollercoaster. To my silicon nanoparticle partner-in-crime, Dr. Alyxandra Thiessen, thank you for your friendship and support both in and out of graduate studies.

I would like to thank my supervisory committee, Professors Alex Brown and Jon G.C. Veinot, for their support and insightful discussions throughout my degree. I also thank Professors Julianne M. Gibbs and Darren H. Brouwer for serving on my PhD defense committee. Thank you to the Alberta/ Technical University of Munich International Graduate School for Hybrid Functional Materials (ATUMS) for the opportunity to live and work in Munich, Germany for a three-month research exchange. Thank you to Professor Job Boekhoven for hosting me in his lab during my research exchange and providing tremendous support as I learned new skills in the field of peptide synthesis.

# Table of Contents

# List of Tables

# List of Figures

recycle delay of 200 s was used to artificially inflate the surface resonance still present at shorter recycle delays. (c) Artistic schematic of a H-SiNP indicating the silicon surface, subsurface, and core with a model of the first ten atomic layers of H-SiNPs.

non-DNP-enhanced (µW off) $^{17}O\{^1H\}$ CP MAS NMR spectra of 40 % $^{17}O$-enriched Fmoc-Leu-OH using 10 mM TEKPol in TCE; an organic solvent was used to maintain crystallinity. Spectra were acquired under magic-angle spinning conditions (MAS, $\omega_r/2\pi$ = 12 kHz), recycle delays of 20 s, and 2048 co-added transients. (c) Two-dimensional $^{17}O\{^1H\}$ HETCOR MAS NMR spectrum of 40 % $^{17}O$-labelled Fmoc-Leu-OH at 18.8 T using a CPMAS cryoprobe and a spinning frequency of 15 kHz. The $^{17}O$-$^1H$ correlation spectrum was acquired with a contact time of 1.5 ms, 128 co-added transients, 120 $t_2$ increments, and recycle delay of 4 s. The structure of Fmoc-Leu-OH is in the inset with the corresponding $^1H$ sites (pink: R-group, orange: α-carbon, green: Fmoc-protecting group, blue: NH, and purple: OH) labelled accordingly. A blue oval is used to highlight the intermolecular correlation between the $^{17}O$ carbonyl oxygen of one molecule and the neighboring amide hydrogen (CO---NH). * indicates spinning sidebands and † indicates the signal coming from the $ZrO_2$ rotor.

# List of Symbols

| | |
|---|---|
| $\alpha, \beta, \gamma$ | Euler Angles Relating to Two NMR Interaction Tensor |
| $\alpha$-Si | Amorphous Silicon |
| $B_0$ | Applied Static Magnetic Field |
| $B_1$ | Applied Dynamic Magnetic Field |
| $c$-Si | Crystalline Silicon |
| $C_Q$ | Quadrupole Coupling Constant |
| $d$ | Diameter |
| $\delta$ | Chemical Shift |
| $\delta_{CG}$ | Centre-of-gravity Chemical Shift |
| $\delta_{iso}$ | Isotropic Chemical Shift |
| $\varepsilon$ | Enhancement Factor |
| $\varepsilon_{DFS}$ | DFS Enhancement |
| $\varepsilon_{DNP}$ | DNP Enhancements |
| $eQ$ | Electric Quadrupole Moment |
| $\Delta E$ | Energy Difference |
| $\Delta J$ | Anisotropy in $J$ |
| $\gamma$ | Gyromagnetic Ratio |
| $h$ | Planck's Constant |
| $\hbar$ | Reduced Planck's Constant |
| $\mathcal{H}_{DD}$ | Direct Dipolar Hamiltonian |
| $\mathcal{H}_J$ | Indirect Spin-spin Hamiltonian |
| $\mathcal{H}_{MS}$ | Magnetic Shielding Hamiltonian |

| | |
|---|---|
| $\mathcal{H}_{NMR}$ | NMR Hamiltonian |
| $\mathcal{H}_Q$ | Quadrupolar Hamiltonian |
| $\mathcal{H}_z$ | Zeeman Hamiltonian |
| $I$ | Nuclear Spin Number |
| $I_{MWon}, I_{Mwoff}$ | Peak Intensities for a Microwave on and off Spectrum |
| $J$ | Indirect Coupling Tensor |
| $\kappa$ | Skew |
| $k$ | Boltzmann Constant |
| $\lambda$ | Distortion Parameter |
| $m$ | Nuclear Spin State |
| $n_\beta, n_\alpha$ | Populations of the Upper and Lower Energy Spin States |
| $\eta_Q$ | Quadrupole Asymmetry Parameter |
| $\Omega$ | Span or Breadth of Spectrum |
| $r$ | Distance Between Spins |
| $R_{DD}$ | Dipolar Coupling Constant |
| $R_{eff}$ | Effective Dipolar Coupling Constant |
| $\sigma$ | Magnetic Shielding |
| $\sigma_{dia}$ | Diamagnetic Shielding Contribution |
| $\sigma_{para}$ | Paramagnetic Shielding Contribution |
| $\sigma_{so}$ | Spin-orbit Shielding Contribution |
| $v$ | Frequency |
| $v_0$ | Nuclear Larmor Frequency |
| $T$ | Temperature |
| $T_1$ | Spin-lattice Relaxation |
| $T_2$ | Spin-spin Relaxation |

| | |
|---|---|
| $T_2*$ | Effective Spin-spin Relaxation |
| $T_B$ | DNP Buildup Time |
| $t_{1/2}$ | Half-life |
| $\tau_1, \tau_2$ | Interpulse and Refocusing Delay |
| $\tau_p$ | Echo Delay |
| $\omega_0$ | Larmor Frequency |
| $\omega_r$ | Rotor Frequency |
| $\mu W_{on}, \mu W_{off}$ | Microwave On (DNP-enhanced) and Microwave Off (non-DNP-enhanced) |

# List of Abbreviations

| | |
|---|---|
| AA | Amino Acid |
| ACN | Acetonitrile |
| ACQ | Acquisition |
| ADF | Amsterdam Density Functional |
| BM | Ball Milling |
| BOC | *Tert*-Butyloxycarbonyl |
| BSVT | Bruker Smart Variable Temperature |
| CE | Cross Effect |
| CP | Cross-polarization |
| CPS | Curved Position-sensitive |
| CSA | Chemical Shift Anisotropy |
| CT | Central Transition |
| CW | Continuous Wave |
| DFS | Double Frequency Sweep |
| DFT | Density Functional Theory |
| DIPEA | N,N-Diisopropylethylamine |
| DMF | Dimethylformamide |
| DMSO | Dimethylsulfoxide |
| DNP | Dynamic Nuclear Polarization |
| DSS | Sodium Trimethylsilylpropanesulfonate |
| EDX | Energy-dispersive X-ray Spectroscopy |
| EFG | Electric Field Gradient |
| EPR | Electron Paramagnetic Resonance |

| | |
|---|---|
| FID | Free-induction Decay |
| FMOC- | Fluorenylmethoxycarbonyl- |
| FMOC-FF | Fluorenylmethoxycarbonyl-diphenylalanine |
| FTIR | Fourier Transform Infrared Spectroscopy |
| FWHM | Full-width at Half-maximum |
| GGA | Generalized Gradient Approximation |
| H-SiNPs | Hydride-terminated Silicon Nanoparticles |
| HBTU | Hexafluorophosphate Benzotriazole Tetramethyl Uronium |
| HETCOR | Heteronuclear Correlation |
| HOBt | Hydroxybenzotriazole |
| HPLC | High-performance Liquid Chromatography |
| HS | Hyperbolic Secant |
| HSQ | Hydrogen Silsesquioxane |
| IDM | Indomethacin |
| IHD | Inverse Halogen Dependence |
| IR | Infrared |
| JEOL | Japan Electron Optics Laboratory |
| LA | Lorentzian Asymmetric |
| LED | Light Emitting Diodes |
| Leu | Leucine |
| MAS | Magic-angle Spinning |
| MCS | Mechanochemical Synthesis |
| Met | Methionine |
| MS | Mass Spectrometry |
| MW | Microwave |

| | |
|---|---|
| NHD | Normal Halogen Dependence |
| NMR | Nuclear Magnetic Resonance |
| NP | Nanoparticle |
| PAS | Principle Axis System |
| Phe | Phenylalanine |
| PL | Photoluminescence |
| PPM | Parts-per-million |
| PRESTO | Phase-shifted Recoupling Effects a Smooth Transfer of Order |
| Q4VP | Quadrupole Zeta with Four Sets of Polarization Functions |
| QD | Quantum Dot |
| RAPT | Rotor-assisted Population Transfer |
| REDOR | Rotational-Echo Double Resonance |
| RF | Radiofrequency |
| RPM | Rotation-per-minute |
| SE | Solid Effect |
| SEM | Scanning Electron Microscopy |
| SiNPs | Silicon Nanoparticles |
| ST | Satellite Transition |
| SQ | Single Quantum |
| S/N | Signal-to-noise |
| TCE | Trichloroethylene |
| TEDOR | Transferred-Echo Double Resonance |
| TEM | Transmission Electron Microscopy |
| TMF | Toxic-metal-free |
| TMS | Tetramethylsilane |

| | |
|---|---|
| TPPM | Two-pulse Phase-modulated |
| USD | United States Dollar |
| UV | Ultraviolet |
| VOCS | Variable Offset Cumulative Spectra |
| VT | Variable Temperature |
| XPS | X-ray Photoelectron Spectroscopy |
| XRD | X-ray Diffraction |
| ZORA | Zeroth-order Regular Approximation |

# Chapter 1

## Introduction

### 1.1 Why Is Structure Important?

Since the beginning of time, humans have adapted and relied on materials to survive. Whether it is the development of wheels for transportation or the invention of modern medicine, technology has continued to evolve to keep up with the fast-paced changes of our modern world. With the rapid release and recycle of technology, researchers are in a battle to constantly improve materials. Thus, researchers turn to the materials science paradigm to streamline the process of developing new substances. The materials science paradigm models the relationship between processing, structure, and property (Figure 1.1). While the consumer is focused on the properties / performance of the product and the developers are focused on the process by which to make the product, the driving force of its performance is structure (i.e., how atoms are arranged). Based on the underlying structure of solids, the corresponding properties can drastically change. Thus, it is imperative to analyze and identify unique structural features such that researchers can tailor the substance to the application of interest.

There are numerous characterization techniques that can be used to analyze and identify unique structural features. Below, a few common characterization techniques are discussed, as well as their limitations for examining certain materials. In this thesis, solid-state nuclear magnetic

resonance (NMR) spectroscopy is the main approach used to ascertain the unique structural relationships in various materials, ranging from optoelectronic perovskites, non-toxic silicon nanoparticles, and biomolecular building blocks.
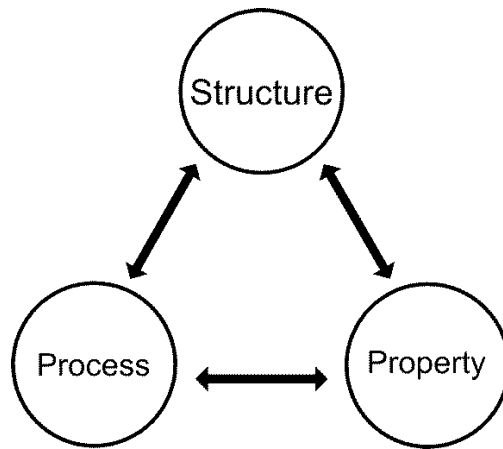


**Figure 1.1.** Materials science paradigm showing the symbiotic relationship between structure, process, and property of materials.

## 1.2 Material Characterization Techniques

### 1.2.1 Determining Size and Image of Materials

Electron microscopes are used to create high-resolution images of the sample of interest. The two most common techniques that use an electron beam to form an image are transmission electron microscopy (TEM) and scanning electron microscopy (SEM). While both techniques use the same radiation source, the mechanism by which the image is detected are different. In TEM, the electron beam is transmitted through the sample creating a two-dimensional image; whereas in SEM, the electron beam scans the surface of the sample and is reflected to create a three-dimensional image. Additionally, the information gathered from each technique is different. Since the electron beam is passing through the sample in TEM, information about the inner crystal structure, shape, and size (when coupled with dynamic light scattering) can be determined. However, the caveat with TEM is that the sample must be thin enough for the electron beam to pass through. Also, high energy electron beams can induce crystal formation which can skew the crystallographic information obtained, as well as being destructive to the sample. On the other hand, SEM provides useful information about surface topography as the electron beam "reflects" off the sample. This allows the researcher to get an understanding on how the sample "looks" and

can determine any surface defects that would affect the application.  However, with SEM, if the material is non-conductive, a thin coat of a conducting metal (such as gold) is applied to prevent the sample from becoming charged when irradiated by electrons. This can then interfere with the compositional analysis of the material.

### 1.2.2 Determining Elemental Analysis

To gain a better understanding on what elements make up a material, researchers can use energy-dispersive X-ray spectroscopy (EDX) or X-ray photoelectron spectroscopy (XPS). While both techniques can provide compositional analysis, the mechanisms are opposite. Firstly, EDX detects the X-rays emitted from a sample when the material is bombarded by an electron beam (such as from TEM or SEM). The electron beam results in an electron in the inner shell being ejected to create an electron hole. When an electron from an outer shell relaxes to fill the electron hole, an X-ray is emitted. However, this technique does not work well with light elements ($Z < 4$, where $Z$ = atomic number of the element) making it difficult for EDX to detect hydrogen, helium, lithium, and beryllium. On the other hand, XPS detects photoelectrons when the material is irradiated with X-rays. Not only can XPS identify the elements in the sample, but it can also provide chemical bonding information (which EDX cannot do). This feature is possible as electrons have varying binding energies depending on how it is chemically bonded with neighbouring atoms, which can be probed using XPS. However, as the x-rays have a limited penetrating power, only electrons within the first few micrometers are affected, making XPS surface sensitive up to 10 nm into the sample. Another limitation of XPS is its inability to detect hydrogen and helium as they do not have core electrons (or only 1 core electron for helium), making it impossible to eject the core electron to produce a photoelectron.

### 1.2.3 Determining Crystallinity of Sample

Often, researchers want to know how the bulk material is orientated depending on its composition, or how crystalline (or ordered) the material is as crystallinity can drastically affect the resulting application. X-ray powder diffraction (XRD) is a technique that identifies crystalline phases in materials based on the diffraction pattern observed after the sample is hit with X-rays. By measuring the peak intensities and angles of the diffracted beam, the positions of the atoms in the crystal, as well as the bonding information can be determined. Not only is this technique

quantitative, XRD is non-destructive, making it ideal for in-situ studies. While XRD remains the top characterization approach for identifying crystal structure, it is unable to detect hydrogen atoms. This inability is due to the small electron cloud (1 electron for hydrogen) which makes it difficult to get a diffraction pattern. Also, if the material that is being analyzed is amorphous (non-ordered), the resulting XRD pattern would produce broad peak(s) with low intensities, making it difficult to extract routine structural information, as the solid lacks long-range order.

**1.2.4 Solid-state Nuclear Magnetic Resonance Spectroscopy**

Solid-state NMR spectroscopy is a powerful characterization technique due to its ability to probe the atomic- and medium-range structure of solids. By subjecting the sample to a magnetic field, the atomic nuclei align with the magnetic field, which are then manipulated to produce an electromagnetic signal corresponding to the nucleus centre that is being studied. Regardless of the sample's crystallinity (amorphous, semi-crystalline, or crystalline), NMR can provide quantitative and qualitative information about the local environment about the nucleus of interest. In addition to being non-destructive, it can probe almost all elements on the periodic table (in theory), making it one of the most versatile and robust analytical methods for studying solids.

## 1.3 Maximizing NMR Sensitivity

While solid-state NMR spectroscopy is a powerful technique for soft and hard materials characterization, it is inherently insensitive due to its low Boltzmann distribution (more information about Boltzmann distribution is discussed in Chapter 2). Additionally, the signal-to-noise ratio (S/N) of the resulting spectrum depends on several different factors, such as sample amount, number of transients averaged together, and/or magnetic field strength. To increase the S/N, spectroscopists can increase the sample amount, experimental time, and/or magnetic field strength; however, this is not always feasible. In this thesis, different approaches used to maximize NMR sensitivity are explored. In Chapter 3, variable temperature $^{119}$Sn NMR spectroscopy is used to probe different phases of methylammonium tin halide perovskites as more ordered samples can provide better S/N with fewer number of transients compared to amorphous material. Spectroscopists can also manipulate the magnetization of insensitive nuclei by transferring polarization from a highly abundant/ sensitive nucleus to the insensitive nucleus of interest. This can be done using experimental pulse sequences such as cross-polarization (CP). This is explored

in Chapter 4 when studying the underlining structure of hydride-terminated silicon nanoparticles (H-SiNPs). Expanding on techniques such as CP, dynamic nuclear polarization (DNP) NMR spectroscopy uses polarization of unpaired electrons to enhance the nucleus of interest. This technique has become more popular in the recent decade due to its commercialization and has resulted in sensitivity enhancements over conventional NMR methods. In Chapter 5, DNP NMR is used tackle the long acquisition times needed to study H-SiNPs as discussed in Chapter 4, as well as discussing future avenues for endogenous radicals to help boost polarization transfers. The most common way to help increase S/N is to isotopically label your sample to increase the number of NMR-active spins that can be detected. However, this can be synthetically challenging and often, very costly. Therefore, in Chapter 6, a fast and cost-effective labelling protocol is introduced to tackle one of the most challenging NMR-active nuclei, oxygen-17. Using this approach, as well as the sensitivity enhancement methods mentioned in the previous chapters, $^{17}O$ NMR studies of fluorenylmethoxycarbonyl- (FMOC-) protected amino acids and site-specific labelled tripeptides are investigated. A technique called cross-polarization cryoprobe (CPMAS cryoprobe) is also introduced as an emerging sensitivity enhancement approach to study complex and challenging materials.

## 1.4 Overview of Thesis

In Chapter 2, a general overview on NMR theory and experiments are presented. As DNP NMR plays a role in Chapters 5 and 6, a brief description of this technique is provided, along with details about computational techniques used in Chapter 3.

Non-renewable energy resources (such as fossil fuels and coal) have been the main source of energy for ages. However, as these sources are depleting and the effects of fossil fuels on our environment increasing, the field of solar energy has expanded exponentially to find the next-generation material that can harness the sun's energy. Hybrid organic-inorganic metal-halide perovskite materials are an emerging class of materials that could profoundly change the optoelectronic and solar research fields. Unfortunately, the leading solar-absorbing candidates contain toxic lead. In addition, its chemical instability leads to decomposition that can result in detrimental environmental concerns. In Chapter 3, a series of non-toxic tin-based hybrid organic-inorganic metal-halide perovskites (methylammonium tin halide, $MASnX_3$ where $MA^+ = CH_3NH_3^+$ and $X^- = Cl^-$, $Br^-$, or $I^-$) are examined as potential solar-absorbing materials. Interestingly,

each of the three candidates have unique phases that occur between 150 and 540 K. Using variable-temperature solid-state NMR spectroscopy, unique chemical shifts corresponding to the changes in the polyhedra about the Sn centre are identified. This is further compared to the chemical shift anisotropy observed when the Sn centre deviates from octahedral symmetry. As chemical instability is a major factor when developing potential candidates, the degradation of MaSnI$_3$ over two weeks is examined, noting that after 30 hours, the $^{119}$Sn NMR resonance significantly broadens and shifts to higher frequency.

There has been a widespread interest in silicon nanoparticles (SiNPs) due to their versatility in the fields of optoelectronics, battery electrodes, and nanomedicine. The nanostructure of these materials influences their properties, so it is imperative to employ a comprehensive study on these game-changing particles. In Chapter 4, a complement of characterization methods, including XPS, TEM, XRD, Fourier transform infrared spectroscopy, and solid-state NMR spectroscopy, is used to systematically investigate the nanoparticle structure of a series of hydride-terminated SiNPs (H-SiNPs) ranging from 3 to 64 nm in diameter. Using NMR, the surface silicon species manifests in a unique chemical shift resonance which gravitates to higher frequencies and becomes sharper as the particles increase in size and crystallinity. These resonances correspond to distinct surface, subsurface, and core silicon species layered within the H-SiNPs. By applying this systematic study using these characterization methods, the structural insights of SiNPs can be determined and provide a foundation for advancements in SiNP-based applications.

While characterization of SiNPs can be performed using $^{29}$Si NMR spectroscopy, the long acquisition times, and poor sensitivity due to low Boltzmann population makes in-depth studies of these materials challenging. For example, a single $^{29}$Si NMR spectrum discussed in Chapter 4 needed 30+ hours of continuous acquisition to obtain a suitable S/N ratio. Thus, in Chapter 5, a complementary magnetic resonance technique, namely dynamic nuclear polarization (DNP) is used to boost $^{29}$Si sensitivity in H-SiNPs. Details on DNP methodology can be ascertained in Chapter 2 of this thesis but in brief, DNP uses hyperpolarized unpaired electrons to increase polarization of the nucleus of interest which allows for reduction in experimental time. When the traditional indirect DNP approach is employed using an exogenous radical, the highly reactive SiNP surface quickly rendered the unpaired electrons null, and minimal DNP enhancements ($\varepsilon \leq 3$) are found. However, by exploiting the silicon surface dangling bonds as an endogenous radical source, respectable DNP enhancements ($\varepsilon = 6$) are obtained using minimal radical concentrations ($< 1$ mM

endogenous radicals vs. 10 mM for exogenous radicals). While the DNP enhancements were small, this results in time savings of 36 (i.e., a $^{29}$Si NMR spectrum that would take 36 hours to complete would only require 1 hour to have the same S/N ratio using DNP). These preliminary findings provide a foundation for future endogenous radical development which would further sensitivity gains.

One way to increase sensitivity is to isotopically label the sample of interest. This is not uncommon in the field of biomolecular NMR where carbon and nitrogen centres are labelled with $^{13}$C and $^{15}$N, respectively. Oxygen is also readily present in amino acids, peptides, and proteins, with their role in hydrogen bonding being vital for secondary and tertiary protein structures. However, isotopically labelling $^{17}$O centres is improbable as it is very costly and time consuming. In Chapter 6, a fast and cost-effective method to $^{17}$O label FMOC-protected amino acid building blocks is developed and used in strategically labelling biologically relevant tripeptides. Using this inexpensive method, higher volumes of sample are labelled and analyzed using $^{17}$O NMR spectroscopy. While good resolution and sensitivity is obtained at high magnetic fields (14.1 T) with strategic labelling, the limit to sensitivity is further probed by employing sensitivity enhancement methods, such as population transfer, DNP, and CPMAS cryoprobe technology. By applying these approaches, substantial time savings over conventional NMR experiments are found.

In Chapter 7, concluding remarks and future works for investigating perovskites, nanoparticles, and proteins are provided.

# Chapter 2

## Theoretical Background

### 2.1 The NMR Hamiltonian

The NMR Hamiltonian ($\mathcal{H}_{\text{NMR}}$) corresponds to the total energy of the system and describes how a nucleus interacts with its environment. In this thesis, the $\mathcal{H}_{\text{NMR}}$ can be split up into the following five terms:

$$\mathcal{H}_{NMR} = \mathcal{H}_Z + \mathcal{H}_{MS} + \mathcal{H}_{DD} + \mathcal{H}_J + \mathcal{H}_Q \qquad\qquad 2.1$$

where, $\mathcal{H}_z$ represents the Zeeman interaction, $\mathcal{H}_{MS}$ is the magnetic shielding term, $\mathcal{H}_{DD}$ is the direct dipolar interaction, $\mathcal{H}_J$ is the indirect spin-spin interactions, and $\mathcal{H}_Q$ represents the quadrupolar interaction.

All NMR active nuclei will experience these interactions (except for $\mathcal{H}_Q$ which is only experienced in quadrupolar nuclei, $I > 1/2$). The Zeeman interaction is referred to as an external interaction as it is under control of the experimentalist (i.e., external to the nuclear environment). On the other hand, $\mathcal{H}_{MS}, \mathcal{H}_{DD}, \mathcal{H}_J$, and $\mathcal{H}_Q$, are referred to as internal interactions as they are sample/system dependent (i.e., molecular properties intrinsic to the nucleus and system at hand). As the internal interactions are influenced by molecular structure, they are orientation-dependent with respect to the applied magnetic field ($B_0$). Thus, these interactions help provide critical structural information on the sample at hand. In this thesis, a general overview of the NMR

interactions will be presented. For more information about solid-state NMR, the reader is referred to the following resources.[1–4]

### 2.1.1 The Zeeman Interaction

When an NMR-active nucleus is placed in an external magnetic field, $B_0$, the energy levels become non-degenerate and split into corresponding nuclear spin states ($m$) (Figure 2.1). The magnetic moments (or nuclear spins) will orient themselves either parallel or antiparallel with $B_0$ and will split into ($2I + 1$) states with even spacing. This is called the Zeeman interaction, which can be defined as the following Hamiltonian:

$$\mathcal{H}_Z = -\gamma \hbar I B_0 \qquad\qquad 2.2$$

where $\gamma$ is the gyromagnetic ratio (intrinsic property to the nucleus), $\hbar$ is the reduced Planck's constant, and $I$ is the spin quantum number.
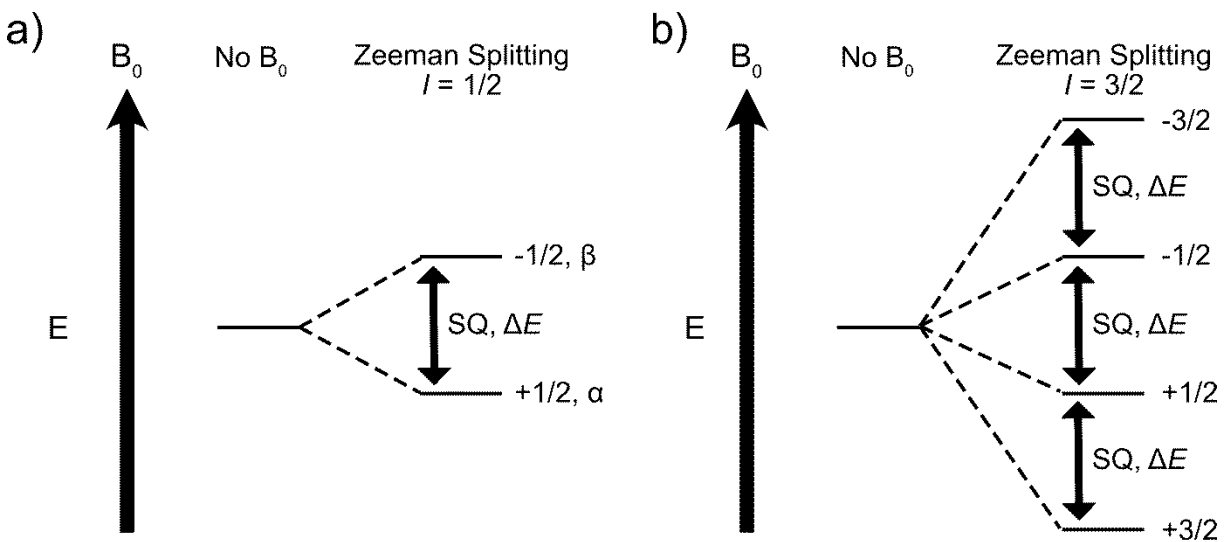


**Figure 2.1**. Spitting of the energy levels due to the Zeeman interaction for an $I = 1/2$ (a) and $I = 3/2$ (b) nucleus. The arrow represents the direction of $B_0$ and SQ refers to the observable single quantum transitions.

The observable single quantum transitions are evenly spaced out by $\Delta m = \pm 1$ and the energy difference ($\Delta E$) is defined by Equation 2.3, where $h$ is Planck's constant and $\nu$ is the nuclear Larmor frequency.

$$\Delta E = \gamma \hbar B_0 = h\nu \qquad\qquad 2.3$$

The nuclear Larmor frequency is the rate at which the magnetic moment precess about the external magnetic field and is defined by Equation 2.4.

$$\nu = \frac{\gamma B_0}{2\pi}$$

2.4

At thermal equilibrium, the population of the nuclear spin states are determined by the Boltzmann distribution (Equation 2.5), where $n_\beta$ and $n_\alpha$ are the populations of the upper and lower energy spin states, $k$ is the Boltzmann constant, and $T$ is temperature in Kelvin.

$$\frac{n_\beta}{n_\alpha} = e^{-\Delta E/kT} = e^{-\gamma \hbar B_0/kT}$$

2.5

As the energy separation between spin states is inversely proportional to the wavelength of light used to irradiate the nuclei, NMR is inherently insensitive as radiofrequency pulses (vide infra) are applied to perturb the small fraction of excess nuclear spins from the lower energy state to the higher energy state. While electronic (UV-Vis spectrophotometry) and vibrational (infrared spectroscopy) spectroscopy are more sensitive techniques as the energy separation between spin states is much larger compared to NMR, the structural information resulting from NMR interactions observed in a spectrum is instrumental in the field of materials science.

### 2.1.2 Magnetic Shielding and Chemical Shift

The magnetic field experienced by the nucleus of an atom is dependent on the local electronic environment. In an external magnetic field, the valence electrons circulate, which generate a secondary magnetic field opposite of the applied magnetic field. This interaction results in the unique environmental information based on the electronic structure at the nucleus and provides characteristic resonance frequencies. The magnetic shielding Hamiltonian can be described as:

$$\mathcal{H}_{MS} = \gamma I B_0 \sigma$$

2.6

where $I$ is the nuclear spin momentum operator of the nucleus and $\sigma$ is the shielding tensor. The shielding tensor (Equation 2.7) can be written in the principal axis system (PAS) where $\sigma_{11} \leq \sigma_{22} \leq \sigma_{33}$ with $\sigma_{11}$ being the least shielded and $\sigma_{33}$ is the most shielded.

$$\bar{\bar{\sigma}}^{PAS} = \begin{bmatrix} \sigma_{11} & 0 & 0 \\ 0 & \sigma_{22} & 0 \\ 0 & 0 & \sigma_{33} \end{bmatrix}$$

2.7

As the magnetic shielding is with respect to a bare nucleus, it is difficult and rarely measured experimentally. Therefore, the magnetic shielding interaction is measured with respect to a reference compound and use the term chemical shift ($\delta$). The chemical shift term can then be calculated using the resonance frequencies ($v$) of the sample and standard reference (Equation 2.8).

$$\delta_{sample} = \left[\frac{v_{sample} - v_{reference}}{v_{reference}}\right] \times 10^6 \qquad \qquad 2.8$$

Chemical shift values are measured in terms of parts-per-million (ppm) and can vary dramatically for nuclei with large chemical shift ranges. The large chemical shift range is ideal as the resulting chemical shifts would be sensitive to small changes in their local structure; thus, providing a detailed investigation on the electronic environment. The notation used to report the chemical shift anisotropy (CSA) interactions in this thesis follow the Maryland Convention[5] and can be expressed as the following:

$$\delta_{iso} = \frac{(\delta_{11} + \delta_{22} + \delta_{33})}{3} \qquad \qquad 2.9$$

$$\Omega = \delta_{11} - \delta_{33} \qquad \qquad 2.10$$

$$\kappa = \frac{3(\delta_{22} - \delta_{iso})}{\Omega} \qquad \qquad 2.11$$

where $\delta_{iso}$ represents the average chemical shift, $\Omega$ (span) represents the magnitude or breadth of the anisotropic pattern, and $\kappa$ (skew) determines the shape of the anisotropy. As the CSA increases linearly with the magnetic field, manipulation of this interaction can occur through magnetic field strength selection (i.e., low $B_0$ is preferred to minimize this interaction).

### 2.1.3 Direct Dipolar Coupling

Direct dipolar coupling is a result of the nuclear magnetic moments of two nuclei (I and S) interacting through space (i.e., they do not need to be bonded together, they just need to be within proximity of each other). This dipole-dipole interaction can occur between the same nuclear spins (I = S, homonuclear dipolar coupling) or with different nuclear spins (I ≠ S, heteronuclear dipolar coupling). Regardless of the interaction, the resulting NMR lineshape is broadened. The direct dipolar Hamiltonian can be described as:

$$\mathcal{H}_{DD} = R_{DD}[A + B + C + D + E + F] \qquad \qquad 2.12$$

11

where $R_{DD}$ is the dipolar coupling constant and the alphabetic terms (A to F) are defined below (Equation 2.14). The dipolar coupling constant is dependent on the gyromagnetic ratios ($\gamma$) of the two nuclei and the distance, $r$, between the spins I and S.

$$R_{DD} = \left(\frac{\mu_o}{4\pi}\right)\left(\frac{\hbar\gamma_I\gamma_S}{r^3}\right) \qquad 2.13$$

While there are 6 terms in the "Dipolar Alphabet", only the A and B terms contribute to the line broadening in the spectrum. More specifically, terms A and B play a role in homonuclear dipole coupling, whereas only term A is apparent in heteronuclear dipole coupling. Terms C to F, on the other hand, only contribute towards relaxation.

$$A = -(3\cos^2\theta - 1)I_zS_z$$

$$B = -\frac{1}{4}(3\cos^2\theta - 1)[I_+S_- + I_-S_+]$$

$$C = -\frac{3}{2}(\sin\theta\cos\theta\, e^{-i\phi})[I_zS_+ + I_+S_z]$$

$$D = -\frac{3}{2}(\sin\theta\cos\theta\, e^{+i\phi})[I_zS_- + I_-S_z] \qquad 2.14$$

$$E = -\frac{3}{4}(\sin^2\theta\, e^{-2i\phi})[I_+S_+]$$

$$E = -\frac{3}{4}(\sin^2\theta\, e^{+2i\phi})[I_-S_-]$$

In both the A and B term, there is a '3cos²θ-1' term present. This term can be minimized or removed (and thus affecting the dipolar coupling) by using a technique called magic-angle spinning. This technique will be discussed in detail below.

There are a few things to consider that can affect the direct dipolar interaction. If the natural abundance of the nuclei of interest is very small, the likelihood of these spins coupling to each other is low. Additionally, if the distance is too great between the two spins, the dipolar coupling would be diminished. However, this interaction is very important for structure determination as it can be manipulated to determine distances, $r$, through-space between the two spins of interest.

### 2.1.4 Indirect Spin-Spin Coupling (*J*-coupling)

The through-bond interactions of the nuclear magnetic moments and the electronic structure is referred to indirect spin-spin coupling or *J*-coupling. The indirect spin-spin Hamiltonian is the following:

$$\mathcal{H}_J = \hbar J I_A I_B \qquad 2.15$$

where *J* is the indirect coupling tensor. The isotropic *J*-coupling causes peak splitting in the resonances corresponding to the coupled nuclei. This effect dominates in liquid-state NMR; however, *J*-coupling is usually overpowered by CSA (and quadrupolar interactions for $I > 1/2$) in solid-state NMR. The anisotropy in $J$ $(\Delta J)$ is very small and cannot be distinguished from direct dipolar couplings. Thus, when measuring the dipolar coupling constant, $R_{DD}$, the resulting value is an effective dipolar coupling constant, $R_{eff}$.

$$R_{eff} = R_{DD} - \frac{\Delta J}{3} \qquad 2.16$$

### 2.1.5 Quadrupolar Interaction

Most NMR-active nuclei have a spin greater than 1/2 ($I > 1/2$) and are referred to as quadrupolar. Unlike for $I = 1/2$ nuclei, the charge distribution for quadrupolar nuclei is non-spherical (Figure 2.2). This results in a nuclear electric quadrupole moment (eQ) which couples anisotropically with the local environment. The charge distribution can either be oblate (football-like) or prolate (disc-like) in shape if the eQ's are negative or positive, respectively.
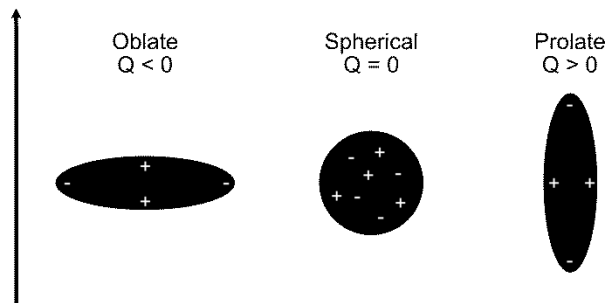


**Figure 2.2.** Nuclear charge distrubtions for a $I = 1/2$ (spherical) and $I > 1/2$ (oblate and prolate) nucleus. The arrow indicates the direction of the applied magnetic field along the Z-axis.

In addition to the NMR interactions discussed above which are between the nucleus and surrounding magnetic environment, quadrupolar nuclei also interact electrically resulting in an electric field gradient (EFG or V). This interaction causes changes in the Zeeman interactions and thus, can affect the central and satellite transitions (Figure 2.3). As the quadrupole interactions are small in comparison to the Zeeman interaction, the quadrupolar Hamiltonian consists of first- and second-order energy corrections to the Zeeman energy levels. There is also a third-order quadrupolar coupling but this is rarely necessary as it is typically very small in 99% of cases.
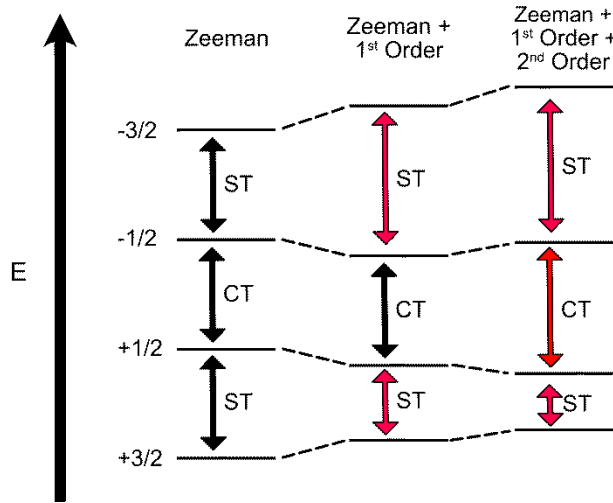


**Figure 2.3.** Energy level splittings due to the Zeeman interaction and the first- and second-order quadrupolar interactions for an $I = 3/2$ nucleus. The black arrows indicate that $\Delta E$ are the same, whereas the red arrows indicate $\Delta E$ has changed from the original energy difference seen by the Zeeman effect. The central transition is denoted as CT and the satellite transition is denoted as ST.

The quadrupolar Hamiltonian consists with the following:

$$\mathcal{H}_Q = \mathcal{H}_Q^1 + \mathcal{H}_Q^2 \qquad 2.17$$

$$\mathcal{H}_Q^1 = \frac{eQ}{4I(2I-1)}\sqrt{\frac{3}{2}}\left[3\hat{I}_z^2 - \hat{I}^2\right]V_0 \qquad 2.18$$

$$\mathcal{H}_Q^2 = -\frac{2}{v_o}\left[\frac{eQ}{4I(2I-1)}\right]^2 \left[V_1V_{-1}\hat{I}_z\left(4\hat{I}^2 - 8\hat{I}_z^2 - 1\right) + V_2V_{-2}\hat{I}_z^2\left(42^2 - 2\hat{I}_z^2 - 1\right)\right] \qquad 2.19$$

where the elements $V_{(x)}$ are as follows:

$$V_0 = 3\sqrt{\frac{1}{6}}V_{zz}$$

$$V_1 = -V_{xz} - iV_{yz}$$

$$V_{-1} = V_{xz} - iV_{yz} \qquad 2.20$$

$$V_2 = \frac{1}{2}\left(V_{xx} - V_{yy}\right) + iV_{xy}$$

$$V_{-2} = \frac{1}{2}\left(V_{xx} - V_{yy}\right) - iV_{xy}$$

The first-order quadrupole interaction does not affect the central transition, although the satellite transitions can either increase or decrease. The second-order interaction affects all energy levels and thus, the central transition is now impacted and results in a shift or broadening of the quadrupolar powder pattern.

The quadrupole interaction can be described by the quadrupole coupling constant ($C_Q$) and the asymmetry parameter ($\eta$) as illustrated in Equations 2.21 and 2.22, respectively.

$$C_Q = \frac{eQV_{ZZ}}{h} \qquad 2.21$$

$$\eta = \frac{V_{XX} - V_{YY}}{V_{ZZ}} \qquad 2.22$$

In select cases, the quadrupole interaction can become zero for a $I > 1/2$ nucleus. As the EFG tensor is traceless and symmetric (Equation 2.23), the $C_Q$ vanishes if the local environment is highly symmetric (i.e., the nucleus is in a cubic position) or if there is isotropic tumbling.

$$\bar{V} = \begin{bmatrix} V_{XX} & 0 & 0 \\ 0 & V_{YY} & 0 \\ 0 & 0 & V_{ZZ} \end{bmatrix} \qquad 2.23$$

## 2.2 Experimental NMR Techniques and Data Processing

### 2.2.1 Magic-angle Spinning (MAS)

In liquid-state NMR spectroscopy, the molecules are rapidly tumbling in solution which allows for the averaging of the orientation of nuclear spins to zero. Therefore, the effects of CSA and dipolar coupling are rarely observed, and sharp resonances (isotropic peaks) are obtained in the resulting spectra. Solid-state NMR spectroscopy on the other hand works with powder ("tiny

crystallites") samples which results in anisotropy. While a lot of information can be gained from a powder pattern, these broad and distorted patterns can be difficult to analyze.

In the 1950's, Edward R. Andrew and Irving J. Lowe independently determined that if the solid sample would spin at a fixed "magic" angle, many anisotropic interactions (such as CSA, direct dipolar coupling, and first-order quadrupolar coupling) would average out.[6,7] This spinning application was thus, referred to as magic-angle spinning (MAS). As the molecular orientation is dependent on a *$3cos^2\theta$-1* term, if the sample is spinning infinitely fast at $\theta = 54.74°$ with respect to $B_0$, the anisotropic term becomes zero and you are left with only the isotropic peaks. However, spinning infinitely fast is impossible so the majority of the time, MAS can attenuate the anisotropic interactions but not completely remove them. There are some cases where the anisotropic interactions can be "spun" out (i.e., interactions average to 0) when the spinning rate of the sample is faster ($\sim$>2 times) than the magnitude of the interaction. At slower spinning speeds, sharp lines called spinning sidebands are produced in addition to the peak corresponding to the isotropic chemical shift. These spinning sidebands are spaced out equidistant with respect to the spinning frequency and thus, would change depending on the spinning frequency used. Since the isotropic peak does not change with respect to the spinning frequency, multiple MAS experiments at various spin rates would then help discern the isotropic chemical shift. Magic-angle spinning has become synonymous with solid-state NMR studies and is routinely used with non-spinning experiments to extract isotropic and anisotropic interactions, respectively.

### 2.2.2 Bloch Pulse

The simplest NMR technique is the Bloch pulse (Figure 2.4), named after Felix Bloch in 1946, which consists of a radiofrequency (RF) pulse which tips the net magnetization at a specific angle (typically $\pi/2$ or less) into the X-Y plane.[8] A short delay follows which allows for the pulse to dissipate from the probe coil and minimize probe ringing before the free-induction decay (FID) is acquired. Finally, a recycle delay is allowed for the Boltzmann population to return to equilibrium (along the Z-axis) before the pulse sequence is repeated (Figure 2.5). Over a course of experimental time dictated by the spectroscopist, the transients (or number of scans) are added together, and the final FID is Fourier-transformed to produce the NMR spectrum.
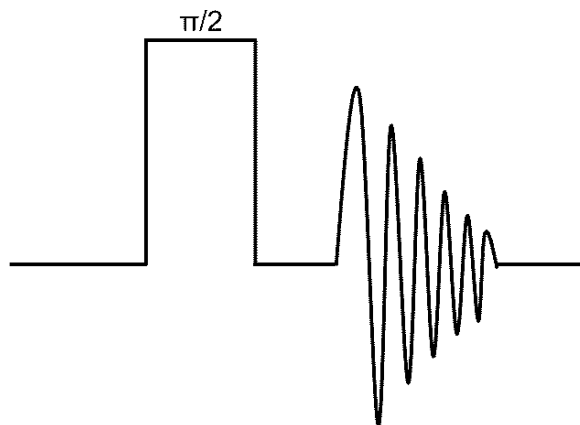
**Figure 2.4.** The Bloch pulse sequence.
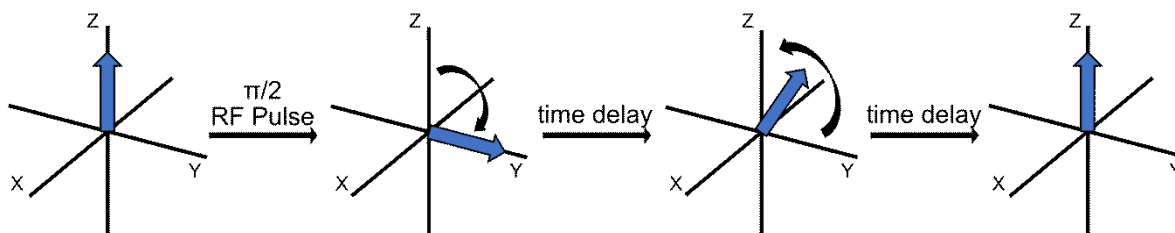


**Figure 2.5.** Illustration of the net magnetization when a Bloch pulse is applied.

### 2.2.3 Spin Echo Pulses

In an ideal world, all nuclear spins in a sample would be equally excited when a pulse is applied and would relax at the same time. However, that is not always the case due to inhomogeneous effects in the magnetic field, as well as variations in relaxation times. In a Bloch pulse, during the delay between the excitation pulse and acquisition, the spins start decaying at different rates and the resulting NMR signal is diminished or the spectrum becomes distorted. In 1950, Erwin L. Hahn first discussed that the transverse magnetization lost could be recovered by using a secondary $\pi/2$ pulse to refocus the spins, producing a spin echo.[9] In 1954, Herman Y. Carr and Edward M. Purcell expanded on this method and used a combination of $\pi/2$ and $\pi$ (90° and 180°) pulses to measure spin-spin ($T_2$) relaxation.[10] While the secondary pulses can be varied, the following discussion about spin-echoes will about the $\pi/2 - \pi$ pulse sequence (Figure 2.6).

17
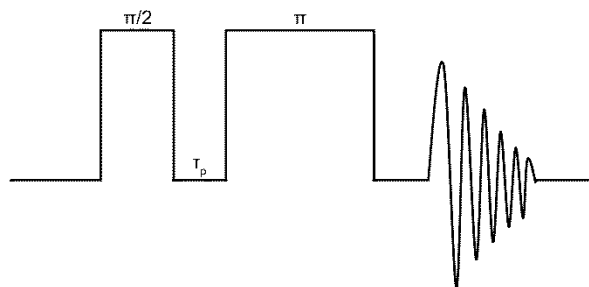
**Figure 2.6.** The Spin Echo pulse sequence where $\tau_p$ is the echo delay.

Similar to the Bloch pulse, a $\pi/2$ pulse is applied to tip the net magnetization into the X-Y plane. During the short delay ($\tau_p$), some spins decay faster or slower due to the magnetic field inhomogeneities. A $\pi$ pulse is then applied to flip the magnetizations, allowing the slower spins to be closer towards the negative y-axis, whereas the faster spins would be further away from meeting at the negative y-axis. Another delay follows to allow all the spins to catch up to the "main" magnetization along the negative y-axis. The echo pulse is then acquired when all spins are completed refocused, followed by the relaxation delay.

## 2.2.4 Cross-polarization (CP) Pulse

One way to boost the signal-to-noise ratio (S/N) of the resulting spectrum is to acquire more transients to minimize the noise level of the FID. However, since relaxation delays can range from seconds to hours, it would be ineffective to signal average within a reasonable timeframe. In 1972, Alexander Pines, Michael Gibby, and John S. Waugh developed a pulse sequence which takes advantage of the abundant spin polarization and short relaxation delays of $^1$H nuclei, namely, Cross-polarization (CP) (Figure 2.7).[11]

18
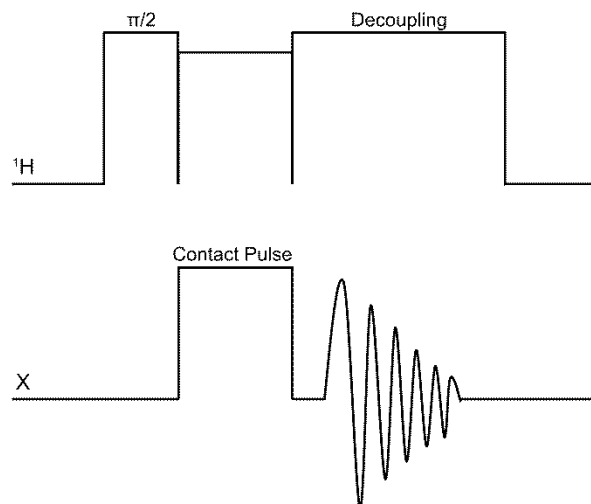
**Figure 2.7.** Cross-polarization pulse sequence where $^1$H is the proton nucleus (or a high gamma nucleus such as $^{19}$F) and X represents the low gamma nucleus of interest.

First, a $\pi/2$ pulse is applied to the $^1$H channel to tip the net magnetization into the X-Y plane. Then a $^1$H spin-lock pulse is applied concurrently with a contact pulse on the X channel. When the Hartmann-Hahn match condition is satisfied, polarization transfer between the $^1$H and X nucleus can occur (Equation 2.24).

$$\gamma^H B_1{}^H = \gamma^X B_1{}^X \qquad\qquad 2.24$$

Following the contact pulse, the FID is measured during the acquisition time while a $^1$H high-power decoupling pulse is applied. The decoupling pulse is used to minimize the heteronuclear dipolar and J-coupling interactions which causes line broadening. Finally, a recycle delay corresponding to the time needed for the $^1$H spins to relax back to equilibrium is applied before the pulse sequence is repeated.

By transferring the $^1$H polarization to the dilute nucleus of interest (such as $^{29}$Si), the signal enhancement increases by a factor of $\gamma^H/\gamma^X$. Additionally, with the shorter relaxation delay seen for $^1$H spins, more scans can be acquired within the same experimental timeframe compared to direct excitation experiments. However, there are a few disadvantages to the application of CP. Inherently, the pulse sequence requires $^1$H spins to be present in your sample. While this is not a problem for biomolecular systems, many inorganic solids may not contain protons. Since the net magnetization of the nucleus of interest is enhanced by the polarization transfer from protons, the corresponding NMR spectrum is not quantitative. To obtain qualitative results, one must use a direct-excitation experiment (such as Bloch pulse or Spin-Echo pulses above). Another technique

called multiCP has also been proven to produce quantitative results using composite $\pi/2$ pulses.[12,13] Despite these disadvantages, CP has become routine for solid-state NMR spectroscopy due to its high turnover rate and sensitivity gains.

**2.2.5 Sensitivity Enhancement Pulse (Double Frequency Sweep – DFS)**

While CP is beneficial for boosting sensitivity for $I = 1/2$ nuclei, implementing CP for quadrupolar nuclei, $I > 1/2$, is not as routine.  One way to maximize sensitivity for quadrupolar nuclei is the use of population transfer techniques, such as double frequency sweeps, which uses adiabatic frequency sweeps across the satellite transitions (ST) to inverse the Boltzmann populations of the ST onto the central transition (CT) before a selective $\pi/2$ pulse is used to perturb the CT (Figure 2.8).[14,15]
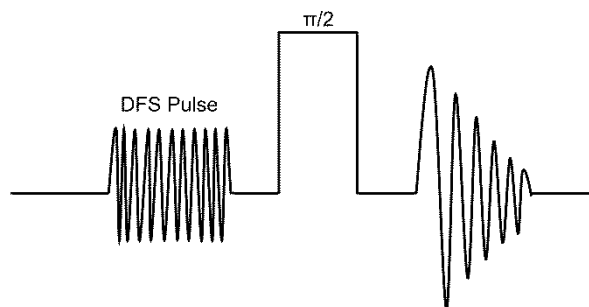


**Figure 2.8.** Double Frequency Sweep (DFS) pulse sequence followed by a selective $\pi/2$ pulse.

Depending on which energy levels are inverted first (i.e., +/- 5/2 to +/- 3/2, followed by +/- 3/2 to +/- 1/2, Type A, or +/-3/2 to +/- 1/2, followed by +/- 5/2 to +/- 3/2, Type B), the theoretical maximum enhancement ($\varepsilon_{DFS}$) can be 5 or 3, respectively for $I = 5/2$ nuclei (Figure 2.9). However, in real-world situations for powder samples, the ST frequencies are not easily distinguishable and thus, the resulting enhancements are smaller than the theoretical maximum. Nevertheless, the small enhancements are still beneficial in boosting the S/N for quadrupolar nuclei.

|  | Thermal Equilibrium | Population Inversion Type A | Population Inversion Type B |
|---|---|---|---|
| -5/2 | (1-5δ) | (1-3δ) | (1-δ) |
| -3/2 | (1-3δ) | (1-1δ) | (1-5δ) |
| -1/2 | (1-δ) | (1-5δ) | (1-3δ) |
| 1/2 | (1+δ) | (1+5δ) | (1+3δ) |
| 3/2 | (1+3δ) | (1+δ) | (1+5δ) |
| 5/2 | (1+5δ) | (1+3δ) | (1+δ) |
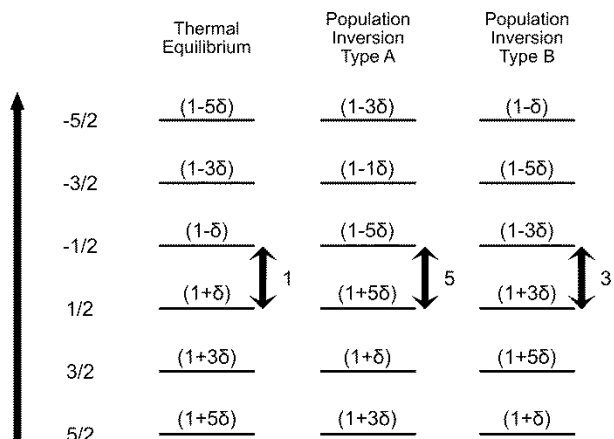
**Figure 2.9.** Enhancement values obtained due to the population inversion of double frequency sweep pulses for an $I = 5/2$ nucleus.

In addition to DFS, hyperbolic secant (HS)[16,17] pulses and rotor-assisted population transfer (RAPT)[18] are other population transfer techniques to increase sensitivity for quadrupolar nuclei. Similar to DFS, HS uses population inversion to transfer the polarization to the CT. On the other hand, RAPT saturates each energy level to boost the sensitivity of the CT.

### 2.2.6 Spectral Simulations (WSOLIDS)

To extract the NMR parameters ($\delta_{iso}$, $\Omega$, $\kappa$, $C_Q$, $\eta_Q$, $\alpha$, $\beta$, and $\gamma$) from the experimental NMR spectra, spectral simulations are completed using the program WSOLIDS1.[19] The experimental NMR spectra are fit using the Maryland Convention,[5,20] proposed by Mason and Herzfeld,[5] and endorsed by IUPAC[21] (*vide supra*). From the fitted data, the corresponding simulated NMR spectra are exported and visualized using TopSpin 4.1.3.

## 2.3 Dynamic Nuclear Polarization (DNP) NMR

Solid-state NMR spectroscopy has been a workhorse characterization technique for decades. However, it is inherently a low-sensitivity technique due to the small nuclear Zeeman polarization, as well as having a multitude of nuclear interactions (such as large anisotropy or quadrupole interactions) which create challenges with interpreting spectra. While there have been advancements in the field with the introduction of MAS, CP, and ultrahigh-field NMR magnets, increasing sensitivity remains at the forefront of NMR development.

Dynamic nuclear polarization (DNP) has expanded the versatility of NMR spectroscopy due to its tremendous sensitivity gains. Using a familiar concept of cross-polarization, where there

is a transfer of polarization from a high-spin abundant spin bath ($^1$H's) to an insensitive nucleus, DNP NMR uses the large electron polarization of unpaired electrons to boost sensitivity. Unlike CP where the transfer of polarization is based on parameters set in the pulse program, the electron-nuclear transitions for DNP are produced using microwave irradiation. Using this technique, sensitivity gains ranging from 10 – 100 times that of traditional NMR spectroscopy can be obtained routinely; thus, allowing for long and complex experiments to be completed in a reasonable timeframe. Below a general overview on DNP basics (such as instrumentation, polarization agents, and polarization transfer approaches) will be given. Readers are directed to the following sources for a more in-depth investigation of DNP and the advancements in this field.[22–32]

### 2.3.1 Dynamic Nuclear Polarization (DNP) Instrumentation

There are four major components which are crucial for dynamic nuclear polarization acquisition: a solid-state NMR spectrometer, a microwave source, cryogenics, and a DNP NMR probe. The solid-state NMR spectrometer needed for DNP is one used with conventional solid-state NMR experiments with a few additional requirements. Firstly, the magnet bore must be wide (89 mm) versus a standard (54 mm) bore to accommodate the electronics needed to perform experiments at cryogenic temperatures, as well as allow for microwave irradiation to reach the sample of interest. Additionally, an optional outer coil can be included to allow for minute adjustments to the main magnetic field. This is crucial for the optimization of the magnetic field strength tailored to the polarizing agent used.

One main difference between the traditional NMR setup with DNP is the addition of a microwave source. Typically, a gyrotron is used to generate high-frequency microwaves which are then guided to the sample of interest using a transmission line. While the gyrotron tube sits inside a similar superconducting magnet to the NMR spectrometer, the gyrotron emits microwaves in the GHz frequency range. Another difference is that all DNP experiments are performed under cryogenic temperatures (<130 K). The purpose of this is to improve the electron and nuclear relaxation behaviour, which allows for effective electron polarization transfer to bulk nuclear spins within the sample. As a constant supply of inert gas at cryogenic temperatures is needed, DNP experiments can be costly due to the additional cost of liquid nitrogen. However, there has been advancements in the development of a closed-loop system to recirculate liquid helium[33,34] or the use of nitrogen gas generators[35,36] to help minimize future costs.

As with all NMR experiments, an NMR probe is needed to send and detect the signal during signal acquisition. With DNP NMR probes, additional components are needed to allow for sample cooling and microwave irradiation of the rotor. To allow for optimal enhancements, sapphire NMR rotors are used as its been shown that sapphire is more transparent to microwaves, providing larger enhancements over the typical zirconia-based NMR rotors. Lastly, the rotor is capped with a zirconia, Torlon® or Vespel® drive cap.

## 2.3.2 Polarizing Agents

The mechanism of dynamic nuclear polarization requires a source of unpaired electron spins. This can be achieved using either endogenous (innate to the sample) or exogeneous radicals called polarizing agents, which are added to the sample of interest during sample preparation. Polarizing agents can be split up into two categories: narrow-line or wide-line radicals, with the distinction based on their corresponding electron paramagnetic resonance (EPR) lineshape. Typically, wide-line radicals are used as they are commercially available, as well as easier to synthesize in comparison to narrow-line radicals. In this work, wide-line radicals, AMUPol / bCTbK, and TEKPol, were used in Chapters 5 and 6, respectively (Figure 2.10).[37–40] Additionally, in Chapter 5, the intrinsic dangling bonds on the silicon nanoparticle surface provided a source of unpaired electrons for endogenous DNP studies.
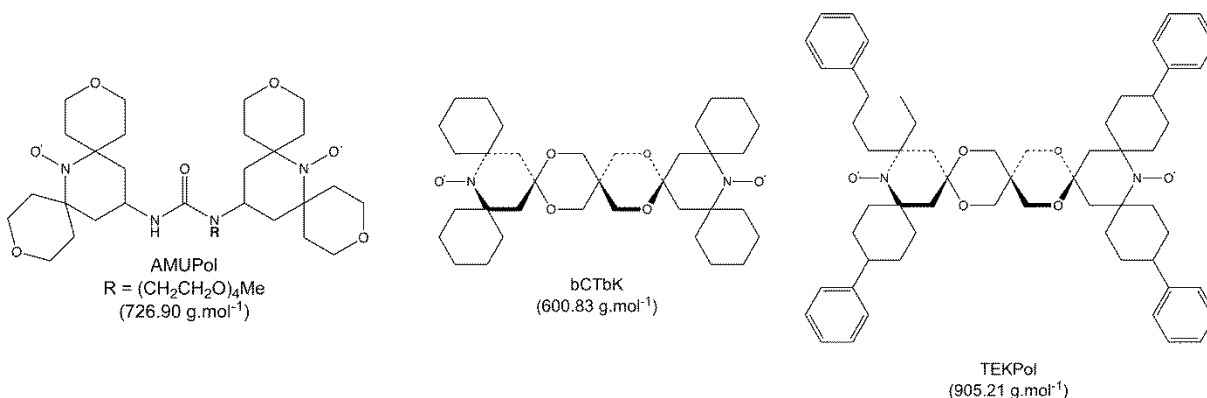


**Figure 2.10.** Chemical structures of the wide-line radicals used as polarization agents in this thesis.

## 2.3.3 Polarization Transfer Approaches and DNP Enhancement Factor (ε)

There are two different polarization transfer approaches for any conventional DNP NMR experiment: direct or indirect DNP. For a direct DNP experiment, the NMR active nucleus (X) is polarized directly from the source of unpaired electrons, e⁻ → X; whereas for an indirect DNP

experiment, the unpaired electrons polarize $^1$H spins followed by a CP step to observe the nucleus of interest, e$^-$ → $^1$H → X (Figure 2.11). Regardless of the method used to polarize the nucleus of interest, two nearly identical experiments must be completed for a DNP study, if studying the overall gain in sensitivity. When microwaves (MW) are on, this is known as a DNP NMR experiment (denoted as $MW_{on}$, or $\mu w_{on}$). The exact same experiment is then acquired without microwaves ($MW_{off}$, or $\mu w_{off}$), which is a standard solid-state NMR experiment. To quantify the gain in sensitivity, the DNP enhancement factor, $\varepsilon$, is then calculated by comparing the peak intensity ($I$) of the NMR spectrum acquired with and without microwaves, $I_{MWon}$ and $I_{MWoff}$, respectively (Equation 2.25).

$$\epsilon = \frac{I_{MWon}}{I_{MWon}}$$

2.25

The resulting reduction in experimental time is therefore determined by a factor of $\varepsilon^2$. Typically, larger gains in sensitivity are achieved using direct DNP polarization as the gyromagnetic ratios between electrons and the lower-$\gamma$ nuclei ($\gamma_e$/$\gamma_X$) are much higher than the ratio between electrons and $^1$H (indirect DNP). Regardless of the polarization transfer approach used, enhancement factors of up to 658 can be achieved using indirect DNP NMR in theory, opening the door for complex and "impossible" experiments to be performed.
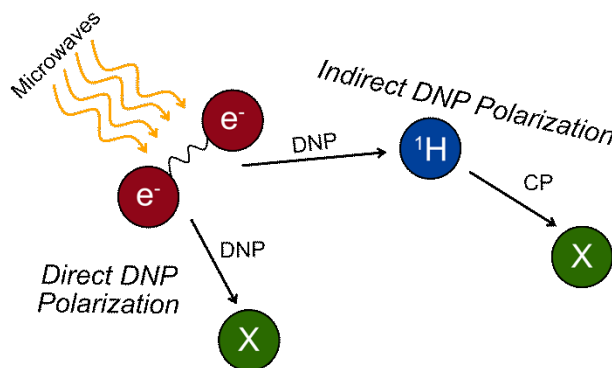


**Figure 2.11.** Illustration of direct and indirect polarization pathways for DNP NMR.

## 2.4 Computational Methods (Amsterdam Density Functional – ADF)

In Chapter 3 of this thesis, density functional theory (DFT) calculations are completed using the Amsterdam density functional (ADF) 2017 modelling suite.[41–43] Computations are used to gauge a better understanding if a certain system is NMR feasible prior to experimental acquisition or to compare if the experimental results are within theoretical reason. By modelling our chemical

systems, we compute NMR parameters ($\sigma$, $\Omega$, and $\kappa$) and then compare them to experimental values extracted using WSOLIDS1. The ADF modelling suite was used as it is a powerful molecular DFT system that allows for accurate modelling of heavy atoms. A zeroth order regular approximation (ZORA) approach is used in all calculations to ensure accurate approximations.

## 2.5 References

(1)     Duer, M. J. *Introduction to Solid-State NMR Spectroscopy*; Blackwell, 2005.

(2)     Harris, R. K. *Nuclear Magnetic Resonance Spectroscopy*; John Wiley and Sons: New York, 1986.

(3)     Apperley, D.; Harris, R.; Hodgkinson, P. *Solid-State NMR: Basic Principles & Practice*; Momentum Press, 2012.

(4)     Farrar, T. C.; Becker, E. D. *Pulse and Fourier Transform NMR*; Elsevier, 1971.

(5)     Herzfeld, J.; Berger, A. E. Sideband Intensities in NMR-Spectra of Samples Spinning at the Magic Angle. *J. Chem. Phys.* **1980**, *73*, 6021−6030.

(6)     Andrew, E. R.; Bradeuey, A.; Eades, R. G. Nuclear Magnetic Resonance Spectra from a Crystal Rotated at High Speed. *Nature* **1958**, *182* (4650), 1659–1659.

(7)     Lowe, I. J. Free Induction Decays of Rotating Solids. *Phys. Rev. Lett.* **1959**, *2* (7), 285–287.

(8)     Bloch, F. Nuclear Induction. *Phys. Rev.* **1946**, *70* (7–8), 460–474.

(9)     Hahn, E. L. Spin Echoes. *Phys. Rev.* **1950**, *80* (4), 580–594.

(10)    Carr, H. Y.; Purcell, E. M. Effects of Diffusion on Free Precession in Nuclear Magnetic Resonance Experiments. *Phys. Rev.* **1954**, *94* (3), 630–638.

(11)    Pines, A.; Gibby, M. G.; Waugh, J. S. Proton-Enhanced Nuclear Induction Spectroscopy. A Method for High Resolution NMR of Dilute Spins in Solids. *J. Chem. Phys.* **1972**, *56* (4), 1776–1777.

(12)    Johnson, R. L.; Schmidt-Rohr, K. Quantitative Solid-State $^{13}$C NMR with Signal Enhancement by Multiple Cross Polarization. *J. Magn. Reson.* **2014**, *239*, 44–49.

(13)    Duan, P.; Schmidt-Rohr, K. Composite-Pulse and Partially Dipolar Dephased MultiCP for Improved Quantitative Solid-State $^{13}$C NMR. *J. Magn. Reson.* **2017**, *285*, 68–78.

(14)    Kentgens, A. P. M.; Verhagen, R. Advantages of Double Frequency Sweeps in Static, MAS and MQMAS NMR of Spin I = 3/2 Nuclei. *Chem. Phys. Lett.* **1999**, *300* (3–4), 435–443.

(15)   Siegel, R.; Nakashima, T. T.; Wasylishen, R. E. Sensitivity Enhancement of NMR Spectra of Half-Integer Quadrupolar Nuclei in the Solid State via Population Transfer. *Concepts Magn. Reson. A* **2005**, *26A* (2), 47–61.

(16)   Silver, M. S.; Joseph, R. I.; Hoult, D. I. Selective Spin Inversion in Nuclear Magnetic Resonance and Coherent Optics through an Exact Solution of the Bloch-Riccati Equation. *Phys. Rev. A* **1985**, *31* (4), 2753–2755.

(17)   Silver, M. S.; Joseph, R. I.; Hoult, D. I. Highly Selective $\pi/2$ and $\pi$ Pulse Generation. *J. Magn. Reson.* **1984**, *59* (2), 347–351.

(18)   Yao, Z.; Kwak, H.-T.; Sakellariou, D.; Emsley, L.; Grandinetti, P. J. Sensitivity Enhancement of the Central Transition NMR Signal of Quadrupolar Nuclei under Magic-Angle Spinning. *Chem. Phys. Letts.* **2000**, *327* (1–2), 85–90.

(19)   Eichele, K. WSolids1. Universität Tübingen 2021.

(20)   Mason, J. Conventions for the Reporting of Nuclear Magnetic Shielding (or Shift) Tensors Suggested by Participants in the NATO ARW on NMR Shielding Constants at the University of Maryland, College Park, July 1992. *Solid State Nucl. Magn. Reson.* **1993**, *2*, 285−288.

(21)   Harris, R. K.; Becker, E. D.; de Menezes, S. M. C.; Granger, P.; Hoffman, R. E.; Zilm, K. W. Further Conventions for NMR Shielding and Chemical Shifts (IUPAC Recommendations 2008). *Pure Appl. Chem.* **2008**, *80*, 59–84.

(22)   Ni, Q. Z.; Daviso, E.; Can, T. v.; Markhasin, E.; Jawla, S. K.; Swager, T. M.; Temkin, R. J.; Herzfeld, J.; Griffin, R. G. High Frequency Dynamic Nuclear Polarization. *Acc. Chem. Res.* **2013**, *46* (9), 1933–1941.

(23)   Rossini, A. J.; Zagdoun, A.; Lelli, M.; Lesage, A.; Copéret, C.; Emsley, L. Dynamic Nuclear Polarization Surface Enhanced NMR Spectroscopy. *Acc. Chem. Res.* **2013**, *46* (9), 1942–1951.

(24)   Michaelis, V. K.; Griffin, R. G.; Corzilius, B.; Vega, S. *Handbook of High Field Dynamic Nuclear Polarization*; Michaelis, V. K., Griffin, R. G., Corzilius, B., Vega, S., Eds.; Wiley, 2020.

(25)   Maly, T.; Debelouchina, G. T.; Bajaj, V. S.; Hu, K.-N.; Joo, C.-G.; Mak–Jurkauskas, M. L.; Sirigiri, J. R.; van der Wel, P. C. A.; Herzfeld, J.; Temkin, R. J.; Griffin, R. G. Dynamic Nuclear Polarization at High Magnetic Fields. *J. Chem. Phys.* **2008**, *128* (5), 052211.

(26) Michaelis, V. K.; Ong, T.-C.; Kiesewetter, M. K.; Frantz, D. K.; Walish, J. J.; Ravera, E.; Luchinat, C.; Swager, T. M.; Griffin, R. G. Topical Developments in High-Field Dynamic Nuclear Polarization. *Isr. J. Chem.* **2014**, *54* (1–2), 207–221.

(27) Bernard, G. M.; Michaelis, V. K. Instrumentation for High-Field Dynamic Nuclear Polarization NMR Spectroscopy. *eMagRes* **2019**, *8* (2), 77–86.

(28) Hooper, R. W.; Klein, B. A.; Michaelis, V. K. Dynamic Nuclear Polarization (DNP) 101: A New Era for Materials. *Chem. Mater.* **2020**, *32* (11), 4425–4430.

(29) Michaelis, V. K.; Bryce, D. L. Editorial: Special Issue on Emerging Frontiers in Dynamic Nuclear Polarization NMR. *Solid State Nucl. Magn. Reson.* **2019**, *102*, 1.

(30) Lee, D.; Hediger, S.; Paëpe, G. de. High-Field Solid-State NMR with Dynamic Nuclear Polarization. In *Modern Magnetic Resonance*; Springer International Publishing: Cham, 2017; pp 1–17.

(31) Ha, M.; Michaelis, V. K. High-Frequency Dynamic Nuclear Polarization NMR for Solids: Part 1 – An Introduction. In *Modern Magnetic Resonance*; Springer International Publishing: Cham, 2017; pp 1–24.

(32) Ha, M.; Michaelis, V. K. High-Frequency Dynamic Nuclear Polarization NMR for Solids: Part 2 – Development and Applications. In *Modern Magnetic Resonance*; Springer International Publishing: Cham, 2017; pp 1–18.

(33) Matsuki, Y.; Idehara, T.; Fukazawa, J.; Fujiwara, T. Advanced Instrumentation for DNP-Enhanced MAS NMR for Higher Magnetic Fields and Lower Temperatures. *J. Magn. Reson.* **2016**, *264*, 107–115.

(34) Bouleau, E.; Saint-Bonnet, P.; Mentink-Vigier, F.; Takahashi, H.; Jacquot, J.-F.; Bardet, M.; Aussenac, F.; Purea, A.; Engelke, F.; Hediger, S.; Lee, D.; de Paëpe, G. Pushing NMR Sensitivity Limits Using Dynamic Nuclear Polarization with Closed-Loop Cryogenic Helium Sample Spinning. *Chem. Sci.* **2015**, *6* (12), 6806–6812.

(35) Matsuki, Y.; Takahashi, H.; Ueda, K.; Idehara, T.; Ogawa, I.; Toda, M.; Akutsu, H.; Fujiwara, T. Dynamic Nuclear Polarization Experiments at 14.1 T for Solid-State NMR. *Phys. Chem. Chem. Phys.* **2010**, *12* (22), 5799.

(36) Barnes, A. B.; Markhasin, E.; Daviso, E.; Michaelis, V. K.; Nanni, E. A.; Jawla, S. K.; Mena, E. L.; DeRocher, R.; Thakkar, A.; Woskov, P. P.; Herzfeld, J.; Temkin, R. J.; Griffin, R. G. Dynamic Nuclear Polarization at 700MHz/460GHz. *J. Magn. Reson.* **2012**, *224*, 1–7.

(37)     Kubicki, D. J.; Casano, G.; Schwarzwälder, M.; Abel, S.; Sauvée, C.; Ganesan, K.; Yulikov, M.; Rossini, A. J.; Jeschke, G.; Copéret, C.; Lesage, A.; Tordo, P.; Ouari, O.; Emsley, L. Rational Design of Dinitroxide Biradicals for Efficient Cross-Effect Dynamic Nuclear Polarization. *Chem. Sci.* **2016**, *7* (1), 550–558.

(38)     Matsuki, Y.; Maly, T.; Ouari, O.; Karoui, H.; le Moigne, F.; Rizzato, E.; Lyubenova, S.; Herzfeld, J.; Prisner, T.; Tordo, P.; Griffin, R. G. Dynamic Nuclear Polarization with a Rigid Biradical. *Angew. Chem. Int. Ed.* **2009**, *48* (27), 4996–5000.

(39)     Zagdoun, A.; Casano, G.; Ouari, O.; Schwarzwälder, M.; Rossini, A. J.; Aussenac, F.; Yulikov, M.; Jeschke, G.; Copéret, C.; Lesage, A.; Tordo, P.; Emsley, L. Large Molecular Weight Nitroxide Biradicals Providing Efficient Dynamic Nuclear Polarization at Temperatures up to 200 K. *J. Am. Chem. Soc.* **2013**, *135* (34), 12790–12797.

(40)     Sauvée, C.; Rosay, M.; Casano, G.; Aussenac, F.; Weber, R. T.; Ouari, O.; Tordo, P. Highly Efficient, Water-Soluble Polarizing Agents for Dynamic Nuclear Polarization at High Frequency. *Angew. Chem. Int. Ed.* **2013**, *52* (41), 10858–10861.

(41)     te Velde, G.; Bickelhaupt, F. M.; Baerends, E. J.; Fonseca Guerra, C.; van Gisbergen, S. J. A.; Snijders, J. G.; Ziegler, T. Chemistry with ADF. *J. Comput. Chem.* **2001**, *22* (9), 931–967.

(42)     Fonseca Guerra, C.; Snijders, J. G.; te Velde, G.; Baerends, E. J. Towards an Order- N DFT Method. *Theor. Chem. Acc.* **1998**, *99* (6), 391–403.

(43)     ADF 2019.3, SCM, Theoretical Chemistry, Vrije Universiteit, Amsterdam, The Netherlands.

# Chapter 3

## Phase Evolution in Methylammonium Tin Halide Perovskites with Variable Temperature Solid-state $^{119}$Sn NMR Spectroscopy

### 3.1 Introduction

Over the last decade the archetypical hybrid methylammonium lead iodide-based (and related modifications) perovskite has been a disruptive technology as a potentially new solar absorbing material with the photoconversion efficiency increasing from 4 % in 2009 to >25 % in 2019.[1] Extending beyond photovoltaic applications, these materials have exhibited exquisitely tailorable bandgaps, often spanning 2 to 3 eV, by adjusting the cation and/or halide compositions. These favorable optical and electronic properties have attracted their development in various applications such as light emitting diodes (LEDs), lasers, X-ray and γ-ray detectors, photocatalysis, etc.[2–6] Perovskites, with a generic formula of $ABX_3$, demonstrate excellent material tunability due to their high degree of elemental substitution in the cation (A and B) and anion (X) positions throughout their three-dimensional crystalline lattice. For example, the A site often incorporates a large inorganic (e.g., $Cs^+$) or small organic cation (e.g., methylammonium, $CH_3NH_3^+$, or formamidinium, $NH_2CH=NH_2^+$); the B site can accommodate $Pb^{2+}$, $Sn^{2+}$ or $Ge^{2+}$; while the X site can be Cl, Br, I or a mixture of these halides.[7–10] Generally, a material must satisfy a few constraints to be called a perovskite; this includes having a general formula, $ABX_3$, the B-site cation being in

an octahedral-like coordination environment, and the 3D network being interconnected through corner sharing $[BX_6]$ octahedra and appropriate tolerance factors.[11]

Although the photoconversion efficiency of $APbX_3$-based materials have surpassed other remarkable photovoltaic materials, such as CdTe, CIGS and amorphous Si, certain environmental and stability concerns exist as these materials contain Pb and have been shown to be sensitive to temperature and water, ultimately leading to decomposition into $PbX_2$.[12–14] Recently, the environmental impact of lead halide perovskites was demonstrated by measuring the bioavailability of plants in perovskite-contaminated soil.[15] The authors found that the lead contamination due to halide perovskites is ten times more bioavailable compared to other lead contaminants found in soil. Also, when exposing plants to the maximum safety level of perovskites in soil, most of them revealed signs of lead toxicity and plant death, suggesting that the safety level for lead needs to be lowered. To circumvent these degradation and environmental concerns, some researchers have shifted their focus to lead-free Sn-variants as new solar absorbing materials.[16–18] To date these materials have received far less attention primarily due to their initial weaker photoconversion efficiencies and the tendency of $Sn^{2+}$ to readily oxidize to $Sn^{4+}$, ultimately impacting the perovskite structure and optical properties.[19–22] However, studies have shown that tin halide perovskites with a cesium cation produce tunable photoluminescence via halide exchange, as well as photocurrents exceeding 22 mA/cm$^2$ when $CsSnI_3$ is used as the absorber in perovskite solar cells.[23,24] Using a mixed Sn-Pb B-site, a research team reported a hybrid perovskite solar cell with a 50:50 ratio of Sn:Pb ($CH_3NH_3Sn_{0.5}Pb_{0.5}I_3$) with a tailorable bandgap and a 4.18 % photoconversion efficiency.[25] Despite the challenges faced with tin-based perovskites, in 2014 $CH_3NH_3SnI_{3-x}Br_x$ and $CH_3NH_3SnI_3$ were successfully used as light harvesters; demonstrating the vast potential of tin-based perovskites as potential next-generation, environmentally-friendly solar cell materials.[26,27]

Understanding the underlying physical properties of Sn-based perovskites is vital if one is to obtain the optimum photoconversion properties for these materials. Recently, NMR spectroscopy has been shown to be an impressive analytical method in assessing cation and anion structural and dynamic aspects in relation to hybrid and non-hybrid lead halide perovskites[28–35] that is non-destructive, qualitative, and quantitative. Solid-state $^{119}$Sn nuclear magnetic resonance (NMR) spectroscopy can be utilized to assess phase changes and the impact of ion substitution on these Sn-based perovskites. Although many researchers use powder X-ray diffraction (XRD) as

their structural analysis method, NMR spectroscopy provides complementary insight into sub-nanometer (local and medium-range) structure, as well as on dynamics, further expanding our understanding of the material's structure-property relationships.

Here we extend this method to hybrid tin-containing halide perovskites as $^{119}$Sn (nuclear spin, $I = 1/2$) has a modest natural abundance of 8.58% and a relatively high magnetogyric ratio of $-10.0318 \cdot 10^{-7}$ rad $T^{-1}$ $s^{-1}$, nearly 1/3 that of $^1$H, making it a sensitive NMR probe nucleus for many materials.[36–42] Using *in situ* variable-temperature $^{119}$Sn NMR spectroscopy ranging from 190 to 540 K, the apparent phase transitions of MASnX$_3$, where X = Cl, Br or I, are investigated. Degradation of MASnI$_3$ is further examined by the impact on the spectral lineshape of the Sn environment. Furthermore, we compare $^{119}$Sn and $^{207}$Pb NMR characteristics of a mixed B-site MA(Sn/Pb)I$_3$ candidate with respect to the respective parent phases. Finally, we examine how the chemical shift and anisotropy are impacted by the halide composition and the extended Sn-X polyhedra using anionic cluster quantum chemical calculations.

## 3.2 Experimental Section

### 3.2.1 Materials and Methods

Tin halide salts, SnX$_2$ (X = Cl, Br or I) as well as distilled HI (57%) and H$_3$PO$_2$ (50%) were purchased from MilliporeSigma. Methylammonium halides (MAX, where X = Cl, Br or I) were sourced from GreatCell Solar (formerly DyeSol). During the course of this research we noticed that different sources (Alfa Aesar vs. Sigma Aldrich) of SnI$_2$ might contain approximately 50:50 mixtures of SnI$_2$ and SnI$_4$ (Figure 3.1); it is advisable that the starting material be screened using NMR and XRD prior to synthesis as mixtures may result in multiple phases of different methylammonium tin halide and tin halide species.
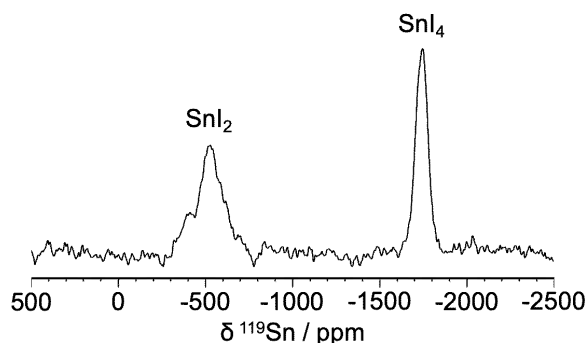
**Figure 3.1.** Solid-state $^{119}$Sn MAS NMR spectrum of freshly purchased $SnI_2$ (purported to be 99%), T = 290 K; $B_0$ = 11.75 T; $\omega_r/2\pi$ = 12 kHz; 2048 co-added transients. The purchased material clearly contains nearly equivalent fractions of both $SnI_2$ and $SnI_4$.

### 3.2.2 Synthesis of the Parent Phases

MASnX$_3$ parent phases were prepared using either solvent synthesis or solid-state reaction methods, or both, following previous published procedures for MASnCl$_3$,[43] MASnBr$_3$[44]and MASnI$_3$.[10]

### 3.2.3 Synthesis of the Mixed B-site Phase

A 100 ml three-necked round bottom flask was charged with a mixture of aqueous HI (6.8 ml, 7.58 M) and aqueous $H_3PO_2$ (1.7 ml, 9.14 M) under an inert atmosphere ($N_2$ gas). Prior to the addition of tin and lead iodide, the flask was purged for two minutes with $N_2$ gas. $SnI_2$ (186 mg; 0.5 mmol) and $PbI_2$ (231 mg; 0.5 mmol) were added to the solution with a stir bar set to 250 RPM. The temperature of the bright yellow solution was maintained between 80 and 90 °C using a mineral oil heating bath. Solid $CH_3NH_3I$ (159 mg, 1 mmol) was added to the solution and dissolved immediately. The mixture was heated to 120 °C until the solution was reduced by approximately half its volume and went from yellow to black (approximately 1 h). The stirring and heating sources were removed to allow the black solution to cool to ambient temperature and allowed to sit for 24 h under a nitrogen atmosphere to initiate crystallization from the mother liquor. The product was filtered and washed with degassed ethanol and stored under $N_2$.

### 3.2.4 Powder X-ray Diffraction (XRD)

Samples were ground to a powder using an agate mortar and pestle and placed on either plastic sample holders or packed into capillary tubes and sealed. XRD patterns were collected on an Inel powder diffractometer equipped with a curved position-sensitive detector (CPS 120) and a Cu $K_{\alpha 1}$ radiation source. $MASnI_3$ and $MASn_{0.5}Pb_{0.5}I_3$ were packed into capillaries and XRD data were acquired using a Bruker D8 Advance Diffractometer equipped with a Cu $K_\alpha$ source and Vantec-500 2D detector.

### 3.2.5 Solid-state Nuclear Magnetic Resonance Spectroscopy

Tin-119 NMR spectra were acquired at a magnetic field strength of 7.05 T (300 MHz $^1$H) with a Bruker AVANCE 300 spectrometer. Non-spinning and magic-angle spinning (MAS) $^{119}$Sn NMR experiments were undertaken using a 4.0 mm double resonance ($^1$H/X) NMR probe, where X was tuned to $^{119}$Sn. Spectra were acquired using a Hahn-echo pulse sequence with recycle delays set between 0.5 to 200 s, a $\gamma B_1/2\pi$ of 62.5 kHz (4.0 μs $\pi/2$ pulses) and 264 to 16,384 co-added transients. Variable temperature (VT) NMR spectra (150 to 360 K) were acquired for $MASnCl_3$, $MASnBr_3$ and $MASnI_3$ using a Bruker NEO 500 spectrometer equipped with a Bruker Smart Variable Temperature (BSVT) unit. The heat exchanger source was liquid nitrogen with a dry nitrogen gas source for temperatures below 235 K or an ethanol/dry ice bath, with dry air as the VT gas for temperatures in the 235 K to room temperature range. The variable offset cumulative spectra (VOCS)[45] approach (3-4 steps with 50 kHz transmitter frequency steps) was used for the complete acquisition of the resulting spectra for $MASnCl_3$, $MASnBr_3$ and decomposing $MASnI_3$. The individual spectra were added using the skyline projection method. To ensure detection of by-products that may have longer spin-lattice relaxation times, recycle delays were set based on arrayed parameter optimizations. Tin-119 NMR spectra were referenced to tetracyclohexyl tin ($\delta_{iso}$ = −97.35 ppm), a secondary reference with respect to $Sn(CH_3)_4$ (0 ppm). Temperature calibrations were performed using $MAPbCl_3$, a method developed by this group.[46]

High-temperature $^{119}$Sn MAS NMR spectra were acquired on a wide-bore Bruker Avance III HD 400 MHz spectrometer equipped with a 7 mm double-resonance probe, spinning at 3.0 kHz. The sample was heated using a 50 W $CO_2$ laser, and the temperature calibrated using the $^{79}$Br NMR signal of KBr as an external standard.[47] The room-temperature spectrum was acquired with a pulse

length of 4.6 μs (90° tip angle), a recycle delay of 20 s, and 20480 coadded transients. At higher temperatures, recycle delays of 5 s (T = 453 K) and 1 s (T = 533 K) were used, with 8k and 4k transients, respectively. Tetramethyltin (25% in $CHCl_3$) was used as the chemical shift reference (0 ppm).

All ^{1}H, ^{13}C, and [207]Pb NMR experiments for $MAPbI_3$ and $MASn_{0.5}Pb_{0.5}I_3$ were performed at 7.05 T (300 MHz ^{1}H) on a Bruker Avance 300 NMR spectrometer using a double resonance (^{1}H/X) NMR probe, where X was tuned to [13]C ($\omega_0/2\pi$ = 75.5 MHz) and [207]Pb ($\omega_0/2\pi$ = 62.9 MHz), respectively. All ^{1}H experiments were performed with a MAS frequency of 12.0 kHz. A 4.0 μs π/2 pulse ($\gamma B_1/2\pi$ = 62.5 kHz), 4 co-added transients and a recycle delay of 60 s were used for each measurement. All ^{1}H NMR spectra were referenced by setting the ^{1}H peak of adamantane to 1.85 ppm with respect to the primary reference sample, TMS with $\delta$(^{1}H) = 0.00 ppm. All ^{13}C experiments were performed under a MAS frequency of 5 kHz. A [1]H-^{13}C cross-polarization (CP)[51] technique with TPPM high-power ^{1}H decoupling[52] ($\gamma B_1/2\pi$ = 62.5 kHz) and 4.0 μs π/2 pulse ($\gamma B_1/2\pi$ = 62.5 kHz) for ^{1}H, a contact time of 3.5 ms, and a recycle delay time of 60 s were used for each measurement. All ^{13}C NMR spectra were referenced at 38.56 ppm for the high frequency ^{13}C resonance of solid adamantane with respect to the primary standard sample, TMS at $\delta$(^{13}C) = 0.00 ppm.[53] All [207]Pb NMR spectra were collected under non-spinning sample conditions. A Hahn-echo (($\pi/2)_x$-$\tau_1$-($\pi)_y$-$\tau_2$-ACQ, where $\tau_1$ and $\tau_2$ represent the interpulse and refocusing delays, respectively)[54] was used, with 0.5 -5.0 s recycle delays. All [207]Pb NMR spectra were referenced to the primary standard, $PbMe_4$ with $\delta$([207]Pb) = 0.0 ppm by setting the [207]Pb peak of $MAPbCl_3$ −647.5 ppm at 293(1) K.[46] All iodine-containing samples were synthesized and packed under $N_2$ with initial analysis in either sealed tubes or under nitrogen gas. Decomposition studies were measured at room temperature under air, without controlling for humidity (over the course of 6 months the average humidity levels in Edmonton, Alberta were between 50 and 75%); at the 6 month mark a series of ^{119}Sn NMR spectra were acquired using identical parameters, as discussed above, with the VOCS approach.

### 3.2.6 Quantum Chemical Calculations

Density functional theory (DFT) calculations on model tin-halide polyhedral anions, $[SnX_6]^{4-}$ where X = Cl, Br and I, were carried out using the Amsterdam Density Functional (ADF)

2017 modeling suite.[55–57] The polyhedral structures were modeled using existing crystal structure data.[10,21,58] Relativistic effects were calculated using the zeroth order regular approximation (ZORA) method along with the ZORA/QZ4P basis set, which is optimized for relativistic calculations.[59,60] All calculations used the BP86 functional in the generalized gradient approximation (GGA).[61,62]

## 3.3 Results and Discussion

Variable temperature $^{119}$Sn NMR experiments were performed on a series of crystalline hybrid tin halide perovskites to gain electronic and structural insight through their magnetic shielding. Below we discuss the chemical shift range observed for the cubic crystalline parent hybrid tin perovskites and the impact on the $^{119}$Sn chemical shift anisotropy (CSA) as the phases change upon cooling. This is further expanded upon using quantum chemical calculations, as well as by examining the changes in $^{119}$Sn and $^{207}$Pb NMR spectra when mixing B-sites (Sn/Pb = 1/1).

### 3.3.1 Parent Materials – MASnX$_3$ (X = Cl, Br and I)

XRD patterns for the solvent-synthesized polycrystalline MASnX$_3$ (X = Cl, Br and I) samples are provided in Figure 3.2a at room temperature and agree with previously reported structures with MASnCl$_3$ (space group P1) material exhibiting a triclinic phase (vide infra) and, MASnBr$_3$ and MASnI$_3$ materials exhibiting a cubic phase (space group Pm$\overline{3}$m) at room temperature. The $^{119}$Sn NMR spectra of MASnX$_3$ (X = Cl, Br and I) in their cubic (Pm$\overline{3}$m) perovskite phases are shown in Figure 3.2b. The local Sn(II) chemical environment is coordinated to six halide anions forming [SnX$_6$]$^{4-}$ octahedral clusters as shown in Figure 3.2c. As expected, the unit cell undergoes an expansion (a = 5.604 Å (Cl) → 5.901 Å (Br) → 6.204 Å (I)) to accommodate the increasing anionic radius (r(Cl$^-$) = 1.81 Å, r(Br$^-$) = 1.96 Å, and r(I$^-$) = 2.20 Å) proceeding down Group 17.[43,63]

With the Sn positioned at a cubic site of symmetry surrounded by six identical halide neighbors, the resulting lineshape for each parent phase is Gaussian-like in nature, with no evidence of chemical shift anisotropy at moderate magnetic field strengths. This is expected due to its spherical symmetry.  For MASnCl$_3$ in the cubic phase, the observed Gaussian lineshape is consistent with that expected from indirect spin-spin coupling between $^{119}$Sn and the six directly

bonded $^{35/37}$Cl nuclei (i.e., $^1J(^{119}$Sn,$^{35/37}$Cl); both $^{35}$Cl and $^{37}$Cl are $I = 3/2$ nuclei). A first-order $^{119}$Sn NMR spectrum contains 19 overlapping peak multiplets (Figure 3.3a) due to $^1J(^{119}$Sn,$^{35}$Cl) and $^1J(^{119}$Sn,$^{37}$Cl).[64] Although a splitting pattern to this interaction is not resolved, reported $^1J(^{119}$Sn,$^{35/37}$Cl) values ranging from 275 to 470 Hz are consistent with the observed linewidth for MASnCl$_3$.[65] However, the possible impact of the $^{35/37}$Cl nuclear quadrupole interactions on the $^{119}$Sn lineshapes cannot be discounted.[31,66] Likewise, indirect spin-spin interactions between $^{119}$Sn and $^{79/81}$Br (both $I = 3/2$) and $^{127}$I ($I = 5/2$, see Fig. 3.3b for the predicted first-order splitting pattern in this case) surely play a role in the observed $^{119}$Sn lineshapes, but the much larger nuclear quadrupole interactions expected for these nuclei preclude a straightforward analysis. See Ref. 31 & 35 for a comparable analysis of $^{207}$Pb-halide spin-spin coupling in MAPbX$_3$ perovskites. We note that the SnI$_6$ polyhedron in MASnI$_3$ is not a perfect octahedron, as previously discussed[10]; DFT results (below) on this very small distortion suggests a very small CSA ($\Omega < 10$ ppm) may be present. Each parent phase has a characteristic isotropic chemical shift ($\delta_{iso}$) with MASnCl$_3$ being the most shielded of the series, $\delta_{iso} = -404$ (1) ppm; MASnBr$_3$ is shifted slightly to higher frequency, $\delta_{iso} = -315$ (1) ppm and MASnI$_3$ is the most deshielded, $\delta_{iso} = 155$ (2) ppm. Over this series, the band gaps span approximately 2.5 eV: 3.69, 2.2 and 1.2 eV, respectively for MASnCl$_3$ (monoclinic, thin film), MASnBr$_3$ (cubic) and MASnI$_3$ (cubic); MASnCl$_3$ is white in color while MASnI$_3$ has a metallic black appearance.[10,19,43,67–69]

The NMR chemical shift is sensitive to the electronic and local structure; therefore, with any change or disturbance about the local nuclear electronic environment, an associated change in the shielding will be detected. The shielding contributions of these semiconducting materials are impacted by the differing contributions of the diamagnetic and paramagnetic shielding components. In this case, the material with the largest bandgap (MASnCl$_3$) is located to lower frequency, experiencing a greater shielding whereas a gradual deshielding is observed as the halide octahedron is replaced by Br and again by I. The halide MASnX$_3$ series spans nearly 550 ppm when in the cubic environment. A linear relationship between the optical bandgaps and the experimentally determined $^{119}$Sn isotropic chemical shifts appear to be present and may prove to be a practical analytical tool to describe solid solutions of these hybrid materials. The nuclear magnetic shielding is sensitive to the electronic structure about the nucleus of interest and thus is impacted by the local structure. Nuclei which have directly bonded halogen atoms usually exhibit

either a normal halogen dependence (NHD), wherein the magnetic shielding increases with the mass of the halogen atom, or such as the [119]Sn nuclei in this study, the inverse halogen dependence (IHD) wherein the magnetic shielding decreases with halide mass. These effects have been attributed to a spin-orbit contribution to the magnetic shielding.[70] In their computational study of Pb(II) and Pb(IV) halides, Dybowski and coworkers found that the spin-orbit contribution to shielding is essentially invariant to halide mass for the Pb(II) nuclei, but is responsible for the NHD for Pb(IV) nuclei. The IHD for the former was attributed to the paramagnetic contribution to magnetic shielding.[71] Table 3.1 summarizes the calculated paramagnetic ($\sigma_{para}$), diamagnetic ($\sigma_{dia}$) and spin-orbit ($\sigma_{so}$) contributions to the Sn magnetic shielding for a series of $[SnX_4]^{4-}$ model compounds. Qualitatively, the experimental trends are reproduced. In particular, the IHD is correctly predicted by these results. However, in contrast to the computational results reported by Dybowski and coworkers for Pb(II) halide complexes, our results suggest that the IHD observed for these Sn(II) complexes cannot be ascribed solely to the paramagnetic term: $\sigma_{para}$ and $\sigma_{so}$ contribute almost equally to the IHD. Both phenomena are impacted by numerous factors, such as structure and the local environment. A detailed study of this phenomenon requires an examination of many more samples and thus is beyond the scope of the present study, but it is a promising avenue that merits future consideration.
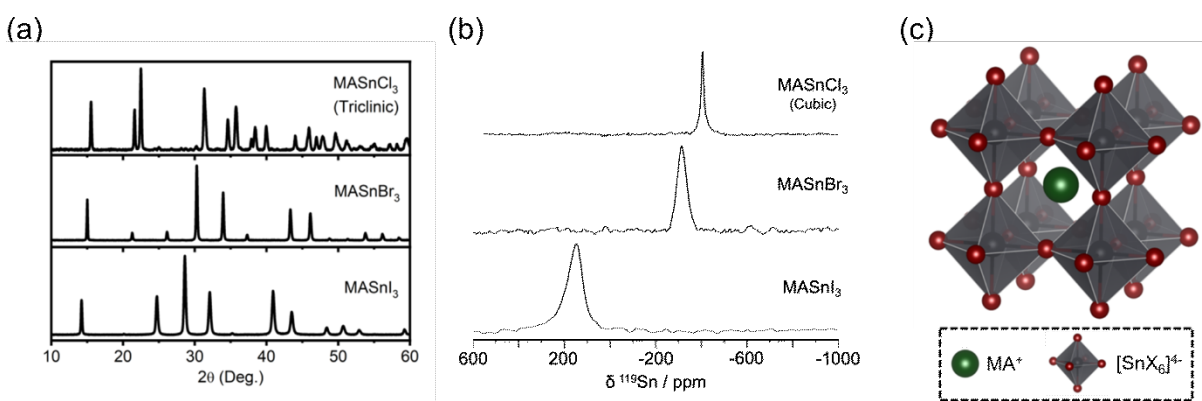


**Figure 3.2.** (a) Room temperature powder X-ray diffraction patterns for freshly synthesized $MASnX_3$ (X = Cl (Triclinic), Br (Cubic) and I (Cubic)). (b) Solid-state ^{119}Sn NMR spectra of cubic methylammonium tin halide perovskites, $MASnX_3$ where X= Cl, Br and I; $MASnCl_3$ ($\omega_r/2\pi = 3$ kHz; 9.4 T; $T_{sample}$ = 533 (5) K), $MASnBr_3$ ($\omega_r/2\pi = 10$ kHz; 7.05 T; $T_{sample}$ = 290 (1) K) and $MASnI_3$ (non-spinning; 7.05 T; $T_{sample}$ = 290 (1) K). (c) Graphic illustration of the arrangement of $[SnX_6]^{4-}$ clusters.

**Table 3.1.** Calculated magnetic shielding parameters for $[SnX_6]^{4-}$ (X = Cl, Br, I).

| | $\sigma_{11}$ | | | | $\sigma_{22}$ | | | | $\sigma_{33}$ | | | | $\sigma_{iso}$ | | | |
|---|---|---|---|---|---|---|---|---|---|---|---|---|---|---|---|---|
| | $\sigma_{para}$ | $\sigma_{dia}$ | $\sigma_{SO}$ | $\sigma_{tot}$ | $\sigma_{para}$ | $\sigma_{dia}$ | $\sigma_{SO}$ | $\sigma_{tot}$ | $\sigma_{para}$ | $\sigma_{dia}$ | $\sigma_{SO}$ | $\sigma_{tot}$ | $\sigma_{para}$ | $\sigma_{dia}$ | $\sigma_{SO}$ | $\sigma_{tot}$ |
| **$SnCl_6^{4-}$** | | | | | | | | | | | | | | | | |
| Cubic | −1974 | 5106 | 436 | 3567 | −1974 | 5106 | 436 | 3567 | −1974 | 5106 | 436 | 3567 | −1974 | 5106 | 436 | 3567 |
| Mono. | −2133 | 5104 | 355 | 3333 | −2074 | 5105 | 362 | 3391 | −1977 | 5106 | 443 | 3567 | −2061 | 5105 | 387 | 3431 |
| Tric. A | −2240 | 5101 | 323 | 3190 | −2153 | 5103 | 328 | 3275 | −1961 | 5104 | 470 | 3609 | −2118 | 5103 | 374 | 3358 |
| Tric. B | −2178 | 5105 | 319 | 3248 | −2086 | 5106 | 359 | 3383 | −1970 | 5108 | 412 | 3544 | −2078 | 5106 | 363 | 3392 |
| **$SnBr_6^{4-}$** | | | | | | | | | | | | | | | | |
| Cubic | −2195 | 5075 | 304 | 3184 | −2195 | 5075 | 304 | 3184 | −2195 | 5075 | 304 | 3184 | −2195 | 5075 | 304 | 3184 |
| Ortho. | −2206 | 5026 | 77 | 2897 | −2181 | 5050 | 183 | 3051 | −2129 | 5053 | 195 | 3120 | −2172 | 5042 | 152 | 3023 |
| **$SnI_6^{4-}$** | | | | | | | | | | | | | | | | |
| Alpha | −2435 | 5091 | −21 | 2635 | −2435 | 5091 | −21 | 2635 | −2430 | 5091 | −19 | 2643 | −2434 | 5091 | −20 | 2638 |
| Beta | −2446 | 5091 | −9 | 2637 | −2446 | 5091 | −9 | 2637 | −2437 | 5091 | 6 | 2661 | −2443 | 5091 | −4 | 2645 |

**Figure 3.3.** First-order $J$-coupling splitting pattern expected for an $I = 1/2$ nucleus coupled to six magnetically equivalent $I = 3/2$ nuclei (i.e., $^{35/37}Cl$ or $^{79/81}Br$) with negligible quadrupolar interactions and with relative peak intensities of 1:6:21:56:120:216:336:456:546:580:546:456: 336:216:120:56:21:6:1(a)[64]; the trace above this pattern illustrates the Gaussian lineshape expected if individual peaks are not resolved. The corresponding pattern for an $I = 1/2$ nucleus indirectly spin-spin coupled to six $I = 5/2$ nuclei (i.e., $^{127}I$) with relative peak intensity ratios of 1:6:21:56:126:252:456:756:1161:1666:2247:5856:3431:3906:4221:4332:4221:3906:3431:2856:2 247:1666:1161: 756:456:252:126:56:21:6:1 (b)[64].

### 3.3.2 MASnCl₃

Methylammonium tin chloride is a white crystalline material that exists in four unique crystallographic phases. Unlike its sister compound MAPbCl₃, which is stable and resides in the cubic phase under ambient conditions, the Sn congener undergoes three phase changes between 300 and 478 K,[31,43] and only resides in a cubic (Pm-3m) crystal phase hexacoordinated to Cl with corner sharing polyhedra above 478 K. At ambient conditions (< 300 K), the crystal structure reverts to a triclinic (space group, P1) structure with Sn being five-coordinate in a distorted square pyramidal type of polyhedron, with a zipper-like Sn-Cl-Sn-Cl-Sn chain structure running along the B axis. Slightly above ambient conditions Furukawa et al. have reported a complex phase change region where the triclinic structure transforms to a monoclinic (space group, Pc) structure at 318 K, followed quickly by the evolution of a rhombohedral (space group, R3m) structure at 350 K.[21] The authors describe this as a breakdown in the symmetric trans Cl-Sn-Cl bonds present above 480 K, whereby the pseudo-cubic phase begins to have an asymmetric Cl-Sn---Cl bond, becoming increasingly stretched (or deformed) as the temperature decreases.[21,72] Figure 3.4 shows the minor response in the CSA to these structural changes using variable-temperature $^{119}Sn$ NMR

spectroscopy of MASnCl$_3$. Beginning at 250 K, the MASnCl$_3$ sample is gradually heated through each phase transition temperature: triclinic ($\Omega = 700$ (15) ppm; T = 245 K) → monoclinic ($\Omega = 643$ (15) ppm; T = 320 K) → rhombohedral ($\Omega = 620$ (10) ppm; T = 360 K) → cubic ($\Omega = 0$ ppm; T = 533 K; full width at half maximum (FWHM) = 2.72 kHz). As the sample is heated towards the cubic phase transition temperature (533 K), the CSA powder pattern drastically decreases (Figure 3.5). The decrease in CSA appears to relate to this Cl-Sn---Cl distortion (e.g., Sn---Cl - 3.19 Å (triclinic) → 3.16 Å (monoclinic) → 3.03 Å (rhombohedral) → 2.88 Å (cubic)) about the Sn environment. These findings are further supported qualitatively by the DFT calculations, where the largest CSA is associated with the triclinic phase, although the experimentally observed span is underestimated by DFT. Table 3.2 summarizes the CSA parameters obtained from fitting both magic-angle spinning (MAS) and non-spinning $^{119}$Sn NMR spectra (Figure 3.4).

**Table 3.2.** Experimental $^{119}$Sn NMR parameters for MASnX$_3$

| Compound | $\delta_{iso}$ (ppm) | Span, $\Omega$ (ppm) | Skew, κ | Space Group | Crystal System | Temperature (K) |
|---|---|---|---|---|---|---|
| MASnCl$_3$ | -405 (1) | - | - | $Pm\bar{3}m$ | Cubic | 533 |
| MASnCl$_3$ | -400 (1) | 620 (10) | 0.95 | $R3m$ | Rhombohedral | 350 |
| MASnCl$_3$ | -396 (1) | 643 (15) | 0.92 | $Pc$ | Monoclinic | 318 |
| MASnCl$_3$ – Sn1 | -394(1) | 700 (15) | 0.97 | $P1$ | Triclinic | 250 |
| | -367 (1) | 710 (15) | 1.0 | | | |
| MASnCl$_3$ – Sn2 | | | | | | |
| MASnBr$_3$ | -315 (2) | - | - | Pm3m | Cubic | 295 |
| MASnBr$_3$ | -340 (5) | 800 | 1.0 | PmC21 | Orthorhombic | 200 |
| $\alpha$-MASnI$_3$ | 155 (2) | - | - | P4mm | Tetragonal | 295 |
| β-MASnI$_3$ | -100 (3) | 190 (6) | 0.55 | I4cm | Tetragonal | < 200 K |
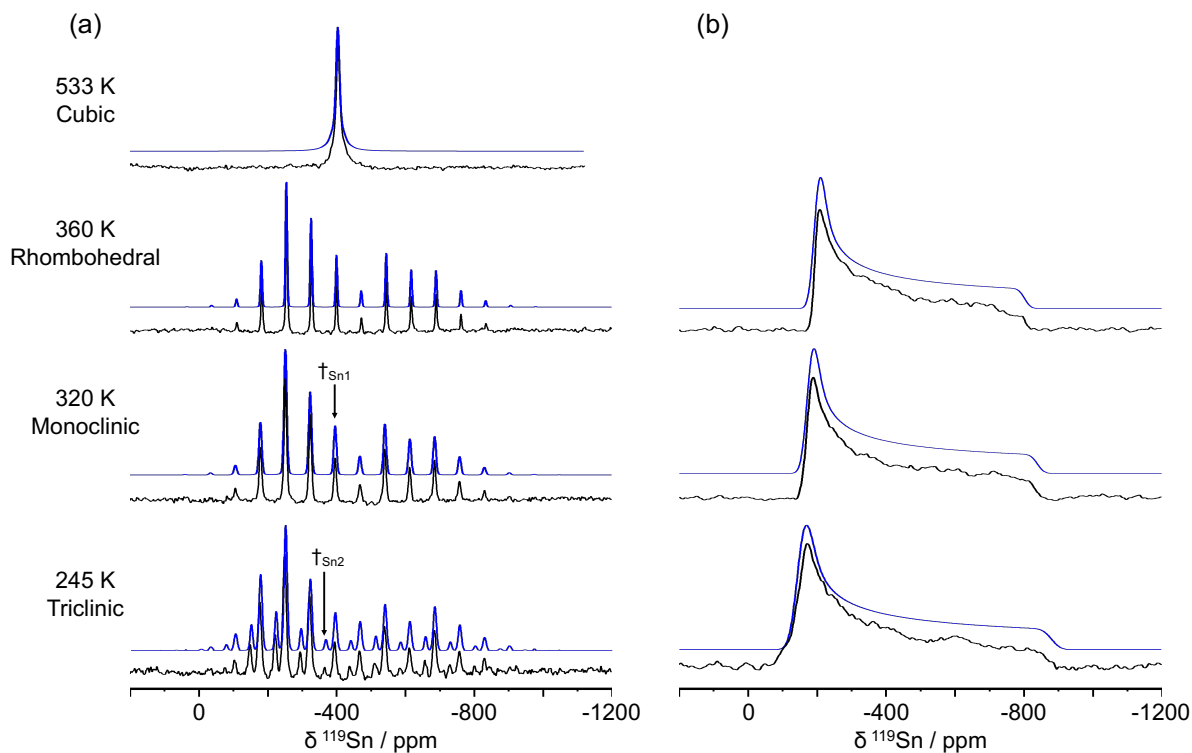
**Figure 3.4.** Experimental (black) and simulated (blue) variable temperature MAS (a) and non-spinning (b) $^{119}$Sn NMR spectra of MASnCl$_3$ for cubic (a, T = 533 K; B$_0$ = 9.4 T; $\omega_r/2\pi$ = 3 kHz; 3202 co-added transients), rhombohedral (a, T = 360 K; B$_0$ = 11.75 T; $\omega_r/2\pi$ = 13.5 kHz; 488 co-added transients and b, T=360 K; B$_0$ = 11.75 T; non-spinning; 256 co-added transients), Monoclinic (a, T = 320 K; B$_0$ = 11.75 T; $\omega_r/2\pi$ = 13.5 kHz; 512 co-added transients and b, T = 318 K; B$_0$ = 11.75 T; non-spinning; 256 co-added transients) and triclinic (a, T = 245 K; B$_0$ = 11.75 T; $\omega_r/2\pi$ = 13.5 kHz; 1024 co-added transients and b, T = 245 K; B$_0$ = 11.75 T; non-spinning; 1024 co-added transients) crystal structures. Note: $\delta_{iso}$ is indicated as †$_{Sn1}$ with a second tin site at 245 K indicated by †$_{Sn2}$.
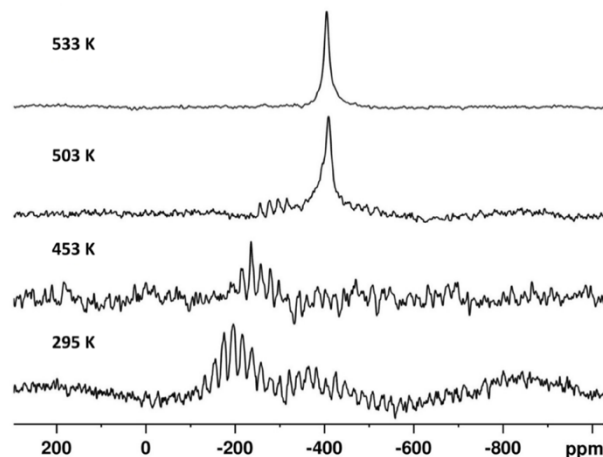
**Figure 3.5.** Variable temperature $^{119}$Sn MAS NMR spectra of MASnCl$_3$ (B$_0$ = 9.4 T; $\omega_r/2\pi$ = 3 kHz).

### 3.3.3 MASnBr$_3$

The unique corner-sharing [BX$_6$] octahedra in the high-temperature aristotype perovskite structure allows for a series of tilts (i.e., cooperative rotations) as the temperature decreases and can enter subsequent phases. As noted above, the high temperature $\alpha$-phase (space group, Pm3m) is cubic with Sn surrounded by six Br$^-$ neighbors forming perfect corner-sharing octahedra with the methylammonium cation sitting in the cuboctahedron site coordinated to 12 Br$^-$.[73] The non-spinning $^{119}$Sn NMR spectrum shows a single Gaussian-like peak, with a FWHM *ca.* 8.0 kHz and an isotropic chemical shift of −315 ppm (Figure 3.6). Onoda-Yamamuro et al. reported that the MASnBr$_3$ perovskite converts from a semiconducting cubic solid to an insulator at 195 K with a rhombohedral crystal structure (R2c or R-3c) when using a deuterated MA cation.[74] A synchrotron study on non-deuterated MASnBr$_3$ (as studied herein) revealed that the only low temperature phase observed is orthorhombic (space group Pmc2$_1$).[58] They further extensively studied the heating and cooling of this material between 188 and 230 K, but could not find evidence of this 3$^{rd}$ rhombohedral phase. The authors suggest this could be due to a strong deuterium isotope effect on the phase boundaries which has been previously reported in MAGeCl$_3$, where CD$_3$ND$_3$GeCl$_3$ is rhombohedral and CH$_3$NH$_3$GeCl$_3$ is cubic at a high temperature (349 K).[9,58,75] To determine the $^{119}$Sn NMR parameters of the low-temperature MASnBr$_3$ orthorhombic phase, the sample was cooled to 200 K (Figure 3.6). The asymmetric $^{119}$Sn lineshape ($\delta_{iso}$ = −340 ppm; $\Omega$ = 790 ppm) is consistent with an orthorhombic phase as the Sn center is no longer in the symmetric environment

seen at higher temperatures. The large CSA determined experimentally is further supported by DFT calculations (vide infra, Table 3.3).
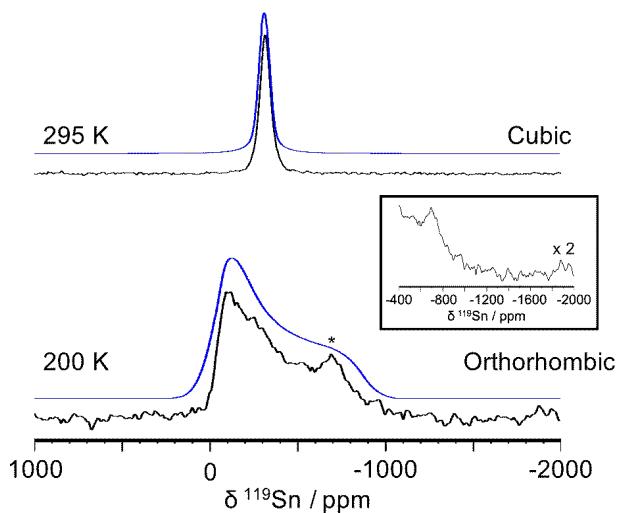


**Figure 3.6.** Experimental (black) and simulated (blue) variable temperature $^{119}$Sn NMR spectra of MASnBr$_3$ (top) cubic (T = 295 K; B$_0$ = 7.05 T; non-spinning; 2048 co-added transients) and (bottom) orthorhombic (T = 200 K; B$_0$ = 11.75 T; non-spinning; 264 co-added transients). Note the presence of a SnBr$_2$ impurity (*, center-of-gravity shift $\delta_{cgs}$ = -639 ppm) is apparent in the spectrum acquired at 200 K; it is also present in the spectrum acquired at 295 K, but less apparent due to the different nuclear relaxation parameters as the sample is cooled and because, unlike MASnBr$_3$, SnBr$_2$ is not in a cubic environment at 295 K and thus its peak is not sharp. Inset is the orthorhombic spectrum vertically scaled by 2 to highlight the SnBr$_2$ ($\delta_{cgs}$ = -639 ppm) impurity present, as well as the region where the potential degradation product, MA$_2$SnBr$_6$, would appear.

**Table 3.3.** Density functional theory (DFT) calculated NMR parameters using ADF 2017, implementing a zero-order regular approximation, quadrupole-zeta basis set (ZORA/QZ4P) and the BP86 functional.

| Compound | $\sigma_{iso}$ (ppm) | Span, $\Omega$ (ppm) | Skew, $\kappa$ | Space Group | Crystal System | Temperature (K) |
|---|---|---|---|---|---|---|
| $[SnCl_6]^{4-}$ | 3567.27 | 0.001 | -1.00 | $Pm\bar{3}m$ | Cubic | 533 |
| $[SnCl_6]^{4-}$ | 3518.17 | 20.30 | 1.00 | $R3m$ | Rhombohedral | 350 |
| $[SnCl_6]^{4-}$ | 3430.57 | 234.2 | 0.50 | $Pc$ | Monoclinic | 318 |
| $[SnCl_6]^{4-}$ | 3391.60 | 295.6 | 0.09 | $P1$ | Triclinic Sn1 | 250 |
| $[SnCl_6]^{4-}$ | 3358.46 | 419.3 | 0.59 | $P1$ | Triclinic Sn2 | 250 |
| $[SnBr_6]^{4-}$ | 3184.40 | 0.001 | 1.00 | $Pm3m$ | Cubic | 295 |
| $[SnBr_6]^{4-}$ | 3022.70 | 223.2 | -0.39 | $PmC21$ | Orthorhombic | 200 |
| $\alpha$-$[SnI_6]^{4-}$ | 2637.90 | 7.245 | 1.00 | $Pm\bar{3}m$ $P4mm^1$ | Cubic | 295 |
| $\beta$-$[SnI_6]^{4-}$ | 2644.50 | 24.08 | 1.00 | $I4cm$ | Tetragonal | 190 |

*1. See discussion in Stoumpus et al., 2013, Inorg. Chem., 52, 9019-9038*

### 3.3.4 MASnI$_3$

MASnI$_3$ is fascinating as, in addition to its attractive semiconducting properties with reported bandgaps of between 1.21 and 1.35 eV being in a suitable range for direct bandgap solar absorbing applications, the Cs and MA perovskites also display some metallic properties.[10,76] As observed for the MASnBr$_3$ material, MASnI$_3$ also can exist in two phases, with the $\alpha$-MASnI$_3$ being cubic (Pm-3m) and more recently reported as *pseudo* cubic (tetragonal with a space group of P4mm), while the low temperature (200 K) $\beta$-MASnI$_3$ phase is tetragonal (I4cm).[10,43,73,77] Figure 3.7 shows the non-spinning $^{119}$Sn NMR spectra for the $\alpha$- and $\beta$-MASnI$_3$ phases at 295 and 190 K, respectively; the $^{119}$Sn NMR spectrum for the $\alpha$-phase has a Gaussian-like lineshape (FWHM *ca.* 8.95 kHz) with $\delta_{iso}$ = 155 ppm, consistent with the nearly cubic structure as reported by Stoumpos et al.[10] As described by these authors, a non-centrosymmetric tetragonal space group is the best description for the hybrid perovskite phase. Unlike a single atom (e.g., Cs$^+$) being able to occupy the 1b Wyckoff position at the center of the cuboctahedron, organic cations (e.g., CH$_3$NH$_3^+$ or HC(NH$_2$)$_2^+$) cannot satisfy this condition, thereby creating structural disorder within the cage and the potential for hydrogen---halide interactions.

The $^{119}$Sn NMR spectrum for the $\beta$-phase displays a small shielding anisotropy of $\Omega$ = 190(10) ppm ($\kappa$ = 0.55), indicating sensitivity to the polyhedron distortion upon cooling, and the chemical shift changes by 250 ppm, shifting to lower frequency at $\delta_{iso}$ = $-100$ (3) ppm. A small deformation in the axial Sn-I bonds occurs as the pseudo-cubic crystalline sample is cooled from 295 to 190 K, which causes one Sn-I bond to shrink (3.057 Å) and the other to lengthen (3.158 Å). This change is directed along the c-axis of the crystal lattice while the four Sn-I ionic bonds arranged in the equatorial square-planar geometry remain constant at 3.1324 Å. The DFT results (below) do predict this increase in shielding anisotropy (as it did for the Cl) but underestimate its magnitude and poorly reproduce the chemical shift even when relativistic effects are incorporated in the calculation. The poor agreement may be due to the impact of the different electronic properties of the two phases and that MASnI$_3$ can display unique semi-conducting and metal properties which may impact the experimental results but are not accurately incorporated in the present quantum chemical computations on an isolated anionic "molecular" complex.
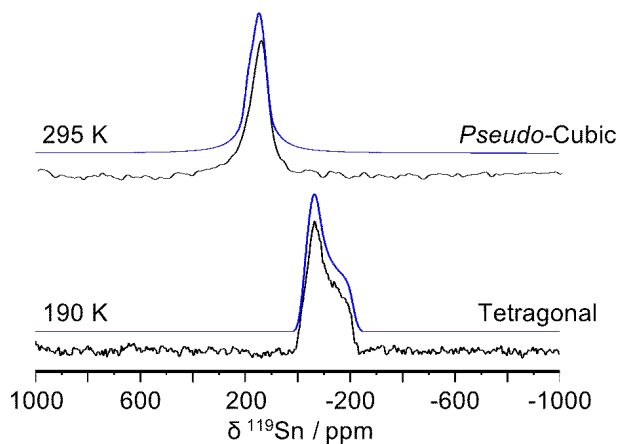
**Figure 3.7.** Experimental (black) and simulated (blue) variable temperature $^{119}$Sn NMR spectra of MASnI$_3$ (top) pseudo-cubic ($\alpha$-phase, T = 295 K; B$_0$ = 7.05 T; non-spinning; 64 co-added transients) and (bottom) tetragonal ($\beta$-phase, T = 190 K; B$_0$=11.75 T; non-spinning; 4098 co-added transients).

### 3.3.5 Tracking MASnI$_3$ Degradation

Degradation of tin(II)-based perovskites has precluded the widespread application of these materials as an alternative to lead-halide perovskite materials. As such, many researchers continue to explore strategies to avoid rapid degradation under ambient conditions, such as encapsulation under an inert atmosphere, polymer coating or ion mixing (A-, B-, or X-sites). In order to investigate the ambient air stability and degradation of MASnX$_3$ materials, we applied solid-state $^{119}$Sn NMR to study freshly synthesized MASnX$_3$ samples; the summary of the results is presented below.

Under ambient conditions (i.e., room temperature, parafilm-sealed vial under air), degradation was not a significant concern when handling MASnCl$_3$ and MASnBr$_3$ compounds. In fact, based on the NMR spectra, there was no indication of degradation of MASnCl$_3$ and MASnBr$_3$ after two years from the date of synthesis. The only other material detected by $^{119}$Sn NMR in MASnBr$_3$ was SnBr$_2$, which we believe is from unreacted starting material (vide supra). Previously, our group investigated the decomposition of MAPbI$_3$ under hydro, thermal and hydrothermal exposure, revealing intricate spectral changes amongst PbI$_2$, MAPbI$_3$, MAPbI$_3$·H$_2$O and MA$_4$PbI$_6$·2H$_2$O.[12] This approach is not feasible for MASnI$_3$ as the compound shows the onset of degradation within an hour of synthesis; some evidence of degradation was also apparent when undertaking NMR studies of the low-temperature phase acquired under dry nitrogen gas. Figure

3.8a shows a spectrum of the freshly synthesized material ($\sim$ 30 min post-synthesis under $N_2$ atmosphere) which is denoted as time (T) = 0 h. As MASnI$_3$ degrades, the linewidth and chemical shift change, with the latter shifting to a higher frequency over a period of hours as noted at T = 4 and 36 h (Figure 3.8a). The overall effect is quite drastic, with the spectral changes plotted in Figure 3.8b. Over a period of 30 hours the $^{119}$Sn NMR resonance broadens significantly from $\sim$10 kHz to >30 kHz (Figure 3.8b). Degradation also leads to a shift of the resonance (center-of-gravity) to higher frequency by $\sim$ 115 ppm over the same period of time. The result of this reactivity can significantly skew the reported $^{119}$Sn NMR results, shifting the center-of-gravity upwards by a few 100 ppm and resulting in drastic changes to both the lineshape and breadth.

Although we cannot determine the exact decomposition product(s) in MASnI$_3$ over this time frame, it is well documented that MASnI$_3$ readily decomposes.[78,79] Some possible candidates include Sn(II)-based species such as SnO and SnI$_2$, or fully oxidized Sn(IV) species such as SnO$_2$, SnI$_4$ or MA$_2$SnI$_6$. During attempts to synthesize pure MASnI$_3$, a series of identifiable and unidentifiable compounds were observed in the XRD. We were able to identify a few oxidized Sn(IV) species such as MA$_2$SnI$_6$, SnO$_2$ or SnI$_4$. Unfortunately, during this study we also determined that various commercial sources of SnI$_2$ contains significant amounts of SnI$_4$ (Figure 3.1). As a result, the presence of both Sn(II)- and Sn(IV)-based iodides may be observed in the XRD due to unreacted impurities in the starting materials. Leading to further complications, the presence of SnI$_4$ (or oxidation of SnI$_2$) may further assist in forming MA$_2$SnI$_6$, while oxidation may occur during the XRD measurement. The pure phase of MASnI$_3$ reported in this work was examined immediately post-synthesis ($\sim$30 min) within a sealed capillary using pure (> 99%) SnI$_2$ as a starting material in tandem with the NMR study. The first 36-hour period after synthesis was continuously monitored using $^{119}$Sn NMR, however none of these degradation products were observed. The difficulty of using NMR to track decomposition is compounded by the fact that degradation products have different nuclear spin-lattice relaxation times (ranging from ms to sec) and suffer from varying degrees of chemical shift anisotropy, making it difficult to optimize acquisition parameters to observe all possible compounds uniformly, especially if the time-consuming VOCS approach is required to cover the large chemical shift range of nearly 13,000 ppm (covering Sn metal to MA$_2$SnI$_6$, spanning over 1 MHz at 7.05 T).[38,41,80,81] Interestingly, six months after the synthesis of the solution-prepared sample, a very broad $^{119}$Sn NMR signal spanning $\sim$ 2800 ppm (315 kHz FWHM) and centered at $\sim$1500 ppm was observed (Figure 3.8c).

The aged MASnI$_3$ appears to be trending towards the reported chemical shift range for Sn metal, indicating some type of intermediate phase(s) (Figure 3.9) that cannot be positively identified but that resonates between the chemical shifts for metallic Sn and the MASnI$_3$ parent phase (Figure 3.8d).[81–83]

While preparing this report, a publication appeared in which a sample of MASnI$_3$ prepared using mechanochemical synthesis (MCS) exhibited a broad (~100 kHz, $T_2$*=10 μs) and slightly asymmetric ^{119}Sn NMR resonance with a reported isotropic chemical shift of 795 ppm.[81] This finding contrasts with the work reported here for a solution-based synthesis under N$_2$, where the non-spinning ^{119}Sn NMR spectrum is Gaussian-like with a FWHM of *ca.* 9 kHz ($T_2$*=110 μs) and with an isotropic chemical shift of 155 ppm. Similar differences are noted with the mixed bromide-iodide MCS sample in that report, where the ^{119}Sn NMR resonance for MASnBr$_{0.9}$I$_{2.1}$ (δ = 1586 ppm) is much broader and shifted to even higher frequency than that of their parent MASnI$_3$ phase. The electronic properties of methylammonium tin halide perovskites would suggest that the NMR signal of a mixed Br/I phase would be located between their reported parent end members (i.e., MASnI$_3$ and MASnBr$_3$), as observed in the case of the analogous MCS-made methylammonium lead halide perovskites, where all halide solid solutions are located between the parent end-members.[28] Likewise, these authors report the incorporation of Cl$^-$ into the MASnI$_3$ lattice, forming MASnCl$_{2.7}$I$_{0.3}$, based on the appearance of a new ^{119}Sn NMR resonance centered at 249 ppm. This new resonance is situated between their reported parent end members (MASnI$_3$, δ = 795 ppm and MASnCl$_3$, δ$_{iso}$ = -395 ppm), and is narrower than either of their reported MASnI$_3$ or MASnBr$_{0.9}$I$_{2.1}$ phases, all prepared using mechanochemical methods. Finally, Kubicki and coworkers detected metallic β-Sn as well as MA$_2$SnI$_6$ and SnO$_2$ in their MCS-made MASnI$_3$ parent sample, achieved using longer acquisition times than attempted in our work.[81]

The ^{119}Sn NMR results for the MCS-made MASnI$_3$ (δ = 795 ppm), MASnBr$_{0.9}$I$_{2.1}$ (δ = 1586 ppm) and MASnCl$_{2.7}$I$_{0.3}$ (δ = 249 ppm) reported by Kubicki et al. all appear at higher chemical shifts than the solution-synthesized MASnI$_3$ phase presented in this work (δ$_{iso}$ = 155 ppm). This difference may lie in structural variants produced by different synthetic methods, viz., MCS vs. solution. For example, we have shown using [207]Pb NMR spectroscopy that MCS reduces resolution when compared to solution synthesis for the solid-solution MAPbCl$_x$Br$_{3-x}$ perovskite series, as it reduces local and long-range ordering; however the chemical shifts and lineshape did not change

significantly.[28]    As $MASnI_3$ and its mixed halides are complex materials, a more thorough investigation is needed to better understand the large changes in chemical shift and linewidth observed between MCS and solution synthesis, in addition to how the degradation of $MASnI_3$-based perovskites is impacted by both synthetic procedures and starting materials. The rapid degradation of $MASnI_3$ observed in this work and the long acquisition times needed to identify the decomposition products may require complementary characterization techniques to arrive at unambiguous conclusions for these complex materials and processes. The intuitive attractiveness of DNP to boost sensitivity and delay decomposition is undermined by the need to conduct such experiments at very low temperatures, which would induce further phase changes.[84–86]
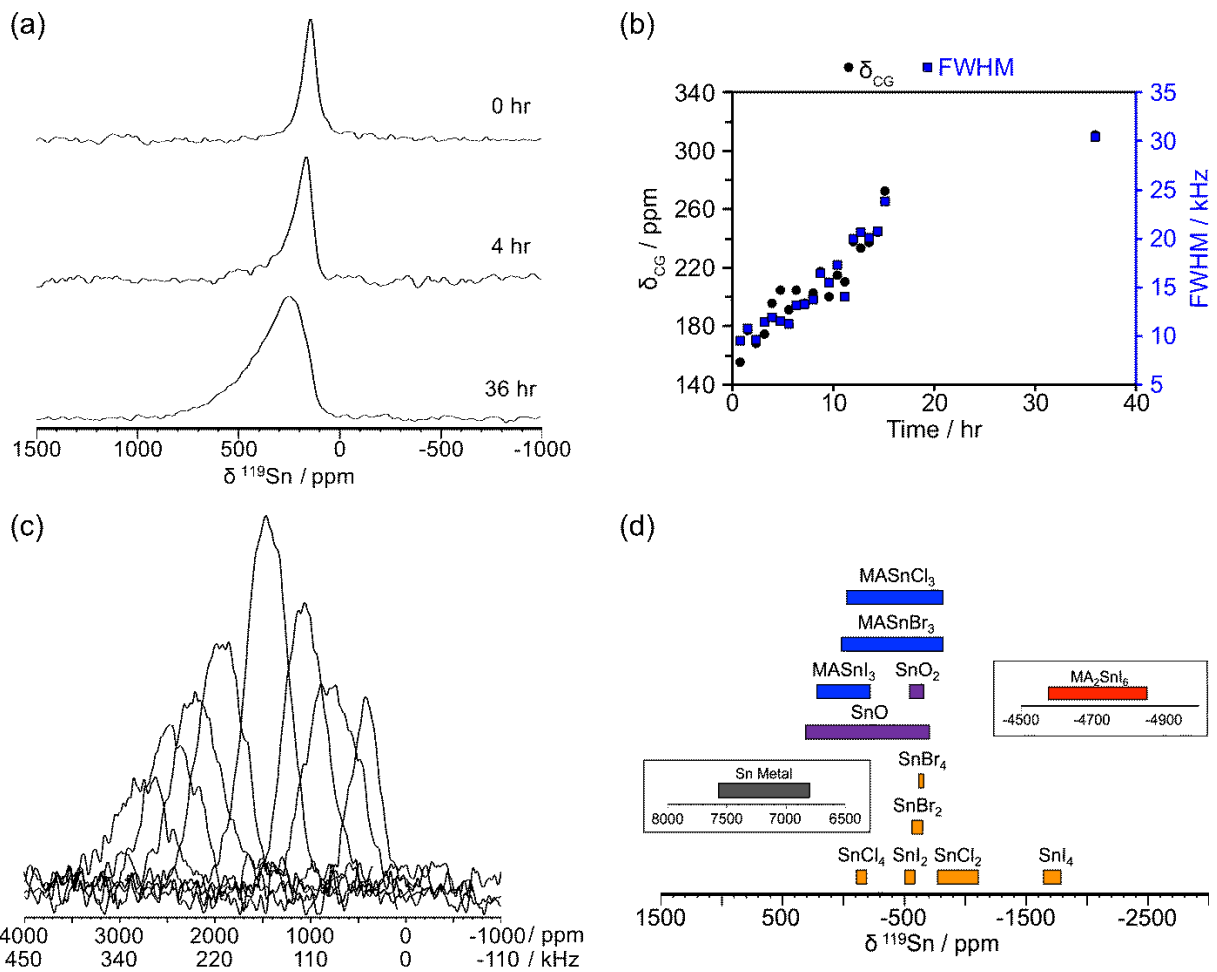
**Figure 3.8.** (a) Non-spinning $^{119}$Sn NMR spectra of MASnI$_3$ of freshly synthesized (0 hr) to aged (36 hrs). (b) Changes in the center-of-gravity shift ($\delta_{CG}$ / ppm) and full-width-half-maximum (FWHM / kHz) of MASnI$_3$ with respect to time. (c) Non-spinning $^{119}$Sn NMR of MASnI$_3$ after 6 months post-synthesis acquired using a VOCS approach. (d) Tin chemical shift scale for other tin halide and oxide compounds.
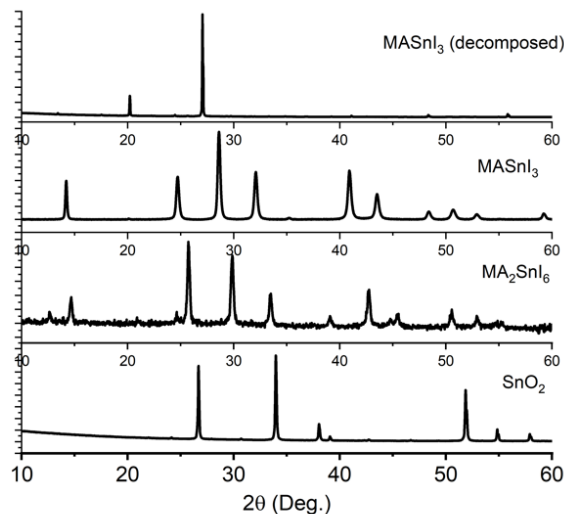
**Figure 3.9.** Powder X-ray diffraction patterns of decomposed MASnI$_3$, pristine MASnI$_3$, MA$_2$SnI$_6$ and SnO$_2$.

### 3.3.6 Impact of X on MASnX$_3$ [119]Sn Magnetic Shielding

A quintessential NMR parameter to assess electronic and chemical structure is the isotropic chemical shift and its sensitivity to local structure. As the ^{119}Sn NMR diamagnetic chemical shift range covers nearly 5,000 ppm depending on the chemical environment, this provides the ability to identify various tin halide species. The chemical shifts determined experimentally expand our understanding of the ranges that can potentially be observed for hybrid tin(II) halide perovskites. As seen for SnX$_2$ salts (e.g., SnCl$_2$ in DMSO ($-384$ ppm) to I ($-152$ ppm)), the [119]Sn in MASnCl$_3$ is the most shielded ($\delta_{\text{iso}} = -400$ ppm) with the Br and I phases gradually shifting to higher frequency, ranging over approximately 600 ppm. To assess the sensitivity to local structure, a series of [SnX$_6$]$^{4-}$ anionic polyhedral clusters were assembled based on crystallographic data, and the Sn chemical shifts were calculated using ADF 2017 implementing a ZORA/QZ4P basis set to compare with experimental values. Figure 3.10a shows the relationship between the calculated magnetic shieldings and experimental chemical shifts for the eight unique phases studied here. The quantum chemical calculations using simple model compounds agree with the trends seen experimentally. To assess the sensitivity of the CSA to the structure of the local tin halide polyhedron, the distortion parameter ($\lambda$) for each crystalline phase was determined from their crystal structures.[87–89] As shown in Figure 3.10b, the gradual change from a perfect Sn octahedron, in the cubic crystal lattice of MASnX$_3$ (where X = Cl, Br or I), to the lower-symmetry tetragonal, orthorhombic, monoclinic and

51

triclinic phases results in a sizable measured CSA which correlates with the distortion about the Sn center.
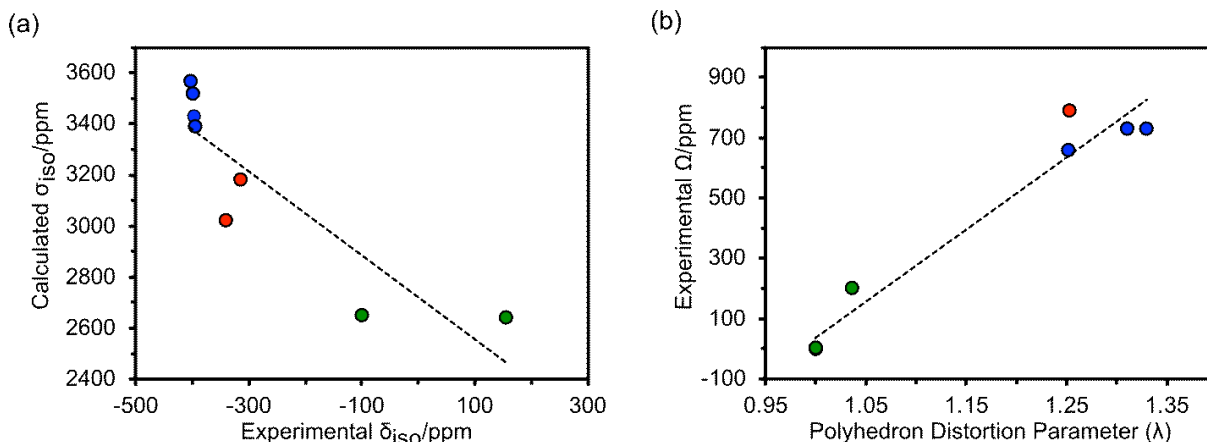


**Figure 3.10.** (a) Calculated $^{119}$Sn magnetic shielding for tin halide polyhedron atomic clusters (blue = MASnCl$_3$, red = MASnBr$_3$, green = MASnI$_3$) using a ZORA/QZ4P basis set as implemented in ADF 2017, and their relationship to experimental $^{119}$Sn chemical shifts. (b) Relationship between the experimental $^{119}$Sn chemical shift spans for methylammonium tin halide perovskites and their polyhedron distortion parameter calculated from known crystal structures. Note that all cubic structures of MASnX$_3$ (X = Cl, Br, I) have identical $^{119}$Sn CSAs and polyhedron distortion parameters (*).

### 3.3.7 MASn$_{0.5}$Pb$_{0.5}$I$_3$ – Insight into Mixed B-site Alloyed Hybrid Perovskites

Mixing the B-site between Sn and Pb has shown improved chemical stability for hybrid Sn(II)-containing perovskites while offering a further dimension to tune optical properties such as bandgap and emission.[90–92] Thus, expanding beyond our past research in mixed halides, we attempted to synthesize a mixed Sn$^{2+}$:Pb$^{2+}$ analogue. Below we focus our discussion on a 1:1 Sn$^{2+}$: Pb$^{2+}$ mole ratio to form the MASn$_{0.5}$Pb$_{0.5}$I$_3$ perovskite solid solution. XRD shows that the MAPbI$_3$ parent adopts a tetragonal phase, whereas the MASnI$_3$ parent adopts a pseudo-cubic phase at room temperature.[10] As shown in Figure 3.11a, the XRD data reveal that the MASn$_{0.5}$Pb$_{0.5}$I$_3$ solid solution adopts the same pseudo-cubic structure as for the MASnI$_3$ parent. We further performed room temperature $^1$H, $^{13}$C, $^{119}$Sn and $^{207}$Pb NMR spectroscopy to gain insight into the atomic-level changes both from the dynamic A-site cation ($^1$H and $^{13}$C) and B-site cation ($^{119}$Sn and $^{207}$Pb) perspectives upon Sn$^{2+}$/Pb$^{2+}$ mixing. MA$^+$ contains distinguishable hydrogens from the ammonium (NH$_3$) and methyl (CH$_3$) groups; the $\delta_{iso}$($^1$H) for the ammonium hydrogens appear to higher frequency than that for the methyl hydrogens. For example, $\delta_{iso}$($^1$H) = 5.3 and 2.4 ppm for NH$_3$

and $CH_3$ in $MASnI_3$, respectively (Figure 3.12a). Closer examination of $^1H$ NMR spectra demonstrates a small but definite change in $\delta_{iso}(^1H)$ to higher frequency for both for $NH_3$ and $CH_3$ hydrogens as $Sn^{2+}$ is replaced with $Pb^{2+}$ (Figure 3.12c). The small shoulder present in the $^1H$ NMR spectrum of $MASnI_3$ is likely assignable to degradation of the parent phase, as this spectrum was acquired between the 3rd and 4th hour decomposition points discussed above. The $^{13}C$ NMR chemical shift is also shifted to higher frequency and the linewidth narrows as Sn is replaced by Pb (Figures 3.12b and 3.12d). As past $^2H$ NMR experiments on deuterium-labeled $MAPbI_3$ demonstrated ultrafast $MA^+$ cation dynamics at room temperature,[31,93] the progressive changes in $^1H$ and $^{13}C$ NMR chemical shifts and linewidths are most likely due to changes in the unit cell volumes on going from $MASnI_3$ to $MAPbI_3$:[10] the larger unit cell volume for $MAPbI_3$ implies a larger cuboctahedron space which allows faster $MA^+$ dynamics and hence a narrowing of the peaks in the $^1H$ and $^{13}C$ NMR spectra.

In contrast to the $MA^+$ cation, the B-site cations (i.e., $Sn^{2+}$ or $Pb^{2+}$), are directly coordinated with six iodides to form $[BI_6]^{4-}$ octahedra in the perovskite structure. The non-spinning $^{207}Pb$ NMR spectra for $MAPbI_3$ and $MASn_{0.5}Pb_{0.5}I_3$ (Figure 3.11) show Gaussian-like line shapes with a linewidth of *ca.* 27 and 28 kHz for $MAPbI_3$ and $MASn_{0.5}Pb_{0.5}I_3$, respectively. $\delta_{iso}(^{207}Pb)$ is shifted towards higher frequency by *ca.* 130 ppm when Pb centered in $MAPbI_3$ is 50% replaced by Sn to form $MASn_{0.5}Pb_{0.5}I_3$. Likewise, the non-spinning $^{119}Sn$ NMR spectra for both $MASnI_3$ and $MASn_{0.5}Pb_{0.5}I_3$ also give Gaussian-like broad line shapes with FWHM of *ca.* 9 and 18 kHz, respectively. However, $\delta_{iso}(^{119}Sn)$ for $MASn_{0.5}Pb_{0.5}I_3$ is shifted to lower frequency by ~70 ppm. Neither the $^{119}Sn$ nor $^{207}Pb$ NMR spectra display any discernable spectral changes over several days (spectra were similar after two weeks in a sealed rotor), further supporting past findings by other researchers where Pb incorporation offsets degradation.[90–92] The NMR linewidths have been previously shown to be impacted by $T_2$, direct and indirect spin-spin coupling between $^{207}Pb$ (or $^{119}Sn$) and the six $^{127}I$ ($I = 5/2$; 100% abundant) nuclei in $[BI_6]^{4-}$ octahedra.[31,32]
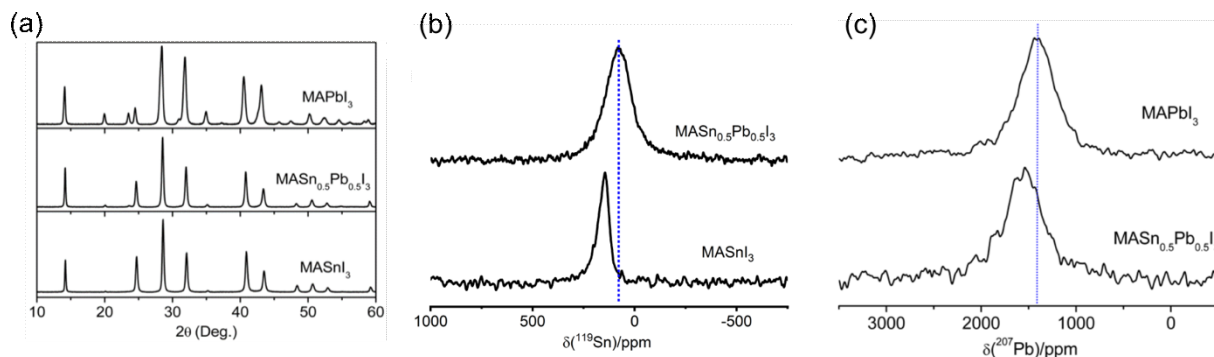
**Figure 3.11.** Experimentally determined room temperature XRD (a) and solid-state $^{119}Sn$ (b) and $^{207}Pb$ (c) NMR spectra for freshly synthesized $MASnI_3$, $MASn_{0.42}Pb_{0.58}I_3$ and $MAPbI_3$ materials.
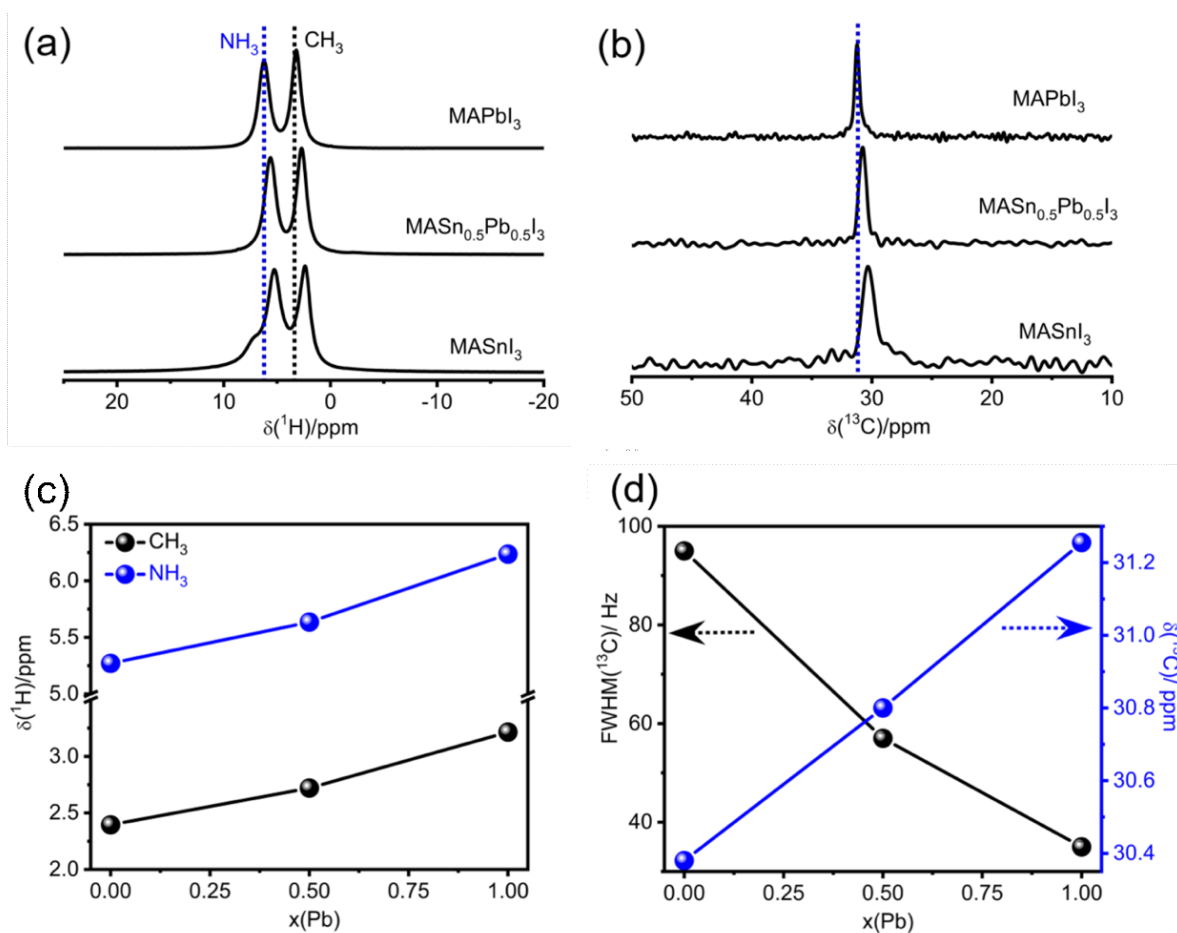


**Figure 3.12.** Room temperature $^{1}H$ (a, $B_0$ = 7.05 T and $\omega_r/2\pi$ = 12 kHz) and $^{13}C$ (b, $B_0$ = 7.05 T and $\omega_r/2\pi$ = 5 kHz) NMR spectra of freshly synthesized $MASn_{1-x}Pb_xI_3$ (x = 0, 0.5 and 1) materials. Change in $^{1}H$ chemical shifts for $CH_3$ and $NH_3$ units in $MA^+$ cation (c) and change in $^{13}C$ NMR chemical shifts (blue) and FWHM values (black) (d) for $MASn_{1-x}Pb_xI_3$ as a function with Pb concentration (x).

54

## 3.4 Conclusion

In this work, we have discussed a series of hybrid methylammonium tin halide perovskites and their chemical shift ranges observed using $^{119}$Sn NMR spectroscopy and quantum chemical calculations. In each parent phase (where the Sn is positioned at a cubic site of symmetry), a distinct $\delta_{iso}$ is determined with a characteristic shift to higher frequency ($-404$ ppm to $-315$ ppm to $+155$ ppm for $MASnCl_3$, $MASnBr_3$ and $MASnI_3$, respectively) as the halide mass increases. This correlates with the changes in band gaps (a decrease of 2.5 eV from $MASnCl_3$ to $MASnI_3$), consistent with the fact that the NMR chemical shift is sensitive to changes in the paramagnetic shielding term and additional contributions from the spin orbit term of the local electronic environment. The relationship between changes in the local environment and the resulting chemical shifts is further explored via variable temperature $^{119}$Sn NMR spectroscopy: upon cooling, we see changes in the $^{119}$Sn CSA with phase changes. As $MASnI_3$ is unstable, we performed an in-situ NMR study over a course of 30 hours to track the changes in linewidths and chemical shifts with respect to time. Within hours, we observed an increase in linewidth and a $\delta_{CG}$ shift to higher frequency; after 6 months a broad resonance spanning nearly 2800 ppm, trending towards Sn metal, appeared. This rapid degradation towards the metal may also help explain the dual semiconducting and metallic physical characteristics being reported for this system.[10,72] With the rapid degradation of $MASnI_3$, the discrepancies between our observed $^{119}$Sn NMR spectra of $MASnI_3$ and those reported recently[81] may be due to the synthetic method used (solvent-based synthesis vs mechanochemical synthesis). In an attempt to improve the chemical stability of $MASnI_3$, we synthesized a mixed B-site ($Sn^{2+}:Pb^{2+} = 1:1$ mole ratio) analogue and discovered that the $MASn_{0.5}Pb_{0.5}I_3$ adopts a pseudo-cubic structure like the $MASnI_3$ parent compound, and has $^1H$, $^{13}C$, $^{119}$Sn and $^{207}$Pb NMR spectral features that are distinct from those of the parent compounds, confirming its solid solution behavior. The incorporation of Pb appears to aid in resisting the degradation of these perovskites, whereby the mixed sample was easily handled and analyzed using both XRD and NMR spectroscopy without evidence of degradation over a two-week period. These findings provide an understanding of atomic-level structural property relationships in methylammonium tin halide perovskites and greater insight into the phase changes, material stability and $MASnI_3$ decomposition that plague the use of tin(II) perovskites as a less toxic alternative to lead-based perovskites. Further research with mixed A, B or X-site analogues is

required to reduce toxicity as one targets efforts to bridge the gap between efficient solar energy conversion and chemical stability to produce a new state-of-the-art solar absorbing material.

## 3.5 References

(1)     National Renewable Energy Laboratory (NREL). Best Research-Cell Efficiency Chart. Https://Www.Nrel.Gov/Pv/Assets/Pdfs/Best-Research-Cell-Efficiencies.20190923.Pdf.

(2)     Tennyson, E. M.; Doherty, T. A. S.; Stranks, S. D. Heterogeneity at Multiple Length Scales in Halide Perovskite Semiconductors. *Nat. Rev. Mater.* **2019**, *4* (9), 573–587.

(3)     Wei, H.; Huang, J. Halide Lead Perovskites for Ionizing Radiation Detection. *Nat. Comm.* **2019**, *10* (1), 1066.

(4)     Fu, Y.; Zhu, H.; Chen, J.; Hautzinger, M. P.; Zhu, X.-Y.; Jin, S. Metal Halide Perovskite Nanostructures for Optoelectronic Applications and the Study of Physical Properties. *Nat. Rev. Mater.* **2019**, *4* (3), 169–188.

(5)     Gao, P.; Bin Mohd Yusoff, A. R.; Nazeeruddin, M. K. Dimensionality Engineering of Hybrid Halide Perovskite Light Absorbers. *Nat. Comm.* **2018**, *9* (1), 5028.

(6)     Sum, T.-C.; Mathews, N. *Halide Perovskites: Photovoltaics, Light Emitting Devices, and Beyond*; 2019.

(7)     Jung, H. S.; Park, N.-G. Perovskite Solar Cells: From Materials to Devices. *Small* **2015**, *11* (1), 10–25.

(8)     Borriello, I.; Cantele, G.; Ninno, D. Ab Initio Investigation of Hybrid Organic-Inorganic Perovskites Based on Tin Halides. *Phys. Rev. B* **2008**, *77* (23), 235214.

(9)     Yamada, K.; Mikawa, K.; Okuda, T.; Knight, K. S. Static and Dynamic Structures of $CD_3ND_3GeCl_3$ Studied by TOF High Resolution Neutron Powder Diffraction and Solid-State NMR. *J. Chem. Soc. Dalt. Trans.* **2002**, (10), 2112–2118.

(10)    Stoumpos, C. C.; Malliakas, C. D.; Kanatzidis, M. G. Semiconducting Tin and Lead Iodide Perovskites with Organic Cations: Phase Transitions, High Mobilities, and near-Infrared Photoluminescent Properties. *Inorg. Chem.* **2013**, *52* (15), 9019–9038.

(11)    Breternitz, J.; Schorr, S. What Defines a Perovskite? *Adv. Energy Mater.* **2018**, *8*, 1802366.

(12)    Askar, A. M.; Bernard, G. M.; Wiltshire, B.; Shankar, K.; Michaelis, V. K. Multinuclear Magnetic Resonance Tracking of Hydro, Thermal, and Hydrothermal Decomposition of $CH_3NH_3PbI_3$. *J. Phys. Chem. C* **2017**, *121*, 1013–1024.

(13)    Wang, D.; Wright, M.; Elumalai, N. K.; Uddin, A. Stability of Perovskite Solar Cells. *Sol. Energy Mater. Sol. Cells* **2016**, *147*, 255–275.

(14)    Juarez-Perez, E. J.; Ono, L. K.; Maeda, M.; Jiang, Y.; Hawash, Z.; Qi, Y. Photodecomposition and Thermal Decomposition in Methylammonium Halide Lead Perovskites and Inferred Design Principles to Increase Photovoltaic Device Stability. *J. Mater. Chem. A* **2018**, *6* (20), 9604–9612.

(15)    Li, J.; Cao, H.-L.; Jiao, W.-B.; Wang, Q.; Wei, M.; Cantone, I.; Lü, J.; Abate, A. Biological Impact of Lead from Halide Perovskites Reveals the Risk of Introducing a Safe Threshold. *Nat. Comm.* **2020**, *11* (1), 310.

(16)    Hu, H.; Dong, B.; Zhang, W. Low-Toxic Metal Halide Perovskites: Opportunities and Future Challenges. *J. Mater. Chem. A* **2017**, *5* (23), 11436–11449.

(17)    Feng, J.; Xiao, B. Effective Masses and Electronic and Optical Properties of Nontoxic $MASnX_3$ (X = Cl, Br, and I) Perovskite Structures as Solar Cell Absorber: A Theoretical Study Using HSE06. *J. Phys. Chem. C* **2014**, *118* (34), 19655–19660

(18)    Hong, Z.; Tan, D.; John, R. A.; Tay, Y. K. E.; Ho, Y. K. T.; Zhao, X.; Sum, T. C.; Mathews, N.; García, F.; Soo, H. Sen. Completely Solvent-Free Protocols to Access Phase-Pure, Metastable Metal Halide Perovskites and Functional Photodetectors from the Precursor Salts. *iScience* **2019**, *16*, 312–325.

(19)    Chiarella, F.; Zappettini, A.; Licci, F.; Borriello, I.; Cantele, G.; Ninno, D.; Cassinese, A.; Vaglio, R. Combined Experimental and Theoretical Investigation of Optical, Structural, and Electronic Properties of $CH_3NH_3SnX_3$ Thin Films (X = Cl, Br). *Phys. Rev. B* **2008**, *77* (4), 045129.

(20)    Lang, L.; Yang, J.-H.; Liu, H.-R.; Xiang, H. J.; Gong, X. G. First-Principles Study on the Electronic and Optical Properties of Cubic $ABX_3$ Halide Perovskites. *Phys. Lett. A* **2014**, *378* (3), 290–293.

(21)    Yamada, K.; Kuranaga, Y.; Ueda, K.; Goto, S.; Okuda, T.; Furukawa, Y. Phase Transition and Electric Conductivity of $ASnCl_3$ (A = Cs and $CH_3NH_3$). *Bull. Chem. Soc. Jpn.* **1998**, *71* (1), 127–134.

(22) Yamada, K.; Nose, S.; Umehara, T.; Okuda, T.; Ichiba, S. [81]Br NQR and [119]Sn Mössbauer Study for $MSnBr_3$ (M = Cs and $CH_3NH_3$). *Bull. Chem. Soc. Jpn.* **1988**, *61* (12), 4265–4268.

(23) Peedikakkandy, L.; Bhargava, P. Composition Dependent Optical, Structural and Photoluminescence Characteristics of Cesium Tin Halide Perovskites. *RSC Adv.* **2016**, *6* (24), 19857–19860.

(24) Kumar, M. H.; Dharani, S.; Leong, W. L.; Boix, P. P.; Prabhakar, R. R.; Baikie, T.; Shi, C.; Ding, H.; Ramesh, R.; Asta, M.; Graetzel, M.; Mhaisalkar, S. G.; Mathews, N. Lead-Free Halide Perovskite Solar Cells with High Photocurrents Realized Through Vacancy Modulation. *Adv. Mater.* **2014**, *26* (41), 7122–7127.

(25) Ogomi, Y.; Morita, A.; Tsukamoto, S.; Saitho, T.; Fujikawa, N.; Shen, Q.; Toyoda, T.; Yoshino, K.; Pandey, S. S.; Ma, T.; Hayase, S. $CH_3NH_3Sn_xPb_{(1-x)}I_3$ Perovskite Solar Cells Covering up to 1060 nm. *J. Phys. Chem. Lett.* **2014**, *5* (6), 1004–1011.

(26) Hao, F.; Stoumpos, C. C.; Cao, D. H.; Chang, R. P. H.; Kanatzidis, M. G. Lead-Free Solid-State Organic–Inorganic Halide Perovskite Solar Cells. *Nat. Photonics* **2014**, *8* (6), 489–494.

(27) Noel, N. K.; Stranks, S. D.; Abate, A.; Wehrenfennig, C.; Guarnera, S.; Haghighirad, A.-A.; Sadhanala, A.; Eperon, G. E.; Pathak, S. K.; Johnston, M. B.; Petrozza, A.; Herz, L. M.; Snaith, H. J. Lead-Free Organic–Inorganic Tin Halide Perovskites for Photovoltaic Applications. *Energy Environ. Sci.* **2014**, *7* (9), 3061–3068.

(28) Karmakar, A.; Askar, A. M.; Bernard, G. M.; Terskikh, V. V.; Ha, M.; Patel, S.; Shankar, K.; Michaelis, V. K. Mechanochemical Synthesis of Methylammonium Lead Mixed-Halide Perovskites: Unraveling the Solid-Solution Behavior Using Solid-State NMR. *Chem. Mater.* **2018**, *30*, 2309–2321.

(29) Karmakar, A.; Dodd, M. S.; Zhang, X.; Oakley, M. S.; Klobukowski, M.; Michaelis, V. K. Mechanochemical Synthesis of 3D and 0D Cesium Lead Mixed Halide Perovskite Solid Solutions. *Chem. Comm.* **2019**, *55*, 5079–5082.

(30) Franssen, W. M. J.; van Es, S. G. D.; Dervişoğlu, R.; de Wijs, G. A.; Kentgens, A. P. M. Symmetry, Dynamics, and Defects in Methylammonium Lead Halide Perovskites. *J. Phys. Chem. Lett.* **2017**, *8* (1), 61–66.

(31)  Bernard, G. M.; Wasylishen, R. E.; Ratcliffe, C. I.; Terskikh, V.; Wu, Q.; Buriak, J. M.; Hauger, T. Methylammonium Cation Dynamics in Methylammonium Lead Halide Perovskites: A Solid-State NMR Perspective. *J. Phys. Chem. A* **2018**, *122* (6), 1560–1573.

(32)  Senocrate, A.; Moudrakovski, I.; Kim, G. Y.; Yang, T.; Gregori, G.; Grätzel, M.; Maier, J. The Nature of Ion Conduction in Methylammonium Lead Iodide: A Multimethod Approach. *Angew. Chem. Int. Ed.* **2017**, *56*, 7755–7759.

(33)  Kubicki, D. J.; Prochowicz, D.; Hofstetter, A.; Péchy, P.; Zakeeruddin, S. M.; Grätzel, M.; Emsley, L. Cation Dynamics in Mixed-Cation $(MA)_x(FA)_{1-x}PbI_3$ Hybrid Perovskites from Solid-State NMR. *J. Am. Chem. Soc.* **2017**, *139*, 10055–10061.

(34)  Kubicki, D. J.; Prochowicz, D.; Hofstetter, A.; Zakeeruddin, S. M.; Grätzel, M.; Emsley, L. Phase Segregation in Potassium-Doped Lead Halide Perovskites from 39 K Solid-State NMR at 21.1 T. *J. Am. Chem. Soc.* **2018**, *140*, 7232−7238.

(35)  Aebli, M.; Piveteau, L.; Nazarenko, O.; Benin, B. M.; Krieg, F.; Verel, R.; Kovalenko, M. V. Lead-Halide Scalar Couplings in [207]Pb NMR of $APbX_3$ Perovskites (A = Cs, Methylammonium, Formamidinium; X = Cl, Br, I). *Sci. Rep.* **2020**, *10* (1), 8229.

(36)  Harris, R. K.; Becker, E. D. NMR Nomenclature: Nuclear Spin Properties and Conventions for Chemical Shifts—IUPAC Recommendations. *J. Magn. Reson.* **2002**, *156* (2), 323–326.

(37)  Mundus, C.; Taillades, G.; Pradel, A.; Ribes, M. A [119]Sn Solid-State Nuclear Magnetic Resonance Study of Crystalline Tin Sulphides. *Solid State Nucl. Magn. Reson.* **1996**, *7* (2), 141–146.

(38)  Eichler, B. E.; Phillips, B. L.; Power, P. P.; Augustine, M. P. Solid-State and High-Resolution Liquid ^{119}Sn NMR Spectroscopy of Some Monomeric, Two-Coordinate Low-Valent Tin Compounds: Very Large Chemical Shift Anisotropies. *Inorg. Chem.* **2000**, *39* (24), 5450–5453.

(39)  Harris, R. K.; Sebald, A. High-Resolution Solid-State ^{119}Sn and [207]Pb NMR Study of Organotin and Organolead Chalcogenides: Observation Of J-Coupling in Solids. *Magn. Reson. Chem.* **1989**, *27* (1), 81–87.

(40)  Grey, C. P.; Cheetham, A. K.; Dobson, C. M. Temperature-Dependent Solid-State ^{119}Sn-MAS NMR of $Nd_2Sn_2O_7$, $Sm_2Sn_2O_7$, and $Y_{1.8}Sm_{0.2}Sn_2O_7$. Three Sensitive Chemical-Shift Thermometers. *J. Magn. Reson., Ser. A* **1993**, *101* (3), 299–306.

(41)   MacKenzie, K.; Smith, M. E. *Multinuclear Solid-State Nuclear Magnetic Resonance of Inorganic Materials, Volume 6*; Pergamon, 2002.

(42)   Gunther, W. R.; Michaelis, V. K.; Caporini, M. A.; Griffin, R. G.; Román-Leshkov, Y. Dynamic Nuclear Polarization NMR Enables the Analysis of Sn-Beta Zeolite Prepared with Natural Abundance [119]Sn Precursors. *J. Am. Chem. Soc.* **2014**, *136* (17), 6219–6222.

(43)   Yamada, K.; Nakada, K.; Takeuchi, Y.; Nawa, K.; Yohei Yamane. Tunable Perovskite Semiconductor $CH_3NH_3SnX_3$ (X: Cl, Br, or I) Characterized by X-Ray and DTA. *Bull. Chem. Soc. Jpn.* **2011**, *84*, 926–932.

(44)   Onoda-Yamamuro, N.; Matsuo, T.; Suga, H. Thermal, Electric, and Dielectric Properties of $CH_3NH_3SnBr_3$ at Low Temperatures. *J. Chem. Thermodyn.* **1991**, *23*, 987–999.

(45)   Bureau, B.; Silly, G.; Buzaré, J. Y.; Legein, C.; Massiot, D. From Crystalline to Glassy Gallium Fluoride Materials: An NMR Study of and Quadrupolar Nuclei. *Solid State Nucl. Magn. Reson.* **1999**, *14* (3–4), 181–190.

(46)   Bernard, G. M.; Goyal, A.; Miskolzie, M.; McKay, R.; Wu, Q.; Wasylishen, R. E.; Michaelis, V. K. Methylammonium Lead Chloride: A Sensitive Sample for an Accurate NMR Thermometer. *J. Magn. Reson.* **2017**, *283*, 14–21.

(47)   Thurber, K. R.; Tycko, R. Measurement of Sample Temperatures under Magic-Angle Spinning from the Chemical Shift and Spin-Lattice Relaxation Rate of [79]Br in KBr Powder. *J. Magn. Reson.* **2009**, *196* (1), 84–87.

(48)   Mason, J. Conventions for the Reporting of Nuclear Magnetic Shielding (or Shift) Tensors Suggested by Participants in the NATO ARW on NMR Shielding Constants at the University of Maryland, College Park, July 1992. *Solid State Nucl. Magn. Reson.* **1993**, *2*, 285−288.

(49)   Herzfeld, J.; Berger, A. E. Sideband Intensities in NMR-Spectra of Samples Spinning at the Magic Angle. *J. Chem. Phys.* **1980**, *73*, 6021−6030.

(50)   Harris, R. K.; Becker, E. D.; De Menezes, S. M. C.; Granger, P.; Hoffman, R. E.; Zilm, K. W. Further Conventions for NMR Shielding and Chemical Shifts (IUPAC Recommendations 2008). *Pure Appl. Chem.* **2008**, *80*, 59–84.

(51)   Pines, A.; Gibby, M. G.; Waugh, J. S. Proton-Enhanced Nuclear Induction Spectroscopy. A Method for High Resolution NMR of Dilute Spins in Solids. *J. Chem. Phys.* **1972**, *56* (4), 1776–1777.

(52)    Bennett, A. E.; Rienstra, C. M.; Auger, M.; Lakshmi, K. V.; Griffin, R. G. Heteronuclear Decoupling in Rotating Solids. *J. Chem. Phys.* **1995**, *103* (16), 6951–6958.

(53)    Earl, W. L.; Vanderbart, D. L. Measurement of $^{13}$C Chemical Shifts in Solids. *J. Magn. Reson.* **1982**, *48* (1), 35–54.

(54)    Hahn, E. L. Spin Echoes. *Phys. Rev.* **1950**, *80* (4), 580–594.

(55)    te Velde, G.; Bickelhaupt, F. M.; Baerends, E. J.; Fonseca Guerra, C.; van Gisbergen, S. J. A.; Snijders, J. G.; Ziegler, T. Chemistry with ADF. *J. Comp. Chem.* **2001**, *22* (9), 931–967.

(56)    ADF 2019.3, SCM, Theoretical Chemistry, Vrije Universiteit, Amsterdam, The Netherlands.

(57)    Fonseca Guerra, C.; Snijders, J. G.; te Velde, G.; Baerends, E. J. Towards an Order-N DFT Method. *Theor. Chem. Accounts* **1998**, *99* (6), 391–403.

(58)    Swainson, I.; Chi, L.; Her, J.-H.; Cranswick, L.; Stephens, P.; Winkler, B.; Wilson, D. J.; Milman, V. Orientational Ordering, Tilting and Lone-Pair Activity in the Perovskite Methylammonium Tin Bromide, $CH_3NH_3SnBr_3$. *Acta Crystallogr. Sect. B Struct. Sci.* **2010**, *66* (4), 422–429.

(59)    Schreckenbach, G.; Ziegler, T. Calculation of NMR Shielding Tensors Using Gauge-Including Atomic Orbitals and Modern Density Functional Theory. *J. Phys. Chem.* **1995**, *99* (2), 606–611.

(60)    van Lenthe, E.; Ehlers, A.; Baerends, E.-J. Geometry Optimizations in the Zero Order Regular Approximation for Relativistic Effects. *J. Chem. Phys.* **1999**, *110* (18), 8943–8953.

(61)    Becke, A. D. Density-Functional Exchange-Energy Approximation with Correct Asymptotic Behavior. *Phys. Rev. A* **1988**, *38* (6), 3098–3100.

(62)    Perdew, J. P.; Yue, W. Accurate and Simple Density Functional for the Electronic Exchange Energy: Generalized Gradient Approximation. *Phys. Rev. B* **1986**, *33* (12), 8800–8802.

(63)    Shannon, R. D. Revised Effective Ionic Radii and Systematic Studies of Interatomic Distances in Halides and Chalcogenides. *Acta Cryst.* **1976**, *A32*, 751–767.

(64)    Lash, T. D.; Lash, S. S. The Use of Pascal-like Triangles in Describing First Order NMR Coupling Patterns. *J. Chem. Ed.* **1987**, *64* (4), 315.

(65)    Sharp, R. R. Rotational Diffusion and Magnetic Relaxation of $^{119}$Sn in Liquid $SnCl_4$ and $SnI_4$. *J. Chem. Phys.* **1972**, *57* (12), 5321–5330.

(66) Grondona, P.; Olivieri, A. C. Quadrupole Effects in Solid-State NMR Spectra of Spin-½ Nuclei: A Perturbation Approach. *Concepts Magn. Reson.* **1993**, *5* (4), 319–339.

(67) Jung, M.-C.; Raga, S. R.; Qi, Y. Properties and Solar Cell Applications of Pb-Free Perovskite Films Formed by Vapor Deposition. *RSC Adv.* **2016**, *6* (4), 2819–2825.

(68) Li, B.; Long, R.; Xia, Y.; Mi, Q. All-Inorganic Perovskite $CsSnBr_3$ as a Thermally Stable, Free-Carrier Semiconductor. *Angew. Chem. Int. Ed.* **2018**, *57* (40), 13154–13158.

(69) Tao, S.; Schmidt, I.; Brocks, G.; Jiang, J.; Tranca, I.; Meerholz, K.; Olthof, S. Absolute Energy Level Positions in Tin- and Lead-Based Halide Perovskites. *Nat. Commun.* **2019**, *10* (1), 2560.

(70) Nakatsuji, H. *Nuclear Magnetic Shieldings and Molecular Structure*; Tossell, J. A., Ed.; Springer Netherlands: Dordrecht, 1993.

(71) Dmitrenko, O.; Bai, S.; Dybowski, C. Prediction of [207]Pb NMR Parameters for the Solid Ionic Lead(II) Halides Using the Relativistic ZORA-DFT Formalism: Comparison with the Lead-Containing Molecular Systems. *Solid State Nucl. Magn. Reson.* **2008**, *34* (3), 186–190.

(72) Yamada, K.; Isobe, K.; Okuda, T.; Furukawa, Y. Successive Phase Transitions and High Ionic Conductivity of Trichlorogermanate (II) Salts as Studied by [35]C1 NQR and Powder X-Ray Diffraction. *Zeitschrift für Naturforschung A* **1994**, *49* (1–2), 258–266.

(73) Weber, D. $CH_3NH_3SnBr_xl_{3-x}$ (x = 0-3), Ein Sn(II)-System Mit Kubischer Perowskitstruktur. *Z. Naturforsch.* **1978**, *33b*, 862–865.

(74) Onoda, N.; Yamamuro, O.; Matsuo, T.; Suga, H.; Oikawa, K.; Tsuchiya, N.; Kamiyama, T.; Asano, H. Neutron-Diffraction Study of $CD_3ND_3SnBr_3$: Semiconductor-Insulator Transition with Orientational Ordering. *Physica B* **1995**, *213 & 214*, 411–413.

(75) Yamada, K.; Isobe, K.; Tsuyama, E.; Okuda, T.; Furukawa, Y. Chloride Ion Conductor $CH_3NH_3GeCl_3$ Studied by Rietveld Analysis of X-Ray Diffraction and [35]Cl NMR. *Solid State Ion.* **1995**, *79*, 152–157.

(76) Chung, I.; Lee, B.; He, J.; Chang, R. P. H.; Kanatzidis, M. G. All-Solid-State Dye-Sensitized Solar Cells with High Efficiency. *Nature* **2012**, *485* (7399), 486–489.

(77) Mancini, A.; Quadrelli, P.; Milanese, C.; Patrini, M.; Guizzetti, G.; Malavasi, L. $CH_3NH_3Sn_xPb_{1-x}Br_3$ Hybrid Perovskite Solid Solution: Synthesis, Structure, and Optical Properties. *Inorg. Chem.* **2015**, *54* (18), 8893–8895.

(78)   Leijtens, T.; Prasanna, R.; Gold-Parker, A.; Toney, M. F.; McGehee, M. D. Mechanism of Tin Oxidation and Stabilization by Lead Substitution in Tin Halide Perovskites. *ACS Energy Lett.* **2017**, *2* (9), 2159–2165.

(79)   Wang, F.; Ma, J.; Xie, F.; Li, L.; Chen, J.; Fan, J.; Zhao, N. Organic Cation-Dependent Degradation Mechanism of Organotin Halide Perovskites. *Adv. Funct. Mater.* **2016**, *26* (20), 3417–3423.

(80)   Wrackmeyer, B. Application of ^{119}Sn NMR Parameters; 1999; pp 203–264.

(81)   Kubicki, D. J.; Prochowicz, D.; Salager, E.; Rakhmatullin, A.; Grey, C. P.; Emsley, L.; Stranks, S. D. Local Structure and Dynamics in Methylammonium, Formamidinium, and Cesium Tin(II) Mixed-Halide Perovskites from ^{119}Sn Solid-State NMR. *J. Am. Chem. Soc.* **2020**, *142* (17), 7813–7826.

(82)   Bloembergen, N.; Rowland, T. J. On the Nuclear Magnetic Resonance in Metals and Alloys. *Acta Metall.* **1953**, *1* (6), 731–746.

(83)   Borsa, F.; Barnes, R. G. Temperature Dependence of the Isotropic and Anisotropic Knight Shift in Polycrystalline Cadmium and β-Tin. *J. Phys. Chem. Solids* **1966**, *27* (3), 567–573.

(84)   Michaelis, V. K.; Griffin, R. G.; Corzilius, B.; Vega, S. *Handbook of High Field Dynamic Nuclear Polarization*, 1st ed.; Michaelis, V. K., Griffin, R. G., Corzilius, B., Vega, S., Eds.; Wiley, 2020.

(85)   Ha, M.; Michaelis, V. K. High-Frequency Dynamic Nuclear Polarization NMR for Solids: Part 1 – An Introduction. In *Modern Magnetic Resonance*; Springer International Publishing: Cham, 2017; pp 1–24.

(86)   Ha, M.; Michaelis, V. K. High-Frequency Dynamic Nuclear Polarization NMR for Solids: Part 2 – Development and Applications. In *Modern Magnetic Resonance*; Springer International Publishing: Cham, 2017; pp 1–18.

(87)   Michaelis, V. K.; Kroeker, S. [73]Ge Solid-State NMR of Germanium Oxide Materials: Experimental and Theoretical Studies. *J. Phys. Chem. C* **2010**, *114* (49), 21736–21744.

(88)   Robinson, K.; Gibbs, G. V.; Ribbe, P. H. Quadratic Elongation: A Quantitative Measure of Distortion in Coordination Polyhedra. *Science* **1971**, *172* (3983), 567–570.

(89)   Fleet, M. E. Distortion Parameters for Coordination Polyhedra. *Mineral. Mag.* **1976**, *40* (313), 531–533.

(90)    Prasanna, R.; Leijtens, T.; Dunfield, S. P.; Raiford, J. A.; Wolf, E. J.; Swifter, S. A.; Werner, J.; Eperon, G. E.; de Paula, C.; Palmstrom, A. F.; Boyd, C. C.; van Hest, M. F. A. M.; Bent, S. F.; Teeter, G.; Berry, J. J.; McGehee, M. D. Design of Low Bandgap Tin–Lead Halide Perovskite Solar Cells to Achieve Thermal, Atmospheric and Operational Stability. *Nat. Energy* **2019**, *4* (11), 939–947.

(91)    Lin, R.; Xiao, K.; Qin, Z.; Han, Q.; Zhang, C.; Wei, M.; Saidaminov, M. I.; Gao, Y.; Xu, J.; Xiao, M.; Li, A.; Zhu, J.; Sargent, E. H.; Tan, H. Monolithic All-Perovskite Tandem Solar Cells with 24.8% Efficiency Exploiting Comproportionation to Suppress Sn(II) Oxidation in Precursor Ink. *Nat. Energy* **2019**, *4* (10), 864–873.

(92)    Zhao, D.; Chen, C.; Wang, C.; Junda, M. M.; Song, Z.; Grice, C. R.; Yu, Y.; Li, C.; Subedi, B.; Podraza, N. J.; Zhao, X.; Fang, G.; Xiong, R.-G.; Zhu, K.; Yan, Y. Efficient Two-Terminal All-Perovskite Tandem Solar Cells Enabled by High-Quality Low-Bandgap Absorber Layers. *Nat. Energy* **2018**, *3* (12), 1093–1100.

(93)    Wasylishen, R. E.; Knop, O.; Macdonald, J. B. Cation Rotation in Methylammonium Lead Halides. *Solid State Commun.* **1985**, *56* (7), 581–582.

# Chapter 4

## Silicon Nanoparticles: Are They Crystalline from Core to the Surface?

## 4.1 Introduction

Semiconductor nanoparticles (i.e., quantum dots; QDs) exhibit exquisitely tunable optoelectronic properties, that make them useful for a variety of applications including displays, photovoltaics, and sensors. Unfortunately, many QDs are based upon toxic constituents (e.g., Cd) that are regulated in many jurisdictions.[1] In this context, identifying, preparing, and tailoring the properties of toxic-metal-free (TMF) QDs is of paramount importance. Silicon nanoparticles (SiNPs) are TMF QDs that are readily prepared using abundant materials;[2,3] they possess tailorable surface chemistry, exhibit size- and surface chemistry-tunable photoluminescence that spans the visible and near-infrared spectral regions with absolute quantum yields that compete with their CdSe-based counterparts,[4,5] possess long-lived (microsecond) excited states,[6] are biologically compatible,[2,7] and reversibly alloy with lithium. As such, SiNPs are being explored as functional materials in luminescence-based biological imaging,[3,8] medical imaging,[9,10] light-emitting diodes,[11] photovoltaics,[12–14] sensors,[15] solar concentrators,[16] and lithium ion battery anodes.[17–19] For many of these applications, SiNP size and surface profoundly impact material performance.[20] For example, when employed in lithium ion battery anodes, the SiNP surface has been implicated in the formation of the solid electrolyte interphase layer that drastically impacts device performance.[19,21] Similarly, the SiNP surface plays an important role in defining their optical

properties (e.g., luminescent color, brightness, photoluminescence (PL) quantum yield, excited state lifetime); by defining the surface bonded moiety, the SiNPs PL can be tuned through the visible range and the excited state lifetime can be defined within the micro- to nano-second regime.[22–24] Furthermore, various ill-defined surfaces (e.g., defects, oxidation, etc.) have been implicated in low SiNP PL quantum yields.[5,25]

In light of their key roles in material properties, establishing an understanding of the SiNP surface and internal structure is of paramount importance. Approaches to probing SiNP surfaces have been multifaceted. Quantum chemical calculations provide insight into the nature of the SiNP-oxide interface for oxide-embedded NPs.[26–28] These modeling studies suggest that, when embedded in oxides, SiNPs possess a strained structure that leads to the formation of species such as distorted (i.e., elongated or shortened) Si-Si bonds, dangling bonds, coordination defects, and Si-O-Si bridging species.[26,27,29] The surfaces of SiNPs have also been interrogated directly using various spectroscopic methods. Raman spectroscopy provides direct probing of Si-Si bonds;[30–32] multiple Si-Si species have been identified for small particles (d ~ 3 nm) and as the particle size is increased, features associated with surface species disappear.[30] Fourier transform infrared spectroscopy (FTIR) also provides information regarding bonding in SiNP surface species, including different Si-$H_x$, Si-O, and Si-$R$ ($R$=alkyl, aryl, etc.);[33–36] however, due to dipole considerations, FTIR does not directly probe Si-Si bonding.

Nuclear magnetic resonance (NMR) spectroscopy is a workhorse method for molecular and materials characterization; ^{1}H NMR spectroscopy has been applied, in combination with other methods (e.g., Raman, FTIR, etc.) to evaluate SiNP surface derivatization.[4,37–46] It, as well as ^{19}F NMR spectroscopy, have also been used to indirectly probe the speciation of surface functionalities on hydride-terminated SiNPs (H-SiNPs) via the evaluation of reaction byproducts.[4] Solid-state NMR spectroscopy is a powerful analytical method that provides data related to atomic-level short- and medium-range structural differences within nanomaterials.[47] Despite suffering from a low natural abundance (4.7%), ^{29}Si is an NMR-active nucleus with a nuclear spin, $I = \frac{1}{2}$, a moderate Larmor frequency (19.9% that of ^{1}H), and chemical shift range. These combined properties result in relatively narrow linewidths and good resolution for solids when using magic-angle spinning (MAS) and allow for identification of a variety of silicon species. To date, applications of solid-state NMR spectroscopy for SiNP evaluation have been largely confined to functionalized,[37–43,45,48] ammonium/chloride capped,[44,49] doped,[50] porous,[46,51] nanoclusters,[52] or micron-sized high

polarization studies,[9,53] while non-doped hydride-terminated studies are less prevalent,[54–56] due in part to their reactivity and limited solution processability. Previously a combination of cross-polarization and single-pulse methods with strategic wetting aided in decoding various Si-based surface species on d ~ 50 nm SiNPs;[54] this approach was quickly expanded to assess the impact of surface functionalization.[55] These examples, and others,[57–65] demonstrate the wide-ranging utility of NMR spectroscopy and its applicability to a diverse array of Si-based nanomaterials.

In this regard, size-dependent $^{29}$Si NMR analyses of SiNPs are expected to provide invaluable insight into their structure that may be used to optimize material performance in far reaching applications. In this work, we describe a methodical investigation of H-SiNPs with predefined dimensions ranging from 3 to 64 nm, employing a complementary suite of characterization methods including X-ray photoelectron spectroscopy (XPS), Fourier transform infrared (FTIR) spectroscopy, bright-field transmission electron microscopy (TEM), powder X-ray diffraction (XRD), and $^{29}$Si solid-state NMR spectroscopy that reveals the size dependent order/disorder within the NPs. We further elucidate an intermediate layer, denoted here as the *subsurface*, using cross-polarization NMR spectroscopy and SiNP size dependent nuclear spin-lattice relaxation behavior.

## 4.2 Experimental Section

### 4.2.1 Materials

Hydrofluoric (Electronic grade, 48–50%) and sulfuric (reagent grade, 95–98%) acids were purchased from Fisher Scientific and Caledon Laboratory Chemicals, respectively. Fuming sulfuric acid (reagent grade, 20% free $SO_3$ bases), trichlorosilane (99%) and toluene (HPLC grade) were purchased from Sigma-Aldrich. Toluene was purified using a Pure-Solv purification system and collected immediately prior to use. Benzene was purchased from EMD Millapore (now Millapore Sigma). All reagents and solvents were used as received unless otherwise specified.

Hydrogen silsesquioxane (HSQ) was synthesized following a modified literature procedure.[66] Briefly, dry toluene (45.0 mL) was added to a mixture of concentrated (15.0 mL) and fuming (7.2 mL) sulfuric acid under inert atmosphere. A second solution of dry toluene (110 mL) and trichlorosilane (16.0 mL) was prepared and added drop-wise to the sulfuric acid mixture over a few hours. The toluene layer was isolated and washed with sulfuric acid solution. After drying

the organic layer over $MgSO_4$ (neutralized with $CaCO_3$ overnight), the volume was initially reduced using a rotary evaporator and then evaporated to dryness *in vacuo* to yield the desired product as a white solid that was stored under vacuum until use.

Thermally induced disproportionation of the HSQ was exploited to produce the well-defined SiNPs used in this study.[67] Briefly, six grams of HSQ was thermally processed in a standard tube furnace under flowing 5% $H_2$/95% Ar at 1100, 1200, 1300, 1400, or 1500 °C. This procedure yielded oxide composites containing SiNPs of predefined sizes (See Table 4.1). The resulting composites containing SiNPs were ground using an agate mortar and pestle followed by shaking in a wrist action shaker with high purity glass beads for six hours. The resulting powder was etched using a 1:1:1 solution of ethanol:deionized water:HF to liberate the H-SiNPs; a typical etching procedure employed ~1 g and 30 mL of composite and etching solution, respectively. The composite was exposed to the etching solution for one hour after which, H-SiNPs were extracted into toluene and isolated by centrifugation. The H-SiNPs were then subjected to two suspension/centrifugation cycles in toluene followed by dispersion in benzene for freeze-drying. The benzene suspension was freeze dried to obtain a free-flowing H-SiNP powder. Samples were packed into $ZrO_2$ NMR rotors and sealed with Kel-F drive caps. Identical samples were also evaluated using FTIR, XPS, and bright-field TEM. All material manipulations were performed in a nitrogen filled dry box to ensure negligible surface oxidation or reaction with water.

### 4.2.2 Fourier Transform Spectroscopy (FTIR)

FTIR was performed on a Thermo Nicolet Continuum FT-IR microscope by drop casting SiNPs onto a silicon wafer from dry toluene suspensions.

### 4.2.3 X-ray Photoelectron Spectroscopy (XPS)

XPS was measured using a Kratos Axis 165 Ultra X-ray photoelectron spectrometer. A monochromatic Al Kα source operating at 140 W with an energy hν = 1486.6 eV was used. Survey spectra were collected with analyzer pass energy of 160 eV and step of 0.3 eV (Figure 4.1). For high-resolution spectra, the pass energy was 20 eV and the step was 0.1 eV with a dwell time of 200 ms. Samples were prepared by drop-coating a dry toluene dispersion of SiNPs onto a copper foil. Spectra were calibrated to the aliphatic C component of the C 1s binding energy of adventitious

carbon (284.8 eV)[68,69] and fit to appropriate spin-orbit pairs using CasaXPS (VAMAS) software taking into account a Shirley-type background. To fit the Si 2p high-resolution spectrum, the spin-orbit couple doublet area ratio was fixed at 2:1 and the peak-to-peak separation was defined to be 0.62 eV (Figure 4.2). The spectral window was fit using a variant of a literature procedure.[70] Briefly, the spectral components (i.e., spin-orbit couple doublet) arising from elemental Si (near 99.4 - 99.5 eV in this work) were fit first using a symmetric Gaussian-Lorentzian line shape for small-size particles. When splitting was observed in the envelope shape (i.e., d ~ 9, 21, and 64 nm), a Lorentzian asymmetric (LA) line shape was applied (LA(1.93, 3.2, n) where n defines the Gaussian width).[71] To account for the decrease structural order with SiNPs arising from decreased particle size, the full-width at half maximum (FWHM) of the spectral components used to fit the elemental Si features were constrained as follows (d, FWHM): 3nm, 1.13 eV; 6 nm, 0.93 eV; 9 nm, 0.63 eV; 21 nm, 0.6 eV; 64 nm, 0.58 eV. The residual area was always fit using a Gaussian-Lorentzian line shape with the same doublet relationship noted above.

### 4.2.4 Transmission Electron Microscopy (TEM)

TEM imaging was performed using a JEOL-2010 electron microscope equipped with a LaB$_6$ source and an accelerating voltage of 200 kV. Specimens were prepared by drop-casting toluene suspensions of H-SiNPs onto carbon-coated copper grids. The NP size was determined by averaging the size of 300 particles using ImageJ software (version 1.51j8), Figure 4.3. Bright field images of d ~ 3 nm SiNPs showed substantial aggregation making imaging impractical for sizing the material. To overcome this, d ~ 3 nm H-SiNPs were functionalized with dodecene using established thermally induced hydrosilylation and subsequently imaged.[72]
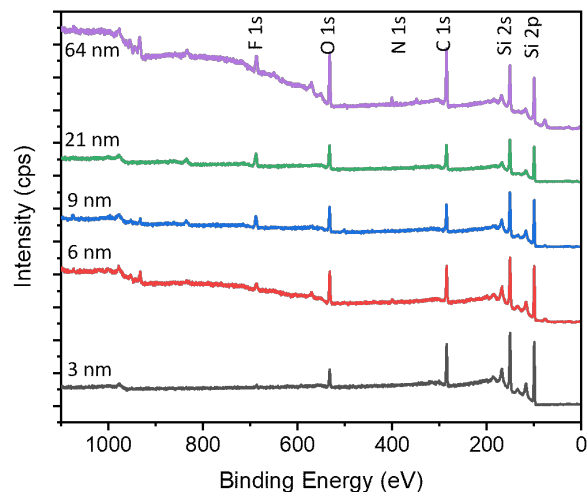
Elemental composition from survey

| Sample | C at% | O at% | Si at% | F at% | Cu at% |
|---|---|---|---|---|---|
| Cu foil | 72.08 | 17.65 | 0 | 0 | 5.79 |
| 3 nm | 40.48 | 13.64 | 38.08 | 7.8 | 0 |
| 6 nm | 36.66 | 14.81 | 44.27 | 4.25 | 0 |
| 9 nm | 36.23 | 11.97 | 44.88 | 6.53 | 0.39 |
| 21 nm | 42.07 | 6.79 | 50.25 | 0.88 | 0 |
| 64 nm | 40.25 | 13.79 | 42.56 | 2.76 | 0.63 |

Peak composition from C 1s

| C 1s | C-C/C-H | C-O | C=O | O-C=O |
|---|---|---|---|---|
| Cu foil | 87.37 | 8.74 | 3.35 | 4.54 |
| 3 nm | 74.01 | 17.88 | 2.01 | 6.1 |
| 6 nm | 74.07 | 17.1 | 3.88 | 4.95 |
| 9 nm | 78.46 | 13.53 | 2.04 | 4.2 |
| 21 nm | 94.17 | 5.83 | 0 | 0 |
| 64 nm | 83.72 | 11.59 | 1.87 | 2.82 |

| Si 2p | eV | |
|---|---|---|
| 3 nm | 99.43 | |
| 6 nm | 99.48 | |
| 9 nm | 99.37 | 99.57 (10%) |
| 21 nm | 99.42 | |
| 64 nm | 99.43 | |

| | O at% from survey | O at% from C 1s |
|---|---|---|
| Cu-foil | 17.65 | 15.26 |
| 3 nm | 13.64 | 12.99 |
| 6 nm | 14.81 | 11.32 |
| 9 nm | 11.97 | 8.68 |
| 21 nm | 6.79 | 2.45 |
| 64 nm | 13.79 | 7.69 |
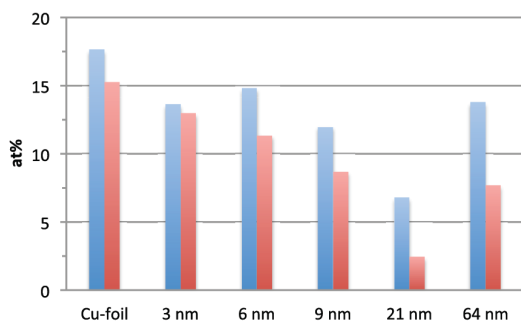
**Figure 4.1.** Survey XPS data for 3 nm (black), 6 nm (red), 9 nm (blue), 21 nm (green) and 64 nm (purple), tabulated elemental composition and peak composition for C and O% from survey.
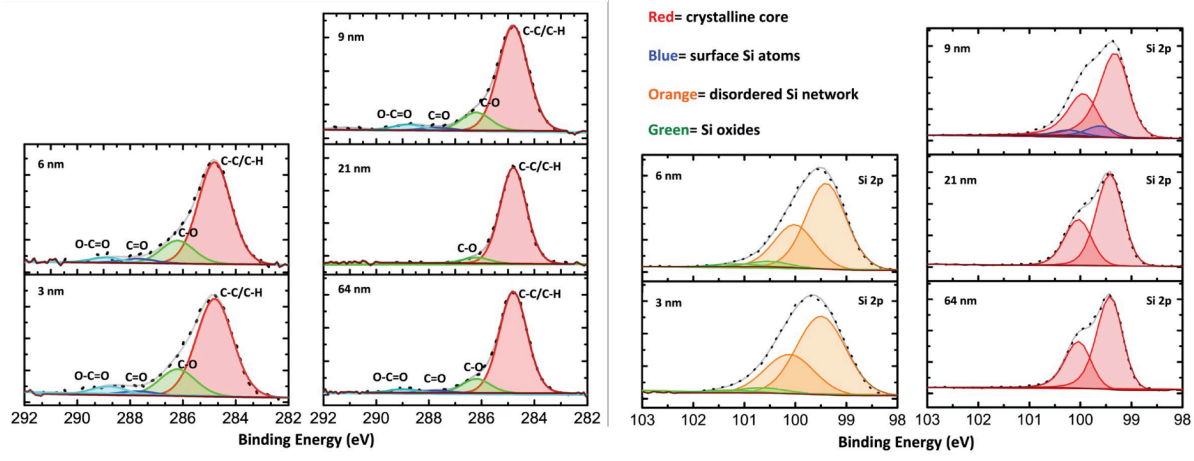
**Figure 4.2.** Peak fitting for C and Si XPS data for 3, 6, 9, 21, and 64 nm nanoparticles.
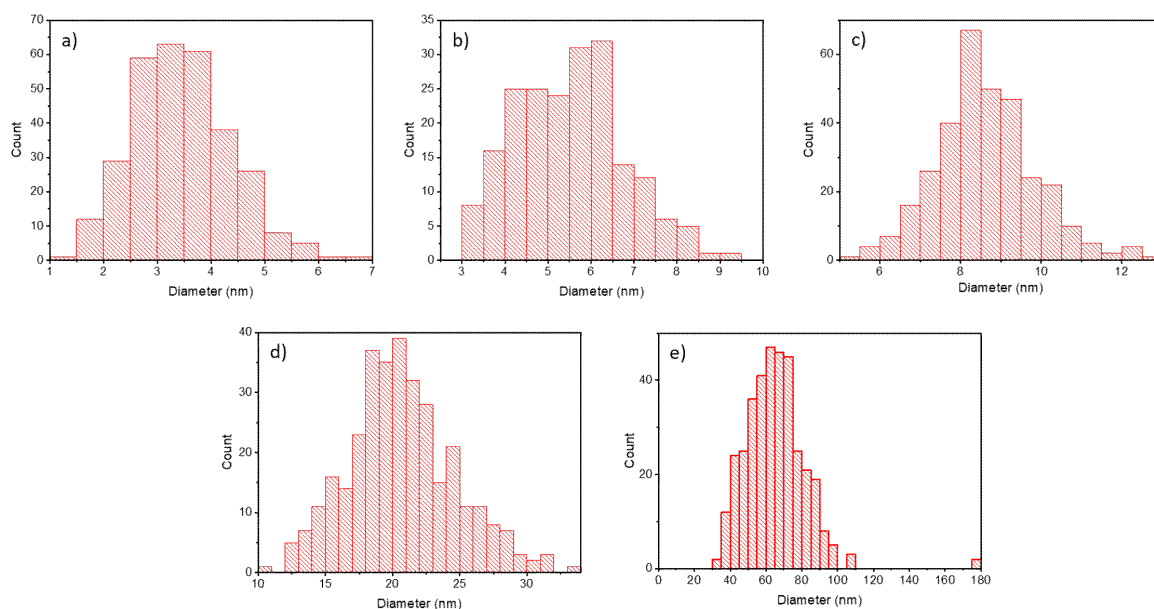


**Figure 4.3.** Histograms showing size distributions for (a) 3 nm, (b) 6 nm, (c) 9 nm, (d) 21 nm, and (e) 64 nm H-SiNPs.

## 4.2.5 Powder X-ray Diffraction (XRD)

Lyophilized samples were placed on a zero-background Si wafer. XRD data were acquired using a Rigaku XRD Ultima IV equipped with a Cu Kα radiation source. Data for H-SiNPs with TEM-determined sizes 64, 21, 9, 6, and 3 nm were analyzed using a series of diffraction line-broadening methods (i.e., integral breadth, FWHM, and Lorentzian broadening) to determine

crystallite sizes. Material properties, as well as instrumental factors contribute to diffraction peak line broadening. Instrumental effects were accounted for by refining a NIST LaB$_6$ standard to ensure instrument alignment and a Si standard was used as an infinitely large crystallite size reference (Figure 4.4). After subtraction of instrumental contribution, line broadening was assumed to result only from size/strain effects. The patterns were analyzed and fit using the TOPAS Academic software package.[73]
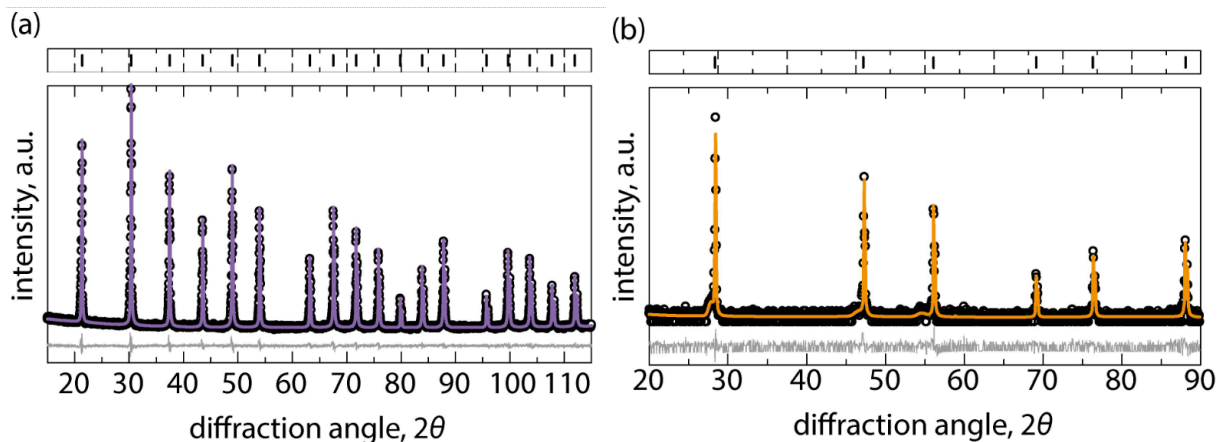


**Figure 4.4.** XRD alignment with (a) LaB$_6$ (NIST) and (b) Si standards.

### 4.2.6 Solid-state Nuclear Magnetic Resonance (NMR) Spectroscopy

Silicon-29 NMR spectra were obtained at 9.39 T ($v_0$ ($^1$H) = 399.95 MHz, $v_0$ ($^{29}$Si) = 79.46 MHz) on a Bruker Avance III HD 400 NMR spectrometer. All data were acquired using a 4 mm double-resonance (H-X) MAS Bruker probe. To ensure that samples had not degraded during analysis, all samples were checked pre- and post-NMR analysis using XPS and FTIR. All NMR data were acquired under magic-angle spinning conditions at ambient temperature with a spinning frequency of 10 ± 0.002 kHz. The data for all experiments were acquired using TPPM[74] $^1$H decoupling ($\gamma B_1/2\pi$ = 62.5 kHz). $^{29}$Si NMR data were referenced to TMS ($\delta$ = 0) by setting the high frequency peak of tetrakistrimethylsilylsilane to −9.8 ppm.[75] All spectral deconvolutions were performed within Origin 2018, $T_1$ data was fit within MATLAB 2017 assuming mono- or bi-exponential recoveries, and NMR data were processed within TOPSPIN using between 50 and 200 Hz Lorentizan broadening. Unless otherwise noted, data were collected with at least 5 × $T_1$ of the longest measured $T_1$ time.

**4.2.6.1 Analysis of H-SiNP Surface and Core**

Direct excitation $^{29}$Si MAS NMR data were acquired using a Bloch[76] pulse with a 4 μs π/2 pulse ($\gamma B_1/2\pi$ = 62.5 kHz), optimized recycle delays (below) between 3.3 minutes and 24 hours, and between 4 and 2048 co-added transients.

**4.2.6.2 Analysis of the H-SiNP Surface**

Cross-polarization[77] (CP) $^{29}$Si{$^1$H} MAS NMR data were acquired with a 4 μs π/2 pulse ($\gamma B_1/2\pi$ = 62.5 kHz) on $^1$H, ramped Hartman-Hahn match on $^{29}$Si, 5 ms contact time, 10 s recycle delay and between 7776 and 10240 co-added transients.

**4.2.6.3 Deconvolution of H-SiNP Surface/Subsurface**

The contact time was varied from 0.05 to 8 ms to further elucidate spectral changes in the CP MAS data, as longer contact times provide time for nuclear spin diffusion to propagate further into the particle. Two-dimensional $^{29}$Si{$^1$H} HETCOR experiment was obtained on the 64 nm particle using 1024 co-added transients, 3 ms contact time (conditions identical to CP experiments above) and 16 $t_2$ increments.

**4.2.6.4 Nuclear Spin-lattice Relaxation**

Spin-lattice $^{29}$Si relaxation data were acquired using the saturation recovery[78] experiment with a pre-saturation train of 16 pulses and a 4 μs π/2 pulse ($\gamma B_1/2\pi$ = 62.5 kHz), 1 - 1024 co-added transients; the relaxation delay was varied from 0.5 to 1000 s (Table 4.1 and Figure 4.5). Note: Due to the large H-SiNPs (d ~ 21 and 64 nm) exhibiting long nuclear $T_1$, additional data points were collected (up to 144 hours).
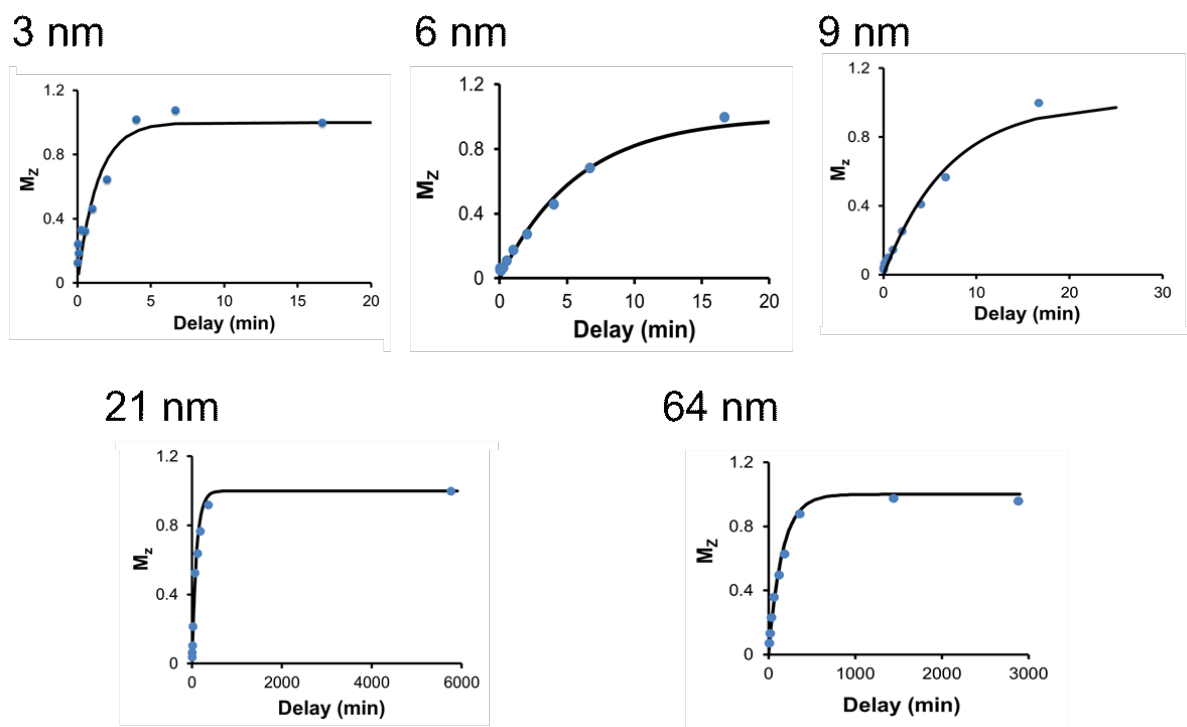
**Figure 4.5.** $T_1$ buildup curves for H-SiNPs using a mono-exponential longitudinal magnetization recovery for smaller H-SiNPs (3 and 6 nm) and a bi-exponential recovery for larger H-SiNPs (9, 21, and 64 nm).

## 4.3 Results and Discussion

Solid-state NMR spectroscopy is an ensemble technique that probes comparatively large quantities of material (i.e., 10s to 100s mgs) and provides information regarding local structure and dynamics. If nanomaterial structural-property relationships are to be elucidated from such investigations, it is imperative that the NP size, shape, and composition be as uniform as possible to allow effective differentiation/identification of the nuclear environments that are present. To achieve this for SiNPs, we have prepared SiNP/SiO$_2$ composites that contain nanoscale inclusions of silicon with pre-defined sizes using a well-established, scalable method involving the thermal processing of HSQ;[6,67,79] high-quality freestanding H-SiNPs are routinely liberated from these composites via alcoholic HF etching. In most cases, H-SiNPs are rendered solution processable and resistant toward oxidation upon surface derivatization using various approaches (e.g., hydrosilylation).[40,80–85] The focus of this study is to investigate the internal SiNP structure free

74

from the influences of surface functionalities; H-SiNPs provide the nearest approximation to 'naked' SiNPs available outside ultrahigh vacuum environments.

X-ray photoelectron spectroscopy is an information rich method that provides data related to material composition and constituent element chemical environment (e.g., oxidation state, nearest neighbor bonding environment, etc.). The survey spectra of the present H-SiNPs were calibrated to the aliphatic C1s signal of adventitious carbon. These data indicate that all specimens contain only Si, C, O, and F (Figure 4.1). Fluorine impurities arise from the alcoholic HF etching procedure that liberates H-SiNPs from the composite and cannot be avoided. Close examination of the C1s high-resolution XP spectra shows evidence of substantial oxygen containing carbon species (i.e., C-O, C=O, O-C=O, etc.; Figure 4.2). The relative ratios of these carbon-containing components are consistent for all sizes of H-SiNPs and are correlated with the amount of oxygen detected in the respective samples (Figure 4.1). From these analyses we conclude that the majority of the oxygen within the present H-SiNP specimens resides within the adventitious carbon species and is not associated with H-SiNP oxidation. This conclusion is further supported by FTIR analyses (Figure 4.6) and the high-resolution Si 2p spectra (Figures 4.7a and 4.2) that are readily deconvolved into Si 2p 3/2 and Si 2p 1/2 spin-orbit couples. For all H-SiNPs, the energy separation of these doublets was fixed at 0.62 eV, and the Si 2p 1/2 to Si 2p 3/2 area was fixed at 0.50. For small H-SiNPs (d ~ 3 and 6 nm), all components (including minor oxide contributions denoted in green) were fit to a Voigt GL(30) line shape (70% Gaussian; 30% Lorentzian). The rationale for applying this fitting procedure lies in the nature of the NP sizes investigated. If NPs are small enough (< 9 nm for the present SiNPs), a considerable number of atoms experience slightly different (disordered) chemical environments (See NMR discussion below) that lead to a distribution of binding energies and symmetric broadening that is Lorentzian in nature. As a result, the overall observed signal is dominated by a symmetric Gaussian/Lorentzian line shape. For the largest SiNPs (d ~ 21 and 64 nm), that represent bulk silicon (See XRD and NMR below), the spectral envelope was fit using a Lorentzian asymmetric line shape LA(a,b,n), where *a* and *b* define the asymmetry and *n* defines the Gaussian width. Similar procedures have been employed when fitting the Si 2p data of bulk crystalline silicon.[71] The d ~ 9 nm H-SiNPs lie within an intermediate size regime where it is possible to isolate the surface and core Si contributions to the Si 2p emission. The Si 2p spectrum of these H-SiNPs was effectively fit by first applying the procedure noted for large NPs (highlighted in red in Figures 4.7a and 4.2) and the remaining residual signal arising

from surface atoms was fit using a GL (30) line shape (highlighted in blue). Of important note, the binding energy of the surface silicon species is shifted to higher energy as a result of electronegativity considerations arising because of bonding interactions with surface hydride moieties (i.e., $SiH_x$).
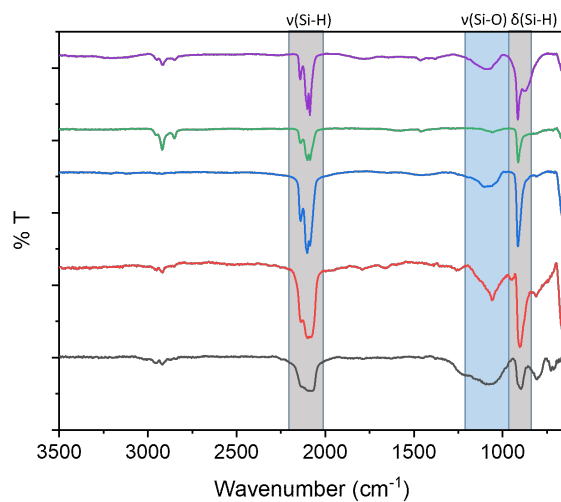


**Figure 4.6.** FTIR spectra for H-SiNPs annealed at 1500 °C (purple), 1400 °C (green), 1300 °C (blue), 1200 °C (red), and 1100 °C (black). The spectra show peaks associated with Si-H (highlighted in gray) and Si-O (highlighted in blue).
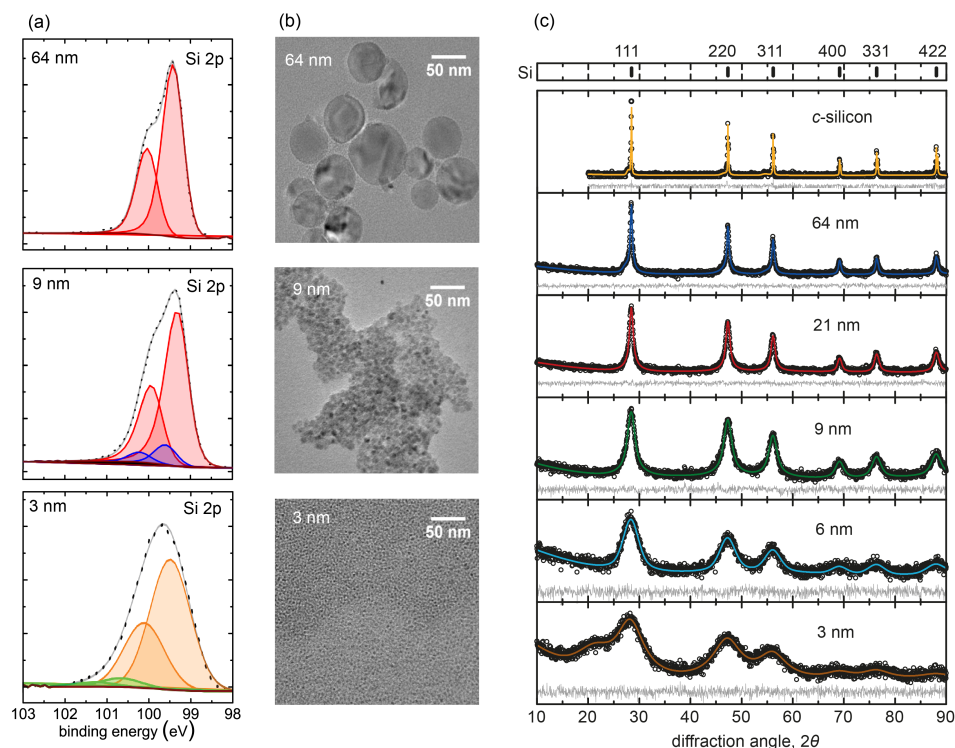
**Figure 4.7.** (a) High-resolution Si 2p XPS showing the 2p$_{3/2}$ emission for 64, 9, and 3 nm H-SiNPs (Si 2p1/2 component was omitted for clarity). The colored traces correspond to : grey = experimental data, dotted black = complete fit, red = crystalline core Si, blue = surface Si, orange = disordered Si, and green = Si oxides. (b) Bright-field TEM images of H-SiNPs (d ~ 64 and 9 nm) and dodecyl-SiNPs (d ~ 3 nm). (c) XRD patterns for d ~ 64 (blue), 21 (red), 9 (green), 6 (cyan), and 3 (brown) nm H-SiNPs, showing characteristic Si 111, 220, 311, 400, 331, and 422 reflections.

TEM imaging of H-SiNPs can be exceptionally challenging because of their limited electron contrast and poor solution processability. NP dimensions determined from bright-field TEM imaging (Figure 4.3) are summarized in Table 4.1. All H-SiNPs were readily imaged with the exception of d ~ 3 nm H-SiNPs, which were heavily agglomerated. To determine the size of these NPs, it was necessary to render them solution processable by modifying their surfaces with dodecyl moieties using standard non-size selective thermally induced hydrosilylation (Figure 4.7b); functionalized NPs obtained from the identical composites used to prepare those evaluated in our NMR studies showed a TEM-derived diameter of 3.5 ± 0.9 nm.

**Table 4.1.** Particle Band Gap and Size Analysis from TEM and XRD

| Nominal (nm) | Annealing Temp. (°C) | Band gap (eV)[b] | TEM (nm) | XRD (nm)[c] |
|---|---|---|---|---|
| 3 | 1100 | 1.57 | 3.5 ± 0.9 | 1.2 ± 1 |
| 6 | 1200 | 1.33 | 5.5 ± 1.2 | 2.5 ± 1 |
| 9 | 1300 | 1.22 | 8.7 ± 1.2 | 4.7 ± 2 |
| 21 | 1400 | 1.14 | 20.7 ± 4.0 | 10.2 ± 3 |
| 64 | 1500 | 1.12 | 64.0 ± 16.9 | 22.4 ± 2 |
| [a]microcrystalline | - | 1.12 | 44 x 10³ | - |

a. Bulk microcrystalline (44 micron) silicon (Aldrich)
b. Band gap determined from Wheeler et al.[25]
c. Values determined from powder X-ray diffraction using the integral breadth method[86]

It is well-established that X-ray powder diffraction peak broadening provides an indirect method for approximating nanocrystal/crystallite size that is complementary to direct TEM imaging. After instrumental contributions are accounted for, only size and strain factors remain. It is possible to qualitatively identify these contributions by considering the dependence of peak broadening on diffraction angle; size-induced broadening follows a $1/\cos\theta$ relationship while strain-induced broadening follows a $\tan\theta$ trend. For the present NPs, the broadening distribution (i.e., full-width at half maximum, FWHM) shows what is expected for size-induced broadening (Figure 4.8) with deviations arising from strain contributions being noted for smaller particles (d ~ 3 and 6 nm). In this context, the peak fits were refined appropriately considering size-dependent strain contributions. Diffraction peak geometry was successfully fit using a pseudo-Voight function. A polynomial background was also included and no over-fitting (absolute correlation) was found for all polynomial terms. In addition, it was necessary to include a synthetic peak 22° effectively describe the peak shapes of the 3 nm particle diffraction pattern. Finally, all diffraction data were analyzed using integral breadth, FWHM, and Lorentzian broadening methods (Table 4.2) that all assume a normal distribution of spherical crystallites.[86] A straightforward comparison of TEM and XRD derived data (Figure 4.7, Table 4.1) shows TEM determined dimensions of H-SiNPs are consistently larger; this is not surprising, and is consistent with present XPS and NMR analyses, given XRD peak broadening only gives a volume-average distribution of crystallite sizes that are routinely smaller than the size of the entire NP (i.e., XRD analyses only probe the crystalline portion of NPs).
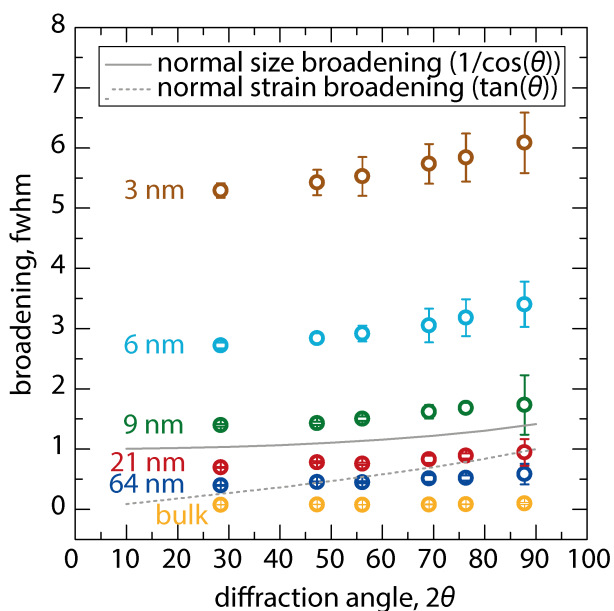
**Figure 4.8.** XRD peak broadening distribution for nanocrystalline materials.

**Table 4.2.** List of common $^{29}$Si chemical shifts for silicon containing materials.

| Bonding Environment | Chemical Shift (ppm) | Ref |
|---|---|---|
| Amorphous – $SiO_2$ | -110 | |
| Quartz – $SiO_2$ | -107 | 62,87 |
| Cristobalite – $SiO_2$ | -109 | |
| $SiO_5$ / $SiO_6$ | -150 / -200 | 62 |
| $SiN_4$ | -49 ($^{[4]}$Si) / -225 ($^{[6]}$Si) | 62,88 |
| $SiC_4$ | -18 | 62 |
| $OSi-H_x$ / $HO-Si(-OSiH_x)_x$ | -89 to -109 | 49,54,55 |
| $-SiH_3$ / $-SiH_2$ / $-SiH$ | -90 to -110 | 89,90 |
| Molecular – $H_3Si-SiH_3$; $H_2Si(-SiH_3)_2$; $HSi(-SiH_3)_3$; $Si(-SiH_3)_4$ | -103 to -165 | 54,91 |

To further evaluate the H-SiNPs, direct excitation (surface and core) and cross polarization (surface) $^{29}$Si MAS NMR spectroscopy was employed. Figure 4.9 shows the direct $^{29}$Si MAS NMR data revealing a considerable evolution from ultrahigh resolution (1 ppm, FWHM) for microcrystalline silicon to a broad resonance spanning nearly 40 ppm, from −75 to −120 ppm as the particle size shrinks to 3 nm. Peak positions and linewidths in the $^{29}$Si NMR spectra are consistent with size-dependent changes in the atomic and/or electronic structure of the NPs. The center-of-gravity chemical shift ($\delta_{cgs}$) of amorphous silicon (*a*-Si*)* has been reported to be −41 ± 3 ppm (with a Gaussian-like resonance that spans 40 to −130 ppm); crystalline (*c*-Si) silicon appears

at lower frequency (isotropic chemical shift, $\delta_{iso}$ = $-80.9 \pm 1$ ppm; 1 ppm FWHM).[92–95] In this context, we attribute the sharp resonance appearing at $-81$ ppm to $c$-Si (i.e., the material possesses a highly ordered structure); this feature shifts to lower frequency with decreasing particle dimensions from 44 μm to 21 nm. As the NP size decreases to below 10 nm a broad resonance emerges, eventually replacing the sharp $c$-Si resonance that would be associated with highly-ordered silicon. We attribute this change in peak shape and breadth to an increased influence of surface states with decreasing NP size. As the surface area of the NP increases (dimensions decrease), the fraction of silicon atoms residing in disordered atomic positions increases (see below). These NP structural changes are manifested in the NMR given the sensitivity of the $^{29}$Si magnetic shielding to local atomic structure (variations in bond angles and lengths, defects caused by dangling bonds, variations in surface species (e.g., SiH$_n$ where n = 1 to 3), and/or combinations thereof, and consistent with previous Raman[30] spectroscopy results). Magnetic shielding can also be influenced by the local electronic structure, which is discussed further below. These effects are not unique to SiNPs and have been reported for numerous nanomaterials, including InP, Zn$_3$P$_2$, ZnSe, Cd, Na, Ag, Pb, etc.[47,96–104]
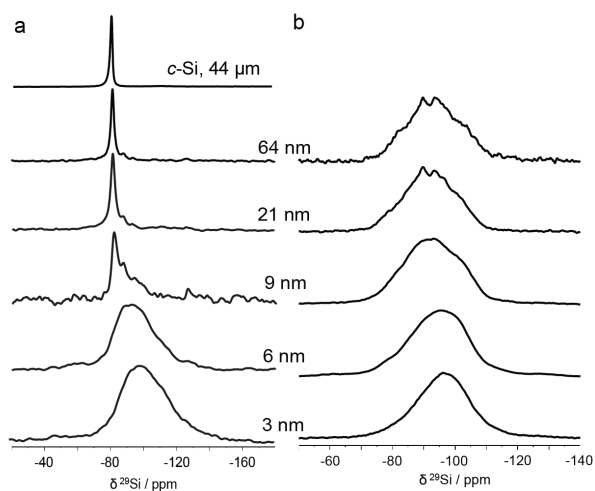


**Figure 4.9.** Direct (a) and CP (b) 29Si MAS NMR spectra of H-SiNPs with varying particle diameter.

To further elucidate the origin of the apparent NP size dependent $^{29}$Si chemical shift, linewidth, and shape, we employed a $^{29}$Si{$^1$H} CP MAS NMR to selectively interrogate silicon atoms at the NP surface.[77,105] This experiment depends on dipole interactions between $^{29}$Si and $^1$H nuclei and enhances signals arising from $^{29}$Si nuclei in close proximity to hydrogen atoms (i.e.,

directly bonded or through space; *ca.* <10 Å). All CP MAS NMR spectra (Figure 4.9b, Figure 4.10) are broad (i.e., −80 to −120 ppm) and featureless for the smallest nanoparticles; features emerge as the NP size increases. Knowing hydride moieties are present on the SiNP surfaces (FTIR; Figure 4.6), we attribute the main broad resonances to surface $Si-H_x$ species that experience substantial structural variability (local disorder). It is reasonable to assume that the Si atomic positions at the NP surfaces are ill-defined (i.e., the structure lacks long-range periodicity) and exist in a distribution of chemical environments (*vide supra*); doubtless the number of Si nuclei chemical environments is compounded by the presence of a distribution, however small it may be, of NP sizes in every sample (Table 4.1).[54–56,106–109]

Closer examination of the spectra obtained for the smallest NPs (d ~ 3 and 6 nm) reveals a broad featureless, slightly asymmetric resonance centered at *ca.* −96 ppm. While crystalline and amorphous $SiO_2$ could appear within a similar chemical shift range ($\delta_{iso}$ ~ −110 ppm)[62,87] our complementary XP analysis confirms oxygen bonded silicon is small (~ 0.7 to 6 atomic %) and FTIR shows no evidence of Si-bonded hydroxyl groups (e.g., Si-OH). Hence, if present, we contend that surface oxides contribute negligibly to the NMR spectra (d ~ 6 to 64 nm) and these features results from $SiH_x$ species (Table 4.2 provides a summary of common $^{29}Si$ chemical shifts). One interesting feature worth noting is the slightly different features of the 3 nm particle when overlaying the direct and CP $^{29}Si$ NMR data. An extra signal from the direct $^{29}Si$ NMR spectrum appears between -100 and -120 ppm, that does not have 1H's nearby. This may be due to a small amount of the Si surface being oxidized (< 7 %, $SiO_x$) or the electronic structure further impacting the chemical shift of these high surface area particles which have a bandgap of ~1.6 eV. As a control illustrating the impact of oxygen on the spectra of H-SiNPs, we purposefully oxidized a sample over a period of months, revealing the formation of $SiO_2$ (Figure 4.11) and would analyze the SiNPs pre- and post-NMR analysis using XPS and FTIR (Figure 4.12).
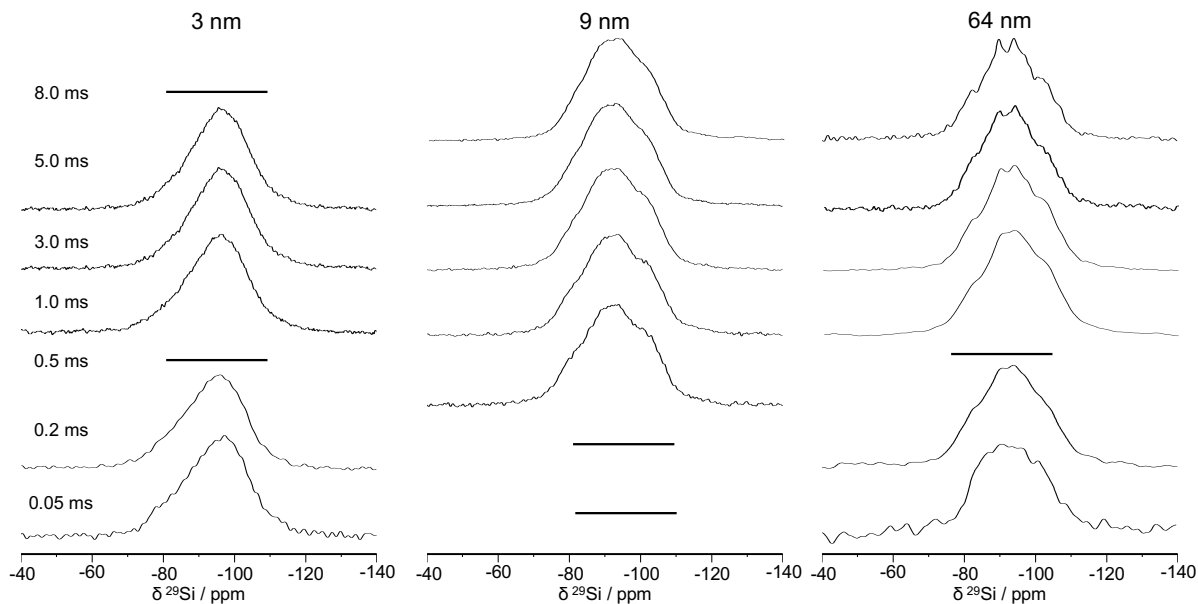
**Figure 4.10.** Contact time array for $^{29}$Si CP MAS ranging from 0.05 to 8.0 ms for 3, 9, and 64 nm H-SiNPs.
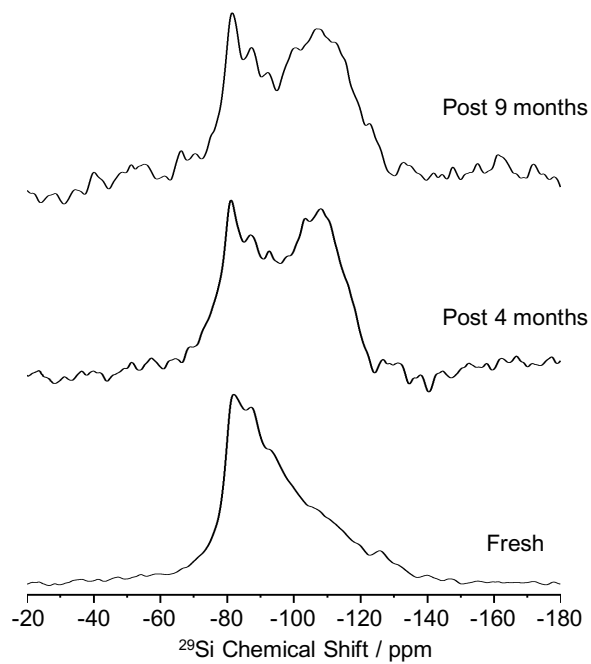


**Figure 4.11.** Silicon-29 NMR spectra for 9 nm H-SiNPs purposefully oxidized over a period of 9 months to indicate contamination of oxygen under ambient storage. Presence of Si-O species at $\delta_{iso}$ of $\sim -110$ ppm 4 and 9 months post-synthesis.
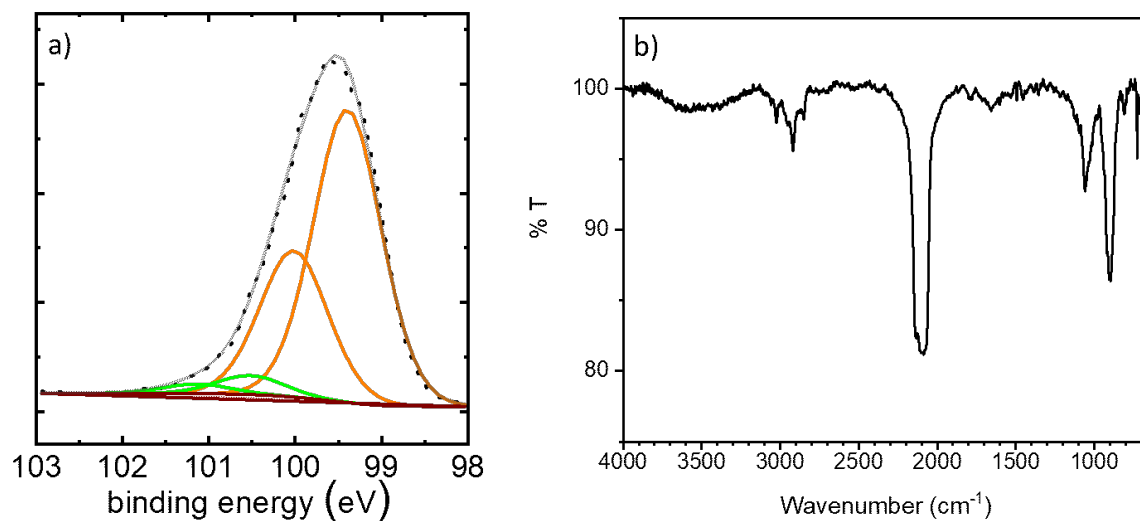
**Figure 4.12.** Sample of the post-NMR analysis of the H-SiNPs (6 nm) using (a) Si 2p high resolution XPS data (with only the $2p_{3/2}$ shown for clarity) and (b) FTIR spectra of 6 nm H-SiNPs.

Turning our attention to the largest NPs considered here (d ~ 21 and 64 nm), they too exhibit a broad resonance with two superimposed sharp features. These features emerge in the 2D $^{29}$Si{$^1$H} HETCOR spectrum (Figure 4.13a) and in the CP MAS NMR data (Figures 4.13b and 4.10) with longer contact times. Closer examination of the $^{29}$Si MAS NMR data (Figures 4.13b and 4.9a) also confirms two new features in low intensity. Their appearance and increased intensity with longer mixing times suggests the presence of an intermediate or sub-surface of quasi-ordered Si atoms. The $^{29}$Si MAS NMR spectra of intermediate dimension of H-SiNPs (d ~ 9 nm) show evidence of these two extremes (Figure 4.9a) consistent with the presence of three structural regimes within the NPs: a crystalline core, quasi-crystalline sub-surface, and disordered surface (Figure 4.13c). Similar effects have been reported in other NPs including $CeO_2$ and noble metal nanomaterials.[104,110]
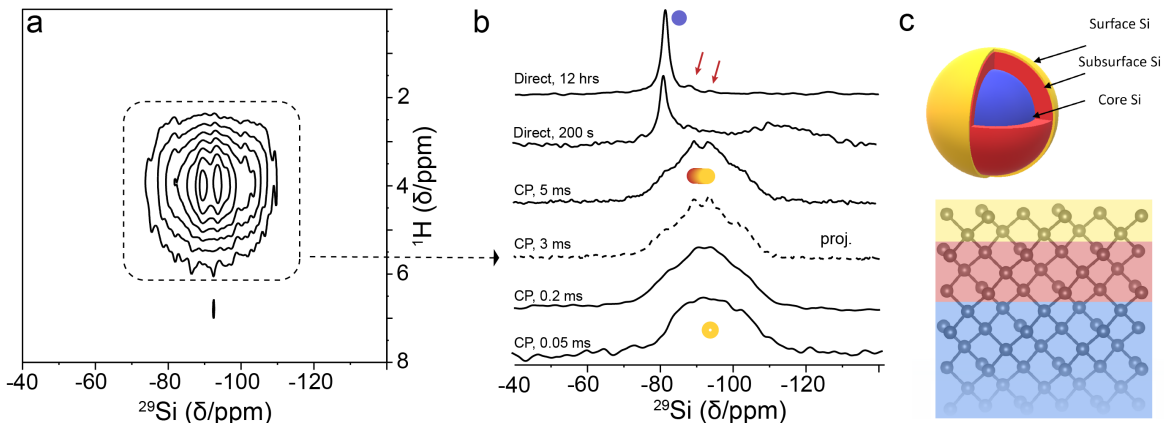
**Figure 4.13.** (a) Two-dimensional $^{29}$Si{$^1$H} HETCOR MAS NMR spectra of 64 nm H-SiNPs with a mixing time of 3.0 ms. (b) Overlay of direct excitation $^{29}$Si MAS NMR and $^{29}$Si{$^1$H} CP MAS NMR with variable mixing times for 64 nm H-SiNP to illustrate NMR features corresponding to H-SiNP surface (yellow), subsurface (red), and core (blue) signatures. Red arrows indicate sharper subsurface NMR features present in the direct excitation $^{29}$Si MAS NMR as seen with $^{29}$Si{$^1$H} CP MAS NMR with a mixing time of 3.0 ms. Direct excitation $^{29}$Si MAS NMR with a recycle delay of 200 s was used to artificially inflate the surface resonance still present at shorter recycle delays. (c) Artistic schematic of a H-SiNP indicating the silicon surface, subsurface, and core with a model of the first ten atomic layers of H-SiNPs.

Building on our understanding of the underlying structure of the presented H-SiNPs, we turn our attention to the NP size-dependence of the $^{29}$Si chemical shift. A disturbance of the local nuclear electronic environment about a given nucleus typically manifests itself in a change of the observed chemical shift. The magnetic shielding interaction[111–113] (chemical and/or Knight shift) could be responsible for the observed effect, depending upon the nanomaterial studied. Knight shifts dominate in metallic systems while SiNP semiconductors are impacted by diamagnetic and paramagnetic chemical shielding contributions.[47,113] Changes in the paramagnetic contributions can be rationalized by the size-dependence of the electronic excitation energy ($\Delta$E),[103,113] whereby decreasing NP size causes an increase in band gap (as the case for the SiNPs considered here). An increase in $\Delta$E causes greater magnetic shielding and the $^{29}$Si chemical shifts appearing at lower frequencies (Figure 4.14a).[47,100,103,113–115] This general reasoning is often invoked when considering the NMR spectra of nanomaterials; originating from molecular systems that have appropriate molecular orbital symmetries.[111,112] Therefore, the changes in $\delta_{cgs}$ observed for the samples studied here appear to be related to size-dependent electronic properties of SiNPs, and are expected to be continuous until the band gap reaches its bulk value of 1.12 eV ($\delta_{iso}$ of d ~ 64 nm ≈ bulk *c*-Si).

Another notable feature of the presented $^{29}$Si NMR spectra is the broad underlying feature whose intensity is inversely related to NP size for dimensions $\leq 21$ nm (Table 4.3). With decreasing NP diameter, the relative contribution from surface nuclei increases such that the contribution from the ordered core becomes minor (even negligible) for the smallest NPs - long-range order simply is not possible within the confines of such small NPs. Nevertheless, the factors discussed previously are still expected to play a role and give rise to a range of chemical shifts for nuclei at or near the surface. These observations are consistent with the XRD data (Figure 4.7c): reflections broaden with decreasing size, as expected with a reduction in the number of repeating units in the NP, which results in structural strain and poorer coherence in the diffraction of the material.[116]
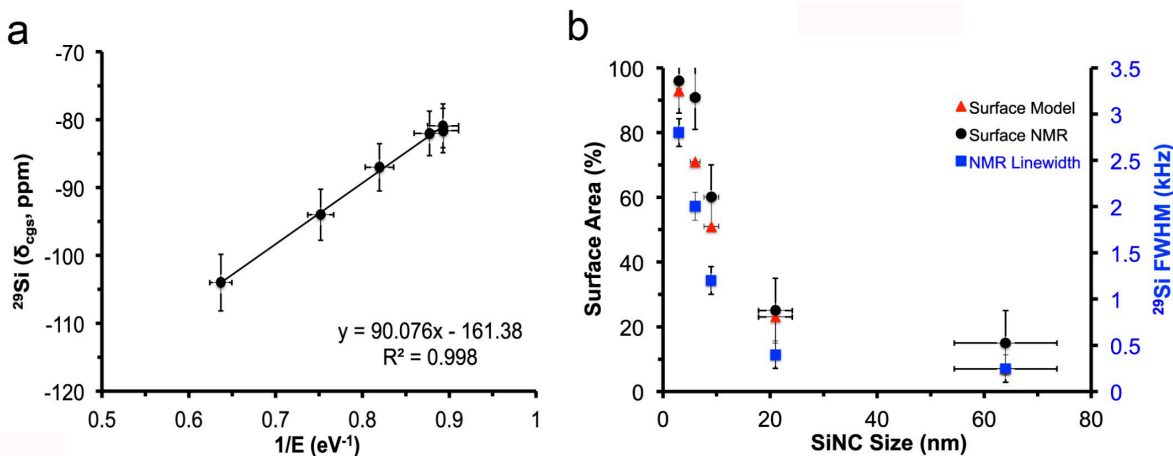


**Figure 4.14.** (a) Relationship of $\delta_{cgs}$ as a function of inverse bandgap of SiNPs. (b) Surface/subsurface area % for NMR experiments (black) and model (red) and $^{29}$Si full-width at half maximum (FWHM, blue) with increasing H-SiNP size. As the H-SiNPs move from a disordered to ordered system, the corresponding surface area % and linewidth decreases as NP size increases.

To investigate the impact of local structure on linewidth, we modeled and estimated (from the $^{29}$Si MAS NMR data) the surface/subsurface volume as a function of particle size (Figure 4.14b and Table 4.3). The number of surface Si atoms on the H-SiNPs was calculated as a function of size based on an assumed icosahedral shape for all sizes except the 64 nm (where a spherical shape was invoked).[117,118] This allowed us to estimate the number of surface/sub-surface atoms (assuming four layers; 5 layers total including the surface) by removing one layer at a time from the surface; the values determined from this analysis are summarized in Table 4.4. Combining these estimates with the XRD data allows an assessment of the reduction in the size of the ordered bulk lattice with

the formation of a disordered surface. With increasing surface area (decreasing NP size), the relative contribution of the ordered core atoms to the NMR spectra at ca. -81 ppm is reduced and no longer resolved for 3 and 6 nm NPs. These observations are consistent with the XRD and TEM particle size determination. Considering the unit cell length for crystalline silicon is 5.4 Å and the smallest particle investigated here has a diameter of 35 Å, only ~ 6 unit cell lengths would be needed for the particle cross section. This reinforces the complementary nature of both XRD (long-range) and NMR (short-range) for materials that exhibit both structural order and local disorder. While we cannot discount the influence of quantum confinement, computational studies show that oxide-embedded 3 nm SiNPs have significant strain throughout the particle.[27] It would follow that this strain would manifest itself as defects including distorted Si-Si bonds, dangling bonds, and coordination defects that are delocalized around the surface of the SiNP, as outlined by Lee *et al.*[26] These defects limit long-range order in the nanoparticle as is evidenced by the extreme broadening of the XRD reflections and NMR spectra. Scherrer analysis of the XRD reveals an average crystallite size of 1.7 nm for 3 nm SiNPs, which correlates to just over three Si unit cell lengths[119], lacking long-range structure.

**Table 4.3.** Experimental $^{29}$Si MAS NMR FWHM, nuclear spin-lattice relaxation times ($T_1$) and surface fraction deconvolutions of the H-SiNPs with varying particle diameters.

| Particle Size /nm | FWHM (± 10%)† | H-SiNC, $T_1$ /min | | $^{29}$Si Surface Fraction /% | |
|---|---|---|---|---|---|
| | kHz | Surface | Core | NMR$^a$ (± 10%) | Model$^b$ |
| 64 | 0.3 | 0.9 ± 0.1 | 158.2 ± 15.0 | 15 | 7 |
| 21 | 0.5 | 3.8 ± 0.4 | 102.1 ± 10.1 | 25 | 23 |
| 9 | 1.2 | 1.3 ± 0.1 | 6.9 ± 0.7 | 60 | 51 |
| 6 | 2.1 | 5.8 ± 0.6* | | 91 | 71 |
| 3 | 2.8 | 1.4 ± 0.1* | | 96 | 93 |

† FWHM reported for the most intense resonances
* Experimental data were best represented using a single exponential (i.e., only a single $T_1$ to describe the 3 and 6 nm H-SiNPs).
$^a$NMR surface fraction estimates were based on fitting of direct NMR data
$^b$Model surface fraction estimates using geometric calculations based on the SiNP structure described by Zhao et al. and Avramov et al. and informed by Si lattice parameters.[117,118]

**Table 4.4.** Calculated fraction of surface, sub-surface and core Si species based on the model by Zhao *et al.* and Avramov *et al.*[117,118]

| Particle Size /nm | Estimated % Fraction of Atoms in Each Structural Component | | |
|---|---|---|---|
| | Surface | Subsurface | Core |
| 64 | 1 | 4 | 95 |
| 21 | 5 | 17 | 78 |
| 9 | 11 | 37 | 52 |
| 6 | 17 | 50 | 33 |
| 3 | 27 | 62 | 11 |

Further exemplifying the combined benefits of preparing well-defined H-SiNPs and evaluating them using NMR spectroscopy, the determination of the nuclear spin lattice relaxation yields an intriguing size dependence (Table 4.3). As expected, smaller NPs (d ~ 3 and 6 nm) exhibit shorter $T_1$ values[9,48,53] with a mono-exponential longitudinal magnetization recovery; larger H-SiNPs (d ~ 9, 21, and 64 nm) show bi-exponential recovery (Figure 4.5). We assign the rapid (i.e., minutes) and slow (i.e., hours) $T_1$ components of the large NPs to surface and core [29]Si species, respectively. To further elucidate the surface of the larger particles, one may select a relaxation time (~ 200 s) which enhances the signal from the surface/subsurface nuclei that have a much shorter $T_1$ relaxation time (on the order of minutes) than the core nuclei. The differences in regard to surface vs. core arise due to the two chemically distinct environments whereby the surface being disordered allows for the ability of more motion and larger distribution of Si environments improving the efficiency in relaxation, while the core aligns itself into a diamond-like structure with a rigid lattice, impeding relaxation as the particle size increases. The presence of unpaired electrons on the surface (i.e., dangling bonds) would cause a reduction in [29]Si spin-lattice relaxation, therefore as the size of the NP increases, the core nuclei become increasingly distant from the surface, resulting in an increase in the experimentally determined nuclear $T_1$.

## 4.4 Conclusions

In this work, we present a state-of-the-art multi-faceted approach to characterizing and understanding the atomic-level structure of H-SiNPs. Using a combination of XPS, bright field

TEM, XRD, FTIR and $^{29}$Si MAS NMR spectroscopy, we probe the complex surface and core structure of H-SiNPs. Solid-state NMR methods allowed us to further interrogate a series of H-SiNPs with dimensions in the range of 3 to 64 nm where three unique structural environments (surface, subsurface and core) were identified. The surface silicon atoms are found between −80 to −120 ppm, while core Si exhibit chemical shifts similar to bulk silicon that become observable in H-SiNPs > 6 nm. Based upon the present experimental data, strain in the long-range periodicity emerges below 9 nm particles, suggesting a critical size-junction; however, the NMR chemical shifts are dominated by changes to the electronic structure of H-SiNPs. Are SiNPs crystalline to the core? Generally yes, but below 3 nm the definition of order vs. disorder becomes unclear since the number of repeating unit cells becomes limited, further straining the surface structure which makes up the bulk of the particle. The structural insight provided by this investigation provides invaluable information key to the rational design and development of SiNP-based applications including, but not limited to, sensors, battery electrodes, optical materials, and contrast agents.

## 4.5 References

(1)     Union, T. E. Publications Office of the European Union. *Official Journal of the European Union* **2017**, *2017/197*, 3.

(2)     Liu, J.; Erogbogbo, F.; Yong, K.-T.; Ye, L.; Liu, J.; Hu, R.; Chen, H.; Hu, Y.; Yang, Y.; Yang, J.; Roy, I.; Karker, N. A.; Swihart, M. T.; Prasad, P. N. Assessing Clinical Prospects of Silicon Quantum Dots: Studies in Mice and Monkeys. *ACS Nano* **2013**, *7* (8).

(3)     Park, J.-H.; Gu, L.; von Maltzahn, G.; Ruoslahti, E.; Bhatia, S. N.; Sailor, M. J. Biodegradable Luminescent Porous Silicon Nanoparticles for in Vivo Applications. *Nat. Mater.* **2009**, *8* (4), 331–336.

(4)     Mobarok, M. H.; Purkait, T. K.; Islam, M. A.; Miskolzie, M.; Veinot, J. G. C. Instantaneous Functionalization of Chemically Etched Silicon Nanocrystal Surfaces. *Angew. Chem. Int. Ed.* **2017**, *56* (22), 6073–6077.

(5)     Islam, M. A.; Mobarok, M. H.; Sinelnikov, R.; Purkait, T. K.; Veinot, J. G. C. Phosphorus Pentachloride Initiated Functionalization of Silicon Nanocrystals. *Langmuir* **2017**, *33* (35), 8766–8773.

(6)     Mastronardi, M. L.; Maier-Flaig, F.; Faulkner, D.; Henderson, E. J.; Kübel, C.; Lemmer, U.; Ozin, G. A. Size-Dependent Absolute Quantum Yields for Size-Separated Colloidally-Stable Silicon Nanocrystals. *Nano Lett.* **2012**, *12* (1), 337–342.

(7)     Bhattacharjee, S.; Rietjens, I. M. C. M.; Singh, M. P.; Atkins, T. M.; Purkait, T. K.; Xu, Z.; Regli, S.; Shukaliak, A.; Clark, R. J.; Mitchell, B. S.; Alink, G. M.; Marcelis, A. T. M.; Fink, M. J.; Veinot, J. G. C.; Kauzlarich, S. M.; Zuilhof, H. Cytotoxicity of Surface-Functionalized Silicon and Germanium Nanoparticles: The Dominant Role of Surface Charges. *Nanoscale* **2013**, *5* (11), 4870.

(8)     Erogbogbo, F.; Yong, K.-T.; Roy, I.; Hu, R.; Law, W.-C.; Zhao, W.; Ding, H.; Wu, F.; Kumar, R.; Swihart, M. T.; Prasad, P. N. In Vivo Targeted Cancer Imaging, Sentinel Lymph Node Mapping and Multi-Channel Imaging with Biocompatible Silicon Nanocrystals. *ACS Nano* **2011**, *5* (1), 413–423.

(9)     Cassidy, M. C.; Chan, H. R.; Ross, B. D.; Bhattacharya, P. K.; Marcus, C. M. In Vivo Magnetic Resonance Imaging of Hyperpolarized Silicon Particles. *Nat. Nanotechnol.* **2013**, *8* (5).

(10)    Tu, C.; Ma, X.; House, A.; Kauzlarich, S. M.; Louie, A. Y. PET Imaging and Biodistribution of Silicon Quantum Dots in Mice. *ACS Med. Chem. Lett.* **2011**, *2* (4), 285–288.

(11)    Liu, X.; Zhao, S.; Gu, W.; Zhang, Y.; Qiao, X.; Ni, Z.; Pi, X.; Yang, D. Light-Emitting Diodes Based on Colloidal Silicon Quantum Dots with Octyl and Phenylpropyl Ligands. *ACS Appl. Mater. Interfaces* **2018**, *10* (6), 5959–5966.

(12)    Dutta, M.; Thirugnanam, L.; Trinh, P. van; Fukata, N. High Efficiency Hybrid Solar Cells Using Nanocrystalline Si Quantum Dots and Si Nanowires. *ACS Nano* **2015**, *9* (7), 6891–6899.

(13)    Švrček, V.; McDonald, C.; Lozac'h, M.; Tayagaki, T.; Koganezawa, T.; Miyadera, T.; Mariotti, D.; Matsubara, K. Stable Ultrathin Surfactant-Free Surface-Engineered Silicon Nanocrystal Solar Cells Deposited at Room Temperature. *Energy Sci. Eng.* **2017**, *5* (4), 184–193.

(14)    Zhao, S.; Pi, X. Colloidal Silicon Quantum Dots and Solar Cells. In *Handbook of Photovoltaic Silicon*; Yang, D., Ed.; Springer Berlin Heidelberg: Berlin, 2017; pp 1–27.

(15)    Gonzalez, C. M.; Veinot, J. G. C. Silicon Nanocrystals for the Development of Sensing Platforms. *J. Mater. Chem. C* **2016**, *4* (22), 4836–4846.

(16)    Meinardi, F.; Ehrenberg, S.; Dhamo, L.; Carulli, F.; Mauri, M.; Bruni, F.; Simonutti, R.; Kortshagen, U.; Brovelli, S. Highly Efficient Luminescent Solar Concentrators Based on Earth-Abundant Indirect-Bandgap Silicon Quantum Dots. *Nat. Photon.* **2017**, *11* (3), 177–185.

(17)    Chan, C. K.; Peng, H.; Liu, G.; McIlwrath, K.; Zhang, X. F.; Huggins, R. A.; Cui, Y. High-Performance Lithium Battery Anodes Using Silicon Nanowires. *Nat. Nanotechnol.* **2008**, *3* (1), 31–35.

(18)    Kim, H.; Seo, M.; Park, M.-H.; Cho, J. A Critical Size of Silicon Nano-Anodes for Lithium Rechargeable Batteries. *Angew. Chem. Int. Ed.* **2010**, *49* (12).

(19)    Su, X.; Wu, Q.; Li, J.; Xiao, X.; Lott, A.; Lu, W.; Sheldon, B. W.; Wu, J. Silicon-Based Nanomaterials for Lithium-Ion Batteries: A Review. *Adv. Energy Mater.* **2014**, *4* (1), 1300882.

(20)    Dohnalová, K.; Gregorkiewicz, T.; Kůsová, K. Silicon Quantum Dots: Surface Matters. *J. Phys. Condens. Matter* **2014**, *26* (17), 173201.

(21)    Chan, C. K.; Ruffo, R.; Hong, S. S.; Cui, Y. Surface Chemistry and Morphology of the Solid Electrolyte Interphase on Silicon Nanowire Lithium-Ion Battery Anodes. *J. Power Sources* **2009**, *189* (2), 1132–1140.

(22)    Dasog, M.; Yang, Z.; Regli, S.; Atkins, T. M.; Faramus, A.; Singh, M. P.; Muthuswamy, E.; Kauzlarich, S. M.; Tilley, R. D.; Veinot, J. G. C. Chemical Insight into the Origin of Red and Blue Photoluminescence Arising from Freestanding Silicon Nanocrystals. *ACS Nano* **2013**, *7* (3), 2676–2685.

(23)    Dasog, M.; de los Reyes, G. B.; Titova, L. v.; Hegmann, F. A.; Veinot, J. G. C. Size *vs* Surface: Tuning the Photoluminescence of Freestanding Silicon Nanocrystals Across the Visible Spectrum *via* Surface Groups. *ACS Nano* **2014**, *8* (9).

(24)    Dasog, M.; Bader, K.; Veinot, J. G. C. Influence of Halides on the Optical Properties of Silicon Quantum Dots. *Chem. Mater.* **2015**, *27* (4).

(25)    Wheeler, L. M.; Anderson, N. C.; Palomaki, P. K. B.; Blackburn, J. L.; Johnson, J. C.; Neale, N. R. Silyl Radical Abstraction in the Functionalization of Plasma-Synthesized Silicon Nanocrystals. *Chem. Mater.* **2015**, *27* (19).

(26)     Lee, B. G.; Hiller, D.; Luo, J.-W.; Semonin, O. E.; Beard, M. C.; Zacharias, M.; Stradins, P. Strained Interface Defects in Silicon Nanocrystals. *Adv. Funct. Mater.* **2012**, *22* (15), 3223–3232.

(27)     Kleovoulou, K.; Kelires, P. C. Stress State of Embedded Si Nanocrystals. *Phys. Rev. B* **2013**, *88* (8), 085424.

(28)     Zhou, Z.; Brus, L.; Friesner, R. Electronic Structure and Luminescence of 1.1- and 1.4-Nm Silicon Nanocrystals: Oxide Shell versus Hydrogen Passivation. *Nano Lett.* **2003**, *3* (2).

(29)     Shu, Y.; Kortshagen, U. R.; Levine, B. G.; Anthony, R. J. Surface Structure and Silicon Nanocrystal Photoluminescence: The Role of Hypervalent Silyl Groups. *J. Phys. Chem. C* **2015**, *119* (47).

(30)     Veprek, S.; Sarott, F.-A.; Iqbal, Z. Effect of Grain Boundaries on the Raman Spectra, Optical Absorption, and Elastic Light Scattering in Nanometer-Sized Crystalline Silicon. *Phys. Rev. B* **1987**, *36* (6).

(31)     Nikitin, T.; Khriachtchev, L. Optical and Structural Properties of Si Nanocrystals in SiO$_2$ Films. *Nanomaterials* **2015**, *5* (2).

(32)     Yogi, P.; Tanwar, M.; Saxena, S. K.; Mishra, S.; Pathak, D. K.; Chaudhary, A.; Sagdeo, P. R.; Kumar, R. Quantifying the Short-Range Order in Amorphous Silicon by Raman Scattering. *Anal. Chem.* **2018**, *90* (13).

(33)     Marra, D. C.; Edelberg, E. A.; Naone, R. L.; Aydil, E. S. Silicon Hydride Composition of Plasma-Deposited Hydrogenated Amorphous and Nanocrystalline Silicon Films and Surfaces. *J. Vac. Sci. Technol.* **1998**, *16* (6).

(34)     Mangolini, L.; Kortshagen, U. Plasma-Assisted Synthesis of Silicon Nanocrystal Inks. *Adv. Mater.* **2007**, *19* (18).

(35)     Jariwala, B. N.; Kramer, N. J.; Petcu, M. C.; Bobela, D. C.; Sanden, M. C. M. van de; Stradins, P.; Ciobanu, C. v.; Agarwal, S. Surface Hydride Composition of Plasma-Synthesized Si Nanoparticles. *J. Phys. Chem. C* **2011**, *115* (42).

(36)     Zipoli, F.; Bernasconi, M. Ab Initio Simulation of the Grafting of Phenylacetylene on Hydrogenated Surfaces of Crystalline Silicon Catalyzed by a Lewis Acid. *J. Phys. Chem. B* **2006**, *110* (46).

(37)     Hua, F.; Swihart, M. T.; Ruckenstein, E. Efficient Surface Grafting of Luminescent Silicon Quantum Dots by Photoinitiated Hydrosilylation. *Langmuir* **2005**, *21* (13).

(38) Hua, F.; Erogbogbo, F.; Swihart, M. T.; Ruckenstein, E. Organically Capped Silicon Nanoparticles with Blue Photoluminescence Prepared by Hydrosilylation Followed by Oxidation. *Langmuir* **2006**, *22* (9).

(39) Giuliani, J. R.; Harley, S. J.; Carter, R. S.; Power, P. P.; Augustine, M. P. Using Liquid and Solid-State NMR and Photoluminescence to Study the Synthesis and Solubility Properties of Amine Capped Silicon Nanoparticles. *Solid State Nucl. Magn. Reson.* **2007**, *32* (1).

(40) Shiohara, A.; Prabakar, S.; Faramus, A.; Hsu, C.-Y.; Lai, P.-S.; Northcote, P. T.; Tilley, R. D. Sized Controlled Synthesis, Purification, and Cell Studies with Silicon Quantum Dots. *Nanoscale* **2011**, *3* (8).

(41) Zou, J.; Kauzlarich, S. M. Functionalization of Silicon Nanoparticles via Silanization: Alkyl, Halide and Ester. *J. Cluster Sci.* **2008**, *19* (2).

(42) Ahire, J. H.; Wang, Q.; Coxon, P. R.; Malhotra, G.; Brydson, R.; Chen, R.; Chao, Y. Highly Luminescent and Nontoxic Amine-Capped Nanoparticles from Porous Silicon: Synthesis and Their Use in Biomedical Imaging. *ACS Appl. Mater. Interfaces* **2012**, *4* (6).

(43) Biesta, W.; van Lagen, B.; Gevaert, V. S.; Marcelis, A. T. M.; Paulusse, J. M. J.; Nielen, M. W. F.; Zuilhof, H. Preparation, Characterization, and Surface Modification of Trifluoroethyl Ester-Terminated Silicon Nanoparticles. *Chem. Mater.* **2012**, *24* (22).

(44) Mayeri, D.; Phillips, B. L.; Augustine, M. P.; Kauzlarich, S. M. NMR Study of the Synthesis of Alkyl-Terminated Silicon Nanoparticles from the Reaction of $SiCl_4$ with the Zintl Salt, NaSi. *Chem. Mater.* **2001**, *13* (3).

(45) Baldwin, R. K.; Pettigrew, K. A.; Ratai, E.; Augustine, M. P.; Kauzlarich, S. M. Solution Reduction Synthesis of Surface Stabilized Silicon Nanoparticles. *Chem. Commun.* **2002**, No. 17.

(46) Carter, R. S.; Harley, S. J.; Power, P. P.; Augustine, M. P. Use of NMR Spectroscopy in the Synthesis and Characterization of Air- and Water-Stable Silicon Nanoparticles from Porous Silicon. *Chem. Mater.* **2005**, *17* (11).

(47) Yesinowski, J. P. Solid-State NMR of Inorganic Semiconductors. In *Solid State NMR*; Chan, J. C. C., Ed.; Springer, Berlin, Heidelberg, 2011.

(48)   Atkins, T. M.; Cassidy, M. C.; Lee, M.; Ganguly, S.; Marcus, C. M.; Kauzlarich, S. M. Synthesis of Long $T_1$ Silicon Nanoparticles for Hyperpolarized $^{29}$Si Magnetic Resonance Imaging. *ACS Nano* **2013**, *7* (2).

(49)   Neiner, D.; Kauzlarich, S. M. Hydrogen-Capped Silicon Nanoparticles as a Potential Hydrogen Storage Material: Synthesis, Characterization, and Hydrogen Release. *Chem. Mater.* **2010**, *22* (2).

(50)   El-Demellawi, J. K.; Holt, C. R.; Abou-Hamad, E.; Al-Talla, Z. A.; Saih, Y.; Chaieb, S. Room-Temperature Reactivity of Silicon Nanocrystals with Solvents: The Case of Ketone and Hydrogen Production from Secondary Alcohols: Catalysis? *ACS Appl. Mater. Interfaces* **2015**, *7* (25).

(51)   Kravitz, K.; Kamyshny, A.; Gedanken, A.; Magdassi, S. Solid State Synthesis of Water-Dispersible Silicon Nanoparticles from Silica Nanoparticles. *J. Solid State Chem.* **2010**, *183* (6).

(52)   Kolyagin, Y. G.; Zakharov, V. N.; Yatsenko, A. v.; Aslanov, L. A. Studies of Silicon Nanocluster Ligand Coating by Solid-State NMR. *Russ. Chem. Bull.* **2015**, *64* (8), 1829–1832.

(53)   Aptekar, J. W.; Cassidy, M. C.; Johnson, A. C.; Barton, R. A.; Lee, M.; Ogier, A. C.; Vo, C.; Anahtar, M. N.; Ren, Y.; Bhatia, S. N.; Ramanathan, C.; Cory, D. G.; Hill, A. L.; Mair, R. W.; Rosen, M. S.; Walsworth, R. L.; Marcus, C. M. Silicon Nanoparticles as Hyperpolarized Magnetic Resonance Imaging Agents. *ACS Nano* **2009**, *3* (12), 4003–4008.

(54)   Faulkner, R.; DiVerdi, J.; Yang, Y.; Kobayashi, T.; Maciel, G. The Surface of Nanoparticle Silicon as Studied by Solid-State NMR. *Materials* **2012**, *6* (1).

(55)   Lee, D.; Kaushik, M.; Coustel, R.; Chenavier, Y.; Chanal, M.; Bardet, M.; Dubois, L.; Okuno, H.; Rochat, N.; Duclairoir, F.; Mouesca, J.; De Paëpe, G. Solid-State NMR and DFT Combined for the Surface Study of Functionalized Silicon Nanoparticles. *Chem. Eur. J.* **2015**, *21* (45).

(56)   Hanrahan, M. P.; Fought, E. L.; Windus, T. L.; Wheeler, L. M.; Anderson, N. C.; Neale, N. R.; Rossini, A. J. Characterization of Silicon Nanocrystal Surfaces by Multidimensional Solid-State NMR Spectroscopy. *Chem. Mater.* **2017**, *29* (24).

(57)   Coleman, N. R. B.; Morris, M. A.; Spalding, T. R.; Holmes, J. D. The Formation of Dimensionally Ordered Silicon Nanowires within Mesoporous Silica. *J. Am. Chem. Soc.* **2001**, *123* (1).

(58)   Davidowski, S. K.; Holland, G. P. Solid-State NMR Characterization of Mixed Phosphonic Acid Ligand Binding and Organization on Silica Nanoparticles. *Langmuir* **2016**, *32* (13).

(59)   Lafon, O.; Thankamony, A. S. L.; Kobayashi, T.; Carnevale, D.; Vitzthum, V.; Slowing, I. I.; Kandel, K.; Vezin, H.; Amoureux, J.-P.; Bodenhausen, G.; Pruski, M. Mesoporous Silica Nanoparticles Loaded with Surfactant: Low Temperature Magic Angle Spinning $^{13}$C and $^{29}$Si NMR Enhanced by Dynamic Nuclear Polarization. *J. Phys. Chem. C* **2013**, *117* (3).

(60)   Sugiyama, Y.; Okamoto, H.; Mitsuoka, T.; Morikawa, T.; Nakanishi, K.; Ohta, T.; Nakano, H. Synthesis and Optical Properties of Monolayer Organosilicon Nanosheets. *J. Am. Chem. Soc.* **2010**, *132* (17).

(61)   Helbich, T.; Lyuleeva, A.; Höhlein, I. M. D.; Marx, P.; Scherf, L. M.; Kehrle, J.; Fässler, T. F.; Lugli, P.; Rieger, B. Radical-Induced Hydrosilylation Reactions for the Functionalization of Two-Dimensional Hydride Terminated Silicon Nanosheets. *Chem. Eur. J.* **2016**, *22* (18).

(62)   MacKenzie, K.; Smith, M. E. *Multinuclear Solid-State Nuclear Magnetic Resonance of Inorganic Materials, Volume 6*; Pergamon, 2002.

(63)   Takeuchi, Y.; Takayama, T. $^{29}$Si NMR Spectroscopy of Organosilicon Compounds. In *The Chemistry of Organic Silicon Compounds*; Rappoport, Z., Apeloig, Y., Eds.; John Wiley & Sons, Ltd: Chichester, UK, 1998; Vol. 2.

(64)   Wrackmeyer, B. Application of $^{119}$Sn NMR Parameters; 1999; pp 203–264.

(65)   Harris, R. K.; Kimber, B. J. $^{29}$Si NMR as a Tool for Studying Silicones. *Appl. Spectrosc. Rev.* **1975**, *10* (1).

(66)   Collins, W. T.; Frye, C. L. Condensed Soluble Hydrogensilsesquioxane Resin. US3615272A, 1968.

(67)   Hessel, C. M.; Henderson, E. J.; Veinot, J. G. C. Hydrogen Silsesquioxane: A Molecular Precursor for Nanocrystalline Si−SiO$_2$ Composites and Freestanding Hydride-Surface-Terminated Silicon Nanoparticles. *Chem. Mater.* **2006**, *18* (26), 6139–6146.

(68)     Barr, T. L.; Seal, S. Nature of the Use of Adventitious Carbon as a Binding Energy
         Standard. *J. Vac. Sci. Technol.* **1995**, *13* (3).

(69)     Payne, B. P.; Biesinger, M. C.; McIntyre, N. S. The Study of Polycrystalline Nickel Metal
         Oxidation by Water Vapour. *J. Electron Spectrosc. Relat. Phenomena* **2009**, *175* (1–3).

(70)     Sublemontier, O.; Nicolas, C.; Aureau, D.; Patanen, M.; Kintz, H.; Liu, X.; Gaveau, M.-
         A.; le Garrec, J.-L.; Robert, E.; Barreda, F.-A.; Etcheberry, A.; Reynaud, C.; Mitchell, J.
         B.; Miron, C. X-Ray Photoelectron Spectroscopy of Isolated Nanoparticles. *J. Phys. Chem.
         Lett.* **2014**, *5* (19).

(71)     Plymale, N. T.; Dasog, M.; Brunschwig, B. S.; Lewis, N. S. A Mechanistic Study of the
         Oxidative Reaction of Hydrogen-Terminated Si(111) Surfaces with Liquid Methanol. *J.
         Phys. Chem. C* **2017**, *121* (8).

(72)     Yang, Z.; Iqbal, M.; Dobbie, A. R.; Veinot, J. G. C. Surface-Induced Alkene
         Oligomerization: Does Thermal Hydrosilylation Really Lead to Monolayer Protected
         Silicon Nanocrystals? *J. Am. Chem. Soc.* **2013**, *135* (46).

(73)     Bruker AXS GmbH. *TOPAS V4: General Profile and Structure Analysis Software for
         Powder Diffraction Data - User's Manual*; Karlsruhe, Germany, 2009; Vol. 4.2.

(74)     Bennett, A. E.; Rienstra, C. M.; Auger, M.; Lakshmi, K. v.; Griffin, R. G. Heteronuclear
         Decoupling in Rotating Solids. *J. Chem. Phys.* **1995**, *103* (16), 6951–6958.

(75)     Hayashi, S.; Hayamizu, K. Chemical Shift Standards in High-Resolution Solid-State NMR
         (1) $^{13}$C, $^{29}$Si, and $^{1}$H Nuclei. *Bull. Chem. Soc. Jpn.* **1991**, *64* (2).

(76)     Bloch, F. Nuclear Induction. *Phys. Rev.* **1946**, *70* (7–8), 460–474.

(77)     Pines, A.; Gibby, M. G.; Waugh, J. S. Proton-Enhanced Nuclear Induction Spectroscopy.
         A Method for High Resolution NMR of Dilute Spins in Solids. *J. Chem. Phys.* **1972**, *56*
         (4), 1776–1777.

(78)     Freeman, R.; Hill, H. D. W. Fourier Transform Study of NMR Spin–Lattice Relaxation by
         "Progressive Saturation." *J. Chem. Phys.* **1971**, *54* (8), 3367–3377.

(79)     Hessel, C. M.; Reid, D.; Panthani, M. G.; Rasch, M. R.; Goodfellow, B. W.; Wei, J.; Fujii,
         H.; Akhavan, V.; Korgel, B. A. Synthesis of Ligand-Stabilized Silicon Nanocrystals with
         Size-Dependent Photoluminescence Spanning Visible to Near-Infrared Wavelengths.
         *Chem. Mater.* **2012**, *24* (2).

(80)   Yu, Y.; Hessel, C. M.; Bogart, T. D.; Panthani, M. G.; Rasch, M. R.; Korgel, B. A. Room Temperature Hydrosilylation of Silicon Nanocrystals with Bifunctional Terminal Alkenes. *Langmuir* **2013**, *29* (5).

(81)   Buriak, J. M. Illuminating Silicon Surface Hydrosilylation: An Unexpected Plurality of Mechanisms. *Chem. Mater.* **2014**, *26* (1).

(82)   Weeks, S. L.; Macco, B.; van de Sanden, M. C. M.; Agarwal, S. Gas-Phase Hydrosilylation of Plasma-Synthesized Silicon Nanocrystals with Short- and Long-Chain Alkynes. *Langmuir* **2012**, *28* (50).

(83)   Nelles, J.; Sendor, D.; Ebbers, A.; Petrat, F. M.; Wiggers, H.; Schulz, C.; Simon, U. Functionalization of Silicon Nanoparticles via Hydrosilylation with 1-Alkenes. *Colloid and Polym. Sci.* **2007**, *285* (7).

(84)   Höhlein, I. M. D.; Kehrle, J.; Helbich, T.; Yang, Z.; Veinot, J. G. C.; Rieger, B. Diazonium Salts as Grafting Agents and Efficient Radical-Hydrosilylation Initiators for Freestanding Photoluminescent Silicon Nanocrystals. *Chem. Eur. J.* **2014**, *20* (15).

(85)   Purkait, T. K.; Iqbal, M.; Wahl, M. H.; Gottschling, K.; Gonzalez, C. M.; Islam, M. A.; Veinot, J. G. C. Borane-Catalyzed Room-Temperature Hydrosilylation of Alkenes/Alkynes on Silicon Nanocrystal Surfaces. *J. Am. Chem. Soc.* **2014**, *136* (52).

(86)   Balzar, D.; Audebrand, N.; Daymond, M. R.; Fitch, A.; Hewat, A.; Langford, J. I.; le Bail, A.; Louër, D.; Masson, O.; McCowan, C. N.; Popa, N. C.; Stephens, P. W.; Toby, B. H. Size–Strain Line-Broadening Analysis of the Ceria Round-Robin Sample. *J. Appl. Crystallogr.* **2004**, *37* (6).

(87)   Smith, J. v.; Blackwell, C. S. Nuclear Magnetic Resonance of Silica Polymorphs. *Nature* **1983**, *303* (5914).

(88)   Sekine, T.; Tansho, M.; Kanzaki, M. $^{29}$Si Magic-Angle-Spinning Nuclear-Magnetic-Resonance Study of Spinel-Type $Si_3N_4$. *Appl. Phys. Lett.* **2001**, *78* (20).

(89)   He, J.; Ba, Y.; Ratcliffe, C. I.; Ripmeester, J. A.; Klug, D. D.; Tse, J. S.; Preston, K. F. Encapsulation of Silicon Nanoclusters in Zeolite Y. *J. Am. Chem. Soc.* **1998**, *120* (41).

(90)   Petit, D.; Chazalviel, J.-N.; Ozanam, F.; Devreux, F. Porous Silicon Structure Studied by Nuclear Magnetic Resonance. *Appl. Phys. Lett.* **1997**, *70* (2).

(91)     Hahn, J. Contributions to the Chemistry of Silicon and Germanium, XXIX [1] $^{29}$Si NMR Spectroscopic Investigations on Straight and Branched Silanes. *Zeitschrift für Naturforschung B* **1980**, *35* (3).

(92)     Hartman, J. S.; Richardson, M. F.; Sherriff, B. L.; Winsborrow, B. G. Magic Angle Spinning NMR Studies of Silicon Carbide: Polytypes, Impurities, and Highly Inefficient Spin-Lattice Relaxation. *J. Am. Chem. Soc.* **1987**, *109* (20).

(93)     Holzman, G. R.; Lauterbur, P. C.; Anderson, J. H.; Koth, W. Nuclear Magnetic Resonance Field Shifts of $^{29}$Si in Various Materials. *J. Chem. Phys.* **1956**, *25* (1).

(94)     Reimer, J. A.; Murphy, P. D.; Gerstein, B. C.; Knights, J. C. Silicon-29 Cross-polarization Magic-angle Sample Spinning Spectra in Amorphous Silicon–Hydrogen Films. *J. Chem. Phys.* **1981**, *74* (2).

(95)     Shao, W.-L.; Shinar, J.; Gerstein, B. C.; Li, F.; Lannin, J. S. Magic-Angle Spinning $^{29}$Si NMR Study of Short-Range Order in *a* -Si. *Phys. Rev. B* **1990**, *41* (13).

(96)     Bercier, J. J.; Jirousek, M.; Graetzel, M.; Klink, J. J. van der. Evidence from NMR for Temperature-Dependent Bardeen-Friedel Oscillations in Nanometre-Sized Silver Particles. *J. Phys. Condens. Mater.* **1993**, *5* (44).

(97)     Charles, R. J.; Harrison, W. A. Size Effect in Nuclear Magnetic Resonance. *Phys. Rev. Lett.* **1963**, *11* (2).

(98)     Terskikh, V. v.; Moudrakovski, I. L.; Ratcliffe, C. I.; Ripmeester, J. A.; Reinhold, C. J.; Anderson, P. A.; Edwards, P. P. Size Effects on the Nuclear Magnetic Resonance of Sodium Metal Confined in Controlled Pore Glasses. In *Magnetic Resonance in Colloid and Interface Science*; Fraissard, J., Lapina, O., Eds.; Springer Netherlands: Dordrecht, 2002; Vol. 76.

(99)     Javadi, M.; Michaelis, V. K.; Veinot, J. G. C. Thermally Induced Evolution of "Ge(OH)$_2$": Controlling the Formation of Oxide-Embedded Ge Nanocrystals. *J. Phys. Chem. C* **2018**, *122* (30).

(100)   Cadars, S.; Smith, B. J.; Epping, J. D.; Acharya, S.; Belman, N.; Golan, Y.; Chmelka, B. F. Atomic Positional Versus Electronic Order in Semiconducting ZnSe Nanoparticles. *Phys. Chem. Lett.* **2009**, *103* (13).

(101) Mobarok, M. H.; Luber, E. J.; Bernard, G. M.; Peng, L.; Wasylishen, R. E.; Buriak, J. M. Phase-Pure Crystalline Zinc Phosphide Nanoparticles: Synthetic Approaches and Characterization. *Chem. Mater.* **2014**, *26* (5).

(102) Ratcliffe, C. I.; Yu, K.; Ripmeester, J. A.; Badruz Zaman, Md.; Badarau, C.; Singh, S. Solid State NMR Studies of Photoluminescent Cadmium Chalcogenide Nanoparticles. *Phys. Chem. Chem. Phys.* **2006**, *8* (30).

(103) Tomaselli, M.; Yarger, J. L.; Bruchez, M.; Havlin, R. H.; deGraw, D.; Pines, A.; Alivisatos, A. P. NMR Study of InP Quantum Dots: Surface Structure and Size Effects. *J. Chem. Phys.* **1999**, *110* (18).

(104) Marbella, L. E.; Millstone, J. E. NMR Techniques for Noble Metal Nanoparticles. *Chem. Mater.* **2015**, *27* (8).

(105) Maciel, G. E.; Sindorf, D. W. Silicon-29 NMR Study of the Surface of Silica Gel by Cross Polarization and Magic-Angle Spinning. *J. Am. Chem. Soc.* **1980**, *102* (25).

(106) Hayashi, S.; Hayamizu, K.; Yamasaki, S.; Matsuda, A.; Tanaka, K. Interpretation of $^{29}$Si Nuclear Magnetic Resonance Spectra of Amorphous Hydrogenated Silicon. *J. Appl. Phys.* **1986**, *60* (5).

(107) Hayashi, S.; Hayamizu, K.; Yamasaki, S.; Matsuda, A.; Tanaka, K. $^{29}$Si Nuclear Magnetic Resonance of Amorphous Hydrogenated Silicon and Amorphous Microcrystalline Mixed-Phase Hydrogenated Silicon. *Phys. Rev. B* **1987**, *35* (10).

(108) Pietraβ, T.; Bifone, A.; Roth, R. D.; Koch, V.-P.; Alivisatos, A. P.; Pines, A. $^{29}$Si High Resolution Solid State Nuclear Magnetic Resonance Spectroscopy of Porous Silicon. *J. Non. Cryst. Solids* **1996**, *202* (1–2).

(109) Hayashi, S.; Hayamizu, K.; Yamasaki, S.; Matsuda, A.; Tanaka, K. Silicon-29 Nuclear Magnetic Resonance Study of Amorphous-Microcrystalline Mixed-Phase Hydrogenated Silicon. *Jpn. J. Appl. Phys.* **1986**, *25* (Part 2, No. 4).

(110) Wang, M.; Wu, X.-P.; Zheng, S.; Zhao, L.; Li, L.; Shen, L.; Gao, Y.; Xue, N.; Guo, X.; Huang, W.; Gan, Z.; Blanc, F.; Yu, Z.; Ke, X.; Ding, W.; Gong, X.-Q.; Grey, C. P.; Peng, L. Identification of Different Oxygen Species in Oxide Nanostructures with $^{17}$O Solid-State NMR Spectroscopy. *Sci. Adv.* **2015**, *1* (1).

(111) Jameson, C. J.; Gutowsky, H. S. Calculation of Chemical Shifts. I. General Formulation and the *Z* Dependence. *J. Chem. Phys.* **1964**, *40* (6).

(112) Ramsey, N. F. Magnetic Shielding of Nuclei in Molecules. *Phys. Rev.* **1950**, *78* (6).

(113) Thayer, A. M.; Steigerwald, M. L.; Duncan, T. M.; Douglass, D. C. NMR Study of Semiconductor Molecular Clusters. *Phys. Rev. Lett.* **1988**, *60* (25).

(114) Bawendi, M. G.; Carroll, P. J.; Wilson, W. L.; Brus, L. E. Luminescence Properties of CdSe Quantum Crystallites: Resonance between Interior and Surface Localized States. *J. Chem. Phys.* **1992**, *96* (2).

(115) Colvin, V. L.; Alivisatos, A. P.; Tobin, J. G. Valence-Band Photoemission from a Quantum-Dot System. *Phys. Rev. Lett.* **1991**, *66* (21).

(116) Comedi, D.; Zalloum, O. H. Y.; Irving, E. A.; Wojcik, J.; Roschuk, T.; Flynn, M. J.; Mascher, P. X-Ray-Diffraction Study of Crystalline Si Nanocluster Formation in Annealed Silicon-Rich Silicon Oxides. *J. Appl. Phys.* **2006**, *99* (2).

(117) Zhao, Y.; Kim, Y.-H.; Du, M.-H.; Zhang, S. First-Principles Prediction of Icosahedral Quantum Dots for Tetravalent Semiconductors. *Phys. Rev. Lett.* **2004**, *93* (1).

(118) Avramov, P. v.; Fedorov, D. G.; Sorokin, P. B.; Chernozatonskii, L. A.; Gordon, M. S. New Symmetric Families of Silicon Quantum Dots and Their Conglomerates as a Tunable Source of Photoluminescence in Nanodevices. *Los Alamos Nat. Lab, Prep. Arch., Condens. Matter* **2007**, 1–19.

(119) Okada, Y.; Tokumaru, Y. Precise Determination of Lattice Parameter and Thermal Expansion Coefficient of Silicon between 300 and 1500 K. *J. Appl. Phys.* **1984**, *56* (2).

# Chapter 5

Endogenous Dynamic Nuclear Polarization NMR of Hydride-Terminated Silicon Nanoparticles

## 5.1 Introduction

Scientific instrumentation and spectroscopic methods have advanced rapidly, making it possible to overcome barriers that have previously limited the characterization, and by extension, the community's understanding of challenging complex biological and energy materials that could revolutionize their respective fields. Solid-state nuclear magnetic resonance (NMR) spectroscopy is among the most powerful non-destructive methods available for characterizing dynamics and atomic-level structure in ordered and disordered solids. Unfortunately, studying nuclear spins often leads to complications related to poor sensitivity, arising from the low Boltzmann polarization, and long acquisition times ranging from hours to days. To circumvent these issues, various approaches, or combinations thereof, have been implemented to improve detection limits and push beyond the status quo. Gains in sensitivity can be achieved via isotopic enrichment or the study of high-$\gamma$ and highly abundant nuclei (e.g., $^1$H or $^{19}$F) in combination with cross-polarization techniques[1], magic angle spinning (MAS) [2,3], and ultrahigh magnetic fields.[4]

High-field dynamic nuclear polarization (DNP) has revolutionized NMR spectroscopy; it is a highly sensitive analytical method that is impacting nearly all fields of chemical research by dramatically and significantly reducing experimental acquisition times and increasing detection limits. These game-changing advancements have been made possible by the large thermal electron spin polarization of a paramagnetic species, achieved by irradiating the sample with high-frequency

microwaves, that can then be transferred to surrounding nuclei.[5–7] The gain in sensitivity is often quantified as the DNP enhancement factor ($\varepsilon$) which is the comparison of the signal-to-noise ratio of the microwave-on and -off NMR spectra acquired under identical conditions; the corresponding reduction in experimental time is thus determined by a factor of $\varepsilon^2$.[8] Often, large gains in sensitivity are achieved using indirect DNP polarization, which is typically accomplished using nitroxide-based biradicals as the electron polarizing agent; examples include TOTAPOL[9], SPIROPOL[10], AMUPol[11], or TEKPOL[12,13], among others.[14–19] Upon microwave irradiation, the polarization of unpaired electrons is transferred to the $^1$H nuclei in the sample of interest, theoretically reaching an enhancement factor of 658 ($\gamma_e/\gamma_{1H}$). The polarization from $^1$H can then be transferred to other lower-$\gamma$ nuclei via cross-polarization; this process facilitates the study of a wide scope of biological and inorganic chemical problems.[8,20–22] Alternatively, electron polarization can be transferred directly to the NMR-active nucleus of interest (direct DNP). In these cases, it is necessary to employ exogenous radicals displaying more effective match conditions; for example, trityl radicals are ideal for polarizing $^2$H ($\gamma_e/\gamma_{2H} = 4291$)[23], $^{17}$O ($\gamma_e/\gamma_{17O} = 4857$)[24], or $^{13}$C ($\gamma_e/\gamma_{13C} = 2616$)[25] nuclei with enhancement factors ranging from 100 to greater than 600 (i.e., > 10,000 reduction in the time required to obtain comparable NMR spectra).[26] Regardless of the polarization transfer mechanism, DNP NMR is a powerful emerging spectroscopic method for both liquids and solids.

To achieve bulk polarization transfer for insulating solids, solid effect (SE) and cross effect (CE) mechanisms are often considered.[27–32] For example, wide-line nitroxide radicals are optimal for CE, while narrow-line radicals such as BDPA are more suited for $^1$H SE. The CE mechanism is often favoured due to its large enhancement factors, the diverse array of commercially available wide-line radicals, less detrimental scaling efficiency with increasing magnetic field strength, and stringent microwave power requirements associated with SE (i.e., forbidden transition).[33]

The study of certain solids may be hampered when using organic biradicals if the radical reacts with the solid of interest (e.g., inducing polymerization or deactivation of the radical) or changes the chemically relevant environment (e.g., binding to a catalytic metal site[34]). To circumvent the need to add an exogenous radical and associated glassing agent(s), various groups have attempted to introduce a paramagnetic center into their chemical system, with the hope of polarizing the nuclei of interest in their solid sample. For example, $Mn^{2+}$ dopants have been successfully used as an endogenous polarizing agent in hammerhead riboyzyme complexes[35], as well as in battery anode materials[36], Griffin and colleagues have successfully polarized $^1$H, $^{13}$C and $^{59}$Co using Cr(III)[37],

while Shumacher and Slicther used the paramagnetic susceptibility of conduction electron spins for $^7$Li enhancements in metallic lithium.[38] Along similar lines, Ramanathan *et al.* utilized the unique feature of dangling bonds within Si microparticles ($\geq$ 0.3 $\mu$m) to polarize $^{29}$Si directly[39], and more recently to investigate the SiO$_x$/H$_2$O interface through $^1$H DNP NMR.[40] In 2008, Ramanathan and colleagues obtained excellent $^{29}$Si DNP enhancements and tunable long nuclear spin-lattice relaxation times ($T_1$) for a series of silicon microparticles ranging in size from ~0.3 to a few $\mu$m. Using a combination of low-field DNP NMR (B$_0$ < 3 T) and ultra-low temperatures (< 30 K), they made use of the endogenous unpaired electrons from dangling bonds within the Si/SiO$_x$ amorphous interface surrounding the crystalline bulk core as the polarizing source.[41] The authors demonstrated the $T_1$s were sensitive to particle size and that the amorphous SiO$_x$ region made up approximately 20% of the total mass.

While most DNP studies have focused on micron-sized silicon particles, there is much interest in analyzing and understanding nanometer-scale particles that lie within the size regime where non-bulk properties emerge. Silicon nanoparticles (SiNPs) with dimensions of 1 to 100 nm hold promise of impacting a wide range of applications including, but not limited to, photovoltaics, thermoelectrics, batteries, and nanomedicine.[42,43] In this context, we build upon previous DNP studies of Si microparticles and explore the effectiveness of exogenous and endogenous radicals for indirect and direct DNP NMR of well-defined non-doped hydride-terminated SiNPs (H-SiNPs; d < 70 nm) prepared using a well-established procedure. The dimensions of the particles studied here are approximately one to two orders of magnitude smaller than those previously reported and do not bear any passivating amorphous "SiO$_x$" surface layer. We demonstrate that dangling bonds at the Si-H terminated surface are present, although in very low concentrations, and that they enable modest direct $^{29}$Si DNP enhancements of the particles using high-field DNP NMR spectroscopy at 400 MHz / 263 GHz and 600 MHz / 395 GHz, at sample temperatures of approximately 100 K.

## 5.2 Experimental Section

### 5.2.1 H-SiNP Synthesis

Hydride-terminated SiNPs were prepared using a well-established procedure as outlined by Hessel *et al.*[44] and characterized via Fourier transform infrared spectroscopy, powder X-ray diffraction, X-ray photoelectron spectroscopy and transmission electron microscopy, to verify purity and size distribution as reported in Thiessen *et al.*.[45]

### 5.2.2 Electron Paramagnetic Resonance (EPR) Spectroscopy of H-SiNPs

EPR experiments were performed directly on DNP samples using a 9.4 GHz X-band Bruker EMXnano spectrometer equipped with a 5 mm sample holder. DNP samples were packed in 3.2 mm sapphire rotors, which were directly inserted into the 5 mm EPR tube and centered in the cavity using a guide. Continuous-wave X-band EPR spectra were acquired with a center field of 3430 G, sweep width of 400 G, modulation amplitude of 4.0 G, and sweep time of 60 s. Spectra were processed in the Bruker Xenon software using a digital filter width of 10 pts. For radical concentration measurements by EPR, the SpinCount module of the Xenon software was used: EPR spectra were baseline corrected using only a zero-order (DC) correction, then double integrated for spin counting. Radical concentrations were calculated accounting for cavity Q, experimental parameters, and sample dimensions.

### 5.2.3 Dynamic Nuclear Polarization Nuclear Magnetic Resonance (DNP NMR) Spectroscopy of H-SiNPs

DNP NMR samples were packed under an inert atmosphere in 3.2 mm sapphire rotors with zirconia top caps; for the exogenous radical samples, a silicone rubber plug was placed between the sample and the zirconia top cap. Silicon-29 DNP NMR spectra were recorded using low-temperature 3.2 mm double resonance (HX) and triple resonance (HXY) MAS DNP probes at 14.1 and 9.4 T, respectively, doubly tuned to $^1$H ($v_L$ = 600.301 MHz and 400.049 MHz) and $^{29}$Si ($v_L$ = 119.262 MHz and 79.471 MHz). All DNP NMR data were acquired at temperatures between 95 and 104 K, with magic angle spinning at a frequency of 8 kHz, 1.3 x $T_B$ recycle delays and between 4 and 128 co-added transients. Spectra were referenced with respect to the $^{13}$C signals of DSS (40.48 ppm).[46] The DNP field profile was performed by sweeping the main magnetic field of the NMR magnet (equipped with a sweep coil) between 9.374 and 9.398 T (399.1 and 400.1 MHz, $^1$H nuclear Larmor frequency). The NMR magnetic field position was adjusted to the maximum of the $^1$H (nitroxide biradical) and $^{29}$Si (endogenous radical) DNP NMR enhancements determined from their respective field profiles. A low-power klystron source (Communications and Power Industries (CPI), Georgetown, Canada)[47,48] was used to generate microwaves with a fixed frequency of 263.58 GHz and an output power of 5.6 W (>5 W at the sample), as verified using a PM5-VDI/Erickson Power Meter (Virginia Diodes Inc., Charlottesville, VA).

### 5.2.3.1 Indirect DNP NMR of An Exogenous Radical

Indirect DNP NMR experiments were performed using a 14.1 T (600 MHz, ^{1}H) Bruker Avance III HD DNP NMR spectrometer equipped with a 395 GHz gyrotron microwave source delivering high-power microwaves (~16 W) to the sample. Cross-polarization (CP)[1] ^{29}Si{^{1}H} DNP MAS NMR experiments were performed using a mixing time of 8.0 ms and an optimized Hartmann-Hahn match condition with a 20% tangential ramp on [1]H. The H-SiNP samples were placed into sapphire rotors with the addition of 20 mM biradical / toluene solution (90% toluene-d[8], 10% toluene) added, followed by slight agitation to ensure wetting of the complete sample; the biradical used was either AMUPol or bCTbK. Toluene was used to suspend hydride-terminated SiNPs and protect the particles from oxidizing as it demonstrates good glassing ability[49] and is an appropriate solvent to dissolve hydrophobic (e.g., bCTbK) nitroxide-based radicals, as well more hydrophilic biradicals (e.g., AMUPol) at high-mM concentrations.

### 5.2.3.2 Direct DNP NMR of Endogenous Radical

Direct DNP NMR experiments were performed on a 9.4 T (400 MHz, ^{1}H) Bruker Avance III HD DNP NMR spectrometer with a 263 GHz EIK microwave source using either a flip-back Bloch[50,51] or Hahn-echo[52] pulse sequence on [29]Si ($\gamma B_1/2\pi$ = 71 kHz) using CW proton decoupling ($\gamma B_1/2\pi$ = 71 kHz).

### 5.2.3.3 DNP Buildup Times

Silicon-29 nuclear buildup times were determined using a saturation recovery[53] experiment with 16 pre-saturation pulses (both ^{1}H and [29]Si) and two co-added transients per data point with varying relaxation delays from $1.0 \times 10^{-3}$ to 600 s for the 3 nm H-SiNP and $3.0 \times 10^{-5}$ to 2.8 hours for 6, 9, 21, and 64 nm H-SiNPs.

## 5.3 Results and Discussion

Hydride-terminated SiNPs prepared through the thermal disproportionation of hydrogen silsesquioxane (HSQ) demonstrate a core-shell type structure, as shown in Figure 5.1b.[45] The surface is comprised of a mixture of Si-H, Si-H[2] and Si-H[3] species which together lead to a disordered surface structure. In contrast, the nanoparticle core is typically comprised of well-ordered crystalline silicon (diameters > 6 nm). In between the inner and surface layers is a semi-

ordered subsurface, which is comprised of a disordered array of silicon atoms that are more ordered than the surface, but less ordered than the crystalline core. The subsurface structure is attributed to the influence of the mismatch between the crystalline Si and the $SiO_2$-like matrix in which the nanoparticles nucleate and grow.[54,55]

Following the proposed structure, it is reasonable that most of the unpaired electrons should be localized within the nanoparticle surface and subsurface layers, where there is less order and dangling bonds are more likely to be present. As outlined previously by Cassidy *et al.*, there should be very few unpaired electrons in the crystalline core.[56] They suggested unpaired electrons lie at the interface between the $Si/SiO_2$ passivating layer. Despite having a hydride-terminated surface, we expect that a similar argument applies in the present system, suggesting the unpaired electrons are located on (or in close proximity to) the surface of the particles. This proposal is further supported by previous work showing that oxidation of the Si-H particles passivates surface defects, decreasing the number of dangling bonds in the system as studied by EPR.[57] In this context, while we cannot discount the presence of unpaired electrons in the nanoparticle core, their contribution will be minimal relative to the concentration of unpaired electrons localized on the surface.

An alternative potential source of unpaired electrons in the SiNP core may come from nitrogen incorporation, much as with nitrogen vacancies in diamond.[58] However, it is well established that even trace nitrogen impurities in the SiNPs will result in a dramatic change in their photoluminescence and manifest as a shift from characteristic red (or near-IR) to blue emission[59]; no such spectral change is observed for the materials investigated. Furthermore, nitrogen and other impurities were not detected in the XPS and EDX analyses of our samples at the detection limit of the methods.

Two DNP NMR protocols were examined here to determine the most effective approach to study a series of hydride-terminated SiNPs. The first method employed nitroxide biradicals incorporated into a glassing agent (e.g., glycerol/water, DMSO/water, TCE, toluene, etc.). This approach is optimized for polarizing $^1$Hs and indirectly enhancing the $^{29}$Si nuclei through CP. The second approach was to determine whether one can effectively enhance the silicon directly without adding an exogenous radical; that is, to utilize the intrinsic endogenous radical present on the SiNPs as a direct $^{29}$Si polarizing agent.

### 5.3.1 Exogenous Organic Biradical Using an Indirect DNP Transfer (e⁻ → ¹H → ²⁹Si)

Using the conventional approach, a 20 mM biradical solution was prepared in toluene-$d_8$ and added to the H-SiNPs, protecting the surface of the particle from oxidation. It is well-established that silicon particle surfaces readily react with radicals[60,61]; the latter were studied using EPR spectroscopy at room temperature. In Table 5.1, we can identify the rapid change within the initial radical concentration (20 mM) and subsequent slower radical quenching via time series measurements. The 9.4 GHz EPR spectrum reveals radical decomposition occurring immediately, with only a small fraction (i.e., 13 mM) of the original radical concentration remaining after a few minutes at room temperature (i.e., the time required for the transfer from the glove box to the EPR). In under 30 minutes, the radical concentration is nearly an order of magnitude lower and within one day, there is no evidence of the biradical even when stored at cryogenic temperatures. The resulting EPR signal that remains arises as a result of the dangling bonds on SiNPs, with no detectable signal from a nitroxide containing mono- or biradical. Although this test was completed using 20 mM AMUPol/toluene-$d_8$, similar effects were observed on the more structurally rigid bCTbK biradical. To work within this short time can be challenging, but, as shown in Figure 5.1c, a DNP-enhanced ²⁹Si{¹H} CP MAS NMR spectrum of 64 nm H-SiNP was obtained at 600 MHz / 395 GHz using bCTbK, achieving an enhancement of 3 for the broad resonance (-80 to -120 ppm). As assigned in a previous study by Thiessen *et al.*[45], this broad resonance corresponds to Si-H$_x$ species on the NP surfaces. Since the polarization transfer goes from the unpaired electrons to ¹H to ²⁹Si, it is not surprising that only the surface and some sub-surface regions of the SiNP show an enhancement. After 12 hours at cryogenic temperatures, no further enhancement was observed; this can be readily understood by considering the absence of nitroxide radical within the prepared sample and later confirmed using X-band EPR spectroscopy.

**Table 5.1.** Total radical concentrations (endogenous and exogenous) measured using X-band EPR of 64 nm H-SiNP after quenching with 20 mM AMUPol in toluene-d$_8$.

| Time after Quench | [Radical] (mM) (± 0.1) | e⁻ (mM) |
|---|---|---|
| DNP Solution | 20 | 40 |
| H-SiNP | 0.6 | 0.6 |
| 1 min | 13.1 | 25.6 |
| 30 min | 3.9 | 7.3 |
| 1.5 days | 0.6 | 0.6 |
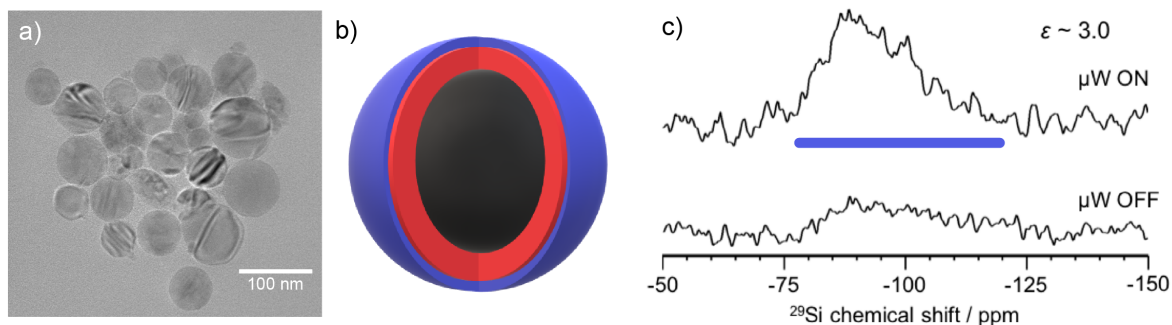


**Figure 5.1.** (a) TEM image of the 64 nm H-SiNP, (b) schematic of a particle identifying the three regions of a SiNP, namely core (black), sub-surface (red) and surface (blue) and (c) DNP-enhanced ($\mu W_{on}$) and non-DNP-enhanced ($\mu W_{off}$) $^{29}$Si{$^1$H} CP MAS NMR spectra of 64 nm hydride-terminated SiNP using 20 mM bCTbk in toluene-d$_8$. The spectrum in (c) was recorded within 15 minutes of the addition of exogenous radical. Typically, during the course of these experiments, glove-box sample preparation and rotor insertion into a DNP probe would require ~ 3-5 minutes; establishing stable spinning and reaching a set point temperature would take another approximately 3-5 minutes.

As a result of the reactive dangling bonds as well as the hydride-terminated SiNP surfaces, the exogenous biradicals are effectively deactivated. The influence of dangling bonds has been demonstrated in studies where the monoradical TEMPO reacts with Si dangling bonds and becomes coordinated to the Si surface.[60,61] Of particular concern in this study is the complete elimination of both radicals from the added biradical / toluene solution after only one day. Based upon what has been reported as a radical coupling reaction between the Si (nanoparticle) and O (biradical) atoms, in principle one would expect the secondary O radical present should still be detected after the initial radical coupling reaction and thus should contribute to the overall radical concentration (i.e., forming a monoradical attached to the nanoparticle surface). However, as

107

shown in Table 5.1, the net radical concentration after 1.5 days is ~ 0, suggesting that both radicals on the organic polarizing agent have been deactivated. Although, the mechanism in which this occurs is not presently known, radical reactions on hydride-terminated silicon surface are known (*e.g.,* radical-initiated hydrosilylation).[61] A possible explanation is that the biradical is quenched via a mechanism similar to radical initiated hydrosilylation, where the NO radical abstracts an H· from the surface to form HNO; leaving a Si· on the surface stabilized by the particle. This Si· can further react with another NO radical, quenching the biradical species, while leaving the dangling bond on SiNPs active. Further insight into the reaction between the NO radical and the H-SiNP is the subject of ongoing investigations.

### 5.3.2 Endogenous Radical Using Direct DNP Transfer (e⁻ → $^{29}$Si)

Shifting to smaller particles at higher magnetic fields and temperatures creates a variety of challenges. In earlier microparticle work, Dementyev *et al*. and Aptekar *et al.* showed a decrease in $T_1$ with decreasing particle size.[39,62] As $T_1$ decreases, less time is available to effectively allow $^{29}$Si-$^{29}$Si spin-diffusion across the sample, leading to a reduction in the ability to build up polarization (i.e., lower enhancements). While going to higher magnetic fields (9.4 /14.1 vs. 2.35 T) increases the nuclear spin-lattice relation time for $^1$H and $^{29}$Si, both the CE and SE polarization mechanisms scale inversely (i.e., ~ $1/B_0$ and $1/B_0^2$, respectively) with magnetic field strength,

which can impact the DNP NMR enhancements. One also needs to consider the number of dangling bonds due to the onset of paramagnetic relaxation and signal quenching. This will have a greater impact on smaller particles (d < 10 nm) where the surface comprises a significant portion of the solid, impacting both spin-lattice relaxation times and NMR lineshapes,[45] as well as effective electron-nuclear polarization transfer.

To assess the feasibility of these pristine H-SiNPs for direct $^{29}$Si DNP NMR at high fields, a range of particle sizes were characterized using EPR measurements to determine the radical concentration present on/in the surface/subsurface of the nanoparticles. Table 5.2 shows the range of radical concentrations associated with SiNPs studied here; in all cases (i.e., d ~ 3 to 64 nm) concentrations are less than 1 mM, consistent with the unpaired electrons arising from dangling bonds residing on the surface layers. The chemical treatment or doping of these particles is a

promising avenue worth exploring in efforts to assess the impact surface modification may play in achieving further gains in DNP enhancements.

**Table 5.2.** Endogenous radical concentrations, enhancement factors ($\varepsilon$), and buildup times ($T_B$) for a series of H-SiNPs.

| Particle Diameter (TEM) /nm | Annealing Temperature / °C | Radical Concentration /mM | Enhancement ($\varepsilon$) | Buildup Time ($T_B$) [c] /s |
|---|---|---|---|---|
| 3 | 1100 | 0.69 | 1.5 | 193 |
| 6 | 1200 | 0.16 / 0.10[a] | 0.92 - 0.94[b] | 270 |
| 9 | 1300 | 0.47 / 0.10[a] | 1.0 | 1733 |
| 21 | 1400 | 0.22 | 1.23 | 3961 |
| 64 | 1500 | 0.70 / 0.42[a] | 1.5 - 6.0[b] | 4733 |

a.  Two batches of H-SiNPs were synthesized to compare endogenous radical concentrations

b.  Ranges correspond to different H-SiNP batches studied, as well as variations in surface/sub-surface vs. core enhancements (0.7 mM is responsible for $\varepsilon$ of 6)

c.  Buildup times for larger particles (21 and 64 nm) are underestimated due to experimental time constraints to fully extrapolate the long $T_B$ values.

Figure 5.2 shows a partial field profile obtained for H-SiNPs of average diameter 64 nm (TEM) that reveals the maximum positive and negative enhancement regions at 9.4 T. Under the conditions investigated here with higher magnetic field strengths and cryogenic liquid nitrogen temperatures, two dominant mechanisms can be considered to effectively enable electron–nuclear polarization transfer: cross-effect (CE) and solid-effect (SE). Although both mechanisms can occur, each has a different set of criteria that must be satisfied if DNP enhancement is to occur. Broadly, the CE mechanism involves a three-spin process involving two electrons and a nuclear spin that are dipolar coupled, whereby the difference in the Larmor frequencies ($\omega_{0S1,2}$) of the two electron spins should approximate the nuclear Larmor frequency ($\omega_{0I}$), where $\omega_{0I} = | \omega_{0Si} - \omega_{0Sii}|$. CE is the dominant mechanism for exogenous nitroxide-containing mono- and biradicals, as their inhomogeneous linewidth of their EPR spectrum is larger than the nuclear Larmor frequency (i.e., 9.4 T – 400 MHz ($^1$H) or 79.5 MHz ($^{29}$Si)), while the homogeneous component is smaller. Conversely, the two-spin SE mechanism can occur when microwave irradiation is applied at the electron-nuclear zero- or double-quantum frequency, where $\omega_{\mu w} = \omega_{0I} \pm \omega_{0S}$. The SE mechanism is typically dominant when

the EPR spectrum is narrow (i.e., when inhomogeneous and homogeneous linewidths are less than the nuclear Larmor frequency).[7,30,32,33,63–67]

The appearance of the EPR resonance and measured field profile (Figure 5.2a) exhibits a full-width-at-half-maximum of ~45 MHz and a full-width-at-the-base of ~96 MHz. The narrow EPR lineshape of 45 MHz (which is less than the [29]Si nuclear Larmor frequency of 79.5 MHz), low radical concentration (< 1 mM, low probability of e⁻ --- e⁻ dipole coupling), and nearly symmetric positions of the positive and negative maxima, would appear to be consistent with a SE DNP mechanism. However, some finer features appear to be lacking, bringing into question whether a contribution from cross-effect can be completely excluded. For example, no plateau is noted between the positive and negative maxima of the symmetric featureless field profile, as is often the case for CE but not SE. The separation between positive and negative enhancement is larger than the expected, $2\omega_{oI} = 159$ MHz, and the EPR spectrum, at its base, is larger than the [29]Si nuclear Larmor frequency (96 MHz > 79.5 MHz). Lastly, the enhancement does not appear to increase with microwave power (i.e., appears saturated) at only ~5 W of output power; while this is not uncommon for the CE, SE typically requires significantly more power to saturate. Therefore, further studies are needed to assess the dominant DNP mechanism between solid- and cross-effect including higher endogenous radical concentration and higher microwave power (i.e., gyrotron vs. klystron). Increasing the [29]Si enhancement and multiple field studies may provide assessment and refinement of the finer nuances within the DNP field profile to determine which mechanism is dominant; studies are ongoing. The overall field profile resembles that observed in a ^{29}Si DNP NMR study of microparticles that were recorded at lower temperatures and magnetic fields and contained higher radical concentrations; in this case the authors attributed the behavior to a thermal mixing process.[39]
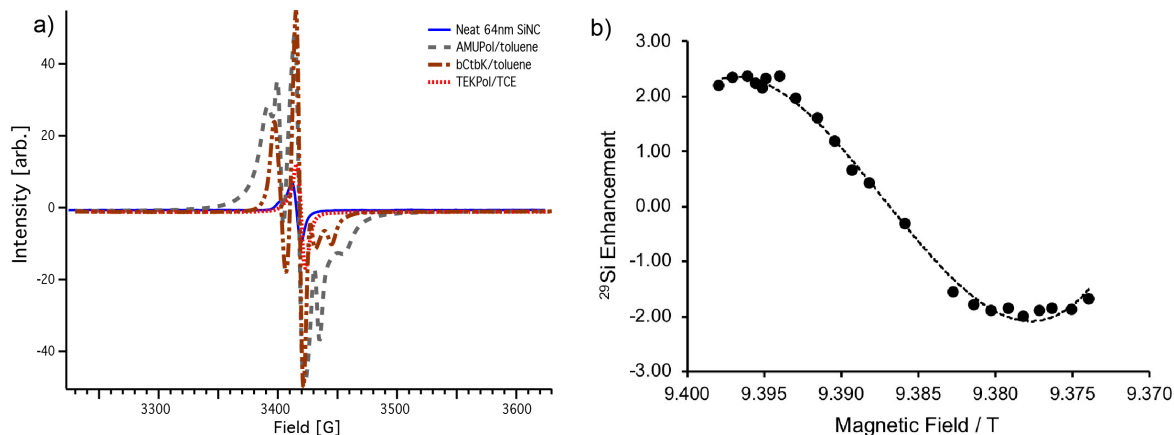
**Figure 5.2.** (a) X-band EPR spectra of 64 nm H-SiNP and indicated nitroxide biradicals and (b) particle field-profile for $^{29}$Si direct DNP of 64 nm hydride-terminated SiNPs at 95 K with MAS frequency of 8 kHz.

Table 5.2 summarizes the enhancements observed for the series of H-SiNPs investigated here. The $^{29}$Si DNP NMR spectrum for the 64 nm H-SiNP is shown in Figure 5.3, along with an NMR (microwave off) spectrum. An enhancement of 6 was obtained for the sharp resonance at $\delta_{iso} \approx$ -85 ppm at 100 K ($\delta_{iso} \approx$ -81 ppm at 300 K) corresponding to the highly ordered (diamond lattice) crystalline SiNP core.[45] The observed change in the $^{29}$Si chemical shift of the core is consistent with our previous study of the interplay between the band gap and $^{29}$Si chemical shift, as the 64 nm particles band gap increases to 1.16 eV at 100 K vs. 1.12 eV at 300 K.[68,69] Furthermore, a low intensity resonance that is sharper than the surface $^{29}$Si shown in Figure 5.1 but broader than the sharp core resonance is observed at lower frequency ($\delta_{iso} \approx$ -93 ppm) and attributed to the intermittent subsurface layer.[45] Although the enhancement is quite small, it was obtained from an endogenous radical concentration of 0.70 mM. We believe that if this radical concentration could be increased by an order of magnitude, the samples would more easily satisfy the three-spin condition for CE, leading to increased DNP enhancements. Nevertheless, the current enhancement, providing a 36-fold reduction in experimental time, demonstrates the practicality of studying SiNP via direct $^{29}$Si DNP from the dangling bonds residing near the surface of the H-SiNPs. Unfortunately, marginal enhancements were obtained for particles smaller than 64 nm. This may arise from lower concentrations of endogenous radicals (< 0.5 mM for 6, 9, and 21 nm H-SiNPs), as well as shorter polarization buildup times (0.05 h for 3 nm vs. > 1.3 h for 64 nm H-SiNPs). The primary interactions responsible for the relaxation behavior of these rigid materials are a balance between $^{29}$Si-$^{29}$Si homonuclear dipolar coupling and paramagnetic relaxation, whereby the smaller

111

particles with larger surface areas are more greatly impacted by the unpaired electrons from dangling bonds. As the particle increases in size, further ordering in the diamond-lattice crystalline core causes the dangling bonds to be isolated on the surface, thereby increasing overall $^{29}$Si spin-lattice relaxation. Additionally, though the positive trend of increasing buildup times with respect to particle size mirrors that seen at room temperature[45] and for microparticles[39], further studies are needed to understand how the chemical environment around the surface dangling bonds affects the buildup times. Subsequently, adjustment of the overall radical concentration and tailoring of the particle surface can be used to boost the enhancement.
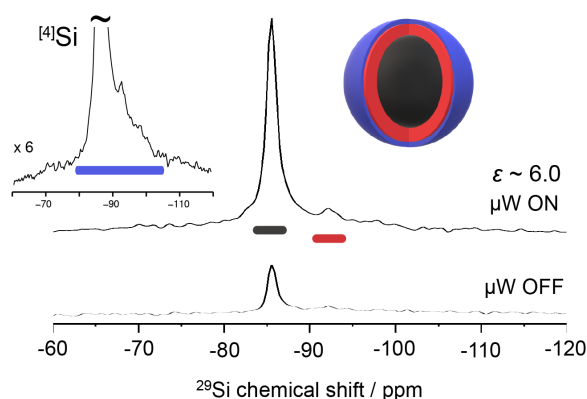


**Figure 5.3.** Silicon-29 DNP NMR spectrum of hydride-terminated SiNPs (64 nm) with an endogenous radical acquired at a MAS frequency of 8 kHz ($\mu$W$_{on}$). The corresponding spectrum acquired without microwave irradiation ($\mu$W$_{off}$). Inset is the $\mu$W$_{on}$ spectrum vertically scaled by 6 to illustrate the surface (blue) of the H-SiNP. The $^{29}$Si resonance at -85 ppm is signal from the crystalline core and the small shoulder to lower frequency (red) is subsurface.[45]

As the DNP process requires the ability to transfer electron polarization (radical source) to its surrounding nuclear environment, the subsequent process of nuclear – nuclear spin diffusion is also a vital component, in particular when dealing with inhomogeneous radical distributions; this is often the case when dealing with crystalline solids. Recently, Wittman *et al.* described a detailed study looking at endohedral fullerene, N@C$_{60}$ sparsely diluted in C$_{60}$ to understand the spin-diffusion barrier under MAS DNP conditions.[70] Thus, they determined electron driven spin-diffusion strongly polarizes the nuclei near the radical (< 15 Å), however, this region of the sample does not contribute to the NMR signal due to impacts on the chemical shifts (paramagnetic interaction) and rapid relaxation. The nuclei near the radical (~ 10 Å) polarize more efficiently at slower spinning frequencies while faster MAS improves the polarization transfer of nuclei further away (> 15 Å). This serves as evidence of a long-hypothesized spin diffusion barrier[28,70,71] over

which polarization must somehow cross in order to achieve long-range diffusion and thereby achieve overall polarization of the sample nuclei. Another important point they discussed through spin-diffusion simulation work is that direct DNP without relay transfer through the nuclear spin network (i.e., inhibiting homonuclear spin diffusion) resulted in no bulk enhancement, as one would expect. Therefore, an efficient crossing of the diffusion barrier will lead to the ability in obtaining a larger polarization of the bulk material, although, if the spin diffusion is hampered by a low concentration of NMR active nuclear spins (e.g., $^{13}$C or $^{29}$Si as in our case), this will cause a slower build-up in DNP polarization. In the same year, Björgvinsdóttir *et al.* discussed an expression for non-spinning samples whereby high polarization of micrometer-sized solids may be achieved through homonuclear spin-diffusion between low-ɣ nuclei.[72] As they pointed out, homonuclear spin diffusion is often neglected for low-ɣ nuclei due to weak dipolar interaction (e.g., $^{29}$Si-$^{29}$Si in SiNPs is 366 Hz, diamond structure, Fd-3m space group). Therefore, even under moderate spinning frequencies one can remove these weak couplings and mitigate spin diffusion.[73] However, only at infinite spinning frequency does the diffusion coefficient go to zero, while under MAS the authors note that one can estimate a decrease of an order or two in magnitude.

How this may impact our results is difficult to directly assess due to the range of endogenous radicals (~100 to 700 ppm), distribution in the sizes of the particles (e.g., 3 ± 1 nm vs. 64 ± 18 nm) and definitive knowledge of the dangling bond locations (i.e. surface/subsurface region). Nonetheless, the three smallest SiNPs (3, 6 and 9 nm) satisfy the regime where the dangling bonds will influence a large portion of the $^{29}$Si nuclear spins with particle radii of 15 ± 5 Å, 30 ± 5 Å and 45 ± 5 Å; considering paramagnetic centers will have direct spherical influence up to ~ 25 Å[70,74] and the surface/subsurface layers will comprise ~ the first 10 Å. Therefore, we can hypothesize an effective electron-nuclear polarization relay to dominate with a minor nuclear spin-diffusion role. As predicted by Wittman *et al.*, the resulting polarization enhancement for these small particles using direct $^{29}$Si DNP is poor.[70] These smaller particles may be best enhanced via indirect DNP through the introduction of exogenous organic radicals if one could circumvent their highly reactive surfaces. The larger 64 nm particle (r = 320 Å) however, demonstrates a long build-up time with a reasonable DNP enhancement of 6 (36 factor savings in time) of the sharp resonance assigned to the core, the minor resonance to lower frequency from the sub-surface, and the broader component nearly hidden for the surface. Therefore, with the radicals isolated to the surface/sub-surface, the region likely to directly receive polarization from unpaired electrons is within 30 to 40

Å of the surface. Transiting the last ~ 280 Å towards the core would require some type of $^{29}$Si-$^{29}$Si homonuclear spin-diffusion; based on the long build-up times observed for these materials, the latter process must be fairly efficient in these samples, with minimal relaxation. Although the spin diffusion will be small and slow (4.7 % natural abundance, low-ɣ), the long relaxation times assist in relaying this polarization inward. Using the approach described by Björgvinsdóttir *et al.*[72], the estimated $^{29}$Si spin diffusion coefficient for SiNPs is 12 nm$^2$/s (i.e., non-spinning conditions). If we assume MAS will decrease the diffusion coefficient by $10^2$, a potential bulk polarization gain of 90 is calculated. In sum, our results are consistent with those of the aforementioned reports on model systems, however, further studies are essential to untangle the complex contributions related to the DNP mechanism, radical location and radical concentration in SiNPs.

## 5.4 Conclusion

In this work, we discuss two DNP NMR protocols to study a series of H-SiNPs. Using EPR, it was observed that, with the conventional DNP NMR approach, the exogenous biradical concentration was reduced significantly within minutes, hampering effectiveness in bulk materials. Thus, the reactive nature of the hydride surfaces renders the use of exogenous radicals for indirect DNP transfer impractical for the study of H-SiNPs. Building upon DNP studies on silicon microparticles using direct $^{29}$Si DNP from intrinsic dangling bonds on the Si surface/sub-surface, we demonstrated the ability to obtain good $^{29}$Si DNP enhancements ($\varepsilon$ = 6 for 64 nm H-SiNPs) from the low endogenous radical concentrations of < 1 mM at high magnetic fields. These promising preliminary results demonstrate the potential for direct DNP polarization transfer using endogenous radicals, followed by $^{29}$Si homonuclear spin-diffusion into the core of the particle assisted by long spin-lattice relaxation values. Future developments in surface modification to control dangling bond formation as well as size control may lead to further gains in sensitivity and the interplay between radical-nuclear polarization transfer and low-ɣ homonuclear spin diffusion.

## 5.5 References

(1)    Pines, A.; Gibby, M. G.; Waugh, J. S. Proton-Enhanced Nuclear Induction Spectroscopy. A Method for High Resolution NMR of Dilute Spins in Solids. *J. Chem. Phys.* **1972**, *56* (4), 1776–1777.

(2) Andrew, E. R.; Bradeuey, A.; Eades, R. G. Nuclear Magnetic Resonance Spectra from a Crystal Rotated at High Speed. *Nature* **1958**, *182* (4650), 1659–1659.

(3) Lowe, I. J. Free Induction Decays of Rotating Solids. *Phys. Rev. Lett.* **1959**, *2* (7), 285–287.

(4) Keeler, E. G.; Michaelis, V. K.; Colvin, M. T.; Hung, I.; Gor'kov, P. L.; Cross, T. A.; Gan, Z.; Griffin, R. G. ^{17}O MAS NMR Correlation Spectroscopy at High Magnetic Fields. *J. Am. Chem. Soc.* **2017**, *139* (49), 17953–17963.

(5) Overhauser, A. W. Polarization of Nuclei in Metals. *Phys. Rev.* **1953**, *92* (2), 411–415.

(6) Carver, T. R.; Slichter, C. P. Polarization of Nuclear Spins in Metals. *Phys. Rev.* **1953**, *92* (1), 212–213.

(7) Maly, T.; Debelouchina, G. T.; Bajaj, V. S.; Hu, K.-N.; Joo, C.-G.; Mak–Jurkauskas, M. L.; Sirigiri, J. R.; van der Wel, P. C. A.; Herzfeld, J.; Temkin, R. J.; Griffin, R. G. Dynamic Nuclear Polarization at High Magnetic Fields. *J. Chem. Phys.* **2008**, *128* (5), 052211.

(8) Ha, M.; Michaelis, V. K. High-Frequency Dynamic Nuclear Polarization NMR for Solids: Part 2 – Development and Applications. In *Modern Magnetic Resonance*; Springer International Publishing: Cham, 2017; pp 1–18.

(9) Song, C.; Hu, K.-N.; Joo, C.-G.; Swager, T. M.; Griffin, R. G. TOTAPOL: A Biradical Polarizing Agent for Dynamic Nuclear Polarization Experiments in Aqueous Media. *J. Am. Chem. Soc.* **2006**, *128* (35), 11385–11390.

(10) Kiesewetter, M. K.; Corzilius, B.; Smith, A. A.; Griffin, R. G.; Swager, T. M. Dynamic Nuclear Polarization with a Water-Soluble Rigid Biradical. *J. Am. Chem. Soc.* **2012**, *134* (10), 4537–4540.

(11) Sauvée, C.; Rosay, M.; Casano, G.; Aussenac, F.; Weber, R. T.; Ouari, O.; Tordo, P. Highly Efficient, Water-Soluble Polarizing Agents for Dynamic Nuclear Polarization at High Frequency. *Angew. Chem. Int. Ed.* **2013**, *52* (41), 10858–10861.

(12) Zagdoun, A.; Casano, G.; Ouari, O.; Schwarzwälder, M.; Rossini, A. J.; Aussenac, F.; Yulikov, M.; Jeschke, G.; Copéret, C.; Lesage, A.; Tordo, P.; Emsley, L. Large Molecular Weight Nitroxide Biradicals Providing Efficient Dynamic Nuclear Polarization at Temperatures up to 200 K. *J. Am. Chem. Soc.* **2013**, *135* (34), 12790–12797.

(13) Kubicki, D. J.; Casano, G.; Schwarzwälder, M.; Abel, S.; Sauvée, C.; Ganesan, K.; Yulikov, M.; Rossini, A. J.; Jeschke, G.; Copéret, C.; Lesage, A.; Tordo, P.; Ouari, O.; Emsley, L.

Rational Design of Dinitroxide Biradicals for Efficient Cross-Effect Dynamic Nuclear Polarization. *Chem. Sci.* **2016**, *7* (1), 550–558.

(14)  Ong, T.-C.; Mak-Jurkauskas, M. L.; Walish, J. J.; Michaelis, V. K.; Corzilius, B.; Smith, A. A.; Clausen, A. M.; Cheetham, J. C.; Swager, T. M.; Griffin, R. G. Solvent-Free Dynamic Nuclear Polarization of Amorphous and Crystalline Ortho -Terphenyl. *J. Phys. Chem. B* **2013**, *117* (10), 3040–3046.

(15)  Sauvée, C.; Casano, G.; Abel, S.; Rockenbauer, A.; Akhmetzyanov, D.; Karoui, H.; Siri, D.; Aussenac, F.; Maas, W.; Weber, R. T.; Prisner, T.; Rosay, M.; Tordo, P.; Ouari, O. Tailoring of Polarizing Agents in the BTurea Series for Cross-Effect Dynamic Nuclear Polarization in Aqueous Media. *Chem. Eur. J.* **2016**, *22* (16), 5598–5606.

(16)  Matsuki, Y.; Maly, T.; Ouari, O.; Karoui, H.; Le Moigne, F.; Rizzato, E.; Lyubenova, S.; Herzfeld, J.; Prisner, T.; Tordo, P.; Griffin, R. G. Dynamic Nuclear Polarization with a Rigid Biradical. *Angew. Chem. Int. Ed.* **2009**, *48* (27), 4996–5000.

(17)  Zagdoun, A.; Casano, G.; Ouari, O.; Lapadula, G.; Rossini, A. J.; Lelli, M.; Baffert, M.; Gajan, D.; Veyre, L.; Maas, W. E.; Rosay, M.; Weber, R. T.; Thieuleux, C.; Coperet, C.; Lesage, A.; Tordo, P.; Emsley, L. A Slowly Relaxing Rigid Biradical for Efficient Dynamic Nuclear Polarization Surface-Enhanced NMR Spectroscopy: Expeditious Characterization of Functional Group Manipulation in Hybrid Materials. *J. Am. Chem. Soc.* **2012**, *134* (4), 2284–2291.

(18)  Mathies, G.; Caporini, M. A.; Michaelis, V. K.; Liu, Y.; Hu, K.-N.; Mance, D.; Zweier, J. L.; Rosay, M.; Baldus, M.; Griffin, R. G. Efficient Dynamic Nuclear Polarization at 800 MHz/527 GHz with Trityl-Nitroxide Biradicals. *Angew. Chem. Int. Ed.* **2015**, *54* (40), 11770–11774.

(19)  Mentink-Vigier, F.; Mathies, G.; Liu, Y.; Barra, A.-L.; Caporini, M. A.; Lee, D.; Hediger, S.; G. Griffin, R.; De Paëpe, G. Efficient Cross-Effect Dynamic Nuclear Polarization without Depolarization in High-Resolution MAS NMR. *Chem. Sci.* **2017**, *8* (12), 8150–8163.

(20)  Lee, D.; Hediger, S.; Paëpe, G. De. High-Field Solid-State NMR with Dynamic Nuclear Polarization. In *Modern Magnetic Resonance*; Springer International Publishing: Cham, 2017; pp 1–17.

(21)   Ni, Q. Z.; Daviso, E.; Can, T. V.; Markhasin, E.; Jawla, S. K.; Swager, T. M.; Temkin, R. J.; Herzfeld, J.; Griffin, R. G. High Frequency Dynamic Nuclear Polarization. *Acc. Chem. Res.* **2013**, *46* (9), 1933–1941.

(22)   Rossini, A. J.; Zagdoun, A.; Lelli, M.; Lesage, A.; Copéret, C.; Emsley, L. Dynamic Nuclear Polarization Surface Enhanced NMR Spectroscopy. *Acc. Chem. Res.* **2013**, *46* (9), 1942–1951.

(23)   Maly, T.; Andreas, L. B.; Smith, A. A.; Griffin, R. G. $^2$H-DNP-Enhanced $^2$H–$^{13}$C Solid-State NMR Correlation Spectroscopy. *Phys. Chem. Chem. Phys.* **2010**, *12* (22), 5872.

(24)   Michaelis, V. K.; Corzilius, B.; Smith, A. A.; Griffin, R. G. Dynamic Nuclear Polarization of $^{17}$O: Direct Polarization. *J. Phys. Chem. B* **2013**, *117* (48), 14894–14906.

(25)   Michaelis, V. K.; Smith, A. A.; Corzilius, B.; Haze, O.; Swager, T. M.; Griffin, R. G. High-Field $^{13}$C Dynamic Nuclear Polarization with a Radical Mixture. *J. Am. Chem. Soc.* **2013**, *135* (8), 2935–2938.

(26)   Michaelis, V. K.; Ong, T.-C.; Kiesewetter, M. K.; Frantz, D. K.; Walish, J. J.; Ravera, E.; Luchinat, C.; Swager, T. M.; Griffin, R. G. Topical Developments in High-Field Dynamic Nuclear Polarization. *Isr. J. Chem.* **2014**, *54* (1–2), 207–221.

(27)   Corzilius, B.; Smith, A. A.; Griffin, R. G. Solid Effect in Magic Angle Spinning Dynamic Nuclear Polarization. *J. Chem. Phys.* **2012**, *137* (5), 054201.

(28)   Smith, A. A.; Corzilius, B.; Barnes, A. B.; Maly, T.; Griffin, R. G. Solid Effect Dynamic Nuclear Polarization and Polarization Pathways. *J. Chem. Phys.* **2012**, *136* (1), 015101.

(29)   Abragam, A.; Proctor, W. G. Une Nouvelle Methode De Polarisation Dynamique Des Noyaux Atomiques Dans Les Solides. *Cr. Hebd. Acad. Sci.* **1958**, *246*, 2253–2256.

(30)   Hwang, C. F.; Hill, D. A. New Effect in Dynamic Polarization. *Phys. Rev. Lett.* **1967**, *18* (4), 110–112.

(31)   Hovav, Y.; Feintuch, A.; Vega, S. Theoretical Aspects of Dynamic Nuclear Polarization in the Solid State – The Cross Effect. *J. Magn. Reson.* **2012**, *214*, 29–41.

(32)   Ha, M.; Michaelis, V. K. High-Frequency Dynamic Nuclear Polarization NMR for Solids: Part 1 – An Introduction. In *Modern Magnetic Resonance*; Springer International Publishing: Cham, 2017; pp 1–24.

(33)   Hu, K.-N.; Bajaj, V. S.; Rosay, M.; Griffin, R. G. High-Frequency Dynamic Nuclear Polarization Using Mixtures of TEMPO and Trityl Radicals. *J. Chem. Phys.* **2007**, *126* (4), 044512.

(34)   Gunther, W. R.; Michaelis, V. K.; Caporini, M. A.; Griffin, R. G.; Román-Leshkov, Y. Dynamic Nuclear Polarization NMR Enables the Analysis of Sn-Beta Zeolite Prepared with Natural Abundance $^{119}$Sn Precursors. *J. Am. Chem. Soc.* **2014**, *136* (17), 6219–6222.

(35)   Wenk, P.; Kaushik, M.; Richter, D.; Vogel, M.; Suess, B.; Corzilius, B. Dynamic Nuclear Polarization of Nucleic Acid with Endogenously Bound Manganese. *J. Biomol. NMR* **2015**, *63* (1), 97–109.

(36)   Wolf, T.; Kumar, S.; Singh, H.; Chakrabarty, T.; Aussenac, F.; Frenkel, A. I.; Major, D. T.; Leskes, M. Endogenous Dynamic Nuclear Polarization for Natural Abundance $^{17}$O and Lithium NMR in the Bulk of Inorganic Solids. *J. Am. Chem. Soc.* **2019**, *141* (1), 451–462.

(37)   Corzilius, B.; Michaelis, V. K.; Penzel, S. A.; Ravera, E.; Smith, A. A.; Luchinat, C.; Griffin, R. G. Dynamic Nuclear Polarization of $^{1}$H, $^{13}$C, and $^{59}$Co in a Tris(Ethylenediamine)Cobalt(III) Crystalline Lattice Doped with Cr(III). *J. Am. Chem. Soc.* **2014**, *136* (33), 11716–11727.

(38)   Schumacher, R. T.; Slichter, C. P. Electron Spin Paramagnetism of Lithium and Sodium. *Phys. Rev.* **1956**, *101* (1), 58–65.

(39)   Dementyev, A. E.; Cory, D. G.; Ramanathan, C. Dynamic Nuclear Polarization in Silicon Microparticles. *Phys. Rev. Lett.* **2008**, *100* (12), 127601.

(40)   Guy, M. L.; van Schooten, K. J.; Zhu, L.; Ramanathan, C. Chemisorption of Water on the Surface of Silicon Microparticles Measured by Dynamic Nuclear Polarization Enhanced NMR. *J. Phys. Chem. C* **2017**, *121* (5), 2748–2754.

(41)   Brodsky, M. H.; Title, R. S. Electron Spin Resonance in Amorphous Silicon, Germanium, and Silicon Carbide. *Phys. Rev. Lett.* **1969**, *23* (11), 581–585.

(42)   Veinot, J. G. C. Synthesis, Surface Functionalization, and Properties of Freestanding Silicon Nanocrystals. *Chem. Comm.* **2006**, No. 40, 4160.

(43)   Santos, H. A.; Mäkilä, E.; Airaksinen, A. J.; Bimbo, L. M.; Hirvonen, J. Porous Silicon Nanoparticles for Nanomedicine: Preparation and Biomedical Applications. *Nanomedicine* **2014**, *9* (4), 535–554.

(44) Hessel, C. M.; Henderson, E. J.; Veinot, J. G. C. Hydrogen Silsesquioxane: A Molecular Precursor for Nanocrystalline Si−SiO$_2$ Composites and Freestanding Hydride-Surface-Terminated Silicon Nanoparticles. *Chem. Mater.* **2006**, *18* (26), 6139–6146.

(45) Thiessen, A. N.; Ha, M.; Hooper, R. W.; Yu, H.; Oliynyk, A. O.; Veinot, J. G. C.; Michaelis, V. K. Silicon Nanoparticles: Are They Crystalline from the Core to the Surface? *Chem. Mater.* **2019**, *31* (3), 678–688.

(46) Morcombe, C. R.; Zilm, K. W. Chemical Shift Referencing in MAS Solid State NMR. *J. Magn. Reson.* **2003**, *162* (2), 479–486.

(47) Rosay, M.; Scrgeyev, I.; Tometich, L.; Hickey, C.; Roitman, A.; Yake, D.; Berry, D. Opportunities and Challenges for EIK's in DNP NMR Applications. In *2018 43$^{rd}$ International Conference on Infrared, Millimeter, and Terahertz Waves (IRMMW-THz)*; IEEE, 2018; pp 1–2.

(48) Roitman, A.; Hyttinen, M.; Deng, H.; Berry, D.; MacHattie, R. Progress in Power Enhancement of Sub-Millimeter Compact EIKs. In *2017 42$^{nd}$ International Conference on Infrared, Millimeter, and Terahertz Waves (IRMMW-THz)*; IEEE, 2017; pp 1–2.

(49) Meyer, B. *Low Temperature Spectroscopy*; American Elsevier: New York, 1971.

(50) Bloch, F. Nuclear Induction. *Phys. Rev.* **1946**, *70* (7–8), 460–474.

(51) Björgvinsdóttir, S.; Walder, B. J.; Pinon, A. C.; Yarava, J. R.; Emsley, L. DNP Enhanced NMR with Flip-Back Recovery. *J. Magn. Reson.* **2018**, *288*, 69–75.

(52) Hahn, E. L. Spin Echoes. *Phys. Rev.* **1950**, *80* (4), 580–594.

(53) Freeman, R.; Hill, H. D. W. Fourier Transform Study of NMR Spin–Lattice Relaxation by "Progressive Saturation." *J. Chem. Phys.* **1971**, *54* (8), 3367–3377.

(54) Lee, B. G.; Hiller, D.; Luo, J.-W.; Semonin, O. E.; Beard, M. C.; Zacharias, M.; Stradins, P. Strained Interface Defects in Silicon Nanocrystals. *Adv. Funct. Mater.* **2012**, *22* (15), 3223–3232.

(55) Kleovoulou, K.; Kelires, P. C. Stress State of Embedded Si Nanocrystals. *Phys. Rev. B* **2013**, *88* (8), 085424.

(56) Cassidy, M. C.; Chan, H. R.; Ross, B. D.; Bhattacharya, P. K.; Marcus, C. M. In Vivo Magnetic Resonance Imaging of Hyperpolarized Silicon Particles. *Nat. Nanotechnol.* **2013**, *8* (5), 363–368.

(57) Lockwood, R.; Yang, Z.; Sammynaiken, R.; Veinot, J. G. C.; Meldrum, A. Light-Induced Evolution of Silicon Quantum Dot Surface Chemistry—Implications for Photoluminescence, Sensing, and Reactivity. *Chem. Mater.* **2014**, *26* (19), 5467–5474.

(58) King, J. P.; Jeong, K.; Vassiliou, C. C.; Shin, C. S.; Page, R. H.; Avalos, C. E.; Wang, H.-J.; Pines, A. Room-Temperature in Situ Nuclear Spin Hyperpolarization from Optically Pumped Nitrogen Vacancy Centres in Diamond. *Nat. Comm.* **2015**, *6* (1), 8965.

(59) Dasog, M.; Yang, Z.; Regli, S.; Atkins, T. M.; Faramus, A.; Singh, M. P.; Muthuswamy, E.; Kauzlarich, S. M.; Tilley, R. D.; Veinot, J. G. C. Chemical Insight into the Origin of Red and Blue Photoluminescence Arising from Freestanding Silicon Nanocrystals. *ACS Nano* **2013**, *7* (3), 2676–2685.

(60) Pitters, J. L.; Piva, P. G.; Tong, X.; Wolkov, R. A. Reversible Passivation of Silicon Dangling Bonds with the Stable Radical TEMPO. *Nano Lett.* **2003**, *3*, 1431–1435.

(61) Yang, Z.; Gonzalez, C. M.; Purkait, T. K.; Iqbal, M.; Meldrum, A.; Veinot, J. G. C. Radical Initiated Hydrosilylation on Silicon Nanocrystal Surfaces: An Evaluation of Functional Group Tolerance and Mechanistic Study. *Langmuir* **2015**, *31* (38), 10540–10548.

(62) Aptekar, J. W.; Cassidy, M. C.; Johnson, A. C.; Barton, R. A.; Lee, M.; Ogier, A. C.; Vo, C.; Anahtar, M. N.; Ren, Y.; Bhatia, S. N.; Ramanathan, C.; Cory, D. G.; Hill, A. L.; Mair, R. W.; Rosen, M. S.; Walsworth, R. L.; Marcus, C. M. Silicon Nanoparticles as Hyperpolarized Magnetic Resonance Imaging Agents. *ACS Nano* **2009**, *3* (12), 4003–4008.

(63) Kessenikh, A. V.; Lushchikov, V. I.; Manenkov, A. A.; Taran, Y. V. Proton Polarization in Irradiated Polyethylenes. *Sov. Phys. Solid State* **1963**, *5*, 321–329.

(64) Wollan, D. S. Dynamic Nuclear Polarization with an Inhomogeneously Broadened ESR Line. I. Theory. *Phys. Rev. B* **1976**, *13* (9), 3671–3685.

(65) Wollan, D. S. Dynamic Nuclear Polarization with an Inhomogeneously Broadened ESR Line. II. Experiment. *Phys. Rev. B* **1976**, *13* (9), 3686–3696.

(66) Abragam, A. *Principles of Nuclear Magnetic Resonance*; Oxford University Press: New York, 1961.

(67) Slichter, C. P. *Principles of Magnetic Resonance*; Harper & Row: New York, 1963.

(68) Varshni, Y. P. Temperature Dependence of the Energy Gap in Semiconductors. *Physica* **1967**, *34* (1), 149–154.

(69)    Sinelnikov, R.; Dasog, M.; Beamish, J.; Meldrum, A.; Veinot, J. G. C. Revisiting an Ongoing Debate: What Role Do Surface Groups Play in Silicon Nanocrystal Photoluminescence? *ACS Photonics* **2017**, *4* (8), 1920–1929.

(70)    Wittmann, J. J.; Eckardt, M.; Harneit, W.; Corzilius, B. Electron-Driven Spin Diffusion Supports Crossing the Diffusion Barrier in MAS DNP. *Phys. Chem. Chem. Phys.* **2018**, *20* (16), 11418–11429.

(71)    Pinon, A. C.; Schlagnitweit, J.; Berruyer, P.; Rossini, A. J.; Lelli, M.; Socie, E.; Tang, M.; Pham, T.; Lesage, A.; Schantz, S.; Emsley, L. Measuring Nano- to Microstructures from Relayed Dynamic Nuclear Polarization NMR. *J. Phys. Chem. C* **2017**, *121* (29), 15993–16005.

(72)    Björgvinsdóttir, S.; Walder, B. J.; Pinon, A. C.; Emsley, L. Bulk Nuclear Hyperpolarization of Inorganic Solids by Relay from the Surface. *J. Am. Chem. Soc.* **2018**, *140* (25), 7946–7951.

(73)    Maricq, M. M.; Waugh, J. S. NMR in Rotating Solids. *J. Chem. Phys.* **1979**, *70* (7), 3300–3316.

(74)    Rogawski, R.; Sergeyev, I. V.; Zhang, Y.; Tran, T. H.; Li, Y.; Tong, L.; McDermott, A. E. NMR Signal Quenching from Bound Biradical Affinity Reagents in DNP Samples. *J. Phys. Chem. B* **2017**, *121* (48), 10770–10781.

# Chapter 6

Racing Toward Fast and Effective $^{17}$O Isotopic Labelling and NMR Spectroscopy of N-formyl-MLF-OH and Associated Building Blocks

## 6.1 Introduction

The field of solid-state nuclear magnetic resonance (NMR) spectroscopy of biomolecules has flourished over the last few decades.[1] With the advancements in higher magnetic field strengths and development of new NMR techniques, the use of NMR spectroscopy to characterize and study the structure and dynamics of small biomolecules, peptides, and proteins has become routine. To date, NMR studies of amino acids, peptides and biomolecules have relied on $^{13}$C and $^{15}$N nuclei as they form the backbone to all biomolecules.[1] With the recent advancement of ultrafast magic-angle spinning (MAS) probe hardware, $^{1}$H-detected NMR studies have now become feasible.[2-7] Oxygen-17 NMR studies, however, remains elusive, despite being an ideal nucleus to study since oxygen is directly involved in hydrogen bonding and dictates how secondary and tertiary protein structures will form. Not only does it provide important structural information, the corresponding functions of peptides and proteins are fine-tuned by their hydrogen bonding abilities. Use of oxygen-17 ($^{17}$O) NMR to study the structure of biomolecules is rare due to a range of issues and only recently gained traction due to advances in ultrahigh-field magnets.[8-12] However, with a chemical shift range of over 1000 ppm, it is highly sensitive to chemical environments. The struggle occurs due to a combination of unfavourable $^{17}$O NMR properties including a low gyromagnetic ratio ($\gamma = -5.774$

MHz T$^{-1}$), resulting in low NMR receptivity and sensitivity observed in the corresponding spectra. Also, $^{17}O$ is a quadrupolar nucleus ($I = 5/2$), with a sizable quadrupole moment[13-15] that causes broad NMR resonances and distinct lineshapes brought upon by the residual second-order quadrupolar broadening. Finally, $^{17}O$ has a low natural abundance (0.037 %), which means that costly isotopic enrichment is needed to perform NMR experiments. While overcoming the first two issues is aided by performing $^{17}O$ NMR experiments at ultrahigh magnetic fields (B$_0$ ≥ 21.1 T) as the second-order quadrupolar broadening scales inversely with magnetic field strength, the issue of low natural abundance continues to plague spectroscopists. This has spurred interest in finding effective and cost-efficient ways to isotopically enrich samples of focus.

Traditionally, an acid-catalyzed exchange reaction is used to $^{17}O$ enrich amino acids by heating the sample of interest in the presence of a strong acid and an excess of H$_2$$^{17}O$.[16] While yield efficiencies ranged from 50 – 85 % of maximum enrichment, the reaction conditions were quite harsh (elevated temperatures and strong acids), costly (need for an excess of H$_2$$^{17}O$), time consuming (reaction times upward to days), and ineffective for protected amino acids or proteins. An alternative procedure that was first introduced for $^{18}O$-enrichment of protected-amino acids in 2010 and then implemented for $^{17}O$-enrichment was a multiple-turnover reaction.[8,17-19] This one-pot reaction was performed under mild conditions using a carbodiimide to selectively activate and hydrolyze the carboxylic acid of interest, resulting in $^{17}O$/$^{18}O$ enrichment efficiencies of > 95 %. Despite the high % enrichment and ideal reaction conditions in comparison to the traditional acid-catalyzed reaction, the procedure is time consuming, needing upward of 24 hrs in-between each carbodiimide addition and thus multiple day reactions. A fast and environmentally friendly mechanochemical enrichment procedure was introduced in 2017[20], using ball milling (BM) and small amounts of solvent to enrich both organic and inorganic compounds. Not only did each synthesis take < 2 hrs to perform but small amounts of 41 % H$_2$$^{17}O$ were needed to enrich their samples, thus making the BM approach very advantageous. However, a caveat to this method is that the % enrichment was lower compared to the traditional acid-catalyzed or multiple-turnover reaction techniques (10 % for BM vs. 80 and 100 % for acid-catalyzed and multiple-turnover reaction techniques, respectively). While in cases of inorganic materials where smaller quadrupolar coupling constants (< 7 MHz) are found and a have surplus of oxygen sites, low % enrichment does not pose as serious of an issue. For biomolecules where interest lies at specific positions, such as terminal carboxylic acid sites and hydroxyl residues on tyrosine or amide positions along the

protein backbone, a higher % enrichment is critical. Recent advances in NMR hardware also help address issues of low % enrichment. This includes dynamic nuclear polarization (DNP) to boost overall sensitivity and ultrahigh fields (1500 MHz, $^1$H / 35 T) to slowly remove limitations faced by $^{17}$O NMR spectroscopy.[11,14,15,21–28]

Stemming from the issues that plague the accessibility of $^{17}$O NMR spectroscopy for biomolecules, we set our focus on identifying an ideal $^{17}$O enrichment scheme that would decrease the reaction times needed and would, importantly, maintain the highest enrichment efficiencies. Using an optimized, cost-effective procedure, three fluorenylmethyloxycarbonyl (Fmoc)-protected amino acid precursors, Fmoc-methionine-OH (Fmoc-Met-OH), Fmoc-leucine-OH (Fmoc-Leu-OH), and Fmoc-phenylalanine-OH (Fmoc-Phe-OH) were investigated using $^{17}$O NMR spectroscopy and then used to prepare site-specific labelled N-acetyl-MLF-OH and its sister form, N-formyl-MLF-OH, a well-studied chemotactic tripeptide. Also, we discuss advantages and considerations for the use of population transfer techniques, DNP, and cross-polarization magic-angle spinning (CPMAS) cryoprobe instrumentation to boost NMR sensitivity.

## 6.2 Experimental Section

### 6.2.1 Materials and Methods

Fmoc-amino acids (Fmoc-methionine, Fmoc-Met-OH; Fmoc-leucine, Fmoc-Leu-OH; Fmoc-phenylalanine, and Fmoc-Phe-OH), 1-ethyl-3-(3-dimethylaminopropyl)carbodiimide hydrochloride (EDC•HCl) and acetonitrile (ACN) were purchased from Sigma-Aldrich and used without any further purification. Pyridine hydrobromide (pyridine HBr) was purchased from Alfa Aesar and used without any further purification. All solvents were reagent grade and used as received. Oxygen-17 labelled water (40 % $H_2$$^{17}$O) was sourced from CortecNet.

### 6.2.2 Preparation of $^{17}$O-labelled Building Blocks

Oxygen-17 labelled Fmoc-amino acids were prepared using a modified multiple-turnover procedure.[8,17] First 1 equiv. of Fmoc-amino acid and 20 equiv. of pyridine HBr were suspended in minimal dimethylformamide (DMF, ~ 5 mL). The reaction mixture was stirred and purged with $N_2$ gas for 10 minutes. Afterward, 10 equiv. of EDC•HCl, along with 30 equiv. 40 % $H_2$$^{17}$O was added to the reaction mixture and was stirred under a $N_2$ atmosphere at room temperature for 2 hours. The reaction mixture was then supplemented with 10 equiv. EDC•HCl and stirred for an additional

2 hours. This was repeated once more and was left for 2 hours (note that the reaction can be left overnight and worked up the following day) for the reaction to reach completion. The reaction mixture was quenched with ~ 25 mL of ethyl acetate and dried with $MgSO_4$, before being washed three times with 0.1 M citric acid (~ 15 mL) and once with 0.1 M citric acid in brine (~ 15 mL). A liquid-liquid extraction with ethyl acetate was then used to purify the $^{17}O$-labelled Fmoc-amino acids, and the excess solvent was removed by slow evaporation. The $^{17}O$-labelled Fmoc-Met-OH, -Leu-OH, and -Phe-OH were recrystallized using ACN/water, ethanol, and DCM/water, respectively.

### 6.2.3 Peptide Synthesis of N-formyl-MLF-OH & N-acetyl-MLF-OH

Peptides were synthesized manually according to previously published solid-phase synthesis protocols[29] using Fmoc-protected L-amino acids purchased from Aapptec and the corresponding $^{17}O$-labelled Fmoc-amino acid. Peptides were elongated by sequential Fmoc deprotection on Wang resin. Synthesis was carried out using 3 equiv. of Fmoc-protected amino acids and coupling was performed with HBTU/HOBt and DIPEA in DMF. Fmoc cleavage was performed using 20 % piperidine in DMF. A capping step was carried out after the ligation of the first amino acid using acetic anhydride and pyridine in DMF. When required, peptide amino-terminal functions were acetylated through a final acetylation step using acetic anhydride and DIPEA in DMF. Peptides were cleaved from the resin after incubation with a TFA solution containing 2.5 % triisopropylsilane and 2.5 % water. The peptides were precipitated in a cold diethyl ether and petroleum ether mixture (70:30 v/v), and then recovered by centrifugation. The remaining ether traces were evaporated under vacuum. All reagents used were purchased from Sigma-Aldrich unless otherwise stated.

### 6.2.4 High-performance Liquid Chromatography (HPLC)

Analytical reverse-phase high-performance liquid chromatography (HPLC) was used to determine the multiple turnover-reaction time by monitoring the EDC•HCl concentration profile, and to determine the concentration of N-acylurea based on variations on pyridine HBr and water concentrations. The reaction conditions and concentrations for determining the multiple turnover-reaction time were adapted from Keeler et al.[8]: 10 mM Fmoc-Phe-OH (1 equiv.), 100 mM EDC•HCl (10 equiv.), 200 mM pyridine HBr (20 equiv.), and 450 mM water (45 equiv.). The concentrations of Fmoc-Phe-OH and EDC•HCl for determining the formation of N-acylurea with

125

change in pyridine HBr and water concentrations were 10 mM (1 equiv.) and 100 mM (10 equiv.), respectively.

## 6.2.5 Reverse-phase High-performance Liquid Chromatography and Mass Spectrometry (HPLC-UV-MS)

The $^{17}O$ labelling of each Fmoc-amino acid and labelled N-formyl-MLF-OH was verified by mass spectrometry. RP-HPLC-MS was performed using an Agilent 1200 SL HPLC System with a Phenomenex Polar C18 reverse-phase analytical column (2.1 x 50 mm, 1.7 μm particle size, 100 Å) (Phenomenex, Torrance, CA, USA) and thermostated at 50 °C followed by mass spectrometric detection.

An aliquot was loaded onto a column at a flow rate of 0.50 mL min$^{-1}$ and an initial buffer composition of 99 % mobile phase A (0.1 % formic acid in $H_2O$) and 1 % mobile phase B (0.1 % formic acid in ACN) and held for 30 seconds to wash away salts. Analytes were eluted using a linear gradient from 1 to 95 % mobile phase B over a period of 5 minutes and held at 95 % mobile phase B for 1 minute to remove all analytes from the column and 95 to 1 % mobile phase B over a period of 30 seconds.

Mass spectra were acquired in negative mode of ionization using an Agilent 6220 Accurate-Mass TOF HPLC/MS system (Santa Clara, CA, USA) equipped with a dual sprayer electrospray ionization source with the second sprayer providing a reference mass solution. Mass spectrometric conditions were drying gas 10 L/min at 325 °C, nebulizer 30 psi, mass range 100-1100 Da, acquisition rate of ~ 1.03 spectra/s, fragmentor 140 V, skimmer 65 V, capillary 3200 V, and instrument state 4 GHz high resolution. Mass correction was performed for every individual spectrum using peaks at m/z 112.9856 and 1033.9881 from the reference solution. Data acquisition was performed using the Mass Hunter software package (ver. B.04.00.). Analysis of the HPLC-UV-MS data was done using the Agilent Mass Hunter Qualitative Analysis software (ver. B.07.00 SP2).

## 6.2.6 Solid-state Nuclear Magnetic Resonance (NMR) Spectroscopy

Oxygen-17 NMR spectra were acquired at a magnetic field strength of 14.1 T (600 MHz, $^1H$) with a Bruker Avance NEO spectrometer and a 3.2 mm triple resonance ($^1H$/X/Y) NMR probe, where X was tuned to $^{17}O$ ($\omega_0/2\pi = 81.3$ MHz). All $^{17}O$ experiments were performed under a MAS frequency of 23.5 kHz using the Hahn-echo pulse sequence ($\gamma B_1/2\pi$ (solid) = 158 kHz) and a

recycle delay of 1.0 s. Non-spinning $^{17}$O NMR experiments were preformed using a Hahn-echo pulse sequence with TPPM $^1$H decoupling[30] ($\gamma B_1/2\pi$ = 50.0 kHz) and a recycle delay time of 1.0 s. A double-frequency sweep (DFS)[31] over 1750 to 300 kHz was used for the population transfer techniques. $^{17}$O NMR spectra were acquired between 4k to 393k co-added transients. All $^{17}$O NMR spectra were referenced at 0 ppm with respect to liquid water.[32]

## 6.2.7 Dynamic Nuclear Polarization Nuclear Magnetic Resonance (DNP NMR) Spectroscopy of 40 % $^{17}$O-enriched Fmoc-Leu-OH

The $^{17}$O-labelled Fmoc-Leu-OH sample was packed into a 3.2 mm zirconia rotor with the addition of 10 mM TEKPol biradical / 1,1,2,2-tetrachloroethane (TCE) solution. The sample was stirred with a wire to encourage radical dispersion before being capped with a silicone rubber plug and zirconia top cap. Cross-polarization (CP)[33] $^{17}$O{$^1$H} DNP MAS NMR spectra were recorded using a low-temperature 3.2 mm double resonance (HX) MAS DNP probe doubly tuned to $^1$H ($\omega_0/2\pi$ = 600.5 MHz) and $^{17}$O ($\omega_0/2\pi$ = 81.4 MHz) with a 14.1 T Bruker Avance III HD DNP NMR spectrometer equipped with a 395 GHz gyrotron microwave source delivering high-power microwaves to the sample. DNP NMR data were acquired at 108 K, with magic-angle spinning at a spinning frequency of 12 kHz, a contact time of 1.0 ms, a recycle delay of 20 s, and 2048 co-added transients. Spectra were referenced with respect to the $^{17}$O signal of liquid water (0 ppm).[32] The NMR magnetic field position was adjusted to the maximum of the $^1$H (nitroxide biradical, TEKPol) DNP NMR enhancements.

## 6.2.8 Cross-polarization Magic-angle Spinning (CPMAS) Cryoprobe Nuclear Magnetic Resonance Spectroscopy of 40 % $^{17}$O-enriched Fmoc-Leu-OH

Oxygen-17 NMR spectra of $^{17}$O-labelled Fmoc-Leu-OH were acquired using a 3.2 mm CPMAS cryoprobe at 18.8 T (800 MHz, $^1$H). All data were acquired under magic-angle spinning with a spinning frequency of 15 kHz. The 1D $^{17}$O Hahn-echo experiment was performed with a $\gamma B_1/2\pi$ (solid) = 192 kHz pulse, frequency-swept TPPM $^1$H decoupling[34] ($\gamma B_1/2\pi$ = 70.0 kHz), 4096 co-added transients and a recycle delay of 1 s. A two-dimensional $^{17}$O{$^1$H} HETCOR experiment was undertaken using a $^1$H recycle delay of 4 s, contact time of 1.5 ms, 128 co-added transients, and 120 $t_2$ increments.

## 6.3 Results and Discussion

### 6.3.1 Kinetics

Selectively labelled amino acids are known to be notoriously difficult to prepare and are very costly. In 2010, a mild and selective reaction for $^{18}$O isotopically labelling amino acids was developed, namely, the non-equilibrium multiple-turnover reaction (Scheme 6.1), which is performed at room temperature under less acidic conditions.[17] This method allowed for the exchange of $^{18}$O water with the carboxylic acid due to the hydrolysis of the *O*-acylisourea intermediate formed when a carboxylic acid reacts with a carbodiimide. While this one-pot reaction results in high $^{18}$O enrichments for both oxygen sites of the carboxylic acid aiding vibrational and mass spectrometry studies, an excess of the coupling reagent (carbodiimide such as EDC) and $H_2^{18}O$, as well as long reaction times are needed to allow for high enrichments. We set out to determine whether we can optimize the more costly ($120 USD/g $H_2^{18}O$ (98 %) vs. $2500 USD/g $H_2^{17}O$ (90 %)) $^{17}$O labelling process needed for NMR studies by targeting a reduction in labelled material (40 % $H_2^{17}O$) and minimizing the turnover reaction time.
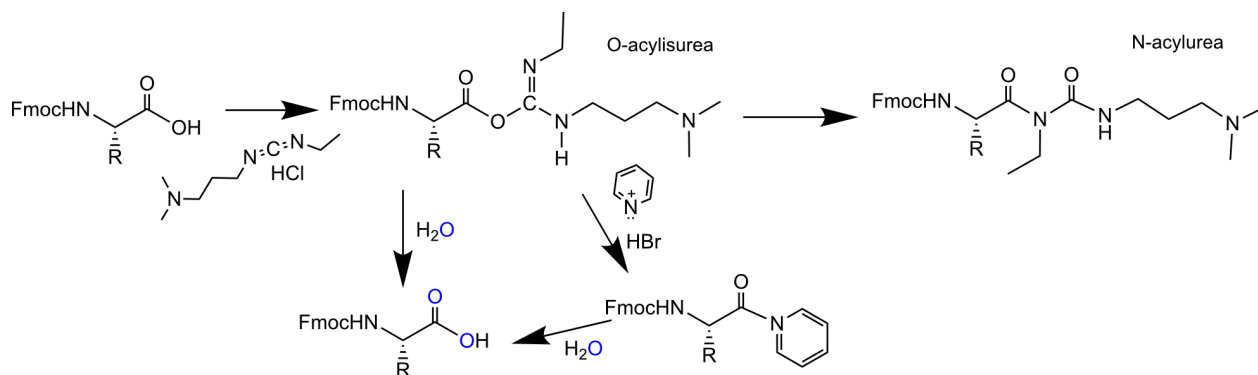


**Scheme 6.1.** Reaction scheme of the carbodiimide-driven chemical multiple-turnover reaction cycle, where Fmoc = fluoroenylmethyloxycarbonyl and R = amino acid side chain.

Our first task was to determine the reaction time needed for the exchange to occur. Previously[8,17], the labelling protocol was a multi-day process where ~ 10 equiv. of EDC was added after every 18 - 24 hours until a total of 45 equiv. of the coupling reagent was reached. This led to reaction times of ~ 4 days without including the time needed for product isolation and recrystallization. To test the amount of time needed between each coupling reagent addition, we used analytical reverse-phase HPLC to monitor the rate of EDC consumption. Since the carbodiimide reacts more rapidly with the carboxylic acid than with water, we know that the rate of reaction is based on the rate of consumption to form the *O*-acylisourea, which then rapidly reacts

with the water to form the labelled amino acid of choice. Following the standard reaction concentrations[8] (10 mM amino acid, 20 mM pyridine HCl, 30 mM EDC, and 45 mM $H_2O$), we determined that all EDC was consumed within 20 minutes of addition, and it had a half-life ($t_{1/2}$) of 4.4 min (Figure 6.1a). Thus, we were able to decrease the reaction time from ~ 98 to < 8 hrs (where 2 hrs was needed in between each addition of the coupling reagent). While we were able to decrease the reaction time by a factor of ~ 10, we further assessed if we could reduce overall costs of the labelling by using minimal amounts of isotopically labelled water to obtain high enrichments. Typically, an excess of $H_2^{17/18}O$ (three to five-fold) is needed to allow for effective labelling. However, we have determined that a 1:1 ratio of EDC to $H_2^{17/18}O$ (40 % $H_2^{17}O$) can be used for effective labelling before high amounts of unwanted byproduct (*N*-acylurea) are formed (Figure 6.1b). This new finding significantly reduces cost from ~ $110 USD/100 mg of amino acid to ~ $25 USD/100 mg, leading to a quick and inexpensive labelling method for [17]O-labelled Fmoc-amino acids.
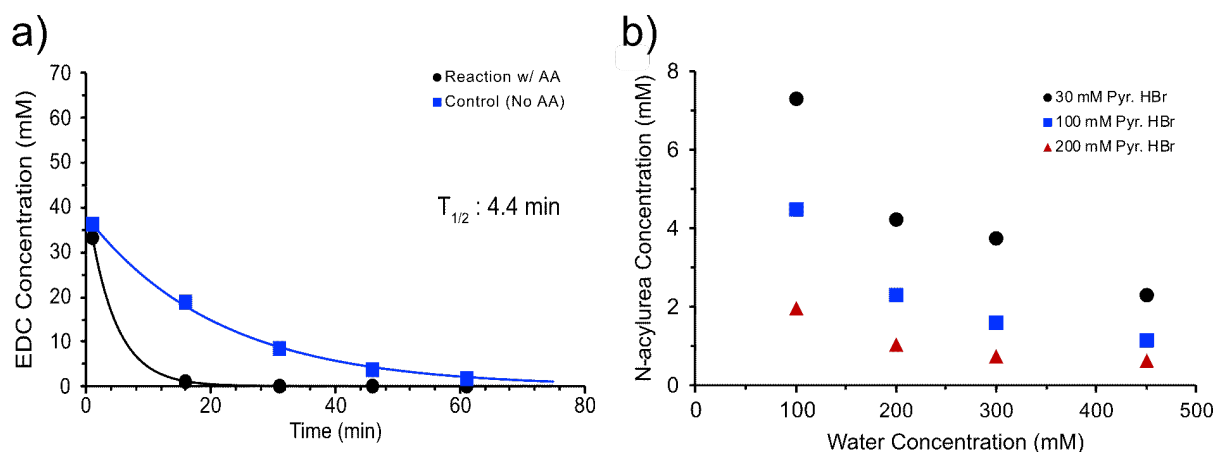


**Figure 6.1.** Kinetic testing of the enrichment of [17]O in 10 mM Fmoc-Phe-OH by a multiple-turnover reaction cycle. (a) Consumption of EDC as a function of time. Markers represent measured data (black circles, full reaction scheme with amino acid (AA) and blue squares, control with no AA added) and the solid line represents data predicted by our kinetic model. (b) Maximum yield of the N-acylurea side product as a function of the amount of pyridine HBr added.

### 6.3.2 Fmoc-Met-OH, Fmoc-Leu-OH & Fmoc-Phe-OH Building Blocks

As a proof of concept, using the modified labelling scheme, *vide supra*, Fmoc-Met-OH, Fmoc-Leu-OH and Fmoc-Phe-OH were [17]O-enriched (both sites at 40-42 %) and verified using reverse-phase HPLC and mass spectrometry (Figure 6.2). During the labelling process, we noted that the 40 % $H_2^{17}O$ water had high levels of $H_2^{18}O$ (~ 44.6 %). This resulted in fragment patterns

129

that strayed from the typical pattern seen for the 40 % $^{17}$O-labelled product (the resulting fragment patterns suggest > 40 % $^{17}$O labelling). However, after taking into consideration $^{18}$O incorporation in the amino acids, the labelling efficiency of the modified multiple-turnover reaction was determined to be 100 % (i.e., 40 % $^{17}$O labels at both oxygen sites).

The chemical shift interactions are described by the isotropic chemical shift ($\delta_{iso}$), span ($\Omega$), and the skew ($\kappa$).[32,35,36] The quadrupolar lineshape is defined by the quadrupolar coupling constant, $C_Q$, and quadrupole asymmetry parameter, $\eta_Q$. The corresponding $^{17}$O MAS and non-spinning NMR spectra of the Fmoc-amino acid precursors and resulting NMR parameters are featured in Figures 6.3 and Table 6.1, respectively.
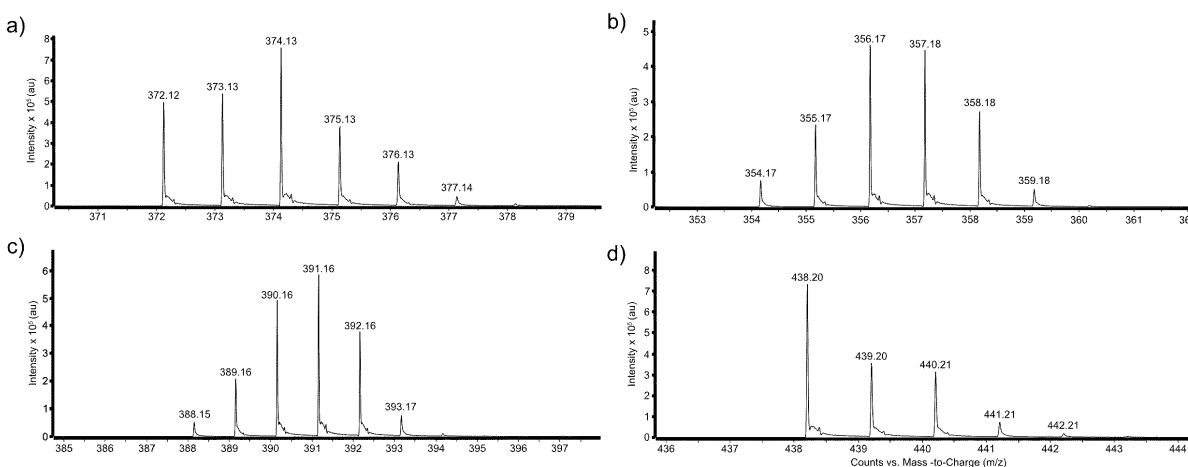


**Figure 6.2.** Experimental mass spectra of $^{17}$O labelled (a) Fmoc-Met-OH, (b) Fmoc-Leu-OH, (c) Fmoc-Phe-OH, and (d) $^{17}$O-enriched Leu of N-formyl-ML*F-OH.
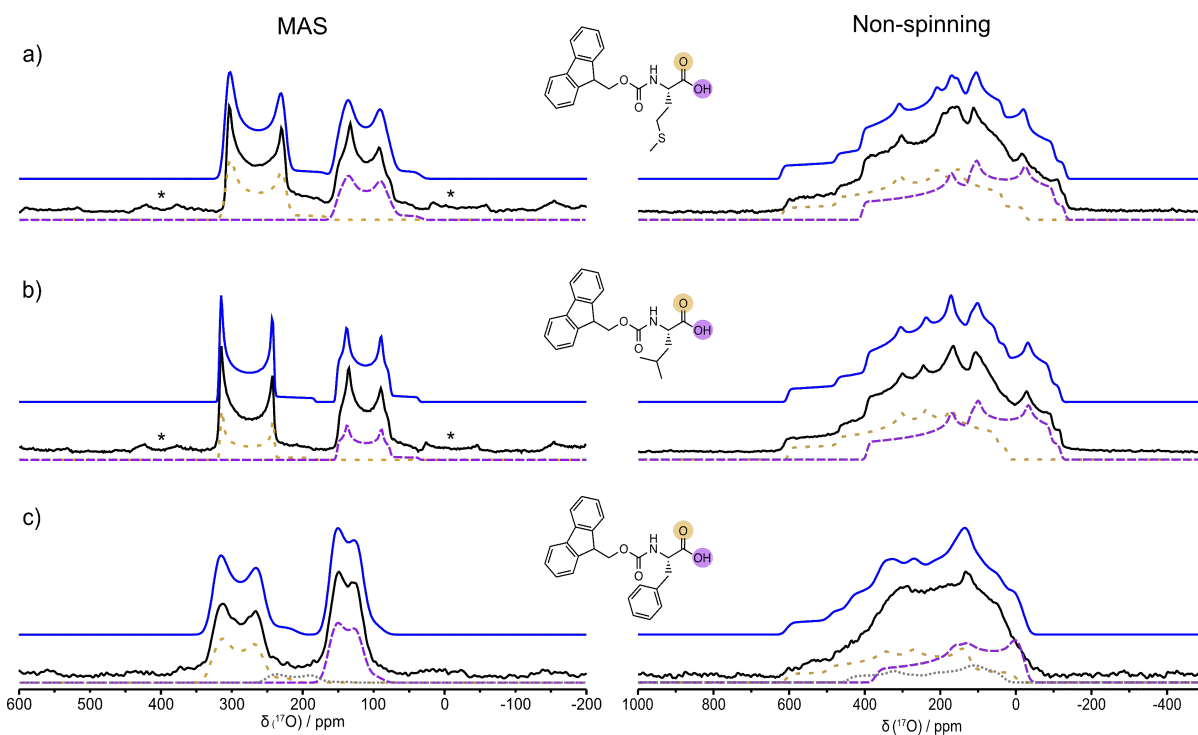
**Figure 6.3.** Experimental (black) and simulated (blue) $^{17}O$ MAS (left) and non-spinning (right) NMR spectra of Fmoc-Met-OH (a), Fmoc-Leu-OH (b), and Fmoc-Phe-OH (c) at 14.1 T ($\omega_{0H}/2\pi$ = 600 MHz) with the corresponding chemical structures (inset) highlighted with the oxygen-enriched site of interest (yellow: CO and purple: COH). The simulations of each oxygen environment are shown below the spectra (short yellow dashes: CO, long purple dashes: COH, grey dots: CO$^-$). Spectra on the left were acquired under magic-angle spinning (MAS, $\omega_r/2\pi$ = 23.5 kHz), with spinning sidebands noted by asterisks (*). Spectra on the right were acquired under non-spinning conditions with $^1H$ decoupling.

At a high magnetic field strength (14.1 T, $\omega_{0H}/2\pi$ = 600 MHz), resolution between the CO and COH groups was obtained. The $^{17}O$ MAS NMR spectrum of Fmoc-Met-OH is shown in Figure 6.3a. The $C_Q$ values of the CO and COH groups for Fmoc-Met-OH were 8.6 and 7.6 MHz, respectively with $\eta_Q$ = 0.0 and 0.25. The $\delta_{iso}$ values were 330 and 164 ppm, with $\Omega$ = 510 and 235 ppm and $\kappa$ = 0.6 and - 1.0 for the CO and COH groups, respectively. These values are consistent with previous reports of other Fmoc- and Boc-protected amino acids.[8,19,20] The recrystallization of Fmoc-Met-OH proved to be challenging when working with small amounts of starting material. Despite purification with preparatory HPLC and further recrystallization, the corresponding $^{17}O$ NMR spectra resulted in poor resolution between the CO and COH group (Figure 6.4). Thus, we advise that larger amounts of starting material may be needed to effectively recrystallize labelled small molecules into their ideal crystal structure. This is not an issue when using these building blocks to form peptides (below). Since the multiple-turnover reaction mechanism described above

allows for requirements for 40 % $H_2^{17}O$ needed and higher reaction turnover rates, we can label larger yields of challenging amino acids more efficiently and economically.
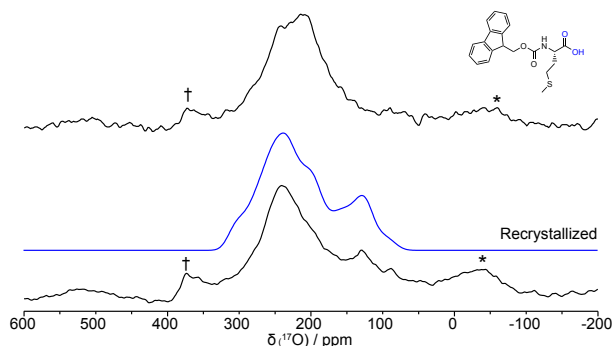


**Figure 6.4.** Experimental (black) and simulated (blue) $^{17}O$ NMR spectra of Fmoc-Met-OH (top) and the above Fmoc-Met-OH sample recrystallized at 14.1 T ($\omega_{0H}/2\pi$ = 600 MHz) with the corresponding chemical structure (inset) highlighted with the oxygen-enriched site of interested. Spectra were acquired under magic-angle spinning (MAS, $\omega_r/2\pi$ = 23.5 kHz), with spinning sidebands noted by asterisks (*). † indicates the signal coming from the $ZrO_2$ rotor.

The $^{17}O$ MAS NMR spectrum of Fmoc-Leu-OH are shown in Figure 6.3b. The NMR parameters for the CO and COH groups were found to be $C_Q$ = 8.3 and 7.5 MHz, $\eta_Q$ = 0.0 and 0.2, $\kappa$ = 0.7 and - 1.0, and $\delta_{iso}$ = 338 and 162 ppm, respectively, and are consistent with the previous reports.[8] We note a small discrepancy for their reported spans of CO and COH groups that were 385 and 320 ppm, respectively, whereas the $\Omega$ values determined in this study are 460 and 230 ppm, respectively. This revised value agrees well with our recent examination of computed $^{17}O$ NMR parameters in a series of Fmoc-amino acids.[19]

The corresponding $^{17}O$ NMR spectrum for Fmoc-Phe-OH is shown in Figure 6.3c. Resolution between CO and COH groups ($\delta_{iso}$ = 341 and 169 ppm, $\Omega$ = 520 and 250 ppm, and $\kappa$ = 0.7 and 0.8) are maintained and are similar to those for both Fmoc-Met-OH and Fmoc-Leu-OH, and the $C_Q$ values of the CO and COH groups were 7.7 and 6.0 MHz, and $\eta_Q$ = 0.1 and 0.1, respectively, are slightly reduced. A previous $^{17}O$ NMR study on related amino acid, N-(tert-butoxycarbonyl)-Phe-OH, BOC-Phe-OH) showed similar parameters for CO and COH groups as those reported here for both Fmoc-Met-OH and Fmoc-Leu-OH.[20] Differences between reported values could be associated with the crystallinity of the sample or molecular dynamics. While Fmoc-Met-OH and Fmoc-Leu-OH both recrystallized into solid white powders, Fmoc-Phe-OH was a white semi-solid, with a gel-like appearance. This suggests that the Fmoc-Phe-OH sample may be experiencing changes in the local environment (H-bonding) and local dynamics about the COOH.[37]

For example, the ^{17}O NMR line shapes drastically change for 4-aminobutane-1-sulfonic acid, resulting in narrowing of line shape and a decrease in the magnitude of the quadrupolar coupling interactions. This is due to the rotational dynamics of the sulfonate groups at higher temperatures.[38] Changes in quadrupolar couplings due to dynamics have also been shown in ^{2}H systems where the vibrational motion of water molecules leads to averaging of quadrupolar couplings.[39,40] In 2016, a reduction in the [17]O quadrupole coupling constant of the bound water in barium chlorate monohydrate ($Ba(ClO_3)_2 \cdot H_2O$) was reported.[41] With decreasing temperature, the observed $C_Q$ was shown to increase and the appearance of [1]H-[17]O dipole couplings emerged due to a reduction in two-fold $H_2O$ hopping dynamics. Nonetheless the hydroxyl and carbonyl carbons observed in the Fmoc-Phe-OH sample are in the appropriate chemical shift range, providing the ability to assemble longer peptides, *vide infra*.

**Table 6.1.** Fmoc-amino acids and N-formyl-MLF-OH tripeptide NMR parameters.

| Sample | [17]O site | $\delta_{iso}$ (ppm, ± 3) | $C_Q$ (MHz, ± 0.1) | $\eta_Q$ (± 0.1) | $\Omega$ (± 50) | $\kappa$ (± 0.1) | $\alpha$ (± 10°) | $\beta$ (± 10°) | $\gamma$ (± 10°) |
|---|---|---|---|---|---|---|---|---|---|
| Fmoc-Met-OH | CO | 330 | 8.6 | 0 | 510 | 0.6 | 0 | 86 | 50 |
| | COH | 164 | 7.6 | 0.25 | 235 | - 1.0 | 0 | 21 | 25 |
| Fmoc-Leu-OH | CO | 338 | 8.3 | 0 | 460 | 0.7 | 0 | 88 | 50 |
| | COH | 162 | 7.5 | 0.2 | 230 | -1.0 | 0 | 22 | 25 |
| Fmoc-Phe-OH | CO | 341 | 7.7 | 0.1 | 530 | 0.7 | 0 | 82 | 50 |
| | COH | 169 | 6.0 | 0.1 | 250 | -0.8 | 0 | 22 | 25 |
| | COO- | 265 | 7.7 | 0.2 | 125 | -1.0 | 0 | 10 | 50 |
| N-acetyl-M*LF-OH | N-CO (Met) | 275 | 8.0 | 0.15 | 460 | 0.8 | 0 | 90 | 45 |
| | amorphous N-CO [†] | 258 | 7.0 | 0.55 | 330 | -0.7 | 0 | 15 | 60 |
| N-formyl-ML*F-OH | N-CO (Leu) | 283 | 7.7 | 0.2 | 520 | 0.7 | 0 | 89 | 78 |
| N-formyl-MLF*-OH | CO | 330 | 8.4 | 0.25 | 700 | 0.55 | 0 | 82 | 50 |
| | COH | 180 | 6.8 | 0.3 | 300 | -0.7 | 0 | 22 | 25 |
| | COO⁻ | 260 | 7.7 | 0.2 | 200 | -0.8 | 0 | 10 | 50 |
| N-formyl-ML*F*-OH | N-CO (Leu) | 290 | 7.7 | 0.2 | 520 | 0.6 | 0 | 89 | 78 |
| | CO | 330 | 8.4 | 0.25 | 730 | 0.45 | 0 | 82 | 50 |
| | COH | 180 | 6.8 | 0.3 | 300 | -0.8 | 0 | 22 | 25 |
| | COO⁻ | 265 | 7.7 | 0.2 | 200 | -0.8 | 0 | 10 | 50 |

[†] Due to the limited sample amount of N-acetyl-M*LF-OH (~ 10 mg), the sample was not recrystallized. This resulted in a mixture of crystalline and amorphous N-acetyl-M*LF-OH

### 6.3.3 Selectively Labelling N-formyl-MLF-OH and N-acetyl-MLF-OH Tripeptides

Building from the single Fmoc-protected amino acid results, we set out to determine the effects of the ^{17}O NMR features on a chemotactic tripeptide, N-formyl-MLF-OH, and its sister form, N-acetyl-MLF-OH. First, we synthesized each peptide using either non-labelled or [17]O-labelled Fmoc-protected amino acids using solid-phase peptide synthesis to yield selectively labelled single amino acid sites (N-acetyl-M*LF-OH, N-formyl-ML*F-OH, and N-formyl-MLF*-OH, where * indicates the [17]O position within the peptide) to compare with the single Fmoc-protected amino acids. When Met is incorporated into N-acetyl-M*LF-OH, a single [17]O site corresponding to the $NCO_{Met}$ ($\delta_{iso} = 275$ ppm, $\Omega = 460$ ppm, $\kappa = 0.8$, $C_Q = 8.0$ MHz, and $\eta_Q = 0.15$) was observed (Figure 6.5a). The NCO site appears at a lower frequency when compared to the free amino acid ($\delta_{iso} = 275$ ppm vs $\delta_{iso} = 330$ ppm). This is expected as the $NCO_{Met}$ no longer loses electron density due to the neighboring OH site in the free amino acid. Due to the limited amount of the tripeptide (~ 10 mg), the labelled sample was not recrystallized, which resulted in a mixture of crystalline and amorphous tripeptides (Table 6.1). Hence, a small secondary site ($\delta_{iso} = 258$ ppm, $\Omega = 330$ ppm, $\kappa = -0.7$, $C_Q = 7.0$ MHz, and $\eta_Q = 0.55$) corresponds to residual amorphous N-acetyl-M*LF-OH. A single [17]O site ($\delta_{iso} = 283$ ppm, $\Omega = 520$ ppm, $\kappa = 0.7$, $C_Q = 7.7$ MHz, and $\eta_Q = 0.2$) was observed for N-formyl-ML*F-OH (Figure 6.5b). Similar to the $NCO_{Met}$ site in N-acetyl-M*LF-OH, the $NCO_{Leu}$ in N-formyl-ML*F-OH appears at a lower frequency compared to the free amino acid ($\delta_{iso} = 283$ ppm vs. $\delta_{iso} = 338$ ppm). This is expected as only the single NCO site of the Leu in the tripeptide is labelled. The ^{17}O MAS NMR spectrum of N-formyl-MLF*-OH is shown in Figure 6.5c. The $C_Q$ values of the CO and COH groups were found to be 8.4 and 8.6 MHz, with $\eta_Q = 0.25$ and 0.25, respectively. The $\delta_{iso}$ values of the CO and COH groups were found to be 330 and 175 ppm, with $\Omega = 700$ and 300 ppm, and $\kappa = 0.55$ and -0.7, respectively. A third minor site (< 5 %) at $\delta_{iso} = 230$ ppm was observed between the CO and COH sites and corresponds to a deprotonated $COO^-$ at the c-terminus.[19] The variation in chemical shift and quadrupolar coupling between amino acids and peptides observed here reinforce the sensitivity of ^{17}O NMR to the functional group and structure.

A natural extension beyond site-specific labels in peptides provides the ability to place multiple labels. Thus, we synthesized N-formyl-ML*F*-OH using [17]O-enriched Fmoc-Leu-OH and Fmoc-Phe-OH resulting in both the Leu and Phe sites being [17]O-enriched to 40 % (Figure 6.5d). Four distinct oxygen environments were found for the N-formyl-ML*F*-OH tripeptide, one on

leucine (NCO) and three on phenylalanine (CO, COO⁻, and COH). The resulting NMR parameters ($\delta_{iso}$, $\Omega$, $\kappa$, $C_Q$, and $\eta_Q$) for each distinct oxygen site were within the error to those observed in the selectively labelled tripeptide (Table 6.1). As expected, the multiple-labelled oxygen sites within the peptide structure do not change (within error) the NMR parameters. This adaptable labelling approach developed here enables researchers to take on multiple labelling strategies for further biomolecular NMR experimentation by maximizing structural model constraints.
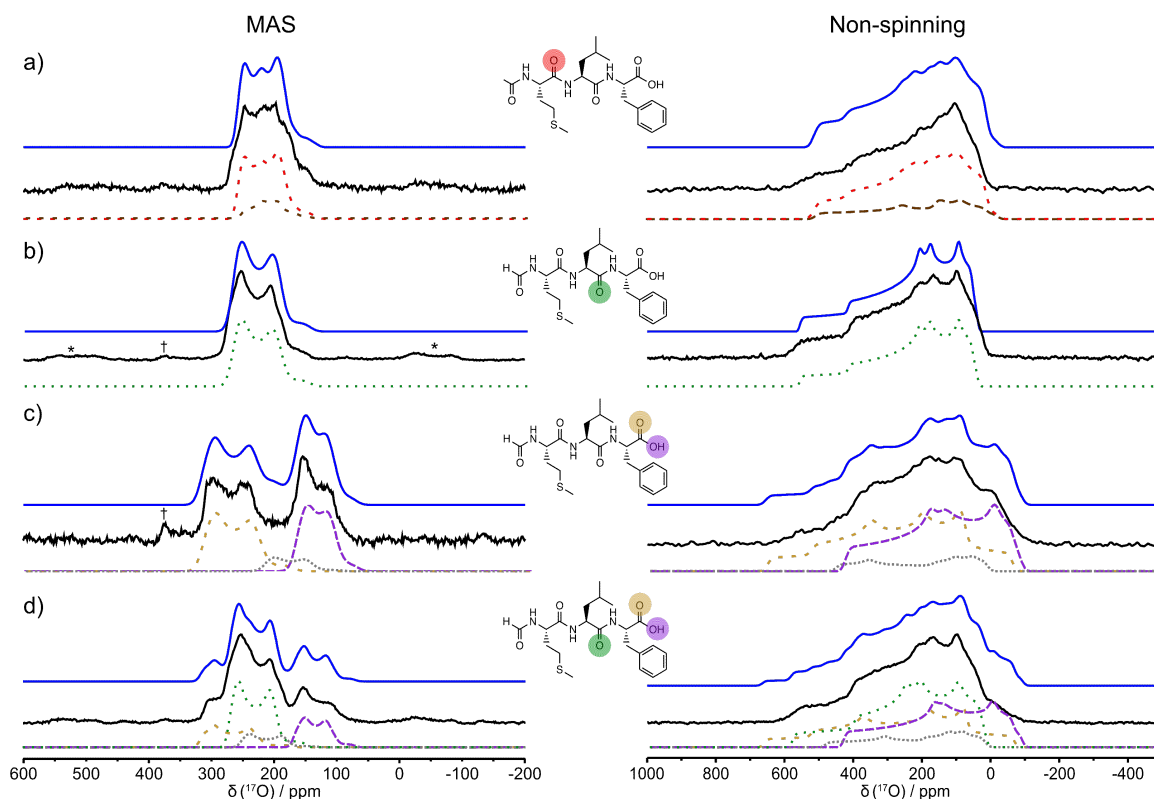


**Figure 6.5.** Experimental (black) and simulated (blue) ¹⁷O MAS (left) and non-spinning (right) NMR spectra of (a) ¹⁷O-enriched Met of N-acetyl-M*LF-OH, (b) ¹⁷O-enriched Leu of N-formyl-ML*F-OH, (c) ¹⁷O-enriched Phe of N-formyl-MLF*-OH, and (d) ¹⁷O-enriched Leu and Phe of N-formyl-ML*F*-OH at 14.1 T ($\omega_{0H}/2\pi = 600$ MHz). The simulations of the individual oxygen environments are shown below the full spectra with the chemical structures (inset) highlighted with the oxygen-enriched site of interest (orange: CO of Met, brown: amorphous Met, green: CO of Leu, yellow: CO of Phe, and purple: COH of Phe). Spectra on the left were acquired under magic-angle spinning (MAS, $\omega_r/2\pi = 23.5$ kHz) conditions, with spinning sidebands denoted by asterisks (*). Spectra on the right were acquired under non-spinning conditions with ¹H decoupling. The N-acetyl-M*LF-OH sample was acquired using a DFS population transfer with ~ 10 mg of sample; all N-formyl-MLF-OH samples utilized the Hahn-echo pulse sequence. † indicates the signal coming from the ZrO2 rotor.

### 6.3.4 Maximizing NMR Sensitivity

Above, we have developed a fast, inexpensive, and effective labelling approach for studying increasingly complex peptides. To further extend sensitivity gains, which will be essential in establishing $^{17}O$ as a viable biomolecular probe nucleus, we assess emerging NMR sensitivity methods and consider a few advantages and disadvantages observed for 40 % $^{17}O$-labelled Fmoc-Leu-OH (Table 6.2) as a model system.

**Table 6.2.** Sensitivity enhancements in 40 % $^{17}O$-labelled Fmoc-Leu-OH using various NMR techniques.

| Method | Field Strength (MHz) | Sample Amount (mg) | S/N | Number of Scans | Experimental Time (min) | S/N / mg /$\sqrt{scans}$ / $B_0$ (x $10^{-3}$) |
|---|---|---|---|---|---|---|
| Hahn-echo NMR | 600 | 21 | 12.85 | 4096 | 68.3 | 0.68 |
| DFS NMR | 600 | 21 | 43.67 | 4096 | 68.3 | 2.30 |
| CPMAS Cryoprobe Hahn-echo | 800 | 18.8 | 62.3 | 4096 | 68.3 | 2.76 |
| DNP CP MAS | 600 | 13 | 31.0 | 2048 | 682.7 | 3.74 |

One way to maximize sensitivity is to use population transfer techniques to improve the S/N of half-integer quadrupolar nuclei. To perform the population transfer, simultaneous saturation of the satellite transitions is needed to transfer the Boltzmann population of these energy levels onto the central transition (CT). This is followed up with a selective $\pi/2$ pulse to perturb the CT and to acquire the spectrum.[22] An example of a population transfer technique is the use of double-frequency sweeps (DFS).[31] This technique uses adiabatic frequency sweeps across the satellite transitions in order to enhance the CT. Using DFS, enhancements ($\varepsilon_{DFS}$) of 1.7 and 2.0 were obtained for the CO and COH NMR features, respectively, in Fmoc-Leu-OH (Figure 6.6a). This resulted in a reduction in experimental time by a factor of 4. Therefore, a non-DFS $^{17}O$ experiment of 40 % labelled Fmoc-Leu-OH that requires 1 hr of continuous acquisition can be completed in 15 min. While the decrease in experimental time is beneficial and accessible on all modern instruments, the experimental setup requires attention. First, a DFS must be generated in the correct

frequency range corresponding to the saturation of the sample's satellite transitions but does not perturb the central transition. This is challenging, as frequency ranges change depending on the sample of interest and the nuclear spin number, $I$. With higher $I$ (such as $I = 5/2$ for $^{17}O$), multiple satellite transitions overlap, thus creating additional complications.[22] In addition to multiple satellite transition overlaps in higher spin numbers, sample systems are in a powder form. This results in a range of angular-dependent quadrupole frequencies for all crystallites and non-ideal adiabatic single-quantum and multiple-quantum transitions that would decrease the maximum theoretical enhancement ($\varepsilon_{DFS} = 5$) that could be achieved.[22]

Dynamic nuclear polarization has been game-changing in the advancement of high-field NMR spectroscopy, allowing for the study of challenging and previously improbable chemical systems.[42] Taking advantage of the large thermal electron spin polarization of paramagnetic radicals irradiated with high-frequency microwaves, this transfer of polarization to neighboring nuclei can allow for a significant reduction in experimental time.[43–45] The gain in NMR sensitivity is quantified by the enhancement factor, $\varepsilon_{DNP}$, which results in a reduction in experimental time by a factor of $\varepsilon^2$. Using 10 mM TEKPol/TCE solution, a DNP-enhanced $^{17}O\{^1H\}$ CP MAS NMR spectrum of $^{17}O$-enriched Fmoc-Leu-OH was obtained at 600 MHz / 395 GHz, resulting in an $\varepsilon_{DNP} = 6$ (Figure 6.6b). This corresponds to a 36-fold reduction in experimental time, under otherwise identical conditions using conventional CP MAS methods at 100 K. Although indirect DNP and direct DNP have been successful in ice and inorganic hydroxides[26,41,46], we were unable to obtain an enhancement using a direct approach and thus refrain from comparing to the Hahn-echo results discussed above. The inability to enhance $^{17}O$ via direct polarization is attributed to low oxygen density, short nuclear spin-lattice relaxation times and low-gamma properties, limiting the ability to build-up bulk nuclear spin polarization.[47–50] Another important consideration in comparing the Hahn-echo results discussed above is the drastically different NMR lineshape obtained using indirect DNP. When CP is used to study quadrupolar nuclei, typically distorted lineshapes result due to poor spin-locking and the fast decay of the quadrupolar spins, which is needed to build up the CP signal.[51] Not only does it become difficult to analyze the resulting spectra, but the signal-to-noise gains are lower in comparison to direct approaches.[52,53] Although the indirect DNP method used here showed good DNP enhancements, we refrain from directly comparing the Hahn-echo results due to the distorted lineshapes. Additionally, there was preferential enhancement of the COH over the CO site due to the proximity of the $^1H$ to $^{17}O$ nuclei. One technique that has been

used to overcome the poor spin dynamics associated with CP of quadrupolar nuclei is Phase-shifted Recoupling Effects a Smooth Transfer of Order (PRESTO).[54–56] This polarization transfer technique uses a selective Hahn-echo pulse on the single central transition of the quadrupolar nuclei, coupled with symmetry-based recoupling sequences on the protons, resulting in improvements in sensitivity and lineshape. Beyond these distortion issues, the $^{17}$O spectral lineshape is further influenced by cryogenic temperatures (< 110 K), which requires additional considerations, such as spinning frequency, dynamics, relaxation time, etc. The cryogenic temperatures used here restricted the spinning frequencies obtainable for a conventional 3.2 mm rotor (i.e., a smaller rotor is required to reach 23.5 kHz at cryogenic temperatures); thus our ability to resolve two signals at 12 kHz at 14.1 T is hampered in this model system, although it could easily be improved with a 1.9 mm probe or strategic labelling. Cryogenic sample temperatures increase the nuclear spin-lattice relaxation time and are particularly harsh for small crystalline molecules. Using CP, where relaxation is dependent on $^{1}$H, the $^{17}$O-labelled Fmoc-Leu-OH required a delay of 20 s for the DNP experiment (vs. 1.0 s delays for direct detection as quadrupolar relaxation dominates). Again, these issues are sample and nucleus dependent ($^{1}$H relaxation is typically a few seconds for larger peptides and proteins) but should be considered when striving to optimize the sensitivity and experimental approach. Despite these issues, the sensitivity was quite remarkable using DNP to perform challenging $^{17}$O{$^{1}$H} CP MAS DNP NMR experiments as shown in Table 6.2.

While DNP can provide tremendous sensitivity gains, it does require specialized hardware (DNP spectrometer, cryogenic probe, microwave source, polarizing agents, etc.). Cryoprobes in solution NMR applications are now routinely used for biomolecular systems. Due to the sample coil and electronics being cooled to cryogenic temperatures, the background thermal noise is significantly reduced and results in sensitivity gains over conventional room-temperature NMR probes. Recently, a cryogenic MAS probe was commercially introduced, allowing for the study of complex biological solids. In 2020, a three-to-four-fold sensitivity enhancements for 1D NMR experiments on large, non-crystalline biological assemblies were reported when using a CPMAS cryoprobe.[57] This sensitivity enhancement provided the ability to perform multidimensional experiments on $^{13}$C, $^{15}$N-labelled protein fibrils, and $^{15}$N-labelled samples with natural abundance carbon sites, a feat that would be unimaginable with a conventional room-temperature probe. Using a CPMAS cryoprobe at 18.8 T ($\omega_{0H}/2\pi$ = 800 MHz), a $^{17}$O Hahn-echo spectrum of 40 % $^{17}$O-labelled Fmoc-Leu-OH was acquired (Figure 6.6a). While we were able to obtain better resolution

between the CO and OH sites due to a decrease in second-order quadrupolar broadening (18.8 vs. 14.1 T), spinning sidebands are not resolved from the CT, due to the associated hardware limitations and magnetic shielding anisotropy present for $^{17}O$ (similar issues arise at 35 T, as this interaction scales with magnetic field strength). Regardless, the advantages in the sensitivity of the CPMAS cryoprobe are clear with the overall sensitivity being 4.0 times larger than those obtained using an identical approach on a standard MAS probe (Table 6.2).

Building upon impressive sensitivity gains and resolution obtained in the 1D CPMAS cryoprobe NMR experiments, we performed a 2D $^{17}O\{^1H\}$ HETCOR experiment of isotopically labelled (40 %, ~ 19 mg) Fmoc-Leu-OH (Figure 6.6c), with resolution between the various $^1H$ features in the fully protonated amino acid. The 2D NMR spectrum clearly reveals a series of intramolecular correlations including the resolved cross-peak between the hydroxyl hydrogen and the $^{17}O$ hydroxyl site ($C^{17}O$-H, purple). Implementing a longer contact time proved to be successful in observing additional intra-molecular and inter-molecular correlations. One particularly distinguishable intermolecular correlation is observed between the amide hydrogen (N-$^1H$) with the carbonyl oxygen (C=$^{17}O$) of the neighboring molecule (blue oval, Figure 6.6c). This is a critical hydrogen bond ($C^{17}O$---HN, bond distance = 2.23 Å) that guides the molecular packing and long-range crystal structure. Additionally, given the alternating packing of the Fmoc-Leu-OH within the unit cell, the correlations between Fmoc $^1H$'s and the two oxygen sites are also due to intermolecular interactions (bond distances ranging from 2.94 – 3.92 Å). The ability to combine high-quality multidimensional NMR with CPMAS cryoprobe technology in conjunction with low sample quantities demonstrates rising potential for studying large biomolecular systems and challenging NMR-active nuclei.
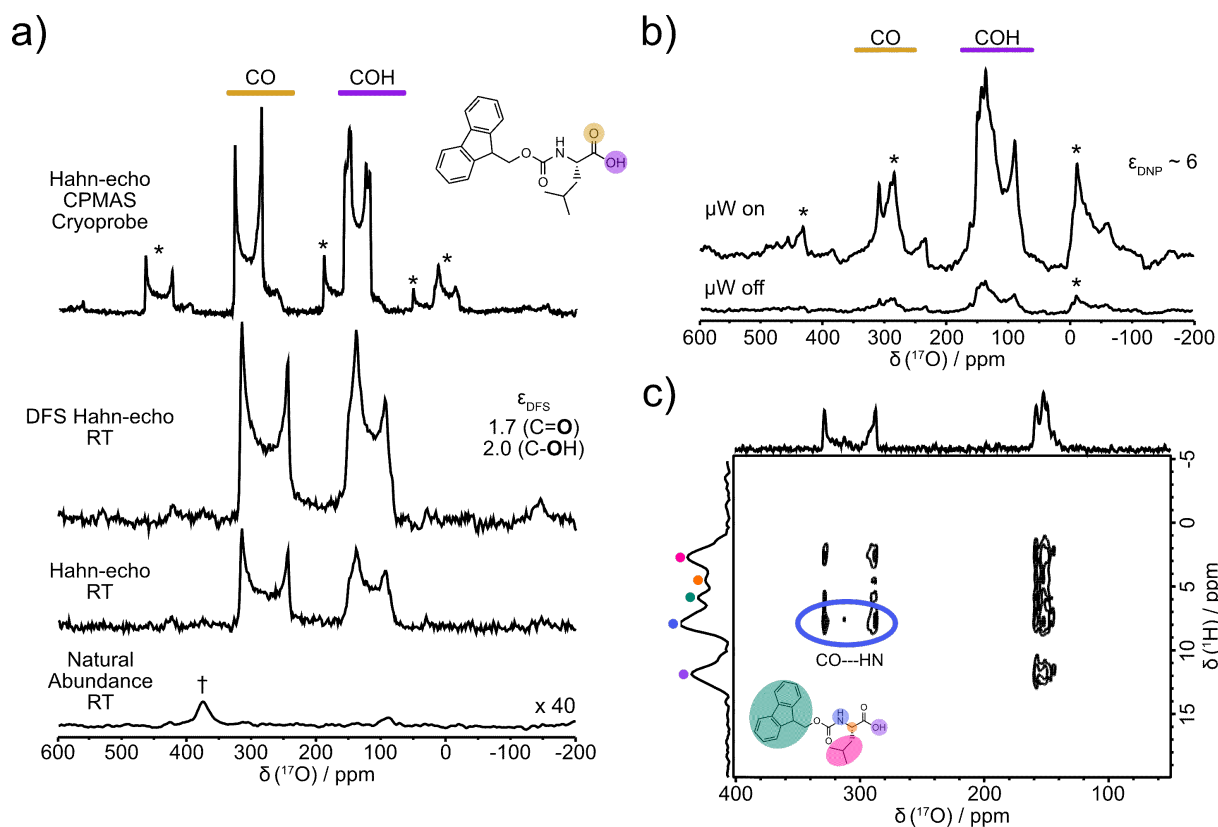
**Figure 6.6.** (a) Experimental $^{17}O$ NMR spectra of 40 % $^{17}O$-enriched Fmoc-Leu-OH acquired over a period of 1.1 hrs with a Hahn-echo pulse sequence using a CPMAS cryoprobe at 18.8 T ($\omega_{0H}/2\pi$ = 800 MHz) and a DFS pulse and Hahn-echo pulse sequence at 14.1 T ($\omega_{0H}/2\pi$ = 600 MHz). The corresponding natural abundance $^{17}O$ NMR spectrum of Fmoc-Leu-OH (magnified by 40) shown at the bottom was signal averaged over 3.8 days (91 hours of continuous acquisition). The CPMAS cryoprobe and room temperature spectra were acquired under magic-angle spinning (MAS) conditions of $\omega_r/2\pi$ = 15 and 23.5 kHz, respectively. The chemical structure of Fmoc-Leu-OH (inset) highlighted with the oxygen-enriched site of interest (yellow: CO and purple: COH) is shown. (b) DNP-enhanced ($\mu W_{on}$) and non-DNP-enhanced ($\mu W_{off}$) $^{17}O\{^1H\}$ CP MAS NMR spectra of 40 % $^{17}O$-enriched Fmoc-Leu-OH using 10 mM TEKPol in TCE; an organic solvent was used to maintain crystallinity. Spectra were acquired under magic-angle spinning conditions (MAS, $\omega_r/2\pi$ = 12 kHz), recycle delays of 20 s, and 2048 co-added transients. (c) Two-dimensional $^{17}O\{^1H\}$ HETCOR MAS NMR spectrum of 40 % $^{17}O$-labelled Fmoc-Leu-OH at 18.8 T using a CPMAS cryoprobe and a spinning frequency of 15 kHz. The $^{17}O$-$^1H$ correlation spectrum was acquired with a contact time of 1.5 ms, 128 co-added transients, 120 $t_2$ increments, and recycle delay of 4 s. The structure of Fmoc-Leu-OH is in the inset with the corresponding $^1H$ sites (pink: R-group, orange: α-carbon, green: Fmoc-protecting group, blue: NH, and purple: OH) labelled accordingly. A blue oval is used to highlight the intermolecular correlation between the $^{17}O$ carbonyl oxygen of one molecule and the neighboring amide hydrogen (CO---NH). * indicates spinning sidebands and † indicates the signal coming from the ZrO$_2$ rotor.

## 6.4 Conclusions

A modified fast one-pot, highly efficient $^{17/18}$O labelling procedure using minimal amounts of 40 % H$_2$$^{17/18}$O was developed. With this approach, one can decrease the reaction time by a factor of 10 and a cost reduction by a factor of 4; resulting in the ability to label Fmoc-protected amino acids to maximum enrichment (i.e., 40 % $^{17}$O AA using 40 % $^{17}$O-enriched water) in less than 8 hours. Using the optimized enrichment scheme, Fmoc-Met-OH, Fmoc-Leu-OH, and Fmoc-Phe-OH were isotopically labelled for $0.25 USD/mg. Importantly, this is a breakthrough in inexpensive $^{17}$O labelling. At high magnetic fields (14.1 T), we obtained excellent sensitivity and resolution between the CO and OH sites and $^{17}$O NMR parameters that add to the limited $^{17}$O NMR parameters in the literature for protected amino acids.[8,19,20] We also demonstrate the ability to strategically label peptides using these Fmoc-amino acid building blocks, preparing site-specific labelled N-acetyl-MLF-OH and N-formyl-MLF-OH tripeptides. This efficient process allows for obtaining high-quality $^{17}$O NMR spectra from small sample sizes (10–15 mg) of 40 % $^{17}$O-labelled tripeptides providing a path to determine unique $^{17}$O NMR parameters for carbonyl, carboxylic acid, and deprotonated oxygen chemical environments in peptides. This approach opens new capabilities to use $^{17}$O NMR as a powerful analytical tool in structural model constraints extending beyond conventional $^{13}$C and $^{15}$N NMR studies. This labelling strategy can be extended further when coupled to sensitivity enhancing methods such as population transfer, DNP, or CPMAS cryoprobes. All three approaches, for example, provided substantial time saving over conventional NMR experiments that will maximize our understanding of complex biomolecular solids. Utilizing our optimized labelling protocol and emerging NMR instrumentation, 1D and 2D $^{17}$O NMR experiments can now be performed in minutes to hours utilizing what is a substantial cost-saving approach by minimizing isotopically labelled water, synthesis, and spectrometer time.

## 6.5 References

(1) *NMR of Biomolecules*; Bertini, I., McGreevy, K. S., Parigi, G., Eds.; Wiley-VCH Verlag GmbH & Co. KGaA: Weinheim, Germany, 2012.

(2) Park, S. H.; Yang, C.; Opella, S. J.; Mueller, L. J. Resolution and Measurement of Heteronuclear Dipolar Couplings of a Noncrystalline Protein Immobilized in a Biological Supramolecular Assembly by Proton-Detected MAS Solid-State NMR Spectroscopy. *J. Magn. Reson.* **2013**, *237*, 164–168.

(3)     Su, Y.; Andreas, L.; Griffin, R. G. Magic Angle Spinning NMR of Proteins: High-Frequency Dynamic Nuclear Polarization and [1]H Detection. *Annu. Rev. Biochem.* **2015**, *84* (1), 465–497.

(4)     Penzel, S.; Smith, A. A.; Agarwal, V.; Hunkeler, A.; Org, M.-L.; Samoson, A.; Böckmann, A.; Ernst, M.; Meier, B. H. Protein Resonance Assignment at MAS Frequencies Approaching 100 kHz: A Quantitative Comparison of J-Coupling and Dipolar-Coupling-Based Transfer Methods. *J. Biomol. NMR* **2015**, *63* (2), 165–186.

(5)     Barbet-Massin, E.; Pell, A. J.; Retel, J. S.; Andreas, L. B.; Jaudzems, K.; Franks, W. T.; Nieuwkoop, A. J.; Hiller, M.; Higman, V.; Guerry, P.; Bertarello, A.; Knight, M. J.; Felletti, M.; Le Marchand, T.; Kotelovica, S.; Akopjana, I.; Tars, K.; Stoppini, M.; Bellotti, V.; Bolognesi, M.; Ricagno, S.; Chou, J. J.; Griffin, R. G.; Oschkinat, H.; Lesage, A.; Emsley, L.; Herrmann, T.; Pintacuda, G. Rapid Proton-Detected NMR Assignment for Proteins with Fast Magic Angle Spinning. *J. Am. Chem. Soc.* **2014**, *136* (35), 12489–12497.

(6)     Knight, M. J.; Webber, A. L.; Pell, A. J.; Guerry, P.; Barbet-Massin, E.; Bertini, I.; Felli, I. C.; Gonnelli, L.; Pierattelli, R.; Emsley, L.; Lesage, A.; Herrmann, T.; Pintacuda, G. Fast Resonance Assignment and Fold Determination of Human Superoxide Dismutase by High-Resolution Proton-Detected Solid-State MAS NMR Spectroscopy. *Angew. Chemie Int. Ed.* **2011**, *50* (49), 11697–11701.

(7)     Böckmann, A.; Ernst, M.; Meier, B. H. Spinning Proteins, the Faster, the Better? *J. Magn. Reson.* **2015**, *253*, 71–79.

(8)     Keeler, E. G.; Michaelis, V. K.; Colvin, M. T.; Hung, I.; Gor'kov, P. L.; Cross, T. A.; Gan, Z.; Griffin, R. G. ^{17}O MAS NMR Correlation Spectroscopy at High Magnetic Fields. *J. Am. Chem. Soc.* **2017**, *139* (49), 17953–17963.

(9)     Paulino, J.; Yi, M.; Hung, I.; Gan, Z.; Wang, X.; Chekmenev, E. Y.; Zhou, H.-X.; Cross, T. A. Functional Stability of Water Wire–Carbonyl Interactions in an Ion Channel. *Proc. Natl. Acad. Sci.* **2020**, *117* (22), 11908–11915.

(10)    Hu, J.; Chekmenev, E. Y.; Gan, Z.; Gor'kov, P. L.; Saha, S.; Brey, W. W.; Cross, T. A. Ion Solvation by Channel Carbonyls Characterized by ^{17}O Solid-State NMR at 21 T. *J. Am. Chem. Soc.* **2005**, *127* (34), 11922–11923.

(11)   Lin, B.; Hung, I.; Gan, Z.; Chien, P.; Spencer, H. L.; Smith, S. P.; Wu, G. ^{17}O NMR Studies of Yeast Ubiquitin in Aqueous Solution and in the Solid State. *ChemBioChem* **2021**, *22* (5), 826–829.

(12)   Špačková, J.; Fabra, C.; Mittelette, S.; Gaillard, E.; Chen, C.-H.; Cazals, G.; Lebrun, A.; Sene, S.; Berthomieu, D.; Chen, K.; Gan, Z.; Gervais, C.; Métro, T.-X.; Laurencin, D. Unveiling the Structure and Reactivity of Fatty-Acid Based (Nano)Materials Thanks to Efficient and Scalable [17]O and ^{18}O-Isotopic Labeling Schemes. *J. Am. Chem. Soc.* **2020**, *142* (50), 21068–21081.

(13)   Harris, R. K.; Becker, E. D. NMR Nomenclature: Nuclear Spin Properties and Conventions for Chemical Shifts—IUPAC Recommendations. *J. Magn. Reson.* **2002**, *156* (2), 323–326.

(14)   Wu, G. Solid-State ^{17}O NMR Spectroscopy of Organic and Biological Molecules. In *Modern Magnetic Resonance*; Springer International Publishing: Cham, 2017; pp 1–20.

(15)   Wu, G. ^{17}O NMR Studies of Organic and Biological Molecules in Aqueous Solution and in the Solid State. *Prog. Nucl. Magn. Reson. Spectrosc.* **2019**, *114–115*, 135–191.

(16)   Steinschneider, A.; Burgar, M. I.; Buku, A.; Fiat, D. Labeling of Amino Acids and Peptides with Isotopic Oxygen As Followed By [17]O-N.M.R.*. *Int. J. Pept. Protein Res.* **1981**, *18* (3), 324–333.

(17)   Seyfried, M. S.; Lauber, B. S.; Luedtke, N. W. Multiple-Turnover Isotopic Labeling of Fmoc- and Boc-Protected Amino Acids with Oxygen Isotopes. *Org. Lett.* **2010**, *12* (1), 104–106.

(18)   Carnahan, S. L.; Lampkin, B. J.; Naik, P.; Hanrahan, M. P.; Slowing, I. I.; Vanveller, B.; Wu, G.; Rossini, A. J. Probing O-H Bonding through Proton Detected [1]H-[17]O Double Resonance Solid-State NMR Spectroscopy. *J. Am. Chem. Soc.* **2019**, *141* (1), 441–450.

(19)   Klein, B. A.; Tkachuk, D. G.; Terskikh, V. V.; Michaelis, V. K. Expanding the NMR Toolkit for Biological Solids: Oxygen-17 Enriched Fmoc-Amino Acids. *New J. Chem.* **2021**, *45* (28), 12384–12398

(20)   Métro, T. X.; Gervais, C.; Martinez, A.; Bonhomme, C.; Laurencin, D. Unleashing the Potential of ^{17}O NMR Spectroscopy Using Mechanochemistry. *Angew. Chem. Int. Ed.* **2017**, *56* (24), 6803–6807.

(21)   Perras, F. A.; Chaudhary, U.; Slowing, I. I.; Pruski, M. Probing Surface Hydrogen Bonding and Dynamics by Natural Abundance, Multidimensional, $^{17}$O DNP NMR Spectroscopy. *J. Phys. Chem. C* **2016**, *120* (21), 11535–11544.

(22)   Siegel, R.; Nakashima, T. T.; Wasylishen, R. E. Sensitivity Enhancement of NMR Spectra of Half-Integer Quadrupolar Nuclei in the Solid State via Population Transfer. *Concepts Magn. Reson. Part A* **2005**, *26A* (2), 47–61.

(23)   Yao, Z.; Kwak, H.-T.; Sakellariou, D.; Emsley, L.; Grandinetti, P. J. Sensitivity Enhancement of the Central Transition NMR Signal of Quadrupolar Nuclei under Magic-Angle Spinning. *Chem. Phys. Lett.* **2000**, *327* (1–2), 85–90.

(24)   Prasad, S.; Kwak, H.-T.; Clark, T.; Grandinetti, P. J. A Simple Technique for Determining Nuclear Quadrupole Coupling Constants with RAPT Solid-State NMR Spectroscopy. *J. Am. Chem. Soc.* **2002**, *124* (18), 4964–4965.

(25)   Jardón-Álvarez, D.; Bovee, M. O.; Baltisberger, J. H.; Grandinetti, P. J. Natural Abundance O-17 and S-33 Nuclear Magnetic Resonance Spectroscopy in Solids Achieved through Extended Coherence Lifetimes. *Phys. Rev. B* **2019**, *100* (14), 1–5.

(26)   Blanc, F.; Sperrin, L.; Jefferson, D. A.; Pawsey, S.; Rosay, M.; Grey, C. P. Dynamic Nuclear Polarization Enhanced Natural Abundance $^{17}$O Spectroscopy. *J. Am. Chem. Soc.* **2013**, *135* (8), 2975–2978.

(27)   Michaelis, V. K.; Markhasin, E.; Daviso, E.; Herzfeld, J.; Griffin, R. G. Dynamic Nuclear Polarization of Oxygen-17. *J. Phys. Chem. Lett.* **2012**, *3* (15), 2030–2034.

(28)   Martins, V.; Xu, J.; Wang, X.; Chen, K.; Hung, I.; Gan, Z.; Gervais, C.; Bonhomme, C.; Jiang, S.; Zheng, A.; Lucier, B. E. G.; Huang, Y. Higher Magnetic Fields, Finer MOF Structural Information: $^{17}$O Solid-State NMR at 35.2 T. *J. Am. Chem. Soc.* **2020**, *142* (35), 14877–14889.

(29)   *Peptide Synthesis and Applications*, 2nd ed.; Jensen, K. J., Tofteng Shelton, P., Pedersen, S. L., Eds.; Methods in Molecular Biology; Humana Press: Totowa, NJ, 2013; Vol. 1047.

(30)   Bennett, A. E.; Rienstra, C. M.; Auger, M.; Lakshmi, K. V.; Griffin, R. G. Heteronuclear Decoupling in Rotating Solids. *J. Chem. Phys.* **1995**, *103* (16), 6951–6958.

(31)   Kentgens, A. P. M.; Verhagen, R. Advantages of Double Frequency Sweeps in Static, MAS and MQMAS NMR of Spin I = 3/2 Nuclei. *Chem. Phys. Lett.* **1999**, *300* (3–4), 435–443.

(32) Harris, R. K.; Becker, E. D.; Cabral de Menezes, S. M.; Granger, P.; Hoffman, R. E.; Zilm, K. W. Further Conventions for NMR Shielding and Chemical Shifts (IUPAC Recommendations 2008). *Pure Appl. Chem.* **2008**, *80* (1), 59–84.

(33) Pines, A.; Gibby, M. G.; Waugh, J. S. Proton-Enhanced Nuclear Induction Spectroscopy. A Method for High Resolution NMR of Dilute Spins in Solids. *J. Chem. Phys.* **1972**, *56* (4), 1776–1777.

(34) Vinod Chandran, C.; Madhu, P. K.; Kurur, N. D.; Bräuniger, T. Swept-Frequency Two-Pulse Phase Modulation (SW f-TPPM) Sequences with Linear Sweep Profile for Heteronuclear Decoupling in Solid-State NMR. *Magn. Reson. Chem.* **2008**, *46* (10), 943–947.

(35) Mason, J. Conventions for the Reporting of Nuclear Magnetic Shielding (or Shift) Tensors Suggested by Participants in the NATO ARW on NMR Shielding Constants at the University of Maryland, College Park, July 1992. *Solid State Nucl. Magn. Reson.* **1993**, *2*, 285−288.

(36) Herzfeld, J.; Berger, A. E. Sideband Intensities in NMR-Spectra of Samples Spinning at the Magic Angle. *J. Chem. Phys.* **1980**, *73*, 6021−6030.

(37) Lu, J.; Hung, I.; Brinkmann, A.; Gan, Z.; Kong, X.; Wu, G. Solid-State $^{17}$O NMR Reveals Hydrogen-Bonding Energetics: Not All Low-Barrier Hydrogen Bonds Are Strong. *Angew. Chem. Int. Ed.* **2017**, *56* (22), 6166–6170.

(38) Kong, X.; O'Dell, L. A.; Terskikh, V.; Ye, E.; Wang, R.; Wu, G. Variable-Temperature $^{17}$O NMR Studies Allow Quantitative Evaluation of Molecular Dynamics in Organic Solids. *J. Am. Chem. Soc.* **2012**, *134* (35), 14609–14617.

(39) Long, J. R.; Ebelhäuser, R.; Griffin, R. G. $^2$H NMR Line Shapes and Spin−Lattice Relaxation in Ba(ClO$_3$)$_2$ · 2 H$_2$O. *J. Phys. Chem. A* **1997**, *101* (6), 988–994.

(40) Chiba, T. Deuteron Magnetic Resonance Study of Barium Chlorate Monohydrate. *J. Chem. Phys.* **1963**, *39* (4), 947–953.

(41) Keeler, E. G.; Michaelis, V. K.; Griffin, R. G. $^{17}$O NMR Investigation of Water Structure and Dynamics. *J. Phys. Chem. B* **2016**, *120* (32), 7851–7858.

(42) Michaelis, V. K.; Griffin, R. G.; Corzilius, B.; Vega, S. *Handbook of High Field Dynamic Nuclear Polarization*, 1st ed.; Michaelis, V. K., Griffin, R. G., Corzilius, B., Vega, S., Eds.; Wiley, 2020.

(43)  Overhauser, A. W. Polarization of Nuclei in Metals. *Phys. Rev.* **1953**, *92* (2), 411–415.

(44)  Maly, T.; Debelouchina, G. T.; Bajaj, V. S.; Hu, K.-N.; Joo, C.-G.; Mak–Jurkauskas, M. L.; Sirigiri, J. R.; van der Wel, P. C. A.; Herzfeld, J.; Temkin, R. J.; Griffin, R. G. Dynamic Nuclear Polarization at High Magnetic Fields. *J. Chem. Phys.* **2008**, *128* (5), 052211.

(45)  Carver, T. R.; Slichter, C. P. Polarization of Nuclear Spins in Metals. *Phys. Rev.* **1953**, *92* (1), 212–213.

(46)  Michaelis, V. K.; Keeler, E. G.; Ong, T. C.; Craigen, K. N.; Penzel, S.; Wren, J. E. C.; Kroeker, S.; Griffin, R. G. Structural Insights into Bound Water in Crystalline Amino Acids: Experimental and Theoretical $^{17}$O NMR. *J. Phys. Chem. B* **2015**, *119* (25), 8024–8036.

(47)  Björgvinsdóttir, S.; Walder, B. J.; Pinon, A. C.; Emsley, L. Bulk Nuclear Hyperpolarization of Inorganic Solids by Relay from the Surface. *J. Am. Chem. Soc.* **2018**, *140* (25), 7946–7951.

(48)  Pinon, A. C.; Schlagnitweit, J.; Berruyer, P.; Rossini, A. J.; Lelli, M.; Socie, E.; Tang, M.; Pham, T.; Lesage, A.; Schantz, S.; Emsley, L. Measuring Nano- to Microstructures from Relayed Dynamic Nuclear Polarization NMR. *J. Phys. Chem. C* **2017**, *121* (29), 15993–16005.

(49)  Wittmann, J. J.; Eckardt, M.; Harneit, W.; Corzilius, B. Electron-Driven Spin Diffusion Supports Crossing the Diffusion Barrier in MAS DNP. *Phys. Chem. Chem. Phys.* **2018**, *20* (16), 11418–11429.

(50)  Ha, M.; Thiessen, A. N.; Sergeyev, I. V.; Veinot, J. G. C.; Michaelis, V. K. Endogenous Dynamic Nuclear Polarization NMR of Hydride-Terminated Silicon Nanoparticles. *Solid State Nucl. Magn. Reson.* **2019**, *100*, 77–84.

(51)  Vega, A. J. CP/MAS of Quadrupolar S = 3/2 Nuclei. *Solid State Nucl. Magn. Reson.* **1992**, *1* (1), 17–32.

(52)  Barrie, P. J. Distorted Powder Lineshapes in $^{27}$Al CP/MAS NMR Spectroscopy of Solids. *Chem. Phys. Lett.* **1993**, *208* (5–6), 486–490.

(53)  Pruski, M.; Lang, D. P.; Fernandez, C.; Amoureux, J. P. Multiple-Quantum Magic-Angle Spinning NMR with Cross-Polarization: Spectral Editing of High-Resolution Spectra of Quadrupolar Nuclei. *Solid State Nucl. Magn. Reson.* **1997**, *7* (4), 327–331.

(54)  Zhao, X.; Hoffbauer, W.; Schmedt auf der Günne, J.; Levitt, M. H. Heteronuclear Polarization Transfer by Symmetry-Based Recoupling Sequences in Solid-State NMR. *Solid State Nucl. Magn. Reson.* **2004**, *26* (2), 57–64.

(55)  van Beek, J. D.; Dupree, R.; Levitt, M. H. Symmetry-Based Recoupling of $^{17}O$–$^1H$ Spin Pairs in Magic-Angle Spinning NMR. *J. Magn. Reson.* **2006**, *179* (1), 38–48.

(56)  Perras, F. A.; Kobayashi, T.; Pruski, M. Natural Abundance $^{17}O$ DNP Two-Dimensional and Surface-Enhanced NMR Spectroscopy. *J. Am. Chem. Soc.* **2015**, *137* (26), 8336–8339.

(57)  Hassan, A.; Quinn, C. M.; Struppe, J.; Sergeyev, I. V.; Zhang, C.; Guo, C.; Runge, B.; Theint, T.; Dao, H. H.; Jaroniec, C. P.; Berbon, M.; Lends, A.; Habenstein, B.; Loquet, A.; Kuemmerle, R.; Perrone, B.; Gronenborn, A. M.; Polenova, T. Sensitivity Boosts by the CPMAS CryoProbe for Challenging Biological Assemblies. *J. Magn. Reson.* **2020**, *311*, 106680.

# Chapter 7

## Conclusion and Future Outlook

### 7.1 Conclusion

In this thesis, we explored the versatility of solid-state NMR spectroscopy as a powerful characterization technique for hard and soft materials. First, we analyzed a series of toxic-metal-free hybrid methylammonium tin halide perovskites and their corresponding chemical shift ranges using NMR spectroscopy and quantum chemical calculations. With the exchange in halides for each parent phase, unique chemical shifts are determined which show a linear relationship with the optical bandgaps. These results demonstrate the sensitivity of the NMR chemical shift to the changes in the local electronic environment (i.e., when the halide mass increases and the band gap decreases, the magnetic shielding decreases demonstrating an inverse halogen dependence). Using variable temperature $^{119}$Sn NMR spectroscopy, changes to the CSA with phase changes were explored. Not only was a $^{119}$Sn chemical shift range for methylammonium tin halide perovskites established, an in-situ NMR study was performed to track the decomposition of MASnI$_3$ based on the changes in linewidths and chemical shifts with respect to time. Using $^{119}$Sn NMR spectroscopy and quantum chemical calculations, a greater understanding of the atomic-level structural-property relationships in methylammonium tin halide perovskites was obtained.

Moving on from the application of future solar absorbing semiconducting materials, we focused our attention of toxic-metal-free silicon nanoparticle quantum dots in Chapter 4. Using a

combination of XPS, TEM, XRD, FTIR and $^{29}$Si NMR spectroscopy, the complex structure arrangement of H-SiNPS was probed. In our series of H-SiNPs ranging from 3 to 64 nm in size, three unique structural environments corresponding to the surface, subsurface, and core layers of the H-SiNPs was discussed. For all H-SiNPs < 3 nm, the amorphous surface structure made up the bulk of the particle, resulting in a broad lineshape between -80 to -120 ppm. As the H-SiNPs increase to 9 nm, the appearance of a semi-ordered subsurface emerged suggesting a critical size-junction for the first time. For particles > 9 nm, the crystalline Si core exhibits a sharp resonance similar to bulk silicon.

While important structural insight was observed using $^{29}$Si NMR spectroscopy on these toxic-metal-free quantum dots, the poor sensitivity, arising from the inherently low Boltzmann polarization and long acquisition times (i.e., hours to days of acquisition for a single NMR spectrum), hindered our ability to do in-depth studies on these game-changing applied functional materials. Therefore, in Chapter 5 two DNP NMR protocols were implemented to increase $^{29}$Si sensitivity in H-SiNPs. Dynamic nuclear polarization has revolutionized NMR spectroscopy by significantly reducing experimental acquisition times and increasing the detection limits for previously improbably NMR studies. Using the intrinsic dangling bonds on the Si surface/subsurface, $^{29}$Si DNP enhancements of $\varepsilon = 6$ for 64 nm H-SiNPs were obtained. This translates to time savings of a factor of 36 (i.e., a $^{29}$Si NMR spectrum that would require 1.5 days can now be acquired within 1 hour using DNP) with < 1 mM of endogenous radical concentrations at high magnetic fields. From these promising preliminary results, the potential endogenous radicals for direct DNP polarization transfers are explored and demonstrate the future of structural characterization using magnetic resonance.

Thus far, the realms for boosting sensitivity for semiconducting materials such as temperature, cross-polarization, and DNP (Chapters 3-5) were explored. To push the boundaries on these techniques, we explored the most challenging biomolecular element $^{17}$O. In Chapter 6, a series of Fmoc-amino acids and tripeptides were studied using a tailored cost-effective $^{17}$O labelling coupled with sensitivity enhancing methods including population transfer, DNP, and CPMAS cryoprobe. Oxygen-17 NMR has plagued the field of biomolecular NMR due to its low gyromagnetic ratio, sizable quadrupole moment, and extremely low natural abundance (0.037 %). Thus, ultrahigh magnetic fields and $^{17}$O isotopic enrichment are needed to overcome these issues. Using minimal amounts of 40 % $H_2^{17/18}O$, a modified one-pot $^{17/18}O$ labelling protocol was

developed resulting in a cost reduction by a factor of 4 and a decrease in reaction time by a factor of 10. This allowed for the isotopic labelling of Fmoc-amino acids for $ 0.25 USD/mg of sample and opening the doors for $^{17}O$ NMR studies for protected amino acids and strategically labelled peptides. Using the ability to effectively label Fmoc-amino acids, site-specific labelled tripeptides (N-acetyl-MLF-OH and N-formyl-MLF-OH) were prepared, and high-quality $^{17}O$ NMR spectra resulted in unique $^{17}O$ NMR parameters for the carbonyl, carboxylic acid, and deprotonated oxygen chemical environments. To further illustrate the advancements in the field of NMR, we utilized population transfer techniques, DNP, and CPMAS cryoprobes to boost NMR sensitivity. All three approaches provided substantial signal-to-noise enhancements by a factor of 3-5 over conventional NMR experiments; demonstrating the potential to study challenging and complex biomolecular solids within a reasonable timeframe.

## 7.2 Future Outlook

As previewed in this thesis, I demonstrated the modern approaches in NMR spectroscopy to maximize sensitivity in extracting structural information for hard and soft materials. Advancements in NMR spectroscopy in the form of sensitivity enhancement pulse programs, CPMAS cryoprobe instrumentation, and DNP NMR spectroscopy are pushing the envelope for materials characterization. This allows for the study of experimentally challenging materials that were once unattainable. Coupled with these techniques, there is a lot of potential for further research on the projects discussed here. For example, the field of perovskite research has exponentially increased within the last decade. Recently, an environmentally friendly tin perovskite solar cell was developed using a tin triple-halide amorphous layer and cesium formamidinium tin iodide (CsFASnI$_3$) polycrystals, resulting in efficiencies over 10%.[1] Using $^{119}Sn$ NMR spectroscopy, the Sn centre can be probed to gain further insight on the stability of the solar cells (i.e., tracking the oxidation from $Sn^{2+}$ to $Sn^{4+}$ and thus, optimizing the Sn centre to prevent the oxidation). Additionally, the junction between the amorphous and crystalline layers can be examined using solid-state NMR, whereby the amorphous layer would be "invisible" using diffraction-based methods. In the 2020 study by Liu and coworkers, they determined that the Sn-3X-based cells (CsFASnI$_3$ – 10 mol%, SnF$_2$-20 mol%, SnCl$_2$; F$^-$, Cl$^-$, and I$^-$) performed the best overall compared to the other Sn-X films.[1] Not only did the polycrystalline film for Sn-3X show the highest crystallization, the addition of SnCl$_2$ drove the formation of the amorphous-

polycrystalline layer, allowing for better moisture and oxygen stability. Unfortunately, little is known about the layering structure and composition of the tin triple-halide amorphous layer, which appears to allow for higher device performance. Thus, solid-state NMR can be used to investigate the balance of the two phases and determine how the $SnCl_2$ incorporation into the amorphous layer affects the resulting solar energy conversion efficiency.

Silicon nanoparticles have far-reaching applications for sensors, optical materials, and biomedical imaging agents. Building upon the surface, subsurface, and core structural study of "naked" SiNPs discussed above, further research on surface modification of SiNPs can be done. For example, SiNPs biocompatibility as therapeutic agents depends on their size, hydrophobicity, and surface properties.[2,3] By altering the particle surface, solid-state NMR can be used to investigate the structural changes within the particle, as well as the relationship between the particle modification and the corresponding biocompatibility. The use of SiNPs as medical imaging agents is of great interest in the field of nanomedicine. As alluded to in Chapter 5, the endogenous radicals within the surface/subsurface of the SiNPs can be examined further to improve not only sensitivity gains, but as suitable particles for in vivo MRI. In 2018, researchers have successfully incorporated exogenous radicals to silicon nanoparticles to improve DNP enhancements, as well as generate in vivo hyperpolarized $^{29}$Si MRI signals.[4] In addition to endogenous radicals, surface functionalization of SiNPs can be done to attach MRI active ligands that can generate hyperpolarized MRI signals. For example, $^{19}$F is an ideal candidate for MRI as it has similar NMR characteristics to $^1$H, is 100% naturally abundant and naturally absent from the body.[5] Fluorine-19 also has shorter $T_1$ relaxation behaviour than $^{29}$Si which improves overall sensitivity and could provide two-dimensional techniques within a reasonable time frame. Further investigations on increasing the concentrations of endogenous radicals, as well as surface functionalization of SiNPs could be of great interest to create duo-action imaging and therapeutic agents for $^{29}$Si or $^{19}$F MRI and drug delivery, respectively.

Throughout this thesis and much of my PhD, a common obstacle that arose is low sensitivity of NMR. Whether it is due to long acquisition times or low natural abundances, researchers are constantly battling to reach large sensitivity gains. Oxygen-17 NMR in particular has plagued spectroscopists due to its costly isotopic labelling. Using the modified, one-pot labelling protocol discussed in Chapter 6, protected amino acids and peptides can be labelled and synthesized for < $1 USD /mg. This protocol allows the study of complex biomolecules for

biomedicine and proteins to be feasible as labelling costs have diminished. A dipeptide that has been of interest in the field of biomedicine is Fmoc-diphenylalanine (Fmoc-FF).[6,7] This dipeptide moiety has been shown to spontaneously self-assemble to form nanofibrils and hydrogels. Since it is known that the self-assembly of fibrils is due to hydrogen bonding and $\pi$-$\pi$ interactions of the Fmoc-protecting group, these interactions have not been examined using solid-state NMR spectroscopy. Multi-dimensional techniques such as Rotational-Echo Double Resonance (REDOR)[8] and Transferred-Echo Double Resonance (TEDOR)[9,10] experiments can be utilized to determine the heteronuclear distances (such as $^{15}$N-$^{17}$O, $^{13}$C-$^{17}$O, or $^{1}$H-$^{17}$O distances) between the helix structure and provide additional structural constraints for examining this self-assembly phenomenon. During the self-assembly, the Fmoc-FF can encapsulate and release drug molecules, making it an excellent candidate for drug delivery. Recently, it has been shown that the hydrophobic drug molecule indomethacin (IDM), a nonsteroidal anti-inflammatory drug which is used to treat rheumatoid arthritis, can be incorporated into Fmoc-FF hydrogels.[11]  As IDM contains a carboxylic acid group, the $^{17}$O labelling approach discussed in Chapter 6 could be implemented to isotopically label it prior to examining the dipolar interactions between the drug molecule and hydrogel network.

Furthermore, advancements in NMR instrumentation in the form of CPMAS cryoprobes for solids applications are opening the door for studies of inorganic materials and biological systems with low level of labelling and/or natural abundances. Though this thesis has illustrated a snippet of the versatility of solid-state NMR spectroscopy and the advancements of NMR technology within the last decade, the ever-growing field of NMR spectroscopy will continue to advance and push the limits of sensitivity gains for studying the next generation of materials that are currently unimaginable. This is very apparent as magnetic field strengths push towards 1.5-2.0 GHz and advances in high sensitivity methods continue at a rapid pace.

## 7.3 References

(1)    Liu, X.; Wang, Y.; Wu, T.; He, X.; Meng, X.; Barbaud, J.; Chen, H.; Segawa, H.; Yang, X.; Han, L. Efficient and Stable Tin Perovskite Solar Cells Enabled by Amorphous-Polycrystalline Structure. *Nature Commun.* **2020**, *11* (1), 2678.

(2)    Hall, J. B.; Dobrovolskaia, M. A.; Patri, A. K.; McNeil, S. E. Characterization of Nanoparticles for Therapeutics. *Nanomedicine* **2007**, *2* (6), 789–803.

(3)     McNeil, S. E. Nanoparticle Therapeutics: A Personal Perspective. *WIREs Nanomedicine and Nanobiotechnology* **2009**, *1* (3), 264–271.

(4)     Hu, J.; Whiting, N.; Bhattacharya, P. Hyperpolarization of Silicon Nanoparticles with TEMPO Radicals. *J. Phys. Chem. C* **2018**, *122* (19), 10575–10581.

(5)     Tirotta, I.; Dichiarante, V.; Pigliacelli, C.; Cavallo, G.; Terraneo, G.; Bombelli, F. B.; Metrangolo, P.; Resnati, G. [19]F Magnetic Resonance Imaging (MRI): From Design of Materials to Clinical Applications. *Chem. Rev.* **2015**, *115* (2), 1106–1129.

(6)     Zhao, F.; Ma, M. L.; Xu, B. Molecular Hydrogels of Therapeutic Agents. *Chem. Soc. Rev.* **2009**, *38* (4), 883.

(7)     Jayawarna, V.; Ali, M.; Jowitt, T. A.; Miller, A. F.; Saiani, A.; Gough, J. E.; Ulijn, R. V. Nanostructured Hydrogels for Three-Dimensional Cell Culture Through Self-Assembly of Fluorenylmethoxycarbonyl–Dipeptides. *Adv. Mater.* **2006**, *18* (5), 611–614.

(8)     Gullion, T.; Schaefer, J. Rotational-Echo Double-Resonance NMR. *J. Mag. Res. (1969)* **1989**, *81* (1), 196–200.

(9)     Hing, A. W.; Vega, S.; Schaefer, J. Transferred-Echo Double-Resonance NMR. *J. Mag. Res. (1969)* **1992**, *96* (1), 205–209.

(10)    Hing, A. W.; Vega, S.; Schaefer, J. Measurement of Heteronuclear Dipolar Coupling by Transferred-Echo Double-Resonance NMR. *J. Mag. Res., Series A* **1993**, *103* (2), 151–162.

(11)    Choe, R.; il Yun, S. Fmoc-Diphenylalanine-Based Hydrogels as a Potential Carrier for Drug Delivery. *e-Polymers* **2020**, *20* (1), 458–468.

# Bibliography

*Chapter 2 References*

(1)     Duer, M. J. *Introduction to Solid-State NMR Spectroscopy*; Blackwell, 2005.

(2)     Harris, R. K. *Nuclear Magnetic Resonance Spectroscopy*; John Wiley and Sons: New York, 1986.

(3)     Apperley, D.; Harris, R.; Hodgkinson, P. *Solid-State NMR: Basic Principles & Practice*; Momentum Press, 2012.

(4)     Farrar, T. C.; Becker, E. D. *Pulse and Fourier Transform NMR*; Elsevier, 1971.

(5)     Herzfeld, J.; Berger, A. E. Sideband Intensities in NMR-Spectra of Samples Spinning at the Magic Angle. *J. Chem. Phys.* **1980**, *73*, 6021−6030.

(6)     Andrew, E. R.; Bradeuey, A.; Eades, R. G. Nuclear Magnetic Resonance Spectra from a Crystal Rotated at High Speed. *Nature* **1958**, *182* (4650), 1659–1659.

(7)     Lowe, I. J. Free Induction Decays of Rotating Solids. *Phys. Rev. Lett.* **1959**, *2* (7), 285–287.

(8)     Bloch, F. Nuclear Induction. *Phys. Rev.* **1946**, *70* (7–8), 460–474.

(9)     Hahn, E. L. Spin Echoes. *Phys. Rev.* **1950**, *80* (4), 580–594.

(10)    Carr, H. Y.; Purcell, E. M. Effects of Diffusion on Free Precession in Nuclear Magnetic Resonance Experiments. *Phys. Rev.* **1954**, *94* (3), 630–638.

(11)    Pines, A.; Gibby, M. G.; Waugh, J. S. Proton-Enhanced Nuclear Induction Spectroscopy. A Method for High Resolution NMR of Dilute Spins in Solids. *J. Chem. Phys.* **1972**, *56* (4), 1776–1777.

(12)    Johnson, R. L.; Schmidt-Rohr, K. Quantitative Solid-State $^{13}$C NMR with Signal Enhancement by Multiple Cross Polarization. *J. Magn. Reson.* **2014**, *239*, 44–49.

(13)    Duan, P.; Schmidt-Rohr, K. Composite-Pulse and Partially Dipolar Dephased MultiCP for Improved Quantitative Solid-State $^{13}$C NMR. *J. Magn. Reson.* **2017**, *285*, 68–78.

(14)    Kentgens, A. P. M.; Verhagen, R. Advantages of Double Frequency Sweeps in Static, MAS and MQMAS NMR of Spin I = 3/2 Nuclei. *Chem. Phys. Lett.* **1999**, *300* (3–4), 435–443.

(15)    Siegel, R.; Nakashima, T. T.; Wasylishen, R. E. Sensitivity Enhancement of NMR Spectra of Half-Integer Quadrupolar Nuclei in the Solid State via Population Transfer. *Concepts Magn. Reson. A* **2005**, *26A* (2), 47–61.

(16)   Silver, M. S.; Joseph, R. I.; Hoult, D. I. Selective Spin Inversion in Nuclear Magnetic Resonance and Coherent Optics through an Exact Solution of the Bloch-Riccati Equation. *Phys. Rev. A* **1985**, *31* (4), 2753–2755.

(17)   Silver, M. S.; Joseph, R. I.; Hoult, D. I. Highly Selective π/2 and π Pulse Generation. *J. Magn. Reson.* **1984**, *59* (2), 347–351.

(18)   Yao, Z.; Kwak, H.-T.; Sakellariou, D.; Emsley, L.; Grandinetti, P. J. Sensitivity Enhancement of the Central Transition NMR Signal of Quadrupolar Nuclei under Magic-Angle Spinning. *Chem. Phys. Letts.* **2000**, *327* (1–2), 85–90.

(19)   Eichele, K. WSolids1. Universität Tübingen 2021.

(20)   Mason, J. Conventions for the Reporting of Nuclear Magnetic Shielding (or Shift) Tensors Suggested by Participants in the NATO ARW on NMR Shielding Constants at the University of Maryland, College Park, July 1992. *Solid State Nucl. Magn. Reson.* **1993**, *2*, 285−288.

(21)   Harris, R. K.; Becker, E. D.; de Menezes, S. M. C.; Granger, P.; Hoffman, R. E.; Zilm, K. W. Further Conventions for NMR Shielding and Chemical Shifts (IUPAC Recommendations 2008). *Pure Appl. Chem.* **2008**, *80*, 59–84.

(22)   Ni, Q. Z.; Daviso, E.; Can, T. v.; Markhasin, E.; Jawla, S. K.; Swager, T. M.; Temkin, R. J.; Herzfeld, J.; Griffin, R. G. High Frequency Dynamic Nuclear Polarization. *Acc. Chem. Res.* **2013**, *46* (9), 1933–1941.

(23)   Rossini, A. J.; Zagdoun, A.; Lelli, M.; Lesage, A.; Copéret, C.; Emsley, L. Dynamic Nuclear Polarization Surface Enhanced NMR Spectroscopy. *Acc. Chem. Res.* **2013**, *46* (9), 1942–1951.

(24)   Michaelis, V. K.; Griffin, R. G.; Corzilius, B.; Vega, S. *Handbook of High Field Dynamic Nuclear Polarization*; Michaelis, V. K., Griffin, R. G., Corzilius, B., Vega, S., Eds.; Wiley, 2020.

(25)   Maly, T.; Debelouchina, G. T.; Bajaj, V. S.; Hu, K.-N.; Joo, C.-G.; Mak–Jurkauskas, M. L.; Sirigiri, J. R.; van der Wel, P. C. A.; Herzfeld, J.; Temkin, R. J.; Griffin, R. G. Dynamic Nuclear Polarization at High Magnetic Fields. *J. Chem. Phys.* **2008**, *128* (5), 052211.

(26)   Michaelis, V. K.; Ong, T.-C.; Kiesewetter, M. K.; Frantz, D. K.; Walish, J. J.; Ravera, E.; Luchinat, C.; Swager, T. M.; Griffin, R. G. Topical Developments in High-Field Dynamic Nuclear Polarization. *Isr. J. Chem.* **2014**, *54* (1–2), 207–221.

(27)   Bernard, G. M.; Michaelis, V. K. Instrumentation for High-Field Dynamic Nuclear Polarization NMR Spectroscopy. *eMagRes* **2019**, *8* (2), 77–86.

(28)   Hooper, R. W.; Klein, B. A.; Michaelis, V. K. Dynamic Nuclear Polarization (DNP) 101: A New Era for Materials. *Chem. Mater.* **2020**, *32* (11), 4425–4430.

(29)   Michaelis, V. K.; Bryce, D. L. Editorial: Special Issue on Emerging Frontiers in Dynamic Nuclear Polarization NMR. *Solid State Nucl. Magn. Reson.* **2019**, *102*, 1.

(30)   Lee, D.; Hediger, S.; Paëpe, G. de. High-Field Solid-State NMR with Dynamic Nuclear Polarization. In *Modern Magnetic Resonance*; Springer International Publishing: Cham, 2017; pp 1–17.

(31)   Ha, M.; Michaelis, V. K. High-Frequency Dynamic Nuclear Polarization NMR for Solids: Part 1 – An Introduction. In *Modern Magnetic Resonance*; Springer International Publishing: Cham, 2017; pp 1–24.

(32)   Ha, M.; Michaelis, V. K. High-Frequency Dynamic Nuclear Polarization NMR for Solids: Part 2 – Development and Applications. In *Modern Magnetic Resonance*; Springer International Publishing: Cham, 2017; pp 1–18.

(33)   Matsuki, Y.; Idehara, T.; Fukazawa, J.; Fujiwara, T. Advanced Instrumentation for DNP-Enhanced MAS NMR for Higher Magnetic Fields and Lower Temperatures. *J. Magn. Reson.* **2016**, *264*, 107–115.

(34)   Bouleau, E.; Saint-Bonnet, P.; Mentink-Vigier, F.; Takahashi, H.; Jacquot, J.-F.; Bardet, M.; Aussenac, F.; Purea, A.; Engelke, F.; Hediger, S.; Lee, D.; de Paëpe, G. Pushing NMR Sensitivity Limits Using Dynamic Nuclear Polarization with Closed-Loop Cryogenic Helium Sample Spinning. *Chem. Sci.* **2015**, *6* (12), 6806–6812.

(35)   Matsuki, Y.; Takahashi, H.; Ueda, K.; Idehara, T.; Ogawa, I.; Toda, M.; Akutsu, H.; Fujiwara, T. Dynamic Nuclear Polarization Experiments at 14.1 T for Solid-State NMR. *Phys. Chem. Chem. Phys.* **2010**, *12* (22), 5799.

(36)   Barnes, A. B.; Markhasin, E.; Daviso, E.; Michaelis, V. K.; Nanni, E. A.; Jawla, S. K.; Mena, E. L.; DeRocher, R.; Thakkar, A.; Woskov, P. P.; Herzfeld, J.; Temkin, R. J.; Griffin, R. G. Dynamic Nuclear Polarization at 700MHz/460GHz. *J. Magn. Reson.* **2012**, *224*, 1–7.

(37)   Kubicki, D. J.; Casano, G.; Schwarzwälder, M.; Abel, S.; Sauvée, C.; Ganesan, K.; Yulikov, M.; Rossini, A. J.; Jeschke, G.; Copéret, C.; Lesage, A.; Tordo, P.; Ouari, O.; Emsley, L. Rational Design of Dinitroxide Biradicals for Efficient Cross-Effect Dynamic Nuclear Polarization. *Chem. Sci.* **2016**, *7* (1), 550–558.

(38)   Matsuki, Y.; Maly, T.; Ouari, O.; Karoui, H.; le Moigne, F.; Rizzato, E.; Lyubenova, S.; Herzfeld, J.; Prisner, T.; Tordo, P.; Griffin, R. G. Dynamic Nuclear Polarization with a Rigid Biradical. *Angew. Chem. Int. Ed.* **2009**, *48* (27), 4996–5000.

(39) Zagdoun, A.; Casano, G.; Ouari, O.; Schwarzwälder, M.; Rossini, A. J.; Aussenac, F.; Yulikov, M.; Jeschke, G.; Copéret, C.; Lesage, A.; Tordo, P.; Emsley, L. Large Molecular Weight Nitroxide Biradicals Providing Efficient Dynamic Nuclear Polarization at Temperatures up to 200 K. *J. Am. Chem. Soc.* **2013**, *135* (34), 12790–12797.

(40) Sauvée, C.; Rosay, M.; Casano, G.; Aussenac, F.; Weber, R. T.; Ouari, O.; Tordo, P. Highly Efficient, Water-Soluble Polarizing Agents for Dynamic Nuclear Polarization at High Frequency. *Angew. Chem. Int. Ed.* **2013**, *52* (41), 10858–10861.

(41) te Velde, G.; Bickelhaupt, F. M.; Baerends, E. J.; Fonseca Guerra, C.; van Gisbergen, S. J. A.; Snijders, J. G.; Ziegler, T. Chemistry with ADF. *J. Comput. Chem.* **2001**, *22* (9), 931–967.

(42) Fonseca Guerra, C.; Snijders, J. G.; te Velde, G.; Baerends, E. J. Towards an Order- N DFT Method. *Theor. Chem. Acc.* **1998**, *99* (6), 391–403.

(43) ADF 2019.3, SCM, Theoretical Chemistry, Vrije Universiteit, Amsterdam, The Netherlands.

*Chapter 3 References*

(1) National Renewable Energy Laboratory (NREL). Best Research-Cell Efficiency Chart. Https://Www.Nrel.Gov/Pv/Assets/Pdfs/Best-Research-Cell-Efficiencies.20190923.Pdf.

(2) Tennyson, E. M.; Doherty, T. A. S.; Stranks, S. D. Heterogeneity at Multiple Length Scales in Halide Perovskite Semiconductors. *Nat. Rev. Mater.* **2019**, *4* (9), 573–587.

(3) Wei, H.; Huang, J. Halide Lead Perovskites for Ionizing Radiation Detection. *Nat. Comm.* **2019**, *10* (1), 1066.

(4) Fu, Y.; Zhu, H.; Chen, J.; Hautzinger, M. P.; Zhu, X.-Y.; Jin, S. Metal Halide Perovskite Nanostructures for Optoelectronic Applications and the Study of Physical Properties. *Nat. Rev. Mater.* **2019**, *4* (3), 169–188.

(5) Gao, P.; Bin Mohd Yusoff, A. R.; Nazeeruddin, M. K. Dimensionality Engineering of Hybrid Halide Perovskite Light Absorbers. *Nat. Comm.* **2018**, *9* (1), 5028.

(6) Sum, T.-C.; Mathews, N. *Halide Perovskites: Photovoltaics, Light Emitting Devices, and Beyond*; 2019.

(7) Jung, H. S.; Park, N.-G. Perovskite Solar Cells: From Materials to Devices. *Small* **2015**, *11* (1), 10–25.

(8)     Borriello, I.; Cantele, G.; Ninno, D. Ab Initio Investigation of Hybrid Organic-Inorganic Perovskites Based on Tin Halides. *Phys. Rev. B* **2008**, *77* (23), 235214.

(9)     Yamada, K.; Mikawa, K.; Okuda, T.; Knight, K. S. Static and Dynamic Structures of $CD_3ND_3GeCl_3$ Studied by TOF High Resolution Neutron Powder Diffraction and Solid-State NMR. *J. Chem. Soc. Dalt. Trans.* **2002**, (10), 2112–2118.

(10)   Stoumpos, C. C.; Malliakas, C. D.; Kanatzidis, M. G. Semiconducting Tin and Lead Iodide Perovskites with Organic Cations: Phase Transitions, High Mobilities, and near-Infrared Photoluminescent Properties. *Inorg. Chem.* **2013**, *52* (15), 9019–9038.

(11)   Breternitz, J.; Schorr, S. What Defines a Perovskite? *Adv. Energy Mater.* **2018**, *8*, 1802366.

(12)   Askar, A. M.; Bernard, G. M.; Wiltshire, B.; Shankar, K.; Michaelis, V. K. Multinuclear Magnetic Resonance Tracking of Hydro, Thermal, and Hydrothermal Decomposition of $CH_3NH_3PbI_3$. *J. Phys. Chem. C* **2017**, *121*, 1013–1024.

(13)   Wang, D.; Wright, M.; Elumalai, N. K.; Uddin, A. Stability of Perovskite Solar Cells. *Sol. Energy Mater. Sol. Cells* **2016**, *147*, 255–275.

(14)   Juarez-Perez, E. J.; Ono, L. K.; Maeda, M.; Jiang, Y.; Hawash, Z.; Qi, Y. Photodecomposition and Thermal Decomposition in Methylammonium Halide Lead Perovskites and Inferred Design Principles to Increase Photovoltaic Device Stability. *J. Mater. Chem. A* **2018**, *6* (20), 9604–9612.

(15)   Li, J.; Cao, H.-L.; Jiao, W.-B.; Wang, Q.; Wei, M.; Cantone, I.; Lü, J.; Abate, A. Biological Impact of Lead from Halide Perovskites Reveals the Risk of Introducing a Safe Threshold. *Nat. Comm.* **2020**, *11* (1), 310.

(16)   Hu, H.; Dong, B.; Zhang, W. Low-Toxic Metal Halide Perovskites: Opportunities and Future Challenges. *J. Mater. Chem. A* **2017**, *5* (23), 11436–11449.

(17)   Feng, J.; Xiao, B. Effective Masses and Electronic and Optical Properties of Nontoxic $MASnX_3$ (X = Cl, Br, and I) Perovskite Structures as Solar Cell Absorber: A Theoretical Study Using HSE06. *J. Phys. Chem. C* **2014**, *118* (34), 19655–19660

(18)   Hong, Z.; Tan, D.; John, R. A.; Tay, Y. K. E.; Ho, Y. K. T.; Zhao, X.; Sum, T. C.; Mathews, N.; García, F.; Soo, H. Sen. Completely Solvent-Free Protocols to Access Phase-Pure, Metastable Metal Halide Perovskites and Functional Photodetectors from the Precursor Salts. *iScience* **2019**, *16*, 312–325.

(19)   Chiarella, F.; Zappettini, A.; Licci, F.; Borriello, I.; Cantele, G.; Ninno, D.; Cassinese, A.; Vaglio, R. Combined Experimental and Theoretical Investigation of Optical, Structural, and Electronic Properties of $CH_3NH_3SnX_3$ Thin Films (X = Cl, Br). *Phys. Rev. B* **2008**, *77* (4), 045129.

(20)  Lang, L.; Yang, J.-H.; Liu, H.-R.; Xiang, H. J.; Gong, X. G. First-Principles Study on the Electronic and Optical Properties of Cubic ABX$_3$ Halide Perovskites. *Phys. Lett. A* **2014**, *378* (3), 290–293.

(21)  Yamada, K.; Kuranaga, Y.; Ueda, K.; Goto, S.; Okuda, T.; Furukawa, Y. Phase Transition and Electric Conductivity of ASnCl$_3$ (A = Cs and CH$_3$NH$_3$). *Bull. Chem. Soc. Jpn.* **1998**, *71* (1), 127–134.

(22)  Yamada, K.; Nose, S.; Umehara, T.; Okuda, T.; Ichiba, S. [81]Br NQR and [119]Sn Mössbauer Study for MSnBr$_3$ (M = Cs and CH$_3$NH$_3$). *Bull. Chem. Soc. Jpn.* **1988**, *61* (12), 4265–4268.

(23)  Peedikakkandy, L.; Bhargava, P. Composition Dependent Optical, Structural and Photoluminescence Characteristics of Cesium Tin Halide Perovskites. *RSC Adv.* **2016**, *6* (24), 19857–19860.

(24)  Kumar, M. H.; Dharani, S.; Leong, W. L.; Boix, P. P.; Prabhakar, R. R.; Baikie, T.; Shi, C.; Ding, H.; Ramesh, R.; Asta, M.; Graetzel, M.; Mhaisalkar, S. G.; Mathews, N. Lead-Free Halide Perovskite Solar Cells with High Photocurrents Realized Through Vacancy Modulation. *Adv. Mater.* **2014**, *26* (41), 7122–7127.

(25)  Ogomi, Y.; Morita, A.; Tsukamoto, S.; Saitho, T.; Fujikawa, N.; Shen, Q.; Toyoda, T.; Yoshino, K.; Pandey, S. S.; Ma, T.; Hayase, S. CH$_3$NH$_3$Sn$_x$Pb$_{(1-x)}$I$_3$ Perovskite Solar Cells Covering up to 1060 nm. *J. Phys. Chem. Lett.* **2014**, *5* (6), 1004–1011.

(26)  Hao, F.; Stoumpos, C. C.; Cao, D. H.; Chang, R. P. H.; Kanatzidis, M. G. Lead-Free Solid-State Organic–Inorganic Halide Perovskite Solar Cells. *Nat. Photonics* **2014**, *8* (6), 489–494.

(27)  Noel, N. K.; Stranks, S. D.; Abate, A.; Wehrenfennig, C.; Guarnera, S.; Haghighirad, A.-A.; Sadhanala, A.; Eperon, G. E.; Pathak, S. K.; Johnston, M. B.; Petrozza, A.; Herz, L. M.; Snaith, H. J. Lead-Free Organic–Inorganic Tin Halide Perovskites for Photovoltaic Applications. *Energy Environ. Sci.* **2014**, *7* (9), 3061–3068.

(28)  Karmakar, A.; Askar, A. M.; Bernard, G. M.; Terskikh, V. V.; Ha, M.; Patel, S.; Shankar, K.; Michaelis, V. K. Mechanochemical Synthesis of Methylammonium Lead Mixed-Halide Perovskites: Unraveling the Solid-Solution Behavior Using Solid-State NMR. *Chem. Mater.* **2018**, *30*, 2309–2321.

(29)  Karmakar, A.; Dodd, M. S.; Zhang, X.; Oakley, M. S.; Klobukowski, M.; Michaelis, V. K. Mechanochemical Synthesis of 3D and 0D Cesium Lead Mixed Halide Perovskite Solid Solutions. *Chem. Comm.* **2019**, *55*, 5079–5082.

(30) Franssen, W. M. J.; van Es, S. G. D.; Dervişoğlu, R.; de Wijs, G. A.; Kentgens, A. P. M. Symmetry, Dynamics, and Defects in Methylammonium Lead Halide Perovskites. *J. Phys. Chem. Lett.* **2017**, *8* (1), 61–66.

(31) Bernard, G. M.; Wasylishen, R. E.; Ratcliffe, C. I.; Terskikh, V.; Wu, Q.; Buriak, J. M.; Hauger, T. Methylammonium Cation Dynamics in Methylammonium Lead Halide Perovskites: A Solid-State NMR Perspective. *J. Phys. Chem. A* **2018**, *122* (6), 1560–1573.

(32) Senocrate, A.; Moudrakovski, I.; Kim, G. Y.; Yang, T.; Gregori, G.; Grätzel, M.; Maier, J. The Nature of Ion Conduction in Methylammonium Lead Iodide: A Multimethod Approach. *Angew. Chem. Int. Ed.* **2017**, *56*, 7755–7759.

(33) Kubicki, D. J.; Prochowicz, D.; Hofstetter, A.; Péchy, P.; Zakeeruddin, S. M.; Grätzel, M.; Emsley, L. Cation Dynamics in Mixed-Cation $(MA)_x(FA)_{1-X}PbI_3$ Hybrid Perovskites from Solid-State NMR. *J. Am. Chem. Soc.* **2017**, *139*, 10055–10061.

(34) Kubicki, D. J.; Prochowicz, D.; Hofstetter, A.; Zakeeruddin, S. M.; Grätzel, M.; Emsley, L. Phase Segregation in Potassium-Doped Lead Halide Perovskites from 39 K Solid-State NMR at 21.1 T. *J. Am. Chem. Soc.* **2018**, *140*, 7232−7238.

(35) Aebli, M.; Piveteau, L.; Nazarenko, O.; Benin, B. M.; Krieg, F.; Verel, R.; Kovalenko, M. V. Lead-Halide Scalar Couplings in $^{207}Pb$ NMR of $APbX_3$ Perovskites (A = Cs, Methylammonium, Formamidinium; X = Cl, Br, I). *Sci. Rep.* **2020**, *10* (1), 8229.

(36) Harris, R. K.; Becker, E. D. NMR Nomenclature: Nuclear Spin Properties and Conventions for Chemical Shifts—IUPAC Recommendations. *J. Magn. Reson.* **2002**, *156* (2), 323–326.

(37) Mundus, C.; Taillades, G.; Pradel, A.; Ribes, M. A $^{119}Sn$ Solid-State Nuclear Magnetic Resonance Study of Crystalline Tin Sulphides. *Solid State Nucl. Magn. Reson.* **1996**, *7* (2), 141–146.

(38) Eichler, B. E.; Phillips, B. L.; Power, P. P.; Augustine, M. P. Solid-State and High-Resolution Liquid $^{119}Sn$ NMR Spectroscopy of Some Monomeric, Two-Coordinate Low-Valent Tin Compounds: Very Large Chemical Shift Anisotropies. *Inorg. Chem.* **2000**, *39* (24), 5450–5453.

(39) Harris, R. K.; Sebald, A. High-Resolution Solid-State $^{119}Sn$ and $^{207}Pb$ NMR Study of Organotin and Organolead Chalcogenides: Observation Of J-Coupling in Solids. *Magn. Reson. Chem.* **1989**, *27* (1), 81–87.

(40) Grey, C. P.; Cheetham, A. K.; Dobson, C. M. Temperature-Dependent Solid-State $^{119}Sn$-MAS NMR of $Nd_2Sn_2O_7$, $Sm_2Sn_2O_7$, and $Y_{1.8}Sm_{0.2}Sn_2O_7$. Three Sensitive Chemical-Shift Thermometers. *J. Magn. Reson., Ser. A* **1993**, *101* (3), 299–306.

(41) MacKenzie, K.; Smith, M. E. *Multinuclear Solid-State Nuclear Magnetic Resonance of Inorganic Materials, Volume 6*; Pergamon, 2002.

(42) Gunther, W. R.; Michaelis, V. K.; Caporini, M. A.; Griffin, R. G.; Román-Leshkov, Y. Dynamic Nuclear Polarization NMR Enables the Analysis of Sn-Beta Zeolite Prepared with Natural Abundance $^{119}$Sn Precursors. *J. Am. Chem. Soc.* **2014**, *136* (17), 6219–6222.

(43) Yamada, K.; Nakada, K.; Takeuchi, Y.; Nawa, K.; Yohei Yamane. Tunable Perovskite Semiconductor $CH_3NH_3SnX_3$ (X: Cl, Br, or I) Characterized by X-Ray and DTA. *Bull. Chem. Soc. Jpn.* **2011**, *84*, 926–932.

(44) Onoda-Yamamuro, N.; Matsuo, T.; Suga, H. Thermal, Electric, and Dielectric Properties of $CH_3NH_3SnBr_3$ at Low Temperatures. *J. Chem. Thermodyn.* **1991**, *23*, 987–999.

(45) Bureau, B.; Silly, G.; Buzaré, J. Y.; Legein, C.; Massiot, D. From Crystalline to Glassy Gallium Fluoride Materials: An NMR Study of and Quadrupolar Nuclei. *Solid State Nucl. Magn. Reson.* **1999**, *14* (3–4), 181–190.

(46) Bernard, G. M.; Goyal, A.; Miskolzie, M.; McKay, R.; Wu, Q.; Wasylishen, R. E.; Michaelis, V. K. Methylammonium Lead Chloride: A Sensitive Sample for an Accurate NMR Thermometer. *J. Magn. Reson.* **2017**, *283*, 14–21.

(47) Thurber, K. R.; Tycko, R. Measurement of Sample Temperatures under Magic-Angle Spinning from the Chemical Shift and Spin-Lattice Relaxation Rate of $^{79}$Br in KBr Powder. *J. Magn. Reson.* **2009**, *196* (1), 84–87.

(48) Mason, J. Conventions for the Reporting of Nuclear Magnetic Shielding (or Shift) Tensors Suggested by Participants in the NATO ARW on NMR Shielding Constants at the University of Maryland, College Park, July 1992. *Solid State Nucl. Magn. Reson.* **1993**, *2*, 285−288.

(49) Herzfeld, J.; Berger, A. E. Sideband Intensities in NMR-Spectra of Samples Spinning at the Magic Angle. *J. Chem. Phys.* **1980**, *73*, 6021−6030.

(50) Harris, R. K.; Becker, E. D.; De Menezes, S. M. C.; Granger, P.; Hoffman, R. E.; Zilm, K. W. Further Conventions for NMR Shielding and Chemical Shifts (IUPAC Recommendations 2008). *Pure Appl. Chem.* **2008**, *80*, 59–84.

(51) Pines, A.; Gibby, M. G.; Waugh, J. S. Proton-Enhanced Nuclear Induction Spectroscopy. A Method for High Resolution NMR of Dilute Spins in Solids. *J. Chem. Phys.* **1972**, *56* (4), 1776–1777.

(52) Bennett, A. E.; Rienstra, C. M.; Auger, M.; Lakshmi, K. V.; Griffin, R. G. Heteronuclear Decoupling in Rotating Solids. *J. Chem. Phys.* **1995**, *103* (16), 6951–6958.

(53) Earl, W. L.; Vanderbart, D. L. Measurement of $^{13}$C Chemical Shifts in Solids. *J. Magn. Reson.* **1982**, *48* (1), 35–54.

(54) Hahn, E. L. Spin Echoes. *Phys. Rev.* **1950**, *80* (4), 580–594.

(55) te Velde, G.; Bickelhaupt, F. M.; Baerends, E. J.; Fonseca Guerra, C.; van Gisbergen, S. J. A.; Snijders, J. G.; Ziegler, T. Chemistry with ADF. *J. Comp. Chem.* **2001**, *22* (9), 931–967.

(56) ADF 2019.3, SCM, Theoretical Chemistry, Vrije Universiteit, Amsterdam, The Netherlands.

(57) Fonseca Guerra, C.; Snijders, J. G.; te Velde, G.; Baerends, E. J. Towards an Order-N DFT Method. *Theor. Chem. Accounts* **1998**, *99* (6), 391–403.

(58) Swainson, I.; Chi, L.; Her, J.-H.; Cranswick, L.; Stephens, P.; Winkler, B.; Wilson, D. J.; Milman, V. Orientational Ordering, Tilting and Lone-Pair Activity in the Perovskite Methylammonium Tin Bromide, $CH_3NH_3SnBr_3$. *Acta Crystallogr. Sect. B Struct. Sci.* **2010**, *66* (4), 422–429.

(59) Schreckenbach, G.; Ziegler, T. Calculation of NMR Shielding Tensors Using Gauge-Including Atomic Orbitals and Modern Density Functional Theory. *J. Phys. Chem.* **1995**, *99* (2), 606–611.

(60) van Lenthe, E.; Ehlers, A.; Baerends, E.-J. Geometry Optimizations in the Zero Order Regular Approximation for Relativistic Effects. *J. Chem. Phys.* **1999**, *110* (18), 8943–8953.

(61) Becke, A. D. Density-Functional Exchange-Energy Approximation with Correct Asymptotic Behavior. *Phys. Rev. A* **1988**, *38* (6), 3098–3100.

(62) Perdew, J. P.; Yue, W. Accurate and Simple Density Functional for the Electronic Exchange Energy: Generalized Gradient Approximation. *Phys. Rev. B* **1986**, *33* (12), 8800–8802.

(63) Shannon, R. D. Revised Effective Ionic Radii and Systematic Studies of Interatomic Distances in Halides and Chalcogenides. *Acta Cryst.* **1976**, *A32*, 751–767.

(64) Lash, T. D.; Lash, S. S. The Use of Pascal-like Triangles in Describing First Order NMR Coupling Patterns. *J. Chem. Ed.* **1987**, *64* (4), 315.

(65) Sharp, R. R. Rotational Diffusion and Magnetic Relaxation of $^{119}$Sn in Liquid $SnCl_4$ and $SnI_4$. *J. Chem. Phys.* **1972**, *57* (12), 5321–5330.

(66) Grondona, P.; Olivieri, A. C. Quadrupole Effects in Solid-State NMR Spectra of Spin-½ Nuclei: A Perturbation Approach. *Concepts Magn. Reson.* **1993**, *5* (4), 319–339.

(67)  Jung, M.-C.; Raga, S. R.; Qi, Y. Properties and Solar Cell Applications of Pb-Free Perovskite Films Formed by Vapor Deposition. *RSC Adv.* **2016**, *6* (4), 2819–2825.

(68)  Li, B.; Long, R.; Xia, Y.; Mi, Q. All-Inorganic Perovskite $CsSnBr_3$ as a Thermally Stable, Free-Carrier Semiconductor. *Angew. Chem. Int. Ed.* **2018**, *57* (40), 13154–13158.

(69)  Tao, S.; Schmidt, I.; Brocks, G.; Jiang, J.; Tranca, I.; Meerholz, K.; Olthof, S. Absolute Energy Level Positions in Tin- and Lead-Based Halide Perovskites. *Nat. Commun.* **2019**, *10* (1), 2560.

(70)  Nakatsuji, H. *Nuclear Magnetic Shieldings and Molecular Structure*; Tossell, J. A., Ed.; Springer Netherlands: Dordrecht, 1993.

(71)  Dmitrenko, O.; Bai, S.; Dybowski, C. Prediction of [207]Pb NMR Parameters for the Solid Ionic Lead(II) Halides Using the Relativistic ZORA-DFT Formalism: Comparison with the Lead-Containing Molecular Systems. *Solid State Nucl. Magn. Reson.* **2008**, *34* (3), 186–190.

(72)  Yamada, K.; Isobe, K.; Okuda, T.; Furukawa, Y. Successive Phase Transitions and High Ionic Conductivity of Trichlorogermanate (II) Salts as Studied by [35]C1 NQR and Powder X-Ray Diffraction. *Zeitschrift für Naturforschung A* **1994**, *49* (1–2), 258–266.

(73)  Weber, D. $CH_3NH_3SnBr_xI_{3-x}$ (x = 0-3), Ein Sn(II)-System Mit Kubischer Perowskitstruktur. *Z. Naturforsch.* **1978**, *33b*, 862–865.

(74)  Onoda, N.; Yamamuro, O.; Matsuo, T.; Suga, H.; Oikawa, K.; Tsuchiya, N.; Kamiyama, T.; Asano, H. Neutron-Diffraction Study of $CD_3ND_3SnBr_3$: Semiconductor-Insulator Transition with Orientational Ordering. *Physica B* **1995**, *213 & 214*, 411–413.

(75)  Yamada, K.; Isobe, K.; Tsuyama, E.; Okuda, T.; Furukawa, Y. Chloride Ion Conductor $CH_3NH_3GeCl_3$ Studied by Rietveld Analysis of X-Ray Diffraction and [35]Cl NMR. *Solid State Ion.* **1995**, *79*, 152–157.

(76)  Chung, I.; Lee, B.; He, J.; Chang, R. P. H.; Kanatzidis, M. G. All-Solid-State Dye-Sensitized Solar Cells with High Efficiency. *Nature* **2012**, *485* (7399), 486–489.

(77)  Mancini, A.; Quadrelli, P.; Milanese, C.; Patrini, M.; Guizzetti, G.; Malavasi, L. $CH_3NH_3Sn_xPb_{1-x}Br_3$ Hybrid Perovskite Solid Solution: Synthesis, Structure, and Optical Properties. *Inorg. Chem.* **2015**, *54* (18), 8893–8895.

(78)  Leijtens, T.; Prasanna, R.; Gold-Parker, A.; Toney, M. F.; McGehee, M. D. Mechanism of Tin Oxidation and Stabilization by Lead Substitution in Tin Halide Perovskites. *ACS Energy Lett.* **2017**, *2* (9), 2159–2165.

(79) Wang, F.; Ma, J.; Xie, F.; Li, L.; Chen, J.; Fan, J.; Zhao, N. Organic Cation-Dependent Degradation Mechanism of Organotin Halide Perovskites. *Adv. Funct. Mater.* **2016**, *26* (20), 3417–3423.

(80) Wrackmeyer, B. Application of $^{119}$Sn NMR Parameters; 1999; pp 203–264.

(81) Kubicki, D. J.; Prochowicz, D.; Salager, E.; Rakhmatullin, A.; Grey, C. P.; Emsley, L.; Stranks, S. D. Local Structure and Dynamics in Methylammonium, Formamidinium, and Cesium Tin(II) Mixed-Halide Perovskites from $^{119}$Sn Solid-State NMR. *J. Am. Chem. Soc.* **2020**, *142* (17), 7813–7826.

(82) Bloembergen, N.; Rowland, T. J. On the Nuclear Magnetic Resonance in Metals and Alloys. *Acta Metall.* **1953**, *1* (6), 731–746.

(83) Borsa, F.; Barnes, R. G. Temperature Dependence of the Isotropic and Anisotropic Knight Shift in Polycrystalline Cadmium and β-Tin. *J. Phys. Chem. Solids* **1966**, *27* (3), 567–573.

(84) Michaelis, V. K.; Griffin, R. G.; Corzilius, B.; Vega, S. *Handbook of High Field Dynamic Nuclear Polarization*, 1st ed.; Michaelis, V. K., Griffin, R. G., Corzilius, B., Vega, S., Eds.; Wiley, 2020.

(85) Ha, M.; Michaelis, V. K. High-Frequency Dynamic Nuclear Polarization NMR for Solids: Part 1 – An Introduction. In *Modern Magnetic Resonance*; Springer International Publishing: Cham, 2017; pp 1–24.

(86) Ha, M.; Michaelis, V. K. High-Frequency Dynamic Nuclear Polarization NMR for Solids: Part 2 – Development and Applications. In *Modern Magnetic Resonance*; Springer International Publishing: Cham, 2017; pp 1–18.

(87) Michaelis, V. K.; Kroeker, S. $^{73}$Ge Solid-State NMR of Germanium Oxide Materials: Experimental and Theoretical Studies. *J. Phys. Chem. C* **2010**, *114* (49), 21736–21744.

(88) Robinson, K.; Gibbs, G. V.; Ribbe, P. H. Quadratic Elongation: A Quantitative Measure of Distortion in Coordination Polyhedra. *Science* **1971**, *172* (3983), 567–570.

(89) Fleet, M. E. Distortion Parameters for Coordination Polyhedra. *Mineral. Mag.* **1976**, *40* (313), 531–533.

(90) Prasanna, R.; Leijtens, T.; Dunfield, S. P.; Raiford, J. A.; Wolf, E. J.; Swifter, S. A.; Werner, J.; Eperon, G. E.; de Paula, C.; Palmstrom, A. F.; Boyd, C. C.; van Hest, M. F. A. M.; Bent, S. F.; Teeter, G.; Berry, J. J.; McGehee, M. D. Design of Low Bandgap Tin–Lead Halide Perovskite Solar Cells to Achieve Thermal, Atmospheric and Operational Stability. *Nat. Energy* **2019**, *4* (11), 939–947.

(91)     Lin, R.; Xiao, K.; Qin, Z.; Han, Q.; Zhang, C.; Wei, M.; Saidaminov, M. I.; Gao, Y.; Xu, J.; Xiao, M.; Li, A.; Zhu, J.; Sargent, E. H.; Tan, H. Monolithic All-Perovskite Tandem Solar Cells with 24.8% Efficiency Exploiting Comproportionation to Suppress Sn(II) Oxidation in Precursor Ink. *Nat. Energy* **2019**, *4* (10), 864–873.

(92)     Zhao, D.; Chen, C.; Wang, C.; Junda, M. M.; Song, Z.; Grice, C. R.; Yu, Y.; Li, C.; Subedi, B.; Podraza, N. J.; Zhao, X.; Fang, G.; Xiong, R.-G.; Zhu, K.; Yan, Y. Efficient Two-Terminal All-Perovskite Tandem Solar Cells Enabled by High-Quality Low-Bandgap Absorber Layers. *Nat. Energy* **2018**, *3* (12), 1093–1100.

(93)     Wasylishen, R. E.; Knop, O.; Macdonald, J. B. Cation Rotation in Methylammonium Lead Halides. *Solid State Commun.* **1985**, *56* (7), 581–582.

*Chapter 4 References*

(1)     Union, T. E. Publications Office of the European Union. *Official Journal of the European Union* **2017**, *2017/197*, 3.

(2)     Liu, J.; Erogbogbo, F.; Yong, K.-T.; Ye, L.; Liu, J.; Hu, R.; Chen, H.; Hu, Y.; Yang, Y.; Yang, J.; Roy, I.; Karker, N. A.; Swihart, M. T.; Prasad, P. N. Assessing Clinical Prospects of Silicon Quantum Dots: Studies in Mice and Monkeys. *ACS Nano* **2013**, *7* (8).

(3)     Park, J.-H.; Gu, L.; von Maltzahn, G.; Ruoslahti, E.; Bhatia, S. N.; Sailor, M. J. Biodegradable Luminescent Porous Silicon Nanoparticles for in Vivo Applications. *Nat. Mater.* **2009**, *8* (4), 331–336.

(4)     Mobarok, M. H.; Purkait, T. K.; Islam, M. A.; Miskolzie, M.; Veinot, J. G. C. Instantaneous Functionalization of Chemically Etched Silicon Nanocrystal Surfaces. *Angew. Chem. Int. Ed.* **2017**, *56* (22), 6073–6077.

(5)     Islam, M. A.; Mobarok, M. H.; Sinelnikov, R.; Purkait, T. K.; Veinot, J. G. C. Phosphorus Pentachloride Initiated Functionalization of Silicon Nanocrystals. *Langmuir* **2017**, *33* (35), 8766–8773.

(6)     Mastronardi, M. L.; Maier-Flaig, F.; Faulkner, D.; Henderson, E. J.; Kübel, C.; Lemmer, U.; Ozin, G. A. Size-Dependent Absolute Quantum Yields for Size-Separated Colloidally-Stable Silicon Nanocrystals. *Nano Lett.* **2012**, *12* (1), 337–342.

(7)     Bhattacharjee, S.; Rietjens, I. M. C. M.; Singh, M. P.; Atkins, T. M.; Purkait, T. K.; Xu, Z.; Regli, S.; Shukaliak, A.; Clark, R. J.; Mitchell, B. S.; Alink, G. M.; Marcelis, A. T. M.; Fink, M. J.; Veinot, J. G. C.; Kauzlarich, S. M.; Zuilhof, H. Cytotoxicity of Surface-Functionalized Silicon and Germanium Nanoparticles: The Dominant Role of Surface Charges. *Nanoscale* **2013**, *5* (11), 4870.

(8)     Erogbogbo, F.; Yong, K.-T.; Roy, I.; Hu, R.; Law, W.-C.; Zhao, W.; Ding, H.; Wu, F.; Kumar, R.; Swihart, M. T.; Prasad, P. N. In Vivo Targeted Cancer Imaging, Sentinel Lymph Node Mapping and Multi-Channel Imaging with Biocompatible Silicon Nanocrystals. *ACS Nano* **2011**, *5* (1), 413–423.

(9)     Cassidy, M. C.; Chan, H. R.; Ross, B. D.; Bhattacharya, P. K.; Marcus, C. M. In Vivo Magnetic Resonance Imaging of Hyperpolarized Silicon Particles. *Nat. Nanotechnol.* **2013**, *8* (5).

(10)    Tu, C.; Ma, X.; House, A.; Kauzlarich, S. M.; Louie, A. Y. PET Imaging and Biodistribution of Silicon Quantum Dots in Mice. *ACS Med. Chem. Lett.* **2011**, *2* (4), 285–288.

(11)    Liu, X.; Zhao, S.; Gu, W.; Zhang, Y.; Qiao, X.; Ni, Z.; Pi, X.; Yang, D. Light-Emitting Diodes Based on Colloidal Silicon Quantum Dots with Octyl and Phenylpropyl Ligands. *ACS Appl. Mater. Interfaces* **2018**, *10* (6), 5959–5966.

(12)    Dutta, M.; Thirugnanam, L.; Trinh, P. van; Fukata, N. High Efficiency Hybrid Solar Cells Using Nanocrystalline Si Quantum Dots and Si Nanowires. *ACS Nano* **2015**, *9* (7), 6891–6899.

(13)    Švrček, V.; McDonald, C.; Lozac'h, M.; Tayagaki, T.; Koganezawa, T.; Miyadera, T.; Mariotti, D.; Matsubara, K. Stable Ultrathin Surfactant-Free Surface-Engineered Silicon Nanocrystal Solar Cells Deposited at Room Temperature. *Energy Sci. Eng.* **2017**, *5* (4), 184–193.

(14)    Zhao, S.; Pi, X. Colloidal Silicon Quantum Dots and Solar Cells. In *Handbook of Photovoltaic Silicon*; Yang, D., Ed.; Springer Berlin Heidelberg: Berlin, 2017; pp 1–27.

(15)  Gonzalez, C. M.; Veinot, J. G. C. Silicon Nanocrystals for the Development of Sensing Platforms. *J. Mater. Chem. C* **2016**, *4* (22), 4836–4846.

(16)  Meinardi, F.; Ehrenberg, S.; Dhamo, L.; Carulli, F.; Mauri, M.; Bruni, F.; Simonutti, R.; Kortshagen, U.; Brovelli, S. Highly Efficient Luminescent Solar Concentrators Based on Earth-Abundant Indirect-Bandgap Silicon Quantum Dots. *Nat. Photon.* **2017**, *11* (3), 177–185.

(17)  Chan, C. K.; Peng, H.; Liu, G.; McIlwrath, K.; Zhang, X. F.; Huggins, R. A.; Cui, Y. High-Performance Lithium Battery Anodes Using Silicon Nanowires. *Nat. Nanotechnol.* **2008**, *3* (1), 31–35.

(18)  Kim, H.; Seo, M.; Park, M.-H.; Cho, J. A Critical Size of Silicon Nano-Anodes for Lithium Rechargeable Batteries. *Angew. Chem. Int. Ed.* **2010**, *49* (12).

(19)  Su, X.; Wu, Q.; Li, J.; Xiao, X.; Lott, A.; Lu, W.; Sheldon, B. W.; Wu, J. Silicon-Based Nanomaterials for Lithium-Ion Batteries: A Review. *Adv. Energy Mater.* **2014**, *4* (1), 1300882.

(20)  Dohnalová, K.; Gregorkiewicz, T.; Kůsová, K. Silicon Quantum Dots: Surface Matters. *J. Phys. Condens. Matter* **2014**, *26* (17), 173201.

(21)  Chan, C. K.; Ruffo, R.; Hong, S. S.; Cui, Y. Surface Chemistry and Morphology of the Solid Electrolyte Interphase on Silicon Nanowire Lithium-Ion Battery Anodes. *J. Power Sources* **2009**, *189* (2), 1132–1140.

(22)  Dasog, M.; Yang, Z.; Regli, S.; Atkins, T. M.; Faramus, A.; Singh, M. P.; Muthuswamy, E.; Kauzlarich, S. M.; Tilley, R. D.; Veinot, J. G. C. Chemical Insight into the Origin of Red and Blue Photoluminescence Arising from Freestanding Silicon Nanocrystals. *ACS Nano* **2013**, *7* (3), 2676–2685.

(23)  Dasog, M.; de los Reyes, G. B.; Titova, L. v.; Hegmann, F. A.; Veinot, J. G. C. Size *vs* Surface: Tuning the Photoluminescence of Freestanding Silicon Nanocrystals Across the Visible Spectrum *via* Surface Groups. *ACS Nano* **2014**, *8* (9).

(24) Dasog, M.; Bader, K.; Veinot, J. G. C. Influence of Halides on the Optical Properties of Silicon Quantum Dots. *Chem. Mater.* **2015**, *27* (4).

(25) Wheeler, L. M.; Anderson, N. C.; Palomaki, P. K. B.; Blackburn, J. L.; Johnson, J. C.; Neale, N. R. Silyl Radical Abstraction in the Functionalization of Plasma-Synthesized Silicon Nanocrystals. *Chem. Mater.* **2015**, *27* (19).

(26) Lee, B. G.; Hiller, D.; Luo, J.-W.; Semonin, O. E.; Beard, M. C.; Zacharias, M.; Stradins, P. Strained Interface Defects in Silicon Nanocrystals. *Adv. Funct. Mater.* **2012**, *22* (15), 3223–3232.

(27) Kleovoulou, K.; Kelires, P. C. Stress State of Embedded Si Nanocrystals. *Phys. Rev. B* **2013**, *88* (8), 085424.

(28) Zhou, Z.; Brus, L.; Friesner, R. Electronic Structure and Luminescence of 1.1- and 1.4-Nm Silicon Nanocrystals: Oxide Shell versus Hydrogen Passivation. *Nano Lett.* **2003**, *3* (2).

(29) Shu, Y.; Kortshagen, U. R.; Levine, B. G.; Anthony, R. J. Surface Structure and Silicon Nanocrystal Photoluminescence: The Role of Hypervalent Silyl Groups. *J. Phys. Chem. C* **2015**, *119* (47).

(30) Veprek, S.; Sarott, F.-A.; Iqbal, Z. Effect of Grain Boundaries on the Raman Spectra, Optical Absorption, and Elastic Light Scattering in Nanometer-Sized Crystalline Silicon. *Phys. Rev. B* **1987**, *36* (6).

(31) Nikitin, T.; Khriachtchev, L. Optical and Structural Properties of Si Nanocrystals in $SiO_2$ Films. *Nanomaterials* **2015**, *5* (2).

(32) Yogi, P.; Tanwar, M.; Saxena, S. K.; Mishra, S.; Pathak, D. K.; Chaudhary, A.; Sagdeo, P. R.; Kumar, R. Quantifying the Short-Range Order in Amorphous Silicon by Raman Scattering. *Anal. Chem.* **2018**, *90* (13).

(33) Marra, D. C.; Edelberg, E. A.; Naone, R. L.; Aydil, E. S. Silicon Hydride Composition of Plasma-Deposited Hydrogenated Amorphous and Nanocrystalline Silicon Films and Surfaces. *J. Vac. Sci. Technol.* **1998**, *16* (6).

(34) Mangolini, L.; Kortshagen, U. Plasma-Assisted Synthesis of Silicon Nanocrystal Inks. *Adv. Mater.* **2007**, *19* (18).

(35) Jariwala, B. N.; Kramer, N. J.; Petcu, M. C.; Bobela, D. C.; Sanden, M. C. M. van de; Stradins, P.; Ciobanu, C. v.; Agarwal, S. Surface Hydride Composition of Plasma-Synthesized Si Nanoparticles. *J. Phys. Chem. C* **2011**, *115* (42).

(36) Zipoli, F.; Bernasconi, M. Ab Initio Simulation of the Grafting of Phenylacetylene on Hydrogenated Surfaces of Crystalline Silicon Catalyzed by a Lewis Acid. *J. Phys. Chem. B* **2006**, *110* (46).

(37) Hua, F.; Swihart, M. T.; Ruckenstein, E. Efficient Surface Grafting of Luminescent Silicon Quantum Dots by Photoinitiated Hydrosilylation. *Langmuir* **2005**, *21* (13).

(38) Hua, F.; Erogbogbo, F.; Swihart, M. T.; Ruckenstein, E. Organically Capped Silicon Nanoparticles with Blue Photoluminescence Prepared by Hydrosilylation Followed by Oxidation. *Langmuir* **2006**, *22* (9).

(39) Giuliani, J. R.; Harley, S. J.; Carter, R. S.; Power, P. P.; Augustine, M. P. Using Liquid and Solid-State NMR and Photoluminescence to Study the Synthesis and Solubility Properties of Amine Capped Silicon Nanoparticles. *Solid State Nucl. Magn. Reson.* **2007**, *32* (1).

(40) Shiohara, A.; Prabakar, S.; Faramus, A.; Hsu, C.-Y.; Lai, P.-S.; Northcote, P. T.; Tilley, R. D. Sized Controlled Synthesis, Purification, and Cell Studies with Silicon Quantum Dots. *Nanoscale* **2011**, *3* (8).

(41) Zou, J.; Kauzlarich, S. M. Functionalization of Silicon Nanoparticles via Silanization: Alkyl, Halide and Ester. *J. Cluster Sci.* **2008**, *19* (2).

(42) Ahire, J. H.; Wang, Q.; Coxon, P. R.; Malhotra, G.; Brydson, R.; Chen, R.; Chao, Y. Highly Luminescent and Nontoxic Amine-Capped Nanoparticles from Porous Silicon: Synthesis and Their Use in Biomedical Imaging. *ACS Appl. Mater. Interfaces* **2012**, *4* (6).

(43) Biesta, W.; van Lagen, B.; Gevaert, V. S.; Marcelis, A. T. M.; Paulusse, J. M. J.; Nielen, M. W. F.; Zuilhof, H. Preparation, Characterization, and Surface Modification of Trifluoroethyl Ester-Terminated Silicon Nanoparticles. *Chem. Mater.* **2012**, *24* (22).

(44)   Mayeri, D.; Phillips, B. L.; Augustine, M. P.; Kauzlarich, S. M. NMR Study of the Synthesis of Alkyl-Terminated Silicon Nanoparticles from the Reaction of $SiCl_4$ with the Zintl Salt, NaSi. *Chem. Mater.* **2001**, *13* (3).

(45)   Baldwin, R. K.; Pettigrew, K. A.; Ratai, E.; Augustine, M. P.; Kauzlarich, S. M. Solution Reduction Synthesis of Surface Stabilized Silicon Nanoparticles. *Chem. Commun.* **2002**, No. 17.

(46)   Carter, R. S.; Harley, S. J.; Power, P. P.; Augustine, M. P. Use of NMR Spectroscopy in the Synthesis and Characterization of Air- and Water-Stable Silicon Nanoparticles from Porous Silicon. *Chem. Mater.* **2005**, *17* (11).

(47)   Yesinowski, J. P. Solid-State NMR of Inorganic Semiconductors. In *Solid State NMR*; Chan, J. C. C., Ed.; Springer, Berlin, Heidelberg, 2011.

(48)   Atkins, T. M.; Cassidy, M. C.; Lee, M.; Ganguly, S.; Marcus, C. M.; Kauzlarich, S. M. Synthesis of Long $T_1$ Silicon Nanoparticles for Hyperpolarized $^{29}Si$ Magnetic Resonance Imaging. *ACS Nano* **2013**, *7* (2).

(49)   Neiner, D.; Kauzlarich, S. M. Hydrogen-Capped Silicon Nanoparticles as a Potential Hydrogen Storage Material: Synthesis, Characterization, and Hydrogen Release. *Chem. Mater.* **2010**, *22* (2).

(50)   El-Demellawi, J. K.; Holt, C. R.; Abou-Hamad, E.; Al-Talla, Z. A.; Saih, Y.; Chaieb, S. Room-Temperature Reactivity of Silicon Nanocrystals with Solvents: The Case of Ketone and Hydrogen Production from Secondary Alcohols: Catalysis? *ACS Appl. Mater. Interfaces* **2015**, *7* (25).

(51)   Kravitz, K.; Kamyshny, A.; Gedanken, A.; Magdassi, S. Solid State Synthesis of Water-Dispersible Silicon Nanoparticles from Silica Nanoparticles. *J. Solid State Chem.* **2010**, *183* (6).

(52)   Kolyagin, Y. G.; Zakharov, V. N.; Yatsenko, A. v.; Aslanov, L. A. Studies of Silicon Nanocluster Ligand Coating by Solid-State NMR. *Russ. Chem. Bull.* **2015**, *64* (8), 1829–1832.

(53)    Aptekar, J. W.; Cassidy, M. C.; Johnson, A. C.; Barton, R. A.; Lee, M.; Ogier, A. C.; Vo, C.; Anahtar, M. N.; Ren, Y.; Bhatia, S. N.; Ramanathan, C.; Cory, D. G.; Hill, A. L.; Mair, R. W.; Rosen, M. S.; Walsworth, R. L.; Marcus, C. M. Silicon Nanoparticles as Hyperpolarized Magnetic Resonance Imaging Agents. *ACS Nano* **2009**, *3* (12), 4003–4008.

(54)    Faulkner, R.; DiVerdi, J.; Yang, Y.; Kobayashi, T.; Maciel, G. The Surface of Nanoparticle Silicon as Studied by Solid-State NMR. *Materials* **2012**, *6* (1).

(55)    Lee, D.; Kaushik, M.; Coustel, R.; Chenavier, Y.; Chanal, M.; Bardet, M.; Dubois, L.; Okuno, H.; Rochat, N.; Duclairoir, F.; Mouesca, J.; De Paëpe, G. Solid-State NMR and DFT Combined for the Surface Study of Functionalized Silicon Nanoparticles. *Chem. Eur. J.* **2015**, *21* (45).

(56)    Hanrahan, M. P.; Fought, E. L.; Windus, T. L.; Wheeler, L. M.; Anderson, N. C.; Neale, N. R.; Rossini, A. J. Characterization of Silicon Nanocrystal Surfaces by Multidimensional Solid-State NMR Spectroscopy. *Chem. Mater.* **2017**, *29* (24).

(57)    Coleman, N. R. B.; Morris, M. A.; Spalding, T. R.; Holmes, J. D. The Formation of Dimensionally Ordered Silicon Nanowires within Mesoporous Silica. *J. Am. Chem. Soc.* **2001**, *123* (1).

(58)    Davidowski, S. K.; Holland, G. P. Solid-State NMR Characterization of Mixed Phosphonic Acid Ligand Binding and Organization on Silica Nanoparticles. *Langmuir* **2016**, *32* (13).

(59)    Lafon, O.; Thankamony, A. S. L.; Kobayashi, T.; Carnevale, D.; Vitzthum, V.; Slowing, I. I.; Kandel, K.; Vezin, H.; Amoureux, J.-P.; Bodenhausen, G.; Pruski, M. Mesoporous Silica Nanoparticles Loaded with Surfactant: Low Temperature Magic Angle Spinning ^{13}C and ^{29}Si NMR Enhanced by Dynamic Nuclear Polarization. *J. Phys. Chem. C* **2013**, *117* (3).

(60)    Sugiyama, Y.; Okamoto, H.; Mitsuoka, T.; Morikawa, T.; Nakanishi, K.; Ohta, T.; Nakano, H. Synthesis and Optical Properties of Monolayer Organosilicon Nanosheets. *J. Am. Chem. Soc.* **2010**, *132* (17).

(61)    Helbich, T.; Lyuleeva, A.; Höhlein, I. M. D.; Marx, P.; Scherf, L. M.; Kehrle, J.; Fässler, T. F.; Lugli, P.; Rieger, B. Radical-Induced Hydrosilylation Reactions for the

Functionalization of Two-Dimensional Hydride Terminated Silicon Nanosheets. *Chem. Eur. J.* **2016**, *22* (18).

(62) MacKenzie, K.; Smith, M. E. *Multinuclear Solid-State Nuclear Magnetic Resonance of Inorganic Materials, Volume 6*; Pergamon, 2002.

(63) Takeuchi, Y.; Takayama, T. $^{29}$Si NMR Spectroscopy of Organosilicon Compounds. In *The Chemistry of Organic Silicon Compounds*; Rappoport, Z., Apeloig, Y., Eds.; John Wiley & Sons, Ltd: Chichester, UK, 1998; Vol. 2.

(64) Wrackmeyer, B. Application of $^{119}$Sn NMR Parameters; 1999; pp 203–264.

(65) Harris, R. K.; Kimber, B. J. $^{29}$Si NMR as a Tool for Studying Silicones. *Appl. Spectrosc. Rev.* **1975**, *10* (1).

(66) Collins, W. T.; Frye, C. L. Condensed Soluble Hydrogensilsesquioxane Resin. US3615272A, 1968.

(67) Hessel, C. M.; Henderson, E. J.; Veinot, J. G. C. Hydrogen Silsesquioxane: A Molecular Precursor for Nanocrystalline Si−SiO$_2$ Composites and Freestanding Hydride-Surface-Terminated Silicon Nanoparticles. *Chem. Mater.* **2006**, *18* (26), 6139–6146.

(68) Barr, T. L.; Seal, S. Nature of the Use of Adventitious Carbon as a Binding Energy Standard. *J. Vac. Sci. Technol.* **1995**, *13* (3).

(69) Payne, B. P.; Biesinger, M. C.; McIntyre, N. S. The Study of Polycrystalline Nickel Metal Oxidation by Water Vapour. *J. Electron Spectrosc. Relat. Phenomena* **2009**, *175* (1–3).

(70) Sublemontier, O.; Nicolas, C.; Aureau, D.; Patanen, M.; Kintz, H.; Liu, X.; Gaveau, M.-A.; le Garrec, J.-L.; Robert, E.; Barreda, F.-A.; Etcheberry, A.; Reynaud, C.; Mitchell, J. B.; Miron, C. X-Ray Photoelectron Spectroscopy of Isolated Nanoparticles. *J. Phys. Chem. Lett.* **2014**, *5* (19).

(71) Plymale, N. T.; Dasog, M.; Brunschwig, B. S.; Lewis, N. S. A Mechanistic Study of the Oxidative Reaction of Hydrogen-Terminated Si(111) Surfaces with Liquid Methanol. *J. Phys. Chem. C* **2017**, *121* (8).

(72)   Yang, Z.; Iqbal, M.; Dobbie, A. R.; Veinot, J. G. C. Surface-Induced Alkene Oligomerization: Does Thermal Hydrosilylation Really Lead to Monolayer Protected Silicon Nanocrystals? *J. Am. Chem. Soc.* **2013**, *135* (46).

(73)   Bruker AXS GmbH. *TOPAS V4: General Profile and Structure Analysis Software for Powder Diffraction Data - User's Manual*; Karlsruhe, Germany, 2009; Vol. 4.2.

(74)   Bennett, A. E.; Rienstra, C. M.; Auger, M.; Lakshmi, K. v.; Griffin, R. G. Heteronuclear Decoupling in Rotating Solids. *J. Chem. Phys.* **1995**, *103* (16), 6951–6958.

(75)   Hayashi, S.; Hayamizu, K. Chemical Shift Standards in High-Resolution Solid-State NMR (1) $^{13}$C, $^{29}$Si, and $^{1}$H Nuclei. *Bull. Chem. Soc. Jpn.* **1991**, *64* (2).

(76)   Bloch, F. Nuclear Induction. *Phys. Rev.* **1946**, *70* (7–8), 460–474.

(77)   Pines, A.; Gibby, M. G.; Waugh, J. S. Proton-Enhanced Nuclear Induction Spectroscopy. A Method for High Resolution NMR of Dilute Spins in Solids. *J. Chem. Phys.* **1972**, *56* (4), 1776–1777.

(78)   Freeman, R.; Hill, H. D. W. Fourier Transform Study of NMR Spin–Lattice Relaxation by "Progressive Saturation." *J. Chem. Phys.* **1971**, *54* (8), 3367–3377.

(79)   Hessel, C. M.; Reid, D.; Panthani, M. G.; Rasch, M. R.; Goodfellow, B. W.; Wei, J.; Fujii, H.; Akhavan, V.; Korgel, B. A. Synthesis of Ligand-Stabilized Silicon Nanocrystals with Size-Dependent Photoluminescence Spanning Visible to Near-Infrared Wavelengths. *Chem. Mater.* **2012**, *24* (2).

(80)   Yu, Y.; Hessel, C. M.; Bogart, T. D.; Panthani, M. G.; Rasch, M. R.; Korgel, B. A. Room Temperature Hydrosilylation of Silicon Nanocrystals with Bifunctional Terminal Alkenes. *Langmuir* **2013**, *29* (5).

(81)   Buriak, J. M. Illuminating Silicon Surface Hydrosilylation: An Unexpected Plurality of Mechanisms. *Chem. Mater.* **2014**, *26* (1).

(82)   Weeks, S. L.; Macco, B.; van de Sanden, M. C. M.; Agarwal, S. Gas-Phase Hydrosilylation of Plasma-Synthesized Silicon Nanocrystals with Short- and Long-Chain Alkynes. *Langmuir* **2012**, *28* (50).

(83)   Nelles, J.; Sendor, D.; Ebbers, A.; Petrat, F. M.; Wiggers, H.; Schulz, C.; Simon, U. Functionalization of Silicon Nanoparticles via Hydrosilylation with 1-Alkenes. *Colloid and Polym. Sci.* **2007**, *285* (7).

(84)   Höhlein, I. M. D.; Kehrle, J.; Helbich, T.; Yang, Z.; Veinot, J. G. C.; Rieger, B. Diazonium Salts as Grafting Agents and Efficient Radical-Hydrosilylation Initiators for Freestanding Photoluminescent Silicon Nanocrystals. *Chem. Eur. J.* **2014**, *20* (15).

(85)   Purkait, T. K.; Iqbal, M.; Wahl, M. H.; Gottschling, K.; Gonzalez, C. M.; Islam, M. A.; Veinot, J. G. C. Borane-Catalyzed Room-Temperature Hydrosilylation of Alkenes/Alkynes on Silicon Nanocrystal Surfaces. *J. Am. Chem. Soc.* **2014**, *136* (52).

(86)   Balzar, D.; Audebrand, N.; Daymond, M. R.; Fitch, A.; Hewat, A.; Langford, J. I.; le Bail, A.; Louër, D.; Masson, O.; McCowan, C. N.; Popa, N. C.; Stephens, P. W.; Toby, B. H. Size–Strain Line-Broadening Analysis of the Ceria Round-Robin Sample. *J. Appl. Crystallogr.* **2004**, *37* (6).

(87)   Smith, J. v.; Blackwell, C. S. Nuclear Magnetic Resonance of Silica Polymorphs. *Nature* **1983**, *303* (5914).

(88)   Sekine, T.; Tansho, M.; Kanzaki, M. $^{29}$Si Magic-Angle-Spinning Nuclear-Magnetic-Resonance Study of Spinel-Type Si$_3$N$_4$. *Appl. Phys. Lett.* **2001**, *78* (20).

(89)   He, J.; Ba, Y.; Ratcliffe, C. I.; Ripmeester, J. A.; Klug, D. D.; Tse, J. S.; Preston, K. F. Encapsulation of Silicon Nanoclusters in Zeolite Y. *J. Am. Chem. Soc.* **1998**, *120* (41).

(90)   Petit, D.; Chazalviel, J.-N.; Ozanam, F.; Devreux, F. Porous Silicon Structure Studied by Nuclear Magnetic Resonance. *Appl. Phys. Lett.* **1997**, *70* (2).

(91)   Hahn, J. Contributions to the Chemistry of Silicon and Germanium, XXIX [1] $^{29}$Si NMR Spectroscopic Investigations on Straight and Branched Silanes. *Zeitschrift für Naturforschung B* **1980**, *35* (3).

(92) Hartman, J. S.; Richardson, M. F.; Sherriff, B. L.; Winsborrow, B. G. Magic Angle Spinning NMR Studies of Silicon Carbide: Polytypes, Impurities, and Highly Inefficient Spin-Lattice Relaxation. *J. Am. Chem. Soc.* **1987**, *109* (20).

(93) Holzman, G. R.; Lauterbur, P. C.; Anderson, J. H.; Koth, W. Nuclear Magnetic Resonance Field Shifts of $^{29}$Si in Various Materials. *J. Chem. Phys.* **1956**, *25* (1).

(94) Reimer, J. A.; Murphy, P. D.; Gerstein, B. C.; Knights, J. C. Silicon-29 Cross-polarization Magic-angle Sample Spinning Spectra in Amorphous Silicon–Hydrogen Films. *J. Chem. Phys.* **1981**, *74* (2).

(95) Shao, W.-L.; Shinar, J.; Gerstein, B. C.; Li, F.; Lannin, J. S. Magic-Angle Spinning $^{29}$Si NMR Study of Short-Range Order in *a* -Si. *Phys. Rev. B* **1990**, *41* (13).

(96) Bercier, J. J.; Jirousek, M.; Graetzel, M.; Klink, J. J. van der. Evidence from NMR for Temperature-Dependent Bardeen-Friedel Oscillations in Nanometre-Sized Silver Particles. *J. Phys. Condens. Mater.* **1993**, *5* (44).

(97) Charles, R. J.; Harrison, W. A. Size Effect in Nuclear Magnetic Resonance. *Phys. Rev. Lett.* **1963**, *11* (2).

(98) Terskikh, V. v.; Moudrakovski, I. L.; Ratcliffe, C. I.; Ripmeester, J. A.; Reinhold, C. J.; Anderson, P. A.; Edwards, P. P. Size Effects on the Nuclear Magnetic Resonance of Sodium Metal Confined in Controlled Pore Glasses. In *Magnetic Resonance in Colloid and Interface Science*; Fraissard, J., Lapina, O., Eds.; Springer Netherlands: Dordrecht, 2002; Vol. 76.

(99) Javadi, M.; Michaelis, V. K.; Veinot, J. G. C. Thermally Induced Evolution of "Ge(OH)$_2$": Controlling the Formation of Oxide-Embedded Ge Nanocrystals. *J. Phys. Chem. C* **2018**, *122* (30).

(100) Cadars, S.; Smith, B. J.; Epping, J. D.; Acharya, S.; Belman, N.; Golan, Y.; Chmelka, B. F. Atomic Positional Versus Electronic Order in Semiconducting ZnSe Nanoparticles. *Phys. Chem. Lett.* **2009**, *103* (13).

(101) Mobarok, M. H.; Luber, E. J.; Bernard, G. M.; Peng, L.; Wasylishen, R. E.; Buriak, J. M. Phase-Pure Crystalline Zinc Phosphide Nanoparticles: Synthetic Approaches and Characterization. *Chem. Mater.* **2014**, *26* (5).

(102) Ratcliffe, C. I.; Yu, K.; Ripmeester, J. A.; Badruz Zaman, Md.; Badarau, C.; Singh, S. Solid State NMR Studies of Photoluminescent Cadmium Chalcogenide Nanoparticles. *Phys. Chem. Chem. Phys.* **2006**, *8* (30).

(103) Tomaselli, M.; Yarger, J. L.; Bruchez, M.; Havlin, R. H.; deGraw, D.; Pines, A.; Alivisatos, A. P. NMR Study of InP Quantum Dots: Surface Structure and Size Effects. *J. Chem. Phys.* **1999**, *110* (18).

(104) Marbella, L. E.; Millstone, J. E. NMR Techniques for Noble Metal Nanoparticles. *Chem. Mater.* **2015**, *27* (8).

(105) Maciel, G. E.; Sindorf, D. W. Silicon-29 NMR Study of the Surface of Silica Gel by Cross Polarization and Magic-Angle Spinning. *J. Am. Chem. Soc.* **1980**, *102* (25).

(106) Hayashi, S.; Hayamizu, K.; Yamasaki, S.; Matsuda, A.; Tanaka, K. Interpretation of [29]Si Nuclear Magnetic Resonance Spectra of Amorphous Hydrogenated Silicon. *J. Appl. Phys.* **1986**, *60* (5).

(107) Hayashi, S.; Hayamizu, K.; Yamasaki, S.; Matsuda, A.; Tanaka, K. [29]Si Nuclear Magnetic Resonance of Amorphous Hydrogenated Silicon and Amorphous Microcrystalline Mixed-Phase Hydrogenated Silicon. *Phys. Rev. B* **1987**, *35* (10).

(108) Pietraβ, T.; Bifone, A.; Roth, R. D.; Koch, V.-P.; Alivisatos, A. P.; Pines, A. [29]Si High Resolution Solid State Nuclear Magnetic Resonance Spectroscopy of Porous Silicon. *J. Non. Cryst. Solids* **1996**, *202* (1–2).

(109) Hayashi, S.; Hayamizu, K.; Yamasaki, S.; Matsuda, A.; Tanaka, K. Silicon-29 Nuclear Magnetic Resonance Study of Amorphous-Microcrystalline Mixed-Phase Hydrogenated Silicon. *Jpn. J. Appl. Phys.* **1986**, *25* (Part 2, No. 4).

(110) Wang, M.; Wu, X.-P.; Zheng, S.; Zhao, L.; Li, L.; Shen, L.; Gao, Y.; Xue, N.; Guo, X.; Huang, W.; Gan, Z.; Blanc, F.; Yu, Z.; Ke, X.; Ding, W.; Gong, X.-Q.; Grey, C. P.; Peng,

L. Identification of Different Oxygen Species in Oxide Nanostructures with $^{17}$O Solid-State NMR Spectroscopy. *Sci. Adv.* **2015**, *1* (1).

(111) Jameson, C. J.; Gutowsky, H. S. Calculation of Chemical Shifts. I. General Formulation and the *Z* Dependence. *J. Chem. Phys.* **1964**, *40* (6).

(112) Ramsey, N. F. Magnetic Shielding of Nuclei in Molecules. *Phys. Rev.* **1950**, *78* (6).

(113) Thayer, A. M.; Steigerwald, M. L.; Duncan, T. M.; Douglass, D. C. NMR Study of Semiconductor Molecular Clusters. *Phys. Rev. Lett.* **1988**, *60* (25).

(114) Bawendi, M. G.; Carroll, P. J.; Wilson, W. L.; Brus, L. E. Luminescence Properties of CdSe Quantum Crystallites: Resonance between Interior and Surface Localized States. *J. Chem. Phys.* **1992**, *96* (2).

(115) Colvin, V. L.; Alivisatos, A. P.; Tobin, J. G. Valence-Band Photoemission from a Quantum-Dot System. *Phys. Rev. Lett.* **1991**, *66* (21).

(116) Comedi, D.; Zalloum, O. H. Y.; Irving, E. A.; Wojcik, J.; Roschuk, T.; Flynn, M. J.; Mascher, P. X-Ray-Diffraction Study of Crystalline Si Nanocluster Formation in Annealed Silicon-Rich Silicon Oxides. *J. Appl. Phys.* **2006**, *99* (2).

(117) Zhao, Y.; Kim, Y.-H.; Du, M.-H.; Zhang, S. First-Principles Prediction of Icosahedral Quantum Dots for Tetravalent Semiconductors. *Phys. Rev. Lett.* **2004**, *93* (1).

(118) Avramov, P. v.; Fedorov, D. G.; Sorokin, P. B.; Chernozatonskii, L. A.; Gordon, M. S. New Symmetric Families of Silicon Quantum Dots and Their Conglomerates as a Tunable Source of Photoluminescence in Nanodevices. *Los Alamos Nat. Lab, Prep. Arch., Condens. Matter* **2007**, 1–19.

(119) Okada, Y.; Tokumaru, Y. Precise Determination of Lattice Parameter and Thermal Expansion Coefficient of Silicon between 300 and 1500 K. *J. Appl. Phys.* **1984**, *56* (2).

*Chapter 5 References*

(1)  Pines, A.; Gibby, M. G.; Waugh, J. S. Proton-Enhanced Nuclear Induction Spectroscopy. A Method for High Resolution NMR of Dilute Spins in Solids. *J. Chem. Phys.* **1972**, *56* (4), 1776–1777.

(2)  Andrew, E. R.; Bradeuey, A.; Eades, R. G. Nuclear Magnetic Resonance Spectra from a Crystal Rotated at High Speed. *Nature* **1958**, *182* (4650), 1659–1659.

(3)  Lowe, I. J. Free Induction Decays of Rotating Solids. *Phys. Rev. Lett.* **1959**, *2* (7), 285–287.

(4)  Keeler, E. G.; Michaelis, V. K.; Colvin, M. T.; Hung, I.; Gor'kov, P. L.; Cross, T. A.; Gan, Z.; Griffin, R. G. $^{17}$O MAS NMR Correlation Spectroscopy at High Magnetic Fields. *J. Am. Chem. Soc.* **2017**, *139* (49), 17953–17963.

(5)  Overhauser, A. W. Polarization of Nuclei in Metals. *Phys. Rev.* **1953**, *92* (2), 411–415.

(6)  Carver, T. R.; Slichter, C. P. Polarization of Nuclear Spins in Metals. *Phys. Rev.* **1953**, *92* (1), 212–213.

(7)  Maly, T.; Debelouchina, G. T.; Bajaj, V. S.; Hu, K.-N.; Joo, C.-G.; Mak–Jurkauskas, M. L.; Sirigiri, J. R.; van der Wel, P. C. A.; Herzfeld, J.; Temkin, R. J.; Griffin, R. G. Dynamic Nuclear Polarization at High Magnetic Fields. *J. Chem. Phys.* **2008**, *128* (5), 052211.

(8)  Ha, M.; Michaelis, V. K. High-Frequency Dynamic Nuclear Polarization NMR for Solids: Part 2 – Development and Applications. In *Modern Magnetic Resonance*; Springer International Publishing: Cham, 2017; pp 1–18.

(9)  Song, C.; Hu, K.-N.; Joo, C.-G.; Swager, T. M.; Griffin, R. G. TOTAPOL: A Biradical Polarizing Agent for Dynamic Nuclear Polarization Experiments in Aqueous Media. *J. Am. Chem. Soc.* **2006**, *128* (35), 11385–11390.

(10) Kiesewetter, M. K.; Corzilius, B.; Smith, A. A.; Griffin, R. G.; Swager, T. M. Dynamic Nuclear Polarization with a Water-Soluble Rigid Biradical. *J. Am. Chem. Soc.* **2012**, *134* (10), 4537–4540.

(11)   Sauvée, C.; Rosay, M.; Casano, G.; Aussenac, F.; Weber, R. T.; Ouari, O.; Tordo, P. Highly Efficient, Water-Soluble Polarizing Agents for Dynamic Nuclear Polarization at High Frequency. *Angew. Chem. Int. Ed.* **2013**, *52* (41), 10858–10861.

(12)   Zagdoun, A.; Casano, G.; Ouari, O.; Schwarzwälder, M.; Rossini, A. J.; Aussenac, F.; Yulikov, M.; Jeschke, G.; Copéret, C.; Lesage, A.; Tordo, P.; Emsley, L. Large Molecular Weight Nitroxide Biradicals Providing Efficient Dynamic Nuclear Polarization at Temperatures up to 200 K. *J. Am. Chem. Soc.* **2013**, *135* (34), 12790–12797.

(13)   Kubicki, D. J.; Casano, G.; Schwarzwälder, M.; Abel, S.; Sauvée, C.; Ganesan, K.; Yulikov, M.; Rossini, A. J.; Jeschke, G.; Copéret, C.; Lesage, A.; Tordo, P.; Ouari, O.; Emsley, L. Rational Design of Dinitroxide Biradicals for Efficient Cross-Effect Dynamic Nuclear Polarization. *Chem. Sci.* **2016**, *7* (1), 550–558.

(14)   Ong, T.-C.; Mak-Jurkauskas, M. L.; Walish, J. J.; Michaelis, V. K.; Corzilius, B.; Smith, A. A.; Clausen, A. M.; Cheetham, J. C.; Swager, T. M.; Griffin, R. G. Solvent-Free Dynamic Nuclear Polarization of Amorphous and Crystalline Ortho -Terphenyl. *J. Phys. Chem. B* **2013**, *117* (10), 3040–3046.

(15)   Sauvée, C.; Casano, G.; Abel, S.; Rockenbauer, A.; Akhmetzyanov, D.; Karoui, H.; Siri, D.; Aussenac, F.; Maas, W.; Weber, R. T.; Prisner, T.; Rosay, M.; Tordo, P.; Ouari, O. Tailoring of Polarizing Agents in the BTurea Series for Cross-Effect Dynamic Nuclear Polarization in Aqueous Media. *Chem. Eur. J.* **2016**, *22* (16), 5598–5606.

(16)   Matsuki, Y.; Maly, T.; Ouari, O.; Karoui, H.; Le Moigne, F.; Rizzato, E.; Lyubenova, S.; Herzfeld, J.; Prisner, T.; Tordo, P.; Griffin, R. G. Dynamic Nuclear Polarization with a Rigid Biradical. *Angew. Chem. Int. Ed.* **2009**, *48* (27), 4996–5000.

(17)   Zagdoun, A.; Casano, G.; Ouari, O.; Lapadula, G.; Rossini, A. J.; Lelli, M.; Baffert, M.; Gajan, D.; Veyre, L.; Maas, W. E.; Rosay, M.; Weber, R. T.; Thieuleux, C.; Coperet, C.; Lesage, A.; Tordo, P.; Emsley, L. A Slowly Relaxing Rigid Biradical for Efficient Dynamic Nuclear Polarization Surface-Enhanced NMR Spectroscopy: Expeditious Characterization of Functional Group Manipulation in Hybrid Materials. *J. Am. Chem. Soc.* **2012**, *134* (4), 2284–2291.

(18)    Mathies, G.; Caporini, M. A.; Michaelis, V. K.; Liu, Y.; Hu, K.-N.; Mance, D.; Zweier, J. L.; Rosay, M.; Baldus, M.; Griffin, R. G. Efficient Dynamic Nuclear Polarization at 800 MHz/527 GHz with Trityl-Nitroxide Biradicals. *Angew. Chem. Int. Ed.* **2015**, *54* (40), 11770–11774.

(19)    Mentink-Vigier, F.; Mathies, G.; Liu, Y.; Barra, A.-L.; Caporini, M. A.; Lee, D.; Hediger, S.; G. Griffin, R.; De Paëpe, G. Efficient Cross-Effect Dynamic Nuclear Polarization without Depolarization in High-Resolution MAS NMR. *Chem. Sci.* **2017**, *8* (12), 8150–8163.

(20)    Lee, D.; Hediger, S.; Paëpe, G. De. High-Field Solid-State NMR with Dynamic Nuclear Polarization. In *Modern Magnetic Resonance*; Springer International Publishing: Cham, 2017; pp 1–17.

(21)    Ni, Q. Z.; Daviso, E.; Can, T. V.; Markhasin, E.; Jawla, S. K.; Swager, T. M.; Temkin, R. J.; Herzfeld, J.; Griffin, R. G. High Frequency Dynamic Nuclear Polarization. *Acc. Chem. Res.* **2013**, *46* (9), 1933–1941.

(22)    Rossini, A. J.; Zagdoun, A.; Lelli, M.; Lesage, A.; Copéret, C.; Emsley, L. Dynamic Nuclear Polarization Surface Enhanced NMR Spectroscopy. *Acc. Chem. Res.* **2013**, *46* (9), 1942–1951.

(23)    Maly, T.; Andreas, L. B.; Smith, A. A.; Griffin, R. G. $^2$H-DNP-Enhanced $^2$H–$^{13}$C Solid-State NMR Correlation Spectroscopy. *Phys. Chem. Chem. Phys.* **2010**, *12* (22), 5872.

(24)    Michaelis, V. K.; Corzilius, B.; Smith, A. A.; Griffin, R. G. Dynamic Nuclear Polarization of $^{17}$O: Direct Polarization. *J. Phys. Chem. B* **2013**, *117* (48), 14894–14906.

(25)    Michaelis, V. K.; Smith, A. A.; Corzilius, B.; Haze, O.; Swager, T. M.; Griffin, R. G. High-Field $^{13}$C Dynamic Nuclear Polarization with a Radical Mixture. *J. Am. Chem. Soc.* **2013**, *135* (8), 2935–2938.

(26)    Michaelis, V. K.; Ong, T.-C.; Kiesewetter, M. K.; Frantz, D. K.; Walish, J. J.; Ravera, E.; Luchinat, C.; Swager, T. M.; Griffin, R. G. Topical Developments in High-Field Dynamic Nuclear Polarization. *Isr. J. Chem.* **2014**, *54* (1–2), 207–221.

(27)   Corzilius, B.; Smith, A. A.; Griffin, R. G. Solid Effect in Magic Angle Spinning Dynamic Nuclear Polarization. *J. Chem. Phys.* **2012**, *137* (5), 054201.

(28)   Smith, A. A.; Corzilius, B.; Barnes, A. B.; Maly, T.; Griffin, R. G. Solid Effect Dynamic Nuclear Polarization and Polarization Pathways. *J. Chem. Phys.* **2012**, *136* (1), 015101.

(29)   Abragam, A.; Proctor, W. G. Une Nouvelle Methode De Polarisation Dynamique Des Noyaux Atomiques Dans Les Solides. *Cr. Hebd. Acad. Sci.* **1958**, *246*, 2253–2256.

(30)   Hwang, C. F.; Hill, D. A. New Effect in Dynamic Polarization. *Phys. Rev. Lett.* **1967**, *18* (4), 110–112.

(31)   Hovav, Y.; Feintuch, A.; Vega, S. Theoretical Aspects of Dynamic Nuclear Polarization in the Solid State – The Cross Effect. *J. Magn. Reson.* **2012**, *214*, 29–41.

(32)   Ha, M.; Michaelis, V. K. High-Frequency Dynamic Nuclear Polarization NMR for Solids: Part 1 – An Introduction. In *Modern Magnetic Resonance*; Springer International Publishing: Cham, 2017; pp 1–24.

(33)   Hu, K.-N.; Bajaj, V. S.; Rosay, M.; Griffin, R. G. High-Frequency Dynamic Nuclear Polarization Using Mixtures of TEMPO and Trityl Radicals. *J. Chem. Phys.* **2007**, *126* (4), 044512.

(34)   Gunther, W. R.; Michaelis, V. K.; Caporini, M. A.; Griffin, R. G.; Román-Leshkov, Y. Dynamic Nuclear Polarization NMR Enables the Analysis of Sn-Beta Zeolite Prepared with Natural Abundance [119]Sn Precursors. *J. Am. Chem. Soc.* **2014**, *136* (17), 6219–6222.

(35)   Wenk, P.; Kaushik, M.; Richter, D.; Vogel, M.; Suess, B.; Corzilius, B. Dynamic Nuclear Polarization of Nucleic Acid with Endogenously Bound Manganese. *J. Biomol. NMR* **2015**, *63* (1), 97–109.

(36)   Wolf, T.; Kumar, S.; Singh, H.; Chakrabarty, T.; Aussenac, F.; Frenkel, A. I.; Major, D. T.; Leskes, M. Endogenous Dynamic Nuclear Polarization for Natural Abundance ^{17}O and Lithium NMR in the Bulk of Inorganic Solids. *J. Am. Chem. Soc.* **2019**, *141* (1), 451–462.

(37)  Corzilius, B.; Michaelis, V. K.; Penzel, S. A.; Ravera, E.; Smith, A. A.; Luchinat, C.; Griffin, R. G. Dynamic Nuclear Polarization of $^1H$, $^{13}C$, and $^{59}Co$ in a Tris(Ethylenediamine)Cobalt(III) Crystalline Lattice Doped with Cr(III). *J. Am. Chem. Soc.* **2014**, *136* (33), 11716–11727.

(38)  Schumacher, R. T.; Slichter, C. P. Electron Spin Paramagnetism of Lithium and Sodium. *Phys. Rev.* **1956**, *101* (1), 58–65.

(39)  Dementyev, A. E.; Cory, D. G.; Ramanathan, C. Dynamic Nuclear Polarization in Silicon Microparticles. *Phys. Rev. Lett.* **2008**, *100* (12), 127601.

(40)  Guy, M. L.; van Schooten, K. J.; Zhu, L.; Ramanathan, C. Chemisorption of Water on the Surface of Silicon Microparticles Measured by Dynamic Nuclear Polarization Enhanced NMR. *J. Phys. Chem. C* **2017**, *121* (5), 2748–2754.

(41)  Brodsky, M. H.; Title, R. S. Electron Spin Resonance in Amorphous Silicon, Germanium, and Silicon Carbide. *Phys. Rev. Lett.* **1969**, *23* (11), 581–585.

(42)  Veinot, J. G. C. Synthesis, Surface Functionalization, and Properties of Freestanding Silicon Nanocrystals. *Chem. Comm.* **2006**, No. 40, 4160.

(43)  Santos, H. A.; Mäkilä, E.; Airaksinen, A. J.; Bimbo, L. M.; Hirvonen, J. Porous Silicon Nanoparticles for Nanomedicine: Preparation and Biomedical Applications. *Nanomedicine* **2014**, *9* (4), 535–554.

(44)  Hessel, C. M.; Henderson, E. J.; Veinot, J. G. C. Hydrogen Silsesquioxane: A Molecular Precursor for Nanocrystalline Si−$SiO_2$ Composites and Freestanding Hydride-Surface-Terminated Silicon Nanoparticles. *Chem. Mater.* **2006**, *18* (26), 6139–6146.

(45)  Thiessen, A. N.; Ha, M.; Hooper, R. W.; Yu, H.; Oliynyk, A. O.; Veinot, J. G. C.; Michaelis, V. K. Silicon Nanoparticles: Are They Crystalline from the Core to the Surface? *Chem. Mater.* **2019**, *31* (3), 678–688.

(46)  Morcombe, C. R.; Zilm, K. W. Chemical Shift Referencing in MAS Solid State NMR. *J. Magn. Reson.* **2003**, *162* (2), 479–486.

(47) Rosay, M.; Scrgeyev, I.; Tometich, L.; Hickey, C.; Roitman, A.; Yake, D.; Berry, D. Opportunities and Challenges for EIK's in DNP NMR Applications. In *2018 43rd International Conference on Infrared, Millimeter, and Terahertz Waves (IRMMW-THz)*; IEEE, 2018; pp 1–2.

(48) Roitman, A.; Hyttinen, M.; Deng, H.; Berry, D.; MacHattie, R. Progress in Power Enhancement of Sub-Millimeter Compact EIKs. In *2017 42nd International Conference on Infrared, Millimeter, and Terahertz Waves (IRMMW-THz)*; IEEE, 2017; pp 1–2.

(49) Meyer, B. *Low Temperature Spectroscopy*; American Elsevier: New York, 1971.

(50) Bloch, F. Nuclear Induction. *Phys. Rev.* **1946**, *70* (7–8), 460–474.

(51) Björgvinsdóttir, S.; Walder, B. J.; Pinon, A. C.; Yarava, J. R.; Emsley, L. DNP Enhanced NMR with Flip-Back Recovery. *J. Magn. Reson.* **2018**, *288*, 69–75.

(52) Hahn, E. L. Spin Echoes. *Phys. Rev.* **1950**, *80* (4), 580–594.

(53) Freeman, R.; Hill, H. D. W. Fourier Transform Study of NMR Spin–Lattice Relaxation by "Progressive Saturation." *J. Chem. Phys.* **1971**, *54* (8), 3367–3377.

(54) Lee, B. G.; Hiller, D.; Luo, J.-W.; Semonin, O. E.; Beard, M. C.; Zacharias, M.; Stradins, P. Strained Interface Defects in Silicon Nanocrystals. *Adv. Funct. Mater.* **2012**, *22* (15), 3223–3232.

(55) Kleovoulou, K.; Kelires, P. C. Stress State of Embedded Si Nanocrystals. *Phys. Rev. B* **2013**, *88* (8), 085424.

(56) Cassidy, M. C.; Chan, H. R.; Ross, B. D.; Bhattacharya, P. K.; Marcus, C. M. In Vivo Magnetic Resonance Imaging of Hyperpolarized Silicon Particles. *Nat. Nanotechnol.* **2013**, *8* (5), 363–368.

(57) Lockwood, R.; Yang, Z.; Sammynaiken, R.; Veinot, J. G. C.; Meldrum, A. Light-Induced Evolution of Silicon Quantum Dot Surface Chemistry—Implications for Photoluminescence, Sensing, and Reactivity. *Chem. Mater.* **2014**, *26* (19), 5467–5474.

(58)   King, J. P.; Jeong, K.; Vassiliou, C. C.; Shin, C. S.; Page, R. H.; Avalos, C. E.; Wang, H.-J.; Pines, A. Room-Temperature in Situ Nuclear Spin Hyperpolarization from Optically Pumped Nitrogen Vacancy Centres in Diamond. *Nat. Comm.* **2015**, *6* (1), 8965.

(59)   Dasog, M.; Yang, Z.; Regli, S.; Atkins, T. M.; Faramus, A.; Singh, M. P.; Muthuswamy, E.; Kauzlarich, S. M.; Tilley, R. D.; Veinot, J. G. C. Chemical Insight into the Origin of Red and Blue Photoluminescence Arising from Freestanding Silicon Nanocrystals. *ACS Nano* **2013**, *7* (3), 2676–2685.

(60)   Pitters, J. L.; Piva, P. G.; Tong, X.; Wolkov, R. A. Reversible Passivation of Silicon Dangling Bonds with the Stable Radical TEMPO. *Nano Lett.* **2003**, *3*, 1431–1435.

(61)   Yang, Z.; Gonzalez, C. M.; Purkait, T. K.; Iqbal, M.; Meldrum, A.; Veinot, J. G. C. Radical Initiated Hydrosilylation on Silicon Nanocrystal Surfaces: An Evaluation of Functional Group Tolerance and Mechanistic Study. *Langmuir* **2015**, *31* (38), 10540–10548.

(62)   Aptekar, J. W.; Cassidy, M. C.; Johnson, A. C.; Barton, R. A.; Lee, M.; Ogier, A. C.; Vo, C.; Anahtar, M. N.; Ren, Y.; Bhatia, S. N.; Ramanathan, C.; Cory, D. G.; Hill, A. L.; Mair, R. W.; Rosen, M. S.; Walsworth, R. L.; Marcus, C. M. Silicon Nanoparticles as Hyperpolarized Magnetic Resonance Imaging Agents. *ACS Nano* **2009**, *3* (12), 4003–4008.

(63)   Kessenikh, A. V.; Lushchikov, V. I.; Manenkov, A. A.; Taran, Y. V. Proton Polarization in Irradiated Polyethylenes. *Sov. Phys. Solid State* **1963**, *5*, 321–329.

(64)   Wollan, D. S. Dynamic Nuclear Polarization with an Inhomogeneously Broadened ESR Line. I. Theory. *Phys. Rev. B* **1976**, *13* (9), 3671–3685.

(65)   Wollan, D. S. Dynamic Nuclear Polarization with an Inhomogeneously Broadened ESR Line. II. Experiment. *Phys. Rev. B* **1976**, *13* (9), 3686–3696.

(66)   Abragam, A. *Principles of Nuclear Magnetic Resonance*; Oxford University Press: New York, 1961.

(67)   Slichter, C. P. *Principles of Magnetic Resonance*; Harper & Row: New York, 1963.

(68)   Varshni, Y. P. Temperature Dependence of the Energy Gap in Semiconductors. *Physica* **1967**, *34* (1), 149–154.

(69)   Sinelnikov, R.; Dasog, M.; Beamish, J.; Meldrum, A.; Veinot, J. G. C. Revisiting an Ongoing Debate: What Role Do Surface Groups Play in Silicon Nanocrystal Photoluminescence? *ACS Photonics* **2017**, *4* (8), 1920–1929.

(70)   Wittmann, J. J.; Eckardt, M.; Harneit, W.; Corzilius, B. Electron-Driven Spin Diffusion Supports Crossing the Diffusion Barrier in MAS DNP. *Phys. Chem. Chem. Phys.* **2018**, *20* (16), 11418–11429.

(71)   Pinon, A. C.; Schlagnitweit, J.; Berruyer, P.; Rossini, A. J.; Lelli, M.; Socie, E.; Tang, M.; Pham, T.; Lesage, A.; Schantz, S.; Emsley, L. Measuring Nano- to Microstructures from Relayed Dynamic Nuclear Polarization NMR. *J. Phys. Chem. C* **2017**, *121* (29), 15993–16005.

(72)   Björgvinsdóttir, S.; Walder, B. J.; Pinon, A. C.; Emsley, L. Bulk Nuclear Hyperpolarization of Inorganic Solids by Relay from the Surface. *J. Am. Chem. Soc.* **2018**, *140* (25), 7946–7951.

(73)   Maricq, M. M.; Waugh, J. S. NMR in Rotating Solids. *J. Chem. Phys.* **1979**, *70* (7), 3300–3316.

(74)   Rogawski, R.; Sergeyev, I. V.; Zhang, Y.; Tran, T. H.; Li, Y.; Tong, L.; McDermott, A. E. NMR Signal Quenching from Bound Biradical Affinity Reagents in DNP Samples. *J. Phys. Chem. B* **2017**, *121* (48), 10770–10781.

*Chapter 6 References*

(1)    *NMR of Biomolecules*; Bertini, I., McGreevy, K. S., Parigi, G., Eds.; Wiley-VCH Verlag GmbH & Co. KGaA: Weinheim, Germany, 2012.

(2)    Park, S. H.; Yang, C.; Opella, S. J.; Mueller, L. J. Resolution and Measurement of Heteronuclear Dipolar Couplings of a Noncrystalline Protein Immobilized in a Biological

Supramolecular Assembly by Proton-Detected MAS Solid-State NMR Spectroscopy. *J. Magn. Reson.* **2013**, *237*, 164–168.

(3)     Su, Y.; Andreas, L.; Griffin, R. G. Magic Angle Spinning NMR of Proteins: High-Frequency Dynamic Nuclear Polarization and [1]H Detection. *Annu. Rev. Biochem.* **2015**, *84* (1), 465–497.

(4)     Penzel, S.; Smith, A. A.; Agarwal, V.; Hunkeler, A.; Org, M.-L.; Samoson, A.; Böckmann, A.; Ernst, M.; Meier, B. H. Protein Resonance Assignment at MAS Frequencies Approaching 100 kHz: A Quantitative Comparison of J-Coupling and Dipolar-Coupling-Based Transfer Methods. *J. Biomol. NMR* **2015**, *63* (2), 165–186.

(5)     Barbet-Massin, E.; Pell, A. J.; Retel, J. S.; Andreas, L. B.; Jaudzems, K.; Franks, W. T.; Nieuwkoop, A. J.; Hiller, M.; Higman, V.; Guerry, P.; Bertarello, A.; Knight, M. J.; Felletti, M.; Le Marchand, T.; Kotelovica, S.; Akopjana, I.; Tars, K.; Stoppini, M.; Bellotti, V.; Bolognesi, M.; Ricagno, S.; Chou, J. J.; Griffin, R. G.; Oschkinat, H.; Lesage, A.; Emsley, L.; Herrmann, T.; Pintacuda, G. Rapid Proton-Detected NMR Assignment for Proteins with Fast Magic Angle Spinning. *J. Am. Chem. Soc.* **2014**, *136* (35), 12489–12497.

(6)     Knight, M. J.; Webber, A. L.; Pell, A. J.; Guerry, P.; Barbet-Massin, E.; Bertini, I.; Felli, I. C.; Gonnelli, L.; Pierattelli, R.; Emsley, L.; Lesage, A.; Herrmann, T.; Pintacuda, G. Fast Resonance Assignment and Fold Determination of Human Superoxide Dismutase by High-Resolution Proton-Detected Solid-State MAS NMR Spectroscopy. *Angew. Chemie Int. Ed.* **2011**, *50* (49), 11697–11701.

(7)     Böckmann, A.; Ernst, M.; Meier, B. H. Spinning Proteins, the Faster, the Better? *J. Magn. Reson.* **2015**, *253*, 71–79.

(8)     Keeler, E. G.; Michaelis, V. K.; Colvin, M. T.; Hung, I.; Gor'kov, P. L.; Cross, T. A.; Gan, Z.; Griffin, R. G. ^{17}O MAS NMR Correlation Spectroscopy at High Magnetic Fields. *J. Am. Chem. Soc.* **2017**, *139* (49), 17953–17963.

(9)     Paulino, J.; Yi, M.; Hung, I.; Gan, Z.; Wang, X.; Chekmenev, E. Y.; Zhou, H.-X.; Cross, T. A. Functional Stability of Water Wire–Carbonyl Interactions in an Ion Channel. *Proc. Natl. Acad. Sci.* **2020**, *117* (22), 11908–11915.

(10)   Hu, J.; Chekmenev, E. Y.; Gan, Z.; Gor'kov, P. L.; Saha, S.; Brey, W. W.; Cross, T. A. Ion Solvation by Channel Carbonyls Characterized by ^{17}O Solid-State NMR at 21 T. *J. Am. Chem. Soc.* **2005**, *127* (34), 11922–11923.

(11)   Lin, B.; Hung, I.; Gan, Z.; Chien, P.; Spencer, H. L.; Smith, S. P.; Wu, G. ^{17}O NMR Studies of Yeast Ubiquitin in Aqueous Solution and in the Solid State. *ChemBioChem* **2021**, *22* (5), 826–829.

(12)   Špačková, J.; Fabra, C.; Mittelette, S.; Gaillard, E.; Chen, C.-H.; Cazals, G.; Lebrun, A.; Sene, S.; Berthomieu, D.; Chen, K.; Gan, Z.; Gervais, C.; Métro, T.-X.; Laurencin, D. Unveiling the Structure and Reactivity of Fatty-Acid Based (Nano)Materials Thanks to Efficient and Scalable [17]O and ^{18}O-Isotopic Labeling Schemes. *J. Am. Chem. Soc.* **2020**, *142* (50), 21068–21081.

(13)   Harris, R. K.; Becker, E. D. NMR Nomenclature: Nuclear Spin Properties and Conventions for Chemical Shifts—IUPAC Recommendations. *J. Magn. Reson.* **2002**, *156* (2), 323–326.

(14)   Wu, G. Solid-State ^{17}O NMR Spectroscopy of Organic and Biological Molecules. In *Modern Magnetic Resonance*; Springer International Publishing: Cham, 2017; pp 1–20.

(15)   Wu, G. ^{17}O NMR Studies of Organic and Biological Molecules in Aqueous Solution and in the Solid State. *Prog. Nucl. Magn. Reson. Spectrosc.* **2019**, *114–115*, 135–191.

(16)   Steinschneider, A.; Burgar, M. I.; Buku, A.; Fiat, D. Labeling of Amino Acids and Peptides with Isotopic Oxygen As Followed By [17]O-N.M.R.*. *Int. J. Pept. Protein Res.* **1981**, *18* (3), 324–333.

(17)   Seyfried, M. S.; Lauber, B. S.; Luedtke, N. W. Multiple-Turnover Isotopic Labeling of Fmoc- and Boc-Protected Amino Acids with Oxygen Isotopes. *Org. Lett.* **2010**, *12* (1), 104–106.

(18)   Carnahan, S. L.; Lampkin, B. J.; Naik, P.; Hanrahan, M. P.; Slowing, I. I.; Vanveller, B.; Wu, G.; Rossini, A. J. Probing O-H Bonding through Proton Detected [1]H-[17]O Double Resonance Solid-State NMR Spectroscopy. *J. Am. Chem. Soc.* **2019**, *141* (1), 441–450.

(19)  Klein, B. A.; Tkachuk, D. G.; Terskikh, V. V.; Michaelis, V. K. Expanding the NMR Toolkit for Biological Solids: Oxygen-17 Enriched Fmoc-Amino Acids. *New J. Chem.* **2021**, *45* (28), 12384–12398

(20)  Métro, T. X.; Gervais, C.; Martinez, A.; Bonhomme, C.; Laurencin, D. Unleashing the Potential of $^{17}$O NMR Spectroscopy Using Mechanochemistry. *Angew. Chem. Int. Ed.* **2017**, *56* (24), 6803–6807.

(21)  Perras, F. A.; Chaudhary, U.; Slowing, I. I.; Pruski, M. Probing Surface Hydrogen Bonding and Dynamics by Natural Abundance, Multidimensional, $^{17}$O DNP NMR Spectroscopy. *J. Phys. Chem. C* **2016**, *120* (21), 11535–11544.

(22)  Siegel, R.; Nakashima, T. T.; Wasylishen, R. E. Sensitivity Enhancement of NMR Spectra of Half-Integer Quadrupolar Nuclei in the Solid State via Population Transfer. *Concepts Magn. Reson. Part A* **2005**, *26A* (2), 47–61.

(23)  Yao, Z.; Kwak, H.-T.; Sakellariou, D.; Emsley, L.; Grandinetti, P. J. Sensitivity Enhancement of the Central Transition NMR Signal of Quadrupolar Nuclei under Magic-Angle Spinning. *Chem. Phys. Lett.* **2000**, *327* (1–2), 85–90.

(24)  Prasad, S.; Kwak, H.-T.; Clark, T.; Grandinetti, P. J. A Simple Technique for Determining Nuclear Quadrupole Coupling Constants with RAPT Solid-State NMR Spectroscopy. *J. Am. Chem. Soc.* **2002**, *124* (18), 4964–4965.

(25)  Jardón-Álvarez, D.; Bovee, M. O.; Baltisberger, J. H.; Grandinetti, P. J. Natural Abundance O-17 and S-33 Nuclear Magnetic Resonance Spectroscopy in Solids Achieved through Extended Coherence Lifetimes. *Phys. Rev. B* **2019**, *100* (14), 1–5.

(26)  Blanc, F.; Sperrin, L.; Jefferson, D. A.; Pawsey, S.; Rosay, M.; Grey, C. P. Dynamic Nuclear Polarization Enhanced Natural Abundance $^{17}$O Spectroscopy. *J. Am. Chem. Soc.* **2013**, *135* (8), 2975–2978.

(27)  Michaelis, V. K.; Markhasin, E.; Daviso, E.; Herzfeld, J.; Griffin, R. G. Dynamic Nuclear Polarization of Oxygen-17. *J. Phys. Chem. Lett.* **2012**, *3* (15), 2030–2034.

(28)   Martins, V.; Xu, J.; Wang, X.; Chen, K.; Hung, I.; Gan, Z.; Gervais, C.; Bonhomme, C.; Jiang, S.; Zheng, A.; Lucier, B. E. G.; Huang, Y. Higher Magnetic Fields, Finer MOF Structural Information: $^{17}$O Solid-State NMR at 35.2 T. *J. Am. Chem. Soc.* **2020**, *142* (35), 14877–14889.

(29)   *Peptide Synthesis and Applications*, 2nd ed.; Jensen, K. J., Tofteng Shelton, P., Pedersen, S. L., Eds.; Methods in Molecular Biology; Humana Press: Totowa, NJ, 2013; Vol. 1047.

(30)   Bennett, A. E.; Rienstra, C. M.; Auger, M.; Lakshmi, K. V.; Griffin, R. G. Heteronuclear Decoupling in Rotating Solids. *J. Chem. Phys.* **1995**, *103* (16), 6951–6958.

(31)   Kentgens, A. P. M.; Verhagen, R. Advantages of Double Frequency Sweeps in Static, MAS and MQMAS NMR of Spin I = 3/2 Nuclei. *Chem. Phys. Lett.* **1999**, *300* (3–4), 435–443.

(32)   Harris, R. K.; Becker, E. D.; Cabral de Menezes, S. M.; Granger, P.; Hoffman, R. E.; Zilm, K. W. Further Conventions for NMR Shielding and Chemical Shifts (IUPAC Recommendations 2008). *Pure Appl. Chem.* **2008**, *80* (1), 59–84.

(33)   Pines, A.; Gibby, M. G.; Waugh, J. S. Proton-Enhanced Nuclear Induction Spectroscopy. A Method for High Resolution NMR of Dilute Spins in Solids. *J. Chem. Phys.* **1972**, *56* (4), 1776–1777.

(34)   Vinod Chandran, C.; Madhu, P. K.; Kurur, N. D.; Bräuniger, T. Swept-Frequency Two-Pulse Phase Modulation (SW f-TPPM) Sequences with Linear Sweep Profile for Heteronuclear Decoupling in Solid-State NMR. *Magn. Reson. Chem.* **2008**, *46* (10), 943–947.

(35)   Mason, J. Conventions for the Reporting of Nuclear Magnetic Shielding (or Shift) Tensors Suggested by Participants in the NATO ARW on NMR Shielding Constants at the University of Maryland, College Park, July 1992. *Solid State Nucl. Magn. Reson.* **1993**, *2*, 285−288.

(36)   Herzfeld, J.; Berger, A. E. Sideband Intensities in NMR-Spectra of Samples Spinning at the Magic Angle. *J. Chem. Phys.* **1980**, *73*, 6021−6030.

(37)   Lu, J.; Hung, I.; Brinkmann, A.; Gan, Z.; Kong, X.; Wu, G. Solid-State $^{17}$O NMR Reveals Hydrogen-Bonding Energetics: Not All Low-Barrier Hydrogen Bonds Are Strong. *Angew. Chem. Int. Ed.* **2017**, *56* (22), 6166–6170.

(38)   Kong, X.; O'Dell, L. A.; Terskikh, V.; Ye, E.; Wang, R.; Wu, G. Variable-Temperature $^{17}$O NMR Studies Allow Quantitative Evaluation of Molecular Dynamics in Organic Solids. *J. Am. Chem. Soc.* **2012**, *134* (35), 14609–14617.

(39)   Long, J. R.; Ebelhäuser, R.; Griffin, R. G. $^2$H NMR Line Shapes and Spin−Lattice Relaxation in Ba(ClO$_3$)$_2$ · 2 H$_2$O. *J. Phys. Chem. A* **1997**, *101* (6), 988–994.

(40)   Chiba, T. Deuteron Magnetic Resonance Study of Barium Chlorate Monohydrate. *J. Chem. Phys.* **1963**, *39* (4), 947–953.

(41)   Keeler, E. G.; Michaelis, V. K.; Griffin, R. G. $^{17}$O NMR Investigation of Water Structure and Dynamics. *J. Phys. Chem. B* **2016**, *120* (32), 7851–7858.

(42)   Michaelis, V. K.; Griffin, R. G.; Corzilius, B.; Vega, S. *Handbook of High Field Dynamic Nuclear Polarization*, 1st ed.; Michaelis, V. K., Griffin, R. G., Corzilius, B., Vega, S., Eds.; Wiley, 2020.

(43)   Overhauser, A. W. Polarization of Nuclei in Metals. *Phys. Rev.* **1953**, *92* (2), 411–415.

(44)   Maly, T.; Debelouchina, G. T.; Bajaj, V. S.; Hu, K.-N.; Joo, C.-G.; Mak–Jurkauskas, M. L.; Sirigiri, J. R.; van der Wel, P. C. A.; Herzfeld, J.; Temkin, R. J.; Griffin, R. G. Dynamic Nuclear Polarization at High Magnetic Fields. *J. Chem. Phys.* **2008**, *128* (5), 052211.

(45)   Carver, T. R.; Slichter, C. P. Polarization of Nuclear Spins in Metals. *Phys. Rev.* **1953**, *92* (1), 212–213.

(46)   Michaelis, V. K.; Keeler, E. G.; Ong, T. C.; Craigen, K. N.; Penzel, S.; Wren, J. E. C.; Kroeker, S.; Griffin, R. G. Structural Insights into Bound Water in Crystalline Amino Acids: Experimental and Theoretical $^{17}$O NMR. *J. Phys. Chem. B* **2015**, *119* (25), 8024–8036.

(47)   Björgvinsdóttir, S.; Walder, B. J.; Pinon, A. C.; Emsley, L. Bulk Nuclear Hyperpolarization of Inorganic Solids by Relay from the Surface. *J. Am. Chem. Soc.* **2018**, *140* (25), 7946–7951.

(48)   Pinon, A. C.; Schlagnitweit, J.; Berruyer, P.; Rossini, A. J.; Lelli, M.; Socie, E.; Tang, M.; Pham, T.; Lesage, A.; Schantz, S.; Emsley, L. Measuring Nano- to Microstructures from Relayed Dynamic Nuclear Polarization NMR. *J. Phys. Chem. C* **2017**, *121* (29), 15993–16005.

(49)   Wittmann, J. J.; Eckardt, M.; Harneit, W.; Corzilius, B. Electron-Driven Spin Diffusion Supports Crossing the Diffusion Barrier in MAS DNP. *Phys. Chem. Chem. Phys.* **2018**, *20* (16), 11418–11429.

(50)   Ha, M.; Thiessen, A. N.; Sergeyev, I. V.; Veinot, J. G. C.; Michaelis, V. K. Endogenous Dynamic Nuclear Polarization NMR of Hydride-Terminated Silicon Nanoparticles. *Solid State Nucl. Magn. Reson.* **2019**, *100*, 77–84.

(51)   Vega, A. J. CP/MAS of Quadrupolar S = 3/2 Nuclei. *Solid State Nucl. Magn. Reson.* **1992**, *1* (1), 17–32.

(52)   Barrie, P. J. Distorted Powder Lineshapes in ^{27}Al CP/MAS NMR Spectroscopy of Solids. *Chem. Phys. Lett.* **1993**, *208* (5–6), 486–490.

(53)   Pruski, M.; Lang, D. P.; Fernandez, C.; Amoureux, J. P. Multiple-Quantum Magic-Angle Spinning NMR with Cross-Polarization: Spectral Editing of High-Resolution Spectra of Quadrupolar Nuclei. *Solid State Nucl. Magn. Reson.* **1997**, *7* (4), 327–331.

(54)   Zhao, X.; Hoffbauer, W.; Schmedt auf der Günne, J.; Levitt, M. H. Heteronuclear Polarization Transfer by Symmetry-Based Recoupling Sequences in Solid-State NMR. *Solid State Nucl. Magn. Reson.* **2004**, *26* (2), 57–64.

(55)   van Beek, J. D.; Dupree, R.; Levitt, M. H. Symmetry-Based Recoupling of [17]O–[1]H Spin Pairs in Magic-Angle Spinning NMR. *J. Magn. Reson.* **2006**, *179* (1), 38–48.

(56)   Perras, F. A.; Kobayashi, T.; Pruski, M. Natural Abundance [17]O DNP Two-Dimensional and Surface-Enhanced NMR Spectroscopy. *J. Am. Chem. Soc.* **2015**, *137* (26), 8336–8339.

(57)    Hassan, A.; Quinn, C. M.; Struppe, J.; Sergeyev, I. V.; Zhang, C.; Guo, C.; Runge, B.; Theint, T.; Dao, H. H.; Jaroniec, C. P.; Berbon, M.; Lends, A.; Habenstein, B.; Loquet, A.; Kuemmerle, R.; Perrone, B.; Gronenborn, A. M.; Polenova, T. Sensitivity Boosts by the CPMAS CryoProbe for Challenging Biological Assemblies. *J. Magn. Reson.* **2020**, *311*, 106680.

*Chapter 7 References*

(1)    Liu, X.; Wang, Y.; Wu, T.; He, X.; Meng, X.; Barbaud, J.; Chen, H.; Segawa, H.; Yang, X.; Han, L. Efficient and Stable Tin Perovskite Solar Cells Enabled by Amorphous-Polycrystalline Structure. *Nature Commun.* **2020**, *11* (1), 2678.

(2)    Hall, J. B.; Dobrovolskaia, M. A.; Patri, A. K.; McNeil, S. E. Characterization of Nanoparticles for Therapeutics. *Nanomedicine* **2007**, *2* (6), 789–803.

(3)    McNeil, S. E. Nanoparticle Therapeutics: A Personal Perspective. *WIREs Nanomedicine and Nanobiotechnology* **2009**, *1* (3), 264–271.

(4)    Hu, J.; Whiting, N.; Bhattacharya, P. Hyperpolarization of Silicon Nanoparticles with TEMPO Radicals. *J. Phys. Chem. C* **2018**, *122* (19), 10575–10581.

(5)    Tirotta, I.; Dichiarante, V.; Pigliacelli, C.; Cavallo, G.; Terraneo, G.; Bombelli, F. B.; Metrangolo, P.; Resnati, G. $^{19}$F Magnetic Resonance Imaging (MRI): From Design of Materials to Clinical Applications. *Chem. Rev.* **2015**, *115* (2), 1106–1129.

(6)    Zhao, F.; Ma, M. L.; Xu, B. Molecular Hydrogels of Therapeutic Agents. *Chem. Soc. Rev.* **2009**, *38* (4), 883.

(7)    Jayawarna, V.; Ali, M.; Jowitt, T. A.; Miller, A. F.; Saiani, A.; Gough, J. E.; Ulijn, R. V. Nanostructured Hydrogels for Three-Dimensional Cell Culture Through Self-Assembly of Fluorenylmethoxycarbonyl–Dipeptides. *Adv. Mater.* **2006**, *18* (5), 611–614.

(8)    Gullion, T.; Schaefer, J. Rotational-Echo Double-Resonance NMR. *J. Mag. Res. (1969)* **1989**, *81* (1), 196–200.

(9)     Hing, A. W.; Vega, S.; Schaefer, J. Transferred-Echo Double-Resonance NMR. *J. Mag. Res. (1969)* **1992**, *96* (1), 205–209.

(10)    Hing, A. W.; Vega, S.; Schaefer, J. Measurement of Heteronuclear Dipolar Coupling by Transferred-Echo Double-Resonance NMR. *J. Mag. Res., Series A* **1993**, *103* (2), 151–162.

(11)    Choe, R.; il Yun, S. Fmoc-Diphenylalanine-Based Hydrogels as a Potential Carrier for Drug Delivery. *e-Polymers* **2020**, *20* (1), 458–468.